

THE UNIVERSITY OF TULSA
THE GRADUATE SCHOOL

RESERVOIR CHARACTERIZATION USING DYNAMIC
WELLTEST/PRODUCTION AND MICROSEISMIC DATA

by
Mei Han

A dissertation submitted in partial fulfillment of
the requirements for the degree of Doctor of Philosophy
in the Discipline of Petroleum Engineering

The Graduate School
The University of Tulsa

2012

THE UNIVERSITY OF TULSA
THE GRADUATE SCHOOL

RESERVOIR CHARACTERIZATION USING DYNAMIC
WELLTEST/PRODUCTION AND MICROSEISMIC DATA


by
Mei Han

A DISSERTATION
APPROVED FOR THE DISCIPLINE OF
PETROLEUM ENGINEERING

By Dissertation Committee


_____, Co-advisor
Gaoming Li


_____, Co-advisor
Albert Reynolds



Jingyi Chen



Mohan Kelkar

ABSTRACT

Mei Han (Doctor of Philosophy in Petroleum Engineering)

Reservoir Characterization Using Dynamic Welltest/Production and Microseismic Data

Directed by Gaoming Li and Albert Reynolds

211 pp., Chapter 5: Conclusions

(500 words)

The goal of this research is to integrate dynamic welltest/production and microseismic data to obtain accurate reservoir characterization, which is necessary for early stage reservoir development planning. The early time dynamic data may include a few days of production and subsequent shut-in pressure data. These dynamic data can be integrated to reduce the uncertainties of the reservoir models. However, it is not possible to resolve the layer reservoir rock properties with these dynamic data alone. One possible solution is to collect production logging data, where layer production rates can be inferred. Here, we also explore another possible solution, namely integration of microseismic data which are available during perforation. Microseismic technology has gained popularity recently with the development of multi-stage hydraulic fracturing in shale gas reservoirs, but the application of microseismic technology is mainly limited to fracture characterization. In this research, we explore the application of microseismic data to reservoir porosity and permeability field characterization which would be beneficial in both conventional reservoir and unconventional shale gas reservoirs.

The transient pressure data can resolve the thickness-weighted average permeability in a layered reservoir but are sensitive to the log-permeability of the high porosity, high permeability layers while the microseismic data are more sensitive to the porosities of the low porosity (high velocity) layers. Therefore, these two types of data are complementary and the integration of both types of data can improve the accuracy of the reservoir characterization.

The forward model that is used to calculate the first arrival times is the finite-difference solution of the Eikonal equation. The forward model that is used to predict production data is the commercial simulator ECLIPSE 100. We use the ensemble Kalman filter (EnKF) to assimilate the data. The EnKF does not require computing the gradient of an objective function, and it can be coupled with any forward model easily. In the procedure for integrating production/pressure data and microseismic data considered here, the static geological/geophysical data are assumed to be encapsulated in a multivariate probability density function characterized by a prior mean and covariance for the joint distribution of the porosity and permeability fields. The method is tested with synthetic reservoir models. Excellent data matches are obtained with EnKF and the observed data fall within the uncertainty bounds of the ensemble data predictions.

In the microseismic event location inversion study, we first present an efficient gradient-based method. A novel method is devised to obtain the gradient of the first arrival times to the event location parameters in addition to the first arrival times in one forward model run. The method is applied to a simple one-stage of hydraulic fracture and obtained good event location parameter estimation. Since the arrival time is least sensitive to the event coordinate in the axis where source and receiver are closest, estimation of the coordinate in this direction is least accurate among all coordinates. EnKF is applied to this same event location inversion case and similar results are obtained. However, the ensemble-base method is advantageous in capturing uncertainties in velocity structure.

ACKNOWLEDGEMENTS

I would like to thank my advisors Dr. Gaoming Li and Dr. Albert Reynolds for their generous support, incredible patience and valuable guidance. I also would like to express my thanks to Dr. Jingyi Chen for his generous instructions and suggestions. Extend special thank to committee member Dr. Mohan Kelkar for his valuable advise on this dissertation. I would like express my appreciation to all other faculty members in the Departments of Petroleum Engineering for their guidance through my courses of study as a graduate student. Acknowledgment is made to the donors of the American Chemical Society Petroleum Research Fund (ACS-PRF# 51041-ND9) for support of this research.

My appreciation extends to all the students in the Department of Petroleum Engineering, who have helped me in a lot in different ways. Special appreciation is extended to students in TUPREP (Tulsa University Petroleum Reservoir Exploration Projects) for their help during my research and courses. I am thankful to Judy Teal, Loreta Watkins and Lori Watts for their care and assistance throughout my study in TU.

This work is dedicated to my parents, Xiuting Han and Xiaoe Mei, for their unconditional love and support.

TABLE OF CONTENTS

	Page
ABSTRACT	iii
ACKNOWLEDGEMENTS	v
TABLE OF CONTENTS	vii
LIST OF TABLES	viii
LIST OF FIGURES	xxi
CHAPTER 1: INTRODUCTION	1
1.1 Background and Literature Review	1
1.1.1 <i>Welltest data assimilation using EnKF</i>	1
1.1.2 <i>Microseismic data</i>	3
1.1.3 <i>Forward modeling of microseism</i>	5
1.2 Objectives and Research Scope	7
CHAPTER 2: ASSIMILATING WELLTEST DATA USING ENKF	9
2.1 Methodology	9
2.1.1 <i>EnKF algorithm for data assimilation</i>	9
2.1.2 <i>Doubly stochastic data assimilation with uncertainty on prior in-</i> <i>formation</i>	12
2.2 Single layer examples	16
2.2.1 <i>Single layer heterogeneous case description</i>	16
2.2.2 <i>Case 1: assimilating pressure data at the active well</i>	18
2.2.3 <i>Case 2: assimilating pressure data at the active and monitor wells</i>	24
2.2.4 <i>Case 3: assimilating pressure data with wrong prior mean</i>	29
2.2.5 <i>Case 4: doubly stochastic data assimilation</i>	35
2.3 Two-layer heterogeneous examples	42
2.3.1 <i>Case description</i>	42
2.3.2 <i>Case 1: assimilating pressure data only</i>	44
2.3.3 <i>Case 2: assimilating pressure and layer rate data</i>	53
CHAPTER 3: ASSIMILATING WELLTEST/MICROSEISMIC DATA FOR LAYERED RESERVOIRS	65
3.1 Microseismic data	65
3.1.1 <i>Overview</i>	65
3.1.2 <i>Forward model for first arrival time calculation</i>	66
3.1.3 <i>Assimilating microseismic and welltest data</i>	71

3.2	Two-layer homogeneous case	72
3.2.1	<i>Case description</i>	72
3.2.2	<i>Assimilating pressure transient data only</i>	79
3.2.3	<i>Assimilating microseismic data only</i>	82
3.2.4	<i>Assimilating both microseismic and pressure data</i>	89
3.2.5	<i>Assimilating pressure and layer rate data</i>	99
3.3	Two-layer heterogeneous case	105
3.3.1	<i>Case description</i>	105
3.3.2	<i>Assimilating pressure data only</i>	108
3.3.3	<i>Assimilating microseismic data only</i>	118
3.3.4	<i>Assimilating both microseismic and pressure data</i>	129
3.3.5	<i>Assimilating pressure and layer rate data</i>	143
3.4	Ten-layer homogeneous case	151
CHAPTER 4: MICROSEISMIC EVENT LOCATION		160
4.1	Overview	160
4.2	Event location inversion methodology	160
4.2.1	<i>Gauss-Newton algorithm</i>	160
4.2.2	<i>Sensitivity matrix calculation</i>	163
4.3	Case study	164
4.3.1	<i>Case description</i>	164
4.3.2	<i>Microseismic event location obtained with Gauss-Newton method</i>	169
4.3.3	<i>Microseismic event location obtained with EnKF method</i>	176
4.4	Event location inversion with uncertain velocity structure	188
4.4.1	<i>Case description</i>	188
4.4.2	<i>Microseismic event location estimated using correct, incorrect and an ensemble of velocity structures</i>	191
4.4.3	<i>Microseismic event location estimated using velocity structure updated from assimilating perforation shot microseismic data</i>	192
CHAPTER 5: CONCLUSIONS		199
NOMENCLATURE		202
BIBLIOGRAPHY		202
APPENDIX A: SENSITIVITY ANALYSIS ON EVENT LOCATION		211

LIST OF TABLES

		Page
2.1	Reservoir fluid properties, single layer example	17
2.2	Geostatistical parameters, single layer example	19
3.1	Fluid Properties	74
3.2	Sandstone Properties	74
3.3	True porosity and log-permeability	75
3.4	Porosity and log-permeability	77
3.5	Prior geostatistical parameters, two-layer heterogeneous example	108
3.6	Mean square error between estimated and true, two-layer heterogeneous example	151
3.7	True and prior of porosity and permeability	152
4.1	Velocity structure for microseismic event location inversion	166
4.2	Fracture dimension	166
4.3	Perforation location	166
4.4	Receiver location in monitor well 1	166
4.5	Receiver location in monitor well 2	167
4.6	Receiver location in monitor well 3	167
4.7	Receiver location in monitor well 4	167
4.8	True and prior of porosity and permeability	188
4.9	The true velocity structure	189
4.10	Receiver location in monitor well 1	189
4.11	Receiver location in monitor well 2	190
4.12	Receiver location in monitor well 3	190

LIST OF FIGURES

		Page
2.1	True property fields, single layer example	17
2.2	The updated ensemble mean of log-permeability field, case 1 of single layer example	19
2.3	The updated ensemble mean of porosity field, case 1 of single layer example	20
2.4	Prior and posterior standard deviation for ϕ and $\ln k$ field, case 1 of single layer example	20
2.5	Posterior to prior standard deviation ratio for ϕ and $\ln k$ field, case 1 of single layer example	21
2.6	Skin when assimilating drawdown and buildup data, case 1 of single layer example	22
2.7	Active well pressure match, case 1 of single layer example	23
2.8	Log-log diagnostic plots of the active well pressure data, case 1 of single layer example	24
2.9	The updated ensemble mean of log-permeability field, case 2 of single layer example	25
2.10	The updated ensemble mean of porosity field, case 2 of single layer example	25
2.11	Prior and posterior standard deviation for ϕ and $\ln k$ field, case 2 of single layer example	26
2.12	Skin after assimilating drawdown and buildup data, case 2 of single layer example	27
2.13	Active well pressure match, case 2 of single layer example	28
2.14	Log-log diagnostic plots of the active well pressure data rerun from time 0, case 2 of single layer example	28

2.15	Monitor well drawdown pressure data match during data assimilation, case 2 of single layer example	29
2.16	Monitor well buildup pressure data match during data assimilation, case 2 of single layer example	30
2.17	Monitor well drawdown pressure data match rerun from time 0, case 2 of single layer example	31
2.18	Monitor well buildup pressure data match rerun from time 0, case 2 of single layer example	32
2.19	The updated ensemble mean of log-permeability field, case 3 of single layer example	32
2.20	The updated ensemble mean of porosity field, case 3 of single layer example	33
2.21	Skin after assimilating drawdown and buildup data, case 3 of single layer example	33
2.22	Active well pressure match, case 3 of single layer example	34
2.23	: Log-log diagnostic plots of the active well pressure data, case 3 of single layer example	34
2.24	Monitor well drawdown pressure data match during data assimilation, case 3 of single layer example	35
2.25	Monitor well buildup pressure data match during data assimilation, case 3 of single layer example	36
2.26	The updated ensemble mean of log-permeability field, case 4 of single layer example	37
2.27	The updated ensemble mean of porosity field, case 4 of single layer example	37
2.28	Ensemble mean of log-permeability and porosity after assimilating drawdown and buildup data, case 4 of single layer example	38
2.29	Skin after assimilating drawdown and buildup data, case 4 of single layer example	38
2.30	Active well pressure match, case 4 of single layer example	39

2.31	Log-log diagnostic plots of the active well pressure data, case 4 of single layer example	40
2.32	Monitor well drawdown pressure data match during data assimilation, case 4 of single layer example	40
2.33	Monitor well buildup pressure data match during data assimilation, case 4 of single layer example	41
2.34	True horizontal log-permeability field, two-layer heterogenous example . .	43
2.35	True porosity field, two-layer heterogenous example	44
2.36	The updated ensemble mean of log-permeability field, case 1 of two-layer heterogeneous example	45
2.37	The updated ensemble mean of porosity field, case 1 of two-layer heterogeneous example	46
2.38	Ratio of posterior to prior STD of porosity and log-permeability, case 1 of two-layer heterogeneous example	47
2.39	Skin of layer 1 when assimilating multi-rate drawdown data, case 1 of two-layer heterogeneous example	48
2.40	Skin of layer 2 when assimilating multi-rate drawdown data, case 1 of two-layer heterogeneous example	49
2.41	Effective skin when assimilating multi-rate drawdown data, case 1 of two-layer heterogeneous example	49
2.42	Active well drawdown pressure match during data assimilation, case 1 of two-layer heterogeneous example	49
2.43	Active well drawdown pressure match rerun from time 0, case 1 of two-layer heterogeneous example	50
2.44	Monitor well pressure data match during drawdown 1 data assimilation, case 1 of two-layer heterogeneous example	50
2.45	Monitor well pressure data match during drawdown 2 data assimilation, case 1 of two-layer heterogeneous example	51

2.46	Monitor well drawdown 1 pressure data match rerun from time 0, case 1 of two-layer heterogeneous example	51
2.47	Monitor well drawdown 2 pressure data match rerun from time 0, case 1 of two-layer heterogeneous example	52
2.48	Layer rate of layer 1 data match during data assimilation, case 1 of two-layer heterogeneous example	53
2.49	Layer rate of layer 1 data match rerun from time 0, case 1 of two-layer heterogeneous example	54
2.50	The updated ensemble mean of log-permeability field, case 2 of two-layer heterogeneous example	55
2.51	The updated ensemble mean of porosity field, case 2 of two-layer heterogeneous example	56
2.52	Ratio of posterior to prior STD of porosity and log-permeability, case 2 of two-layer heterogeneous example	57
2.53	Skin of layer 1 when assimilating multi-rate drawdown data, case 2 of two-layer heterogeneous example	58
2.54	Skin of layer 2 when assimilating multi-rate drawdown data, case 2 of two-layer heterogeneous example	59
2.55	Effective skin when assimilating multi-rate drawdown data, case 2 of two-layer heterogeneous example	59
2.56	Active well drawdown pressure match during data assimilation, case 2 of two-layer heterogeneous example	60
2.57	Layer rate of layer 1 data match during data assimilation, case 2 of two-layer heterogeneous example	61
2.58	Monitor well pressure data match during drawdown 1 data assimilation, case 2 of two-layer heterogeneous example	61
2.59	Monitor well pressure data match during drawdown 2 data assimilation, case 2 of two-layer heterogeneous example	62

2.60	Active well drawdown pressure match rerun from time 0, case 2 of two-layer heterogeneous example	62
2.61	Layer rate of layer 1 data match during data assimilation, case 2 of two-layer heterogeneous example	63
2.62	Monitor well drawdown 1 pressure data match rerun from time 0, case 2 of two-layer heterogeneous example	63
2.63	Monitor well drawdown 2 pressure data match rerun from time 0, case 2 of two-layer heterogeneous example	64
3.1	2D Eikonal equation model	67
3.2	Travel time calculation in the 2D Eikonal equation model	67
3.3	2D Eikonal equation model of local minimum	68
3.4	2D travelttime calculation scheme	71
3.5	Microseismic measurement diagram	72
3.6	Velocity structure of the two-layer homogeneous example	76
3.7	Simulated first arrival time map from perforation shot at the bottom reservoir layer, two-layer homogeneous example	76
3.8	Simulated first arrival time map from perforation shot at the top reservoir layer, two-layer homogeneous example	76
3.9	Prior $\ln k$ vs. ϕ , two-layer homogeneous example	78
3.10	$\ln k$ vs. ϕ , after assimilating pressure data only, two layer homogeneous example	80
3.11	Porosity and log-permeability in layer 1 and layer 2 during pressure data assimilation, two layer homogeneous example	81
3.12	Active well pressure data match assimilating pressure data only, two layer homogeneous example	82
3.13	Prior and posterior porosity in layer 1 and layer 2 after assimilating first arrival time of perforation shot of layer 1, two layer homogeneous example	84
3.14	Prior and posterior $\ln k$ in layer 1 and layer 2 after assimilating first arrival time of perforation shot in layer 1, two layer homogeneous example	85

3.15 Prediction assimilating first arrival time of perforation shot in layer 1, two layer homogeneous example	86
3.16 Box plot schematic	87
3.17 $\ln k$ vs. ϕ , after assimilating first arrival times from perforation shot at layer 1, two layer homogeneous example	88
3.18 Porosity in layer 1 and layer 2 after assimilating first arrival time of both perforation shots, two-layer homogeneous example	90
3.19 $\ln k$ in layer 1 and layer 2 after assimilating first arrival time of both perforation shots, two-layer homogeneous example	91
3.20 $\ln k$ vs. ϕ , after assimilating microseismic data, two-layer homogeneous example	92
3.21 First arrival time data match from perforation shot at layer 2, two-layer homogeneous example	92
3.22 Porosity and log-permeability in layer 1 and layer 2 during pressure data assimilation after assimilating microseismic data, two-layer homogeneous example	93
3.23 $\ln k$ vs. ϕ , after assimilating microseismic and pressure data, two-layer homogeneous example	94
3.24 Pressure data match during data assimilation and rerun from time zero, microseismic + pressure data, two-layer homogeneous example	95
3.25 First arrival time data match after assimilating microseismic and pressure data, two-layer homogeneous example	96
3.26 Thickness-weighted average permeability	97
3.27 Layer 1 log-permeability of 10 different ensembles, two-layer homogeneous example	99
3.28 Layer 2 log-permeability of 10 different ensembles, two-layer homogeneous example	100
3.29 Prediction of Layer rate in layer 1 at time day 2 rerunning from time 0 of all ensembles, two-layer homogeneous example	101

3.30	Porosity and log-permeability when assimilating pressure and layer rate data, two-layer homogeneous example	102
3.31	$\ln k$ vs. ϕ , after assimilating pressure and layer rate data, two-layer homogeneous example	103
3.32	pressure prediction after assimilating microseismic and pressure data, two-layer homogeneous example	104
3.33	Layer rate prediction after assimilating microseismic and pressure data, two-layer homogeneous example	104
3.34	Reservoir and well schematic, two-layer heterogeneous example	105
3.35	True porosity and log-permeability distributions, two-layer heterogeneous example	106
3.36	A cross-section of the velocity structure, two-layer heterogeneous example	107
3.37	Prior mean of porosity and log-permeability fields calculated from the 100 initial ensemble members, two-layer heterogeneous example	109
3.38	Prior STD of porosity and log-permeability calculated from the 100 initial ensemble members, two-layer heterogeneous example	110
3.39	Porosity and log-permeability posterior mean after assimilating pressure data only, two-layer heterogeneous example	111
3.40	Porosity and log-permeability posterior STD after assimilating pressure data only, two-layer heterogeneous example	112
3.41	Posterior to prior STD ratio of porosity and log-permeability assimilating pressure data only, two-layer heterogeneous example	113
3.42	Porosity and log-permeability field of the 43rd initial ensemble member, two-layer heterogeneous example	114
3.43	Porosity and log-permeability field of the 43rd ensemble member after assimilating pressure data only, two-layer heterogeneous example	115
3.44	Porosity and log-permeability field of the 78th initial ensemble member, two-layer heterogeneous example	116

3.45	Porosity and log-permeability field of the 78th ensemble member after assimilating pressure data only, two-layer heterogeneous example	117
3.46	Pressure data match of the active well after assimilating pressure data only, two-layer heterogeneous example	119
3.47	Pressure data match of monitor well 1 after assimilating pressure data only, two-layer heterogeneous example	120
3.48	Porosity and log-permeability posterior mean after assimilating microseismic data from perforation shot of layer 1, two-layer heterogeneous example	121
3.49	Porosity and log-permeability posterior STD after assimilating microseismic data from perforation shot of layer 1, two-layer heterogeneous example	122
3.50	Posterior /prior STD ratio of porosity and log-permeability after assimilating microseismic data from perforation shot of layer 1, two-layer heterogeneous example	123
3.51	The first arrival time data match at receivers in monitor well 1 from perforation shot of layer 1, two-layer heterogeneous example	124
3.52	Porosity and log-permeability posterior mean after assimilating microseismic data from perforation shot of layer 2, two-layer heterogeneous example	125
3.53	Porosity and log-permeability posterior STD of layer 1 and 2 after assimilating microseismic data from perforation shot of layer 2, two-layer heterogeneous example	126
3.54	Posterior STD ratio of porosity and log-permeability before and after assimilating the microseismic data from the perforation shot of layer 2, two-layer heterogeneous example	127
3.55	Posterior to prior STD ratio of porosity and log-permeability after assimilating the microseismic data from perforation shots of both layers, two-layer heterogeneous example	128
3.56	First arrival time data match at receivers in monitor well 1 when assimilating microseismic data from perforation shot of layer 2, two-layer heterogeneous example	129

3.57	Porosity and log-permeability posterior mean after assimilating microseismic and pressure data, two-layer heterogeneous example	131
3.58	Porosity and log-permeability posterior STD after assimilating microseismic and pressure data, two-layer heterogeneous example	132
3.59	Posterior STD ratio of porosity and log-permeability between assimilating both pressure and microseismic data and assimilating microseismic data only, two-layer heterogeneous example	133
3.60	Posterior to prior STD ratio of porosity and log-permeability after assimilating both microseismic and pressure data, two-layer heterogeneous example	134
3.61	Active well pressure data match after assimilating microseismic and pressure data during data assimilation and rerun from time 0, two-layer heterogeneous example	135
3.62	Monitor well 1 pressure data match after assimilating microseismic and pressure data during data assimilation and rerun from time 0, two-layer heterogeneous example	136
3.63	Prediction of rate of layer 2 with/without assimilating microseismic data, two-layer heterogeneous example	137
3.64	Ensemble mean of log-permeability field in layer 1 after assimilating pressure data only	138
3.65	Ensemble mean of log-permeability field in layer 1 after assimilating microseismic and pressure data	139
3.66	Ensemble mean of log-permeability field in layer 2 after assimilating pressure data only	140
3.67	Ensemble mean of log-permeability field in layer 2 after assimilating microseismic and pressure data	140
3.68	Prior well gridblock log-permeability of all ensembles, two-layer heterogeneous example	141

3.69	Layer 1 well gridblock log-permeability of all ensembles after data assimilation, two-layer heterogeneous example	141
3.70	Layer 2 well gridblock log-permeability of all ensembles after data assimilation, two-layer heterogeneous example	142
3.71	Predicted layer rate of layer 1 at end of day 2 rerunning from time 0 of all ensembles after data assimilation, two-layer heterogeneous example . . .	144
3.72	Porosity and log-permeability posterior mean after assimilating pressure and layer rate data, two-layer heterogeneous example	145
3.73	Porosity and log-permeability posterior STD after assimilating pressure and layer rate data, two-layer heterogeneous example	146
3.74	Posterior to prior STD ratio of porosity and log-permeability after assimilating pressure and layer rate data, two-layer heterogeneous example . .	147
3.75	Active well pressure data match after assimilating pressure and layer rate data, two-layer heterogeneous example	148
3.76	Pressure data match at monitor well 1 after assimilating pressure and layer rate data, two-layer heterogeneous example	149
3.77	Layer rate data match in layer 1 after assimilating pressure and layer rate data, two-layer heterogeneous example	149
3.78	Layer 1 well gridblock log-permeability of all ensembles after data assimilation, two-layer heterogeneous example	150
3.79	first arrival time and velocity	152
3.80	Prior and posterior porosity and $\ln k$ distribution before and after assimilating microseismic data	153
3.81	Posterior porosity and $\ln k$ by assimilating pressure data and/or microseismic data	154
3.82	Posterior porosity and $\ln k$ uncertainty reduction by assimilating pressure data and/or microseismic data	156
3.83	Thickness average permeability	157
3.84	Prediction after assimilating microseismic and pressure data	158

3.85	Prediction after assimilating pressure data only	159
4.1	Schematic of the first arrival time gradient calculation using Eikonal equation	164
4.2	True microseismic event location in 3D, X-Y and X-Z plots	168
4.3	True vs estimated microseismic location after assimilating first arrival times from monitor well 1 (Gauss-Newton)	171
4.4	The cross-plot of the microseismic event location (x, y, z) and event oc- currence time between the true and the estimated after assimilating first arrival times at monitor well 1 (Gauss-Newton)	172
4.5	True vs estimated microseismic location after assimilating first arrival times from monitor wells 1 and 2 (Gauss-Newton)	173
4.6	The cross-plot of the microseismic event location (x, y, z) and event oc- currence time between the true and the estimated after assimilating first arrival times from monitor wells 1 and 2 (Gauss-Newton)	174
4.7	True vs estimated microseismic location after assimilating first arrival times from monitor wells 1 to 3 (Gauss-Newton)	175
4.8	The cross-plot of the microseismic event location (x, y, z) and event oc- currence time between the true and the estimated after assimilating first arrival times from monitor wells 1 to 3 (Gauss-Newton)	176
4.9	True vs estimated microseismic location after assimilating first arrival times from all 4 monitor wells (Gauss-Newton)	178
4.10	The cross-plot of the microseismic event location (x, y, z) and event oc- currence time between the true and the estimated after assimilating first arrival times from all 4 monitor wells (Gauss-Newton)	179
4.11	True vs estimated microseismic location after assimilating first arrival times from monitor well 1 (EnKF)	180
4.12	The cross-plot of the microseismic event location (x, y, z) and event oc- currence time between the true and the estimated assimilating first arrival times from monitor well 1 (EnKF)	181

4.13	True vs estimated microseismic location after assimilating first arrival times from monitor wells 1 and 2 (EnKF)	182
4.14	The cross-plot of the microseismic event location (x, y, z) and event occurrence time between the true and the estimated after assimilating first arrival times from monitor wells 1 and 2 (EnKF)	183
4.15	True vs estimated microseismic location with 3 monitor wells after assimilating first arrival times from monitor wells 1 to 3 (EnKF)	184
4.16	The cross-plot of the microseismic event location (x, y, z) and event occurrence time between the true and the estimated after assimilating first arrival times from monitor wells 1 to 3 (EnKF)	185
4.17	True vs estimated microseismic location estimation after assimilating first arrival times from all 4 monitor wells (EnKF)	186
4.18	The cross-plot of the microseismic event location (x, y, z) and event occurrence time between the true and the estimated after assimilating first arrival times from all 4 monitor wells (EnKF)	187
4.19	Velocity structure	189
4.20	True microseismic event location in 3D, X-Y and X-Z plots	193
4.21	Initial ensemble of velocity structure model for scenario 3	194
4.22	The cross-plot of the microseismic event location (x, y, z) and event occurrence time between the true and the estimated using correct velocity structure	194
4.23	The cross-plot of the microseismic event location (x, y, z) and event occurrence time between the true and the estimated using incorrect velocity structure	195
4.24	The cross-plot of the microseismic event location (x, y, z) and event occurrence time between the true and the estimated using an ensemble of velocity structure	195
4.25	The cross-plot of z-coordinate between the true and the estimated using correct, incorrect and an ensemble of velocity	196

4.26	Prior and posterior porosity and $\ln k$ assimilating microseismic data . . .	197
4.27	Ensemble of velocity structures updated from assimilating first arrival times of the perforation shots	197
4.28	The cross-plot of the microseismic event location (x, y, z) and event occurrence time between the true and the estimated using the updated velocity structure after assimilating first arrival time from perforation shots . . .	198
4.29	The cross-plot of z-coordinate between the true and the estimated using correct and updated velocity structure	198

CHAPTER 1

INTRODUCTION

1.1 Background and Literature Review

1.1.1 *Welltest data assimilation using EnKF*

In today's environment, it is common to make critical reservoir development decisions based on models developed from geological and geophysical data interpretation prior to obtaining any long-term production data. Although well-testing data are often available, in most cases well test analysis is customarily interpreted based on analytical solutions that assume single-phase flow for a homogeneous reservoir model or, at most, assumes some simple form of heterogeneity, e.g., permeability variation in only the radial direction [48] or only the linear direction [40], or layered reservoirs with each layer homogeneous [39, 35, 33, 13, 32, 36, 37]. While the interpretation of pressure transient data using these analytical solutions are of enormous value, one objective of this work is to integrate pressure transient data into a complex, highly heterogeneous geological model. As when development decisions are made, the only dynamic data available may be those obtained from an extended well test, it is hoped that conditioning a geological model directly to well testing data may reduce the uncertainty in the original geological model and aid early development decisions.

To condition reservoir models obtained from a prior geological or geostatistical model to pressure data, we employ a reservoir simulator (Eclipse 100) as the forward model. To obtain predicted data of reasonable accuracy, we use a hybrid grid with radial grid refinement around a vertical well. The general approach considered has been applied previously to both synthetic data [26, 27, 54, 76] and field data [28]. The procedure used in these works relied on applying a Gauss-Newton method to minimize an objective

function to obtain a MAP estimate or to minimize a set of objective functions to generate an approximate sampling of a probability density function, derived from Bayes theorem, using the randomized maximum likelihood (RML) method [49]. Unfortunately using the Gauss-Newton method relies on generating all sensitivity coefficients, which in general, is not feasible, for large scale problems where the number of data and number of model parameters are both large. In the examples considered here, the model parameters are the gridblock horizontal log-permeabilities and porosities and the permeability in the skin zone(s) where the skin factor is defined by the formula of Hawkins [25]. To condition a set of realizations of the rock property fields to well test data, we assimilate data sequentially using the ensemble Kalman filter (EnKF) [17, 46, 19]. The popularity of EnKF for history matching production or time-lapse seismic data arises from its computational efficiency: data are assimilated sequentially in time with only one forward simulation run for each reservoir model, large covariance matrices do not need to be computed or stored, and one obtains at least an approximate measure of uncertainty in the model estimate (ensemble mean) and future predicted performance. Moreover, it is easy to couple EnKF with any commercial reservoir simulator.

Although EnKF often appears to work well for nonlinear problems including real history matching problems [24, 20, 4], there is always a potential of a consistency issue arising. Specifically for the problem considered here, at each data assimilation time we not only update the rock property fields, we also update the pressure field before predicting forward to the next data assimilation time. The assumption is that the updated dynamic variables (here the pressure field) has the same mean and covariance as the pressure fields that would be obtained if we reran the reservoir simulator from time zero using the updated ensemble of rock property fields. Unfortunately, statistical consistency cannot be proved unless the dynamical system is linear and predicted data are linearly related to the model parameters [60]. For a linear dynamical system with appropriate Gaussian statistics and other reasonable assumptions, it can be shown that EnKF samples the posterior probability density function for the model and state parameters (rock property and pressure field) correctly as the ensemble size becomes infinite [20]. In fact under these

assumptions, EnKF and RML becomes statistically equivalent [72]. Here, the dynamical system is represented by the reservoir simulation equations which, for single-phase flow, are not highly nonlinear. Therefore, it is reasonable to expect that for the assimilation of single-phase flow well test data, statistical consistency may approximately hold, and the final ensemble of reservoir models may give approximate sampling of the posterior pdf conditioned to well test data. However, for a layered reservoir, the pressure transient data cannot resolve the reservoir model parameters of each individual layer. In this situation, reasonable estimates of layer permeabilities and skin factors can be obtained by matching both pressure data and layer rate data from production logging [33, 13, 42].

1.1.2 Microseismic data

Another possible source of data that can help resolve layer reservoir properties are the microseismic data. During hydraulic fracturing stimulation, microseismic energy is released along the propagating fracture. Microseismic waves propagate outwards and the signals are picked up by the receivers placed in the nearby monitor wells or at the surface. Inversion of the microseismic data can yield the microseismic event source locations, which coincide with the hydraulic fractures created during stimulation operations [29, 66]. Microseismic monitoring has become a common practice to characterize the distribution, orientation and extent of hydraulic fractures in tight/shale gas reservoirs [56]. The volume of rock stimulated by hydraulic fracturing can be imaged by detecting and locating the microseismic events [3]. An accurate velocity structure between the treatment and monitor wells is required to locate the microseismic events from microseismic inversion. Sonic logs from the treatment and monitor wells are used for constructing the velocity structure, but it may give very different velocity structure from the perforation timing measurement inversion. Warpinski et al. [67] suggested that the estimated velocity structure from perforation timing inversion is more accurate, and when it is applied to invert the fracture locations from microseismic data obtained during fracture stimulation, it yields a more reasonable fracture location. The velocity structure of the formation can be related to the reservoir rock properties through rock physical models.

The travel velocity of P- and S-wave is a function of porosity and rock elastic properties and the amplitude and its attenuation in microseismic data is related to permeability [80]. Hence the microseismic data can be used to reduce the uncertainty of rock properties. On the other hand, production/welltest data can further improve the accuracy of the velocity model for microseismic event location and give a better hydraulic fracture characterization. Due to the fact that the production/welltest data can only resolve the thickness-weighted average properties but are more sensitive to the log-permeability of the high productive (high porosity, high permeability) layers and the microseismic data are more sensitive to the high velocity (low porosity, low permeability) regions, these two types of data are complimentary to each other in resolving the reservoir rock properties.

Microseismic data have been applied to reservoir characterization in other studies. Rothert and Shapiro [55, 58] developed an approach for 3-D mapping of the permeability distribution in heterogeneous geothermal reservoirs and aquifers using the seismic emission (microseismicity) induced in rocks by fluid injections (e.g., borehole hydraulic tests). The approach, called seismicity-based reservoir characterization (SBRC), is based on the hypothesis that microseismicity can be activated by perturbations of the pore pressure caused by fluid injection. The pore-pressure is a function of the tensor of the hydraulic diffusivity which is proportional to the permeability tensor. In our study, we are going to resolve the velocity structure, which is a function of porosity, by assimilating the first arrival time data of microseismic events. The log-permeability, assumed to be correlated with porosity, can be characterized once the velocity structure is determined.

The inversion of hypocenter (event location) has been extensively investigated in seismology [38, 2]. A least-squares inverse method is generally used to minimize the difference between the observed and predicted data assuming the velocity structure is known. Due to the uncertainty in the velocity structure used in event location inversion, the joint hypocenter-velocity inversion of local earthquake arrival-time data has been investigated since the mid-1970s [2]. Fehler et al. [22] first applied the methodology to a set of hypocenters that were occurred during a hydraulic injection to estimate the orientations of the major seismically active fracture planes. Eisner et al. [14] highlighted

several common sources of error related to the location of microseismic events using both surface and downhole arrays of geophones. However the study of Eisner et al. [14] is based on the assumption that the medium in which the acoustic wave travels is isotropic and homogeneous in all directions, even in the vertical direction. Maxwell [44] demonstrated the influence of velocity model errors on the event location by showing an example which results in significant mislocation of microseismic events with an incorrect velocity model. The variation in event location uncertainty associated with different geophone array locations is demonstrated in Maxwell [44]. The joint hypocenter-velocity inversion was applied to hydraulic fracturing study with the hypocenter parameters and the velocity structure either being explicitly coupled, also referred to as separation of parameters [61, 6] or fully implicitly coupled [12, 71, 7]. However, the joint hypocenter-velocity inversion is not in the scope of this study.

In our study of microseismic event location inversion, once the first arrival times are predicted from the source-receiver pairs, an objective function is constructed. The objective function includes two parts: 1) the mismatch between the predicted data and the observations; 2) the mismatch between the current estimated parameters and the prior knowledge of the model parameters. In our case, the prior knowledge of the event location parameters are the perforation locations. The second part is used to constrain the optimization problem in case there is not enough information to uniquely determine the well location parameters [49]. Minimization of the objective function gives the estimated event locations that are not far from the constraints (perforation locations), but match the observed first arrival times.

1.1.3 Forward modeling of microseism

The seismic wave traveltimes through different media can be calculated in a variety of ways. The first one is raytracing, which can be divided into shooting raytracing and bending raytracing. The ray path that the energy travels is computed by using Snell's law. Raytracing is based on the concept that the seismic energy of infinitely high frequency follows a trajectory determined by the raytracing equations. In shooting

raytracing methods, a fan of rays is shot from the source at many different take-off angles. The travel time is calculated using the ray that connects the source and receiver [31, 10]. Bending raytracing methods start with an initial, probably incorrect guess for the ray path. The ray path is bent by a perturbation method until it satisfies a minimum travelttime criterion [61, 63, 5]. Although the raytracing technique was applied to hydraulic fracture mapping, the velocity structure models used in these studies are assumed to be homogeneous layers [6, 67, 50]. The raytracing methods also have two disadvantages. First, raytracing cannot handle the strongly varying velocity fields and the raypath may not be unique. To ascertain the minimum travelttime, all these paths should be computed and compared, which is time consuming. Second, raytracing can not deal with the shadow zones, even in a smooth medium. Shadow zones are areas in which rays cannot be found [64].

To overcome the problems in raytracing, some authors introduced modified raytracing methods or applied the raytracing methods to anisotropic and laterally heterogeneous media [75, 69, 70, 8, 68, 11]. But the velocity models used in their papers are represented by layer or block structures. It is difficult to adapt the method to represent a complex geologic model. Other authors proposed raytracing methods with a triangular mesh, which can be used to represent complex geological structures, but it still has the multi-path problem [9, 62]. In addition, minimum travelttime tree algorithm (MTTT) was proposed by Nakanishi and Yamaguchi [47], and was developed by Zhao et al. [78]. However, MTTT needs a large computation cost compared to the finite-difference method, which will be used in our study.

Finite-difference solution of the Eikonal equation was developed to replace ray tracing in some applications for the first-arrival time calculation. Vidale [64, 65] first introduced a finite-difference method to solve the Eikonal equation. The improved version was developed by Qin et al. [52], but it fails to handle media with high velocity contrast. Zhao [79] greatly improved the finite-difference method by combining the Eikonal equation, Fermats principle and Huygens principle. In addition, both the idea (considering all possible waves) of Podvin and Lecomte [51] and the method based on curved

wavefront [57] are used in his study. The traveltime calculation in his method [79] avoids shadow-zone problems and can handle arbitrary velocity variations. In this dissertation, we will use the finite-difference solution to the Eikonal equation as the forward model for predicting the microseismic first arrival times for heterogeneous media [74]. Although the finite-difference method has been applied to the anisotropic media [30, 21, 59, 34], it is beyond the scope of this study. The velocity of each grid cell can be different and the velocity is related to the porosity and rock mechanical properties through a functional form [53, 16]. Considering all possible ray paths (transmission, refraction, and defraction) and wave mapping directions (four outward wave directions and four reverse wave directions), there are sixteen traveltimes calculated at each point in the model by the finite-difference solution to Eikonal equation. The one with the minimum travel time is the first arrival time.

1.2 Objectives and Research Scope

The goal of this research is to integrate dynamic welltest/production and microseismic data to obtain accurate reservoir characterization. The specific items considered in the research plan are:

1. To integrate well test data into heterogeneous reservoir models generated from geological and geophysical data using the ensemble Kalman filter (EnKF). In the single layer case, to assimilate pressure transient data at active well and interference pressure data at monitor wells during drawdown and buildup to improve estimation of the porosity and permeability field. To investigate the effect of an incorrect prior model on the posterior model with and without considering the uncertainty in the prior model. In the layered reservoir case, to further reduce the uncertainty in rock property fields by integration of production log data (layer flow rates).
2. To assimilate both microseismic and dynamic production/welltest data to reduce the uncertainty of the porosity and permeability fields using the EnKF. The strategy is to assimilate the microseismic data first to reduce the uncertainty of rock proper-

ties in the low porosity layers and then assimilate the dynamic production/welltest data to reduce the uncertainty of the rock properties of the high porosity layers.

3. To apply gradient-based and ensemble-based methods to determine the microseismic event locations given an accurate velocity profile or uncertain velocity structure. The microseismic event location parameters may include the event location and its time of occurrence, which may be used to characterize the fracture propagation and distribution. Accurate fracture characterization will help reservoir modeling and hence future reservoir production forecasts.

CHAPTER 2

ASSIMILATING WELLTEST DATA USING ENKF

2.1 Methodology

2.1.1 *EnKF algorithm for data assimilation*

The ensemble Kalman filter(EnKF) is introduced by Evensen [17] as an alternative to extended Kalman filter. The EnKF is a Monte Carlo method in which an ensemble of states is employed to represent the mean and covariance, which are updated sequentially in time [15]. The EnKF equations are typically introduced by defining the N_m -dimensional column vector of model parameters denoted by m , which may include reservoir gridblock porosities and permeabilities, skin factor etc in reservoir characterization cases. We let $t_n, n = 1, 2, \dots$, denote the simulation time steps and let N_p -dimensional column vector, p^n denote the vector of dynamical variables which are primary variables of the reservoir simulation equations at time t_n , such as reservoir gridblock pressures and saturations. The vector d^n represents the N_n -dimensional column vector of predicted data at time t_n . The reservoir simulator relation between the N_n -dimensional column vector of predicted data given at the n th data assimilation step is denoted by

$$d^n = g_n(m, p^n). \quad (2.1)$$

Define the $N_y = N_m + N_p$ -dimensional state vector, y^n as

$$y^n = \begin{bmatrix} m^n \\ p^n \end{bmatrix}, \quad (2.2)$$

where the state vector at t_n contains both the reservoir model parameters and information

on the state of the reservoir system. Although m contains only static variables, we use m^n in Eq. 2.2 to indicate that the estimation of m changes at every data assimilation step.

Assuming that measurement errors at any two distinct data assimilation times are independent, it can be shown using Bayes theorem that the probability density function (pdf) for y^n conditional to all data at times up to and including those at t_n is given by

$$f(y^n | d_{obs}^n \cdots d_{obs}^1) = a f(d_{obs}^n | y^n) f(y^n | d_{obs}^{n-1} \cdots d_{obs}^1), \quad (2.3)$$

where a is the normalizing constant and throughout the derivation, f always denotes a pdf. The pdf $f(y^n | d_{obs}^{n-1} \cdots d_{obs}^1)$ represents the prior pdf for y^n before assimilation data d_{obs}^n . We use a subscript p to represent prior and assume this prior is Gaussian with mean $\overline{y^{n,p}}$ and covariance matrix $C_{Y^{n,p}}$. We also assume that the vector of measurement errors at any t_n is Gaussian with mean zero and covariance C_{D^n} . With the above assumptions, Eq. 2.3 can be written as

$$f(y^n | d_{obs}^n \cdots d_{obs}^1) = a \exp\left(-\frac{1}{2}(y^n - \overline{y^{n,p}})^T C_{Y^{n,p}}^{-1} (y^n - \overline{y^{n,p}}) - \frac{1}{2}(d^n - d_{obs}^n)^T C_{D^n}^{-1} (d^n - d_{obs}^n)\right), \quad (2.4)$$

which represents the pdf we wish to sample.

The derivation of EnKF for a nonlinear data functional can be done by conveniently adding the predicted data to the original state vector to obtain the augmented state vector [18] defined by

$$\tilde{y}^n = \begin{bmatrix} m^n \\ p^n \\ d^n \end{bmatrix}, \quad (2.5)$$

for $n = 1, 2, \dots$. Letting

$$H = [O \quad I_{N_n}], \quad (2.6)$$

where O is an $N_n \times (N_m + N_p)$ null matrix and I_{N_n} is an $N_n \times N_n$ identity matrix. We see that

$$d^n = H\tilde{y}^n. \quad (2.7)$$

So by the trick of adding d^n to the state vector, we have a linear relationship between the data vector d^n and the augmented state vector \tilde{y}^n , making it possible to write down the formula for the analysis step analytically. However, this trick does not remove the effect of the nonlinearity. As shown in Li and Reynolds [43], augmenting the state vector with data results in a correct procedure for sampling the pdf if, and only if, at every data assimilation time step, the predicted data vector is a linear function of the combined (unaugmented) state vector [15]. Using the assumptions made in the derivations of Zafari and Reynolds [72] and Li and Reynolds [43], the pdf in Eq. 2.4 can be written as

$$\begin{aligned} f(\tilde{y}^n | d_{obs}^n \cdots d_{obs}^1) = \\ a \exp\left(-\frac{1}{2}(\tilde{y}^n - \overline{\tilde{y}^{n,p}})^T C_{\tilde{Y}^{n,p}}^{-1} (\tilde{y}^n - \overline{\tilde{y}^{n,p}}) - \frac{1}{2}(H\tilde{y}^n - d_{obs}^n)^T C_{D^n}^{-1} (H\tilde{y}^n - d_{obs}^n)\right). \end{aligned} \quad (2.8)$$

The posteriori pdf of Eq. 2.8 can be sampled using the randomized maximum likelihood (RML) and a corresponding sample is

$$\tilde{y}_i^{n,u} = \tilde{y}_i^{n,p} + C_{\tilde{Y}^{n,p}} H^T (C_{D^n} + H C_{\tilde{Y}^{n,p}} H^T)^{-1} (d_{uc,i}^n - H\tilde{y}_i^{n,p}), \quad (2.9)$$

where $\tilde{y}_i^{n,p}$ is a sample of the prior Gaussian pdf for \tilde{y}^n and $d_{uc,i}^n$ is a sample of the Gaussian pdf which has mean d_{obs}^n and covariance C_{D^n} . The covariance matrix $C_{\tilde{Y}^{n,p}}$ is estimated by

$$C_{\tilde{Y}^{n,p}} = \frac{1}{N_e - 1} \sum_{i=1}^{N_e} (\tilde{y}_i^{n,p} - \overline{\tilde{y}^{n,p}})(\tilde{y}_i^{n,p} - \overline{\tilde{y}^{n,p}})^T, \quad (2.10)$$

where

$$\overline{\tilde{y}^{n,p}} = \frac{1}{N_e} \sum_{i=1}^{N_e} \tilde{y}_i^{n,p} \quad (2.11)$$

and N_e is the number of ensemble members. Define the Kalman gain matrix as

$$K^n = C_{\tilde{Y}^{n,p}} H^T (C_{D^n} + H C_{\tilde{Y}^{n,p}} H^T)^{-1} \quad (2.12)$$

where

$$C_{\tilde{Y}^{n,p}} H^T = \frac{1}{N_e - 1} \sum_{i=1}^{N_e} (\tilde{y}_i^{n,p} - \overline{\tilde{y}^{n,p}}) (d_i^{n,p} - \overline{d^{n,p}})^T, \quad (2.13)$$

$$H C_{\tilde{Y}^{n,p}} H^T = \frac{1}{N_e - 1} \sum_{i=1}^{N_e} (d_i^{n,p} - \overline{d^{n,p}}) (d_i^{n,p} - \overline{d^{n,p}})^T. \quad (2.14)$$

Then, Eq. 2.9 becomes

$$\tilde{y}_i^{n,u} = \tilde{y}_i^{n,p} + K^n (d_{uc,i}^n - H \tilde{y}_i^{n,p}). \quad (2.15)$$

One of the advantages that EnKF has is that these covariance matrices do not need to be explicitly computed or stored as C_Y is approximated from these set of predictions [43].

2.1.2 Doubly stochastic data assimilation with uncertainty on prior information

As the prior mean and covariance of the property fields obtained from core, log and other geological data can sometimes be erroneous, a doubly stochastic model is applied to account for the uncertainty in the prior information. In the doubly stochastic model, a correction to the prior mean and covariance matrix is adjusted together with the heterogeneous field during history matching [42].

Here, we only consider the partially "doubly-stochastic" model, where the prior mean is uncertain. We assume that the prior covariance matrix is accurately known. The Gaussian random column vector $m_{\ln k}$ denotes the log-permeability field with mean $\overline{m}_{\ln k}$ and covariance matrix $C_{m_{\ln k}}$. The Gaussian random column vector m_ϕ denotes the porosity field with mean \overline{m}_ϕ and covariance matrix C_{m_ϕ} . As the prior mean is uncertain, we define $\theta_{\ln k}$ and θ_ϕ , respectively, as the Gaussian random correction column vectors to the prior means of the log-permeability and porosity fields. Note that we may use

different corrections for each facies or geologic layer. The mean and covariance matrix of the correction column vector $\theta_{\ln k}$ for log-permeability are $\bar{\theta}_{\ln k}$ and $C_{\Theta_{\ln k}}$, respectively. The corresponding mean and covariance matrix of the correction column vector θ_ϕ for porosity are $\bar{\theta}_\phi$ and C_{Θ_ϕ} .

The complete set of reservoir model parameters is contained in the column vector defined by

$$m = [m_{\ln k}^T, \theta_{\ln k}^T, m_\phi^T, \theta_\phi^T, s^T]^T \quad (2.16)$$

where s is a Gaussian random vector of well skin factors or the skin zone log-permeabilities. For simplicity, we define

$$x_{\ln k} = \begin{bmatrix} m_{\ln k} \\ \theta_{\ln k} \end{bmatrix}, x_\phi = \begin{bmatrix} m_\phi \\ \theta_\phi \end{bmatrix} \quad (2.17)$$

and then

$$m = \begin{bmatrix} x_{\ln k} \\ x_\phi \\ s \end{bmatrix}. \quad (2.18)$$

The prior mean of the model parameter vector m is denoted as

$$\bar{m} = [\bar{m}_{\ln k}^T, \bar{\theta}_{\ln k}^T, \bar{m}_\phi^T, \bar{\theta}_\phi^T, \bar{s}^T]^T = [\bar{x}_{\ln k}^T, \bar{x}_\phi^T, \bar{s}^T]^T. \quad (2.19)$$

The prior covariance matrix is given by

$$C_M = \begin{bmatrix} C_{M_{\ln k}} & O & C_{M_{\ln k, \phi}} & O & O \\ O & C_{\Theta_{\ln k}} & O & O & O \\ C_{M_{\ln k, \phi}} & O & C_{M_\phi} & O & O \\ O & O & O & C_{\Theta_\phi} & O \\ O & O & O & O & C_s \end{bmatrix} = \begin{bmatrix} C_{x_{\ln k}} & C_{x_{\ln k, \phi}} & O \\ C_{x_{\ln k, \phi}} & C_{x_\phi} & O \\ O & O & C_s \end{bmatrix} \quad (2.20)$$

where $C_{M_{\ln k, \phi}}$ is the cross-covariance between $\ln k$ and ϕ and

$$C_{x_{\ln k}} = \begin{bmatrix} C_{M_{\ln k}} & O \\ O & C_{\Theta_{\ln k}} \end{bmatrix} \quad (2.21)$$

$$C_{x_{\phi}} = \begin{bmatrix} C_{M_{\phi}} & O \\ O & C_{\Theta_{\phi}} \end{bmatrix} \quad (2.22)$$

$$C_{x_{\ln k, \phi}} = \begin{bmatrix} C_{M_{\ln k, \phi}} & O \\ O & O \end{bmatrix}. \quad (2.23)$$

Here, we assume the corrections to the prior means θ_{ϕ} and $\theta_{\ln k}$, and s are independent of each other and are also independent of the Gaussian random vectors m_{ϕ} and $m_{\ln k}$. Under the above assumptions, the prior probability density function (pdf) for m is,

$$\begin{aligned} f(m) &= \alpha \exp\left\{-\frac{1}{2}(m - \bar{m})^T C_M^{-1}(m - \bar{m})\right\} = \\ &\alpha \exp\left\{-\frac{1}{2} \begin{bmatrix} m_{\ln k} - \bar{m}_{\ln k} \\ m_{\phi} - \bar{m}_{\phi} \end{bmatrix}^T \begin{bmatrix} C_{M_{\ln k}} & C_{M_{\ln k, \phi}} \\ C_{M_{\ln k, \phi}} & C_{M_{\ln k}} \end{bmatrix}^{-1} \begin{bmatrix} m_{\ln k} - \bar{m}_{\ln k} \\ m_{\phi} - \bar{m}_{\phi} \end{bmatrix}\right\} \\ &\exp\left\{-\frac{1}{2}(\theta_{\ln k} - \bar{\theta}_{\ln k})^T C_{\Theta_{\ln k}}^{-1}(\theta_{\ln k} - \bar{\theta}_{\ln k})\right\} \\ &\exp\left\{-\frac{1}{2}(\theta_{\phi} - \bar{\theta}_{\phi})^T C_{\Theta_{\phi}}^{-1}(\theta_{\phi} - \bar{\theta}_{\phi})\right\} \\ &\exp\left\{-\frac{1}{2}(s - \bar{s})^T C_s^{-1}(s - \bar{s})\right\} \end{aligned} \quad (2.24)$$

where α is a normalizing coefficient. To generate the initial ensemble of N_e realizations of the model parameters, we need to sample from the pdf of Eq. 2.24. In the example that will be presented in Chapter 2.2.5, the initial ensemble of correlated log-permeability and porosity fields ($m_{\ln k}$ and m_{ϕ}) are generated using Gaussian co-simulation [23]. The realizations of the corrections to the prior means $\theta_{\ln k}$ and θ_{ϕ} and skin factors s are generated by sampling their individual Gaussian prior pdfs.

Note that the reservoir characteristic parameters (log-permeability and porosity

fields), which are input into the reservoir simulator, are obtained by

$$\ln k = m_{\ln k} + E\theta_{\ln k} = [I \ E]x_{\ln k} \quad (2.25)$$

and

$$\phi = m_{\phi} + E\theta_{\phi} = [I \ E]x_{\phi}, \quad (2.26)$$

where E is a matrix whose i th column has a value 1 for every gridblock corresponding to the prior mean for $\theta_{\ln k, i}$ or $\theta_{\phi, i}$ of the i th geological facies or layer and 0 otherwise, i.e., $E\theta_{\ln k}$ is vector of the same dimension as $m_{\ln k}$ with the j th component of $E\theta_{\ln k}$ equals to the correction to the prior mean for the j th component of $m_{\ln k}$, and a similar relation holds for $E\theta_{\phi}$. For example, for a two-layer case where we have different prior means for each layer, the Gaussian random vector for porosity is given by

$$m_{\phi} = \begin{bmatrix} m_{\phi 1} \\ \vdots \\ m_{\phi N_g} \\ m_{\phi N_g + 1} \\ \vdots \\ m_{\phi 2N_g} \end{bmatrix} \quad (2.27)$$

where N_g is the number of gridblocks in each layer.

$$E = \begin{bmatrix} 1 & 0 \\ \vdots & \vdots \\ 1 & 0 \\ 0 & 1 \\ \vdots & \vdots \\ 0 & 1 \end{bmatrix} \quad (2.28)$$

$$\theta_\phi = \begin{bmatrix} \theta_{\phi 1} \\ \theta_{\phi 2} \end{bmatrix} \quad (2.29)$$

where $\theta_{\phi 1}$ and $\theta_{\phi 2}$ are the corrections to the prior means of porosity in the first and second layers. Then,

$$\phi = m_\phi + E\theta_\phi = \begin{bmatrix} m_{\phi 1} + \theta_{\phi 1} \\ \vdots \\ m_{\phi N_g} + \theta_{\phi 1} \\ m_{\phi N_g+1} + \theta_{\phi 2} \\ \vdots \\ m_{\phi 2N_g} + \theta_{\phi 2} \end{bmatrix}. \quad (2.30)$$

2.2 Single layer examples

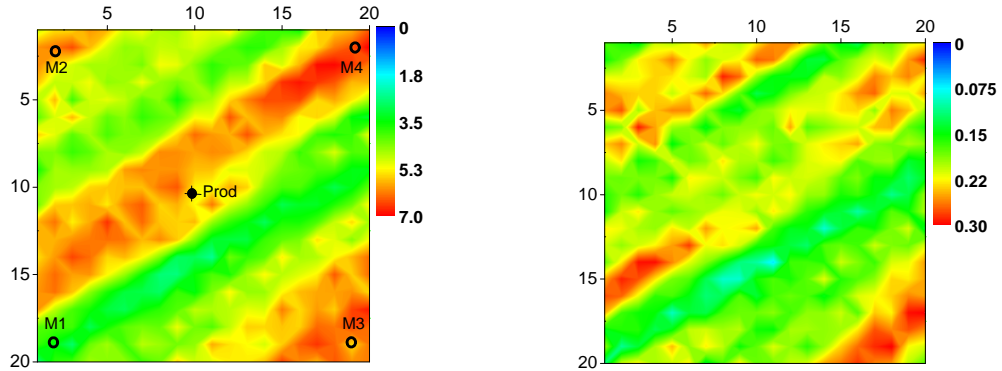
2.2.1 Single layer heterogeneous case description

First we consider a one-layer synthetic heterogeneous reservoir in this example. The reservoir consists of a 20 by 20 grid system. For each gridblock, $\Delta x = \Delta y = 200$ ft. The thickness of the reservoir is 20 ft. The reservoir is assumed to be isotropic and the true horizontal log-permeability is shown in Fig. 2.1(a). There is a long high permeability channel running from the lower left corner to the upper right corner. The true porosity is correlated with log-permeability and its distribution is shown in Fig. 2.1(b). There are five wells drilled in the reservoir, as shown in the log-permeability map (Fig. 2.1(a)). An active well is located at the center of the reservoir inside the high permeability channel and four monitor wells are located at the four corners to provide interference test data. To capture early transient behavior, we use a radial type local grid refinement around the active well with 20 radial rings. In which first 5 radial rings close to the wellbore are treated as the skin zone. To simulate the skin effect, we define the first 5 radial rings close to the wellbore as the skin zone with a radius of 1.1 ft. The true skin factor is

1.525, calculated using the Hawkins's formula, i.e.,

$$s = \left(\frac{k_{wG}}{k_s} - 1 \right) \ln \left(\frac{r_s}{r_w} \right) \quad (2.31)$$

where k_{wG} is the well gridblock permeability; k_s is the skin zone permeability; r_s is the skin zone radius; and r_w is the wellbore radius. The reservoir fluid properties are listed in Table 2.1. The initial reservoir pressure is 5000 psi. The initial water saturation is equal to irreducible water saturation, $S_{iw} = 0.1$. In addition, water is slightly compressible (Table 2.1), so we effectively have only single-phase oil flow in the reservoir during the well test.



(a) Horizontal log-permeability

(b) Porosity

Figure 2.1: True property fields, single layer example

p_i , psi	5000
B_{oi} , RB/STB	1.004
B_w , RB/STB	1.0
c_o , psi^{-1}	1.4×10^{-6}
c_w , psi^{-1}	4.0×10^{-6}
μ_o , cp	2.0
μ_w , cp	1.0
ρ_o , lbm/ft^3	40.0
ρ_w , lbm/ft^3	62.4
S_{iw}	0.1
S_{wi}	0.1

Table 2.1: Reservoir fluid properties, single layer example

The test consists of a 2-day drawdown period followed by a 2-day buildup period. In this case, we assimilate pressure drawdown and buildup data of the active well alone or with the interference pressure data of the monitor wells to estimate log-permeability, porosity distribution and skin zone log-permeability.

For the single layer example, we consider four cases. In case 1 and case 2, we assume that the prior means for $\ln k$ and ϕ are known exactly and all the realizations are generated using the same mean as the one used to generate the true geological field. In case 1, we only assimilate pressure drawdown and buildup data from the active well while in case 2 we assimilating pressure drawdown and buildup data from active well and the interference pressure data of four monitor wells. In case 3, we use incorrect prior means but do not consider the uncertainty in these prior means, and hence the initial ensemble of realizations are generated using prior means different from the true geological field. In case 4, we consider the uncertainty of the prior means using a partially doubly stochastic model. The measurement error for pressure is 1 psi.

2.2.2 Case 1: assimilating pressure data at the active well

In this case, we assimilate pressure drawdown and buildup data of the active well only. The ensemble size is 90 and the initial ensemble of porosity and log-permeability realizations are generated using Gaussian co-simulation with statistical parameters given in Table 2.2. We assume that the prior means for log permeability and porosity are known exactly and all the realizations are generated using the same mean as the one used to generate the true geological field. The ensemble of the skin factor realizations are generated with a mean equal to 3 and a variance equal to 2.

Fig. 2.2 shows the ensemble mean of the log-permeability distribution after matching the drawdown data (Fig. 2.2(a)) and then buildup data (Fig. 2.2(b)). Compared to the truth (Fig. 2.1(a)), the estimated log-permeability field after assimilating pressure drawdown and buildup data gives a reasonable approximation of the true geology. The channel direction is close to the truth and the estimated channel connects the active well and well M4 as in the truth. A good estimate of the low permeability zone between

Mean of $\ln k$	5.0
Mean of ϕ	0.2
Standard deviation of $\ln k$, $\sigma_{\ln k}$	0.8
Standard deviation of ϕ , σ_{ϕ}	0.05
Correlation coefficient, $\rho_{\ln k, \phi}$	0.6
Angle α	30°
Long range, r_1 (ft)	8000
Short range, r_2 (ft)	600

Table 2.2: Geostatistical parameters, single layer example

the active well and monitor well M3 was also obtained. The estimated porosity field is of similar quality compared to the truth as shown in Fig. 2.3. Good estimates of the porosity are obtained as porosity is fairly strongly correlated with log-permeability as shown in Table 2.2. Moreover, at the end of the drawdown test, we have reached the pseudo-steady state flow. Fig. 2.4 shows prior and posterior standard deviation for porosity and log-permeability field and Fig. 2.5 shows the posterior to prior STD ratio fields by dividing the posterior STD by prior STD. Standard deviations of both porosity and log-permeability fields are significantly reduced, especially in log-permeability around the well region.

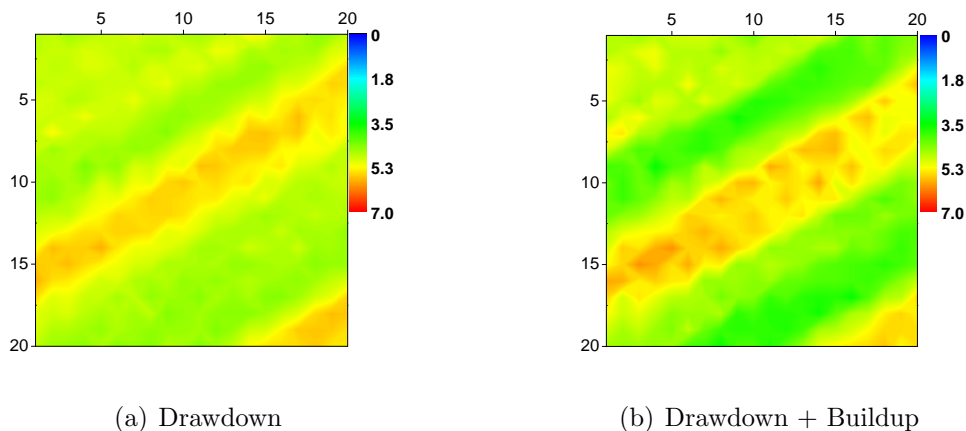
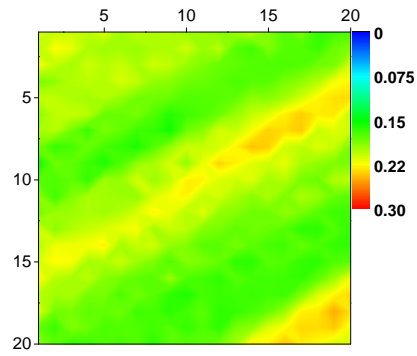
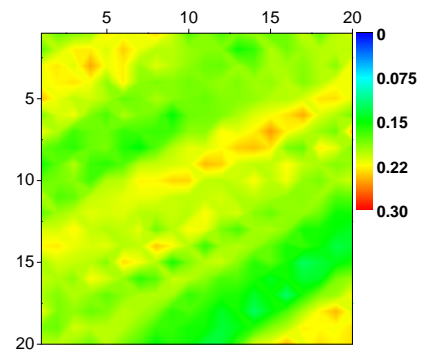


Figure 2.2: The updated ensemble mean of log-permeability field, case 1 of single layer example

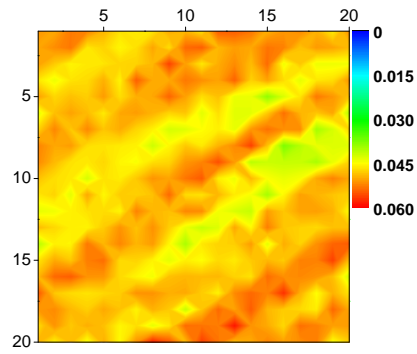


(a) Drawdown

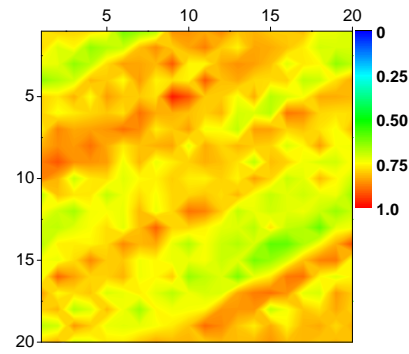


(b) Drawdown + Buildup

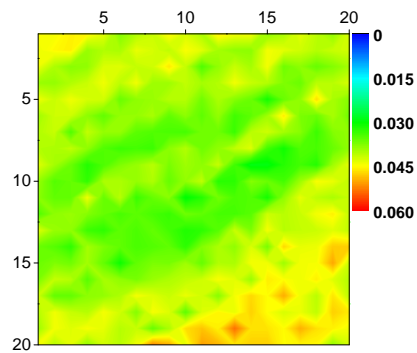
Figure 2.3: The updated ensemble mean of porosity field, case 1 of single layer example



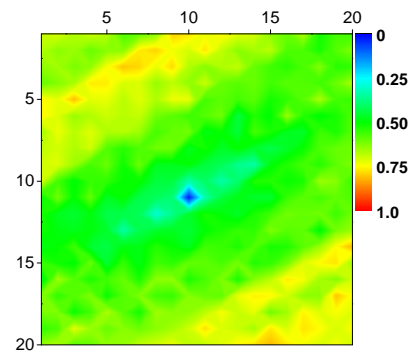
(a) Prior standard deviation of ϕ



(b) Prior standard deviation of $\ln k$

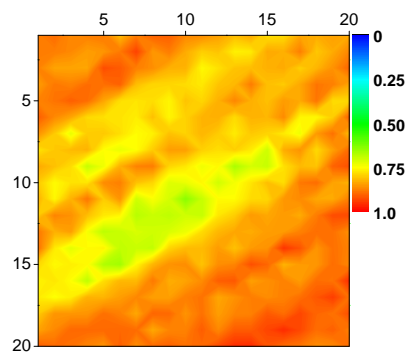


(c) Posterior standard deviation of ϕ

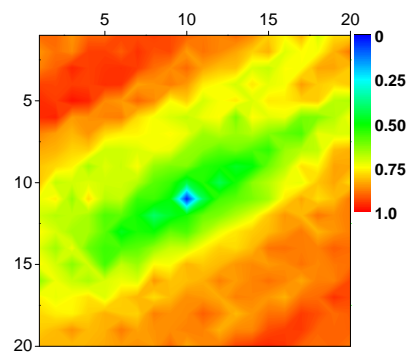


(d) Posterior standard deviation of $\ln k$

Figure 2.4: Prior and posterior standard deviation for ϕ and $\ln k$ field, case 1 of single layer example



(a) Prior standard deviation of ϕ



(b) Prior standard deviation of $\ln k$

Figure 2.5: Posterior to prior standard deviation ratio for ϕ and $\ln k$ field, case 1 of single layer example

Fig. 2.6(c) shows the evolution of the estimated well gridblock log-permeability, skin zone log-permeability and skin factor during data assimilation. The x-axis is the data assimilation step index. The first 15 steps pertain to the assimilation of the drawdown pressure data and the second 15 steps pertain to the assimilation of the buildup data. As mentioned earlier, we use 5 local radial rings to represent the skin zone around the well. During data assimilation, we estimate the skin zone log-permeability $\ln k_s$, instead of the skin factor directly. The skin factor is calculated using Hawkin's formula (Eq. 2.31). Throughout, in Fig. 2.6(c) and similar figures, a red straight line represents the true value; a curve through circles is the ensemble mean (the parameter estimate) and the two curves through triangles are the ensemble mean plus or minus 3 standard deviations which give a characterization of the uncertainty in the estimated parameters. From Fig. 2.6(a), we see that the uncertainty in the well gridblock log-permeability is reduced significantly after the assimilation of the first few pressure drawdown data, and then does not change substantially until the assimilation of early time buildup data further reduces the uncertainty. The evolution of the estimate and uncertainty in skin zone log-permeability (Fig. 2.6(b)) and the skin factor (Fig. 2.6(c)) are similar. Good estimates of all the well gridblock log-permeability, skin zone log-permeability and the active well skin factor are obtained. The improved estimates of the active well gridblock $\ln k$ that occurs during buildup may at first seem surprising because standard superposition results indicate that buildup pressure is not directly influenced by the well skin factor. However, this appears to be an advantage in the case of a finite skin zone.

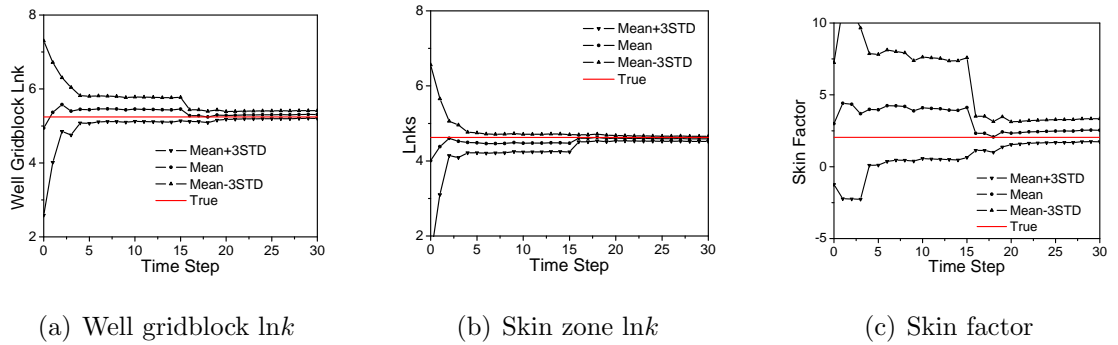


Figure 2.6: Skin when assimilating drawdown and buildup data, case 1 of single layer example

Fig. 2.7 shows the predictions of bottomhole pressure during data assimilation and Fig. 2.8 shows the log-log diagnostic plots of the active well pressure data predictions obtained from time zero using the updated ensemble of rock property fields and active well skin factors obtained at the last data assimilation step. In the log-log diagnostic plots, Δp is the pressure difference from start of test while the effective time which is also known as Agarwal equivalent time [1] is determined by:

$$t_e = \frac{t_p \Delta t}{t_p + \Delta t}. \quad (2.32)$$

In Fig. 2.7 and similar plots, the pink line represents true, gray lines represent ensemble members and black dots are observed data. As shown in Fig. 2.7, the pressure prediction of the ensemble converged in the first several time steps and matched observed data throughout the remaining time steps. The behavior of the very early-time buildup data is strongly influenced by the skin zone permeability as can be seen in the derivative plot of Fig. 2.8(b) and the assimilation of the very first buildup pressure data subsequent to shutin significantly reduces the uncertainty in the estimate of the skin factor, and subsequent buildup data reduce the uncertainty in the estimate of $\ln k$ in the active well gridblock. The unit slope in the derivative plot at the end of the drawdown (Fig. 2.8(a)) shows that we have reached pseudo-steady state.

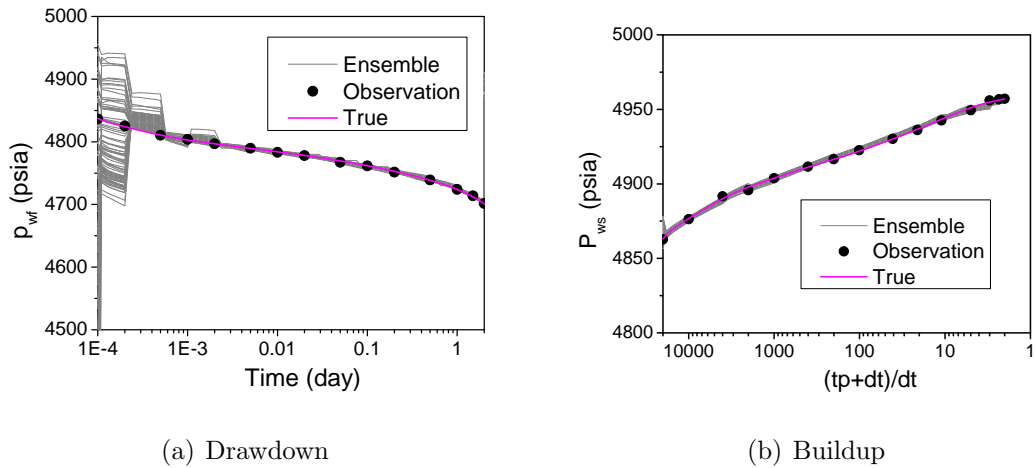


Figure 2.7: Active well pressure match, case 1 of single layer example

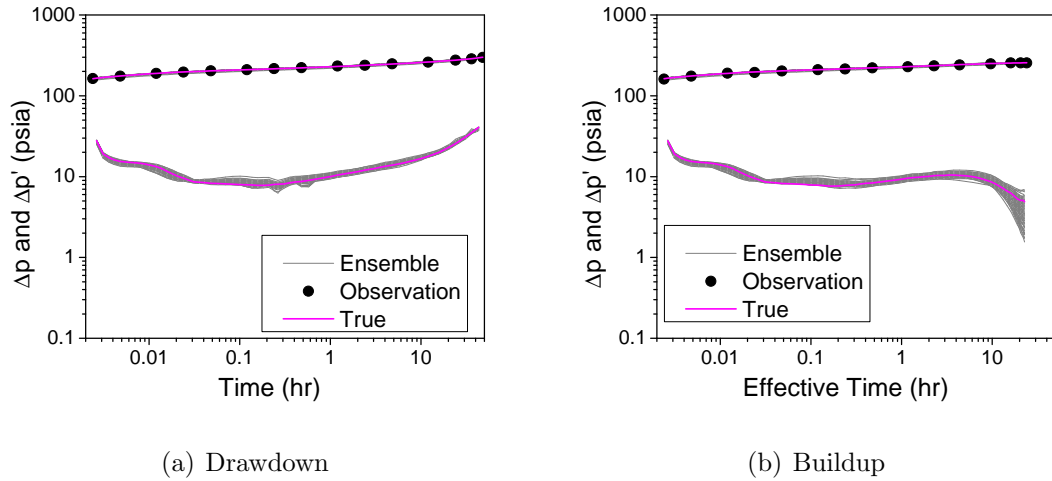


Figure 2.8: Log-log diagnostic plots of the active well pressure data, case 1 of single layer example

2.2.3 Case 2: assimilating pressure data at the active and monitor wells

In this case, we assimilate pressure drawdown and buildup data of the active well and the interference pressure data of the monitor wells. The model is same as case 1 in previous section, except there are 4 monitor wells in the corners to monitoring interference pressure.

The ensemble means of the log-permeability and porosity fields are shown in Fig. 2.9 and Fig. 2.10. The white gridblocks in Fig. 2.9(b) and Fig. 2.10(b) represent values higher than the maximum value of the scale. The maximum value in the estimated log-permeability field after matching both drawdown and buildup pressure data is 7.36 (1572 md) compared to the maximum value of 7 (1097 md) in the true log-permeability field. The ensemble mean and log-permeability in the right bottom corner is higher than maximum value of the scale because the high permeability area is underestimated, but the true is still within ensemble uncertainty. The overshooting of porosity in the same area is due to its correlation with log-permeability that is overcorrected. Similar to the property field obtained by assimilating only the active well pressure data, the estimated log-permeability and porosity fields after assimilating pressure data from both active well and monitor well also gives a reasonable approximation of the true geology.

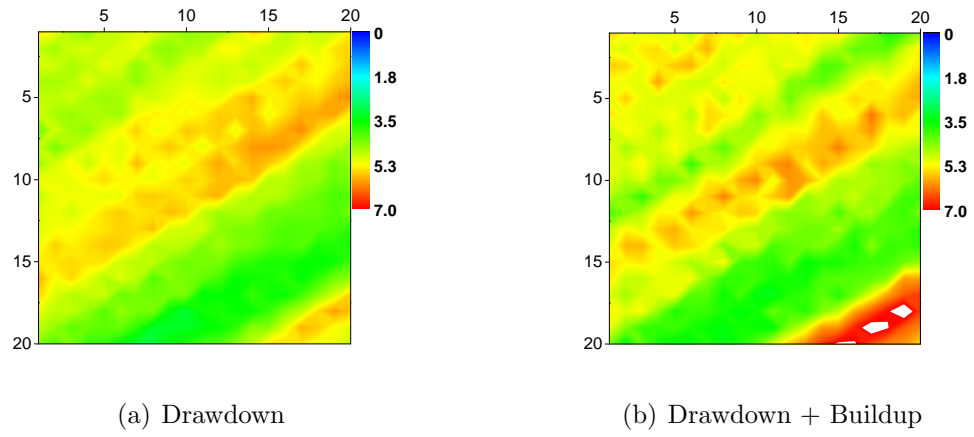


Figure 2.9: The updated ensemble mean of log-permeability field, case 2 of single layer example

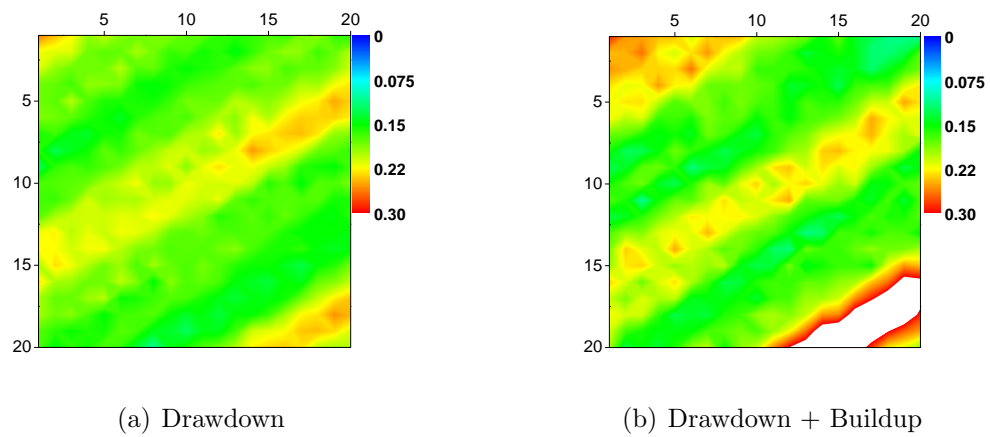
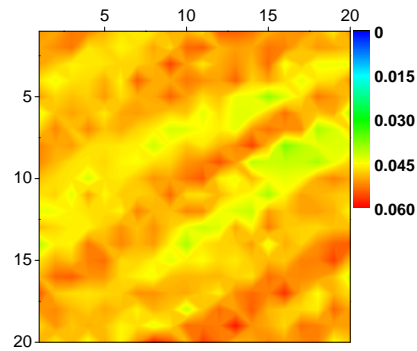
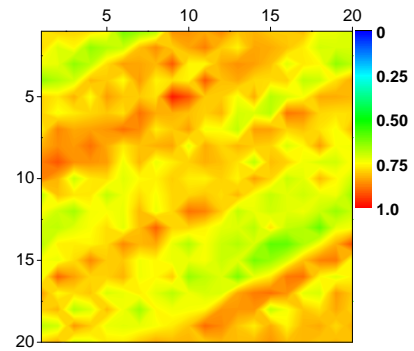


Figure 2.10: The updated ensemble mean of porosity field, case 2 of single layer example

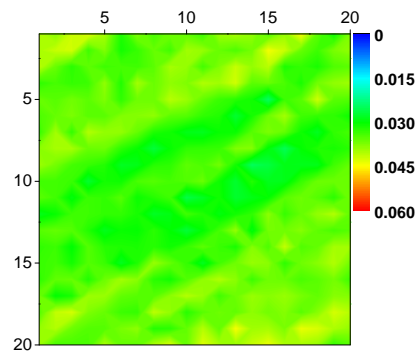
As shown in Fig. 2.11, the posterior standard deviation for the porosity and log-permeability field is further reduced by assimilating interference pressure data of the monitor wells compared to Fig. 2.4, especially on the top left corner and bottom right corner that are far from the near well region. Interference pressure data on the monitor wells help decrease the uncertainty of the properties in the region around the monitor wells.



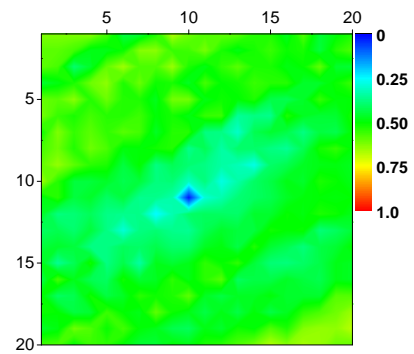
(a) Prior standard deviation of ϕ



(b) Prior standard deviation of $\ln k$



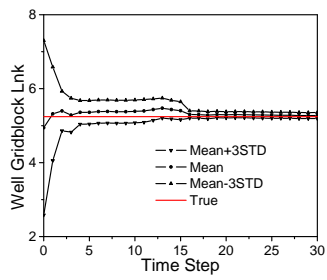
(c) Posterior standard deviation of ϕ



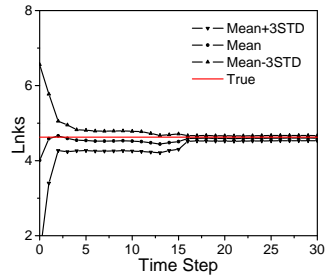
(d) Posterior standard deviation of $\ln k$

Figure 2.11: Prior and posterior standard deviation for ϕ and $\ln k$ field, case 2 of single layer example

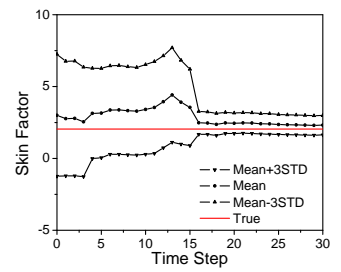
Similar to the results of assimilating only pressure data only on the active well as shown in Fig. 2.6(c), reasonable estimate of well gridblock log-permeability, skin zone permeability and skin factor are obtained as shown in Fig. 2.12.



(a) Well gridblock $\ln k$



(b) Skin zone $\ln k$



(c) Skin factor

Figure 2.12: Skin after assimilating drawdown and buildup data, case 2 of single layer example

As shown in Fig. 2.13 and Fig. 2.14, the predicted pressure data on the active well and the derivative of pressure change during data assimilation and rerun from time 0 are close to the true (the purple line).

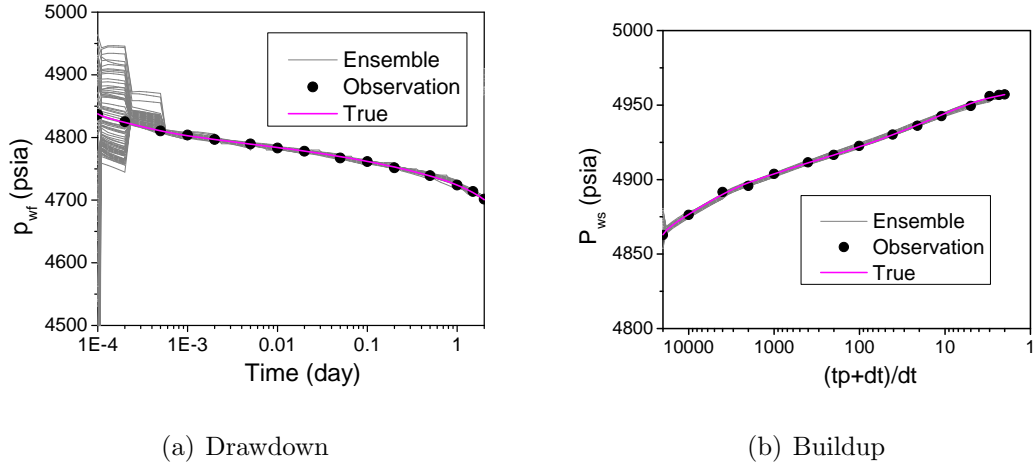


Figure 2.13: Active well pressure match, case 2 of single layer example

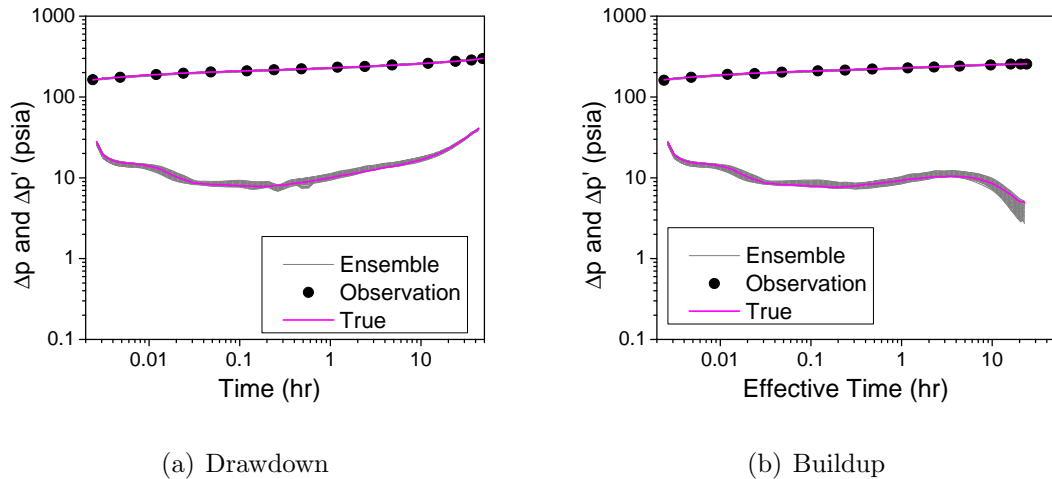


Figure 2.14: Log-log diagnostic plots of the active well pressure data rerun from time 0, case 2 of single layer example

Fig. 2.15, Fig. 2.16, Fig. 2.17 and Fig. 2.18 show the pressure drawdown, buildup data prediction during data assimilation and rerun from time 0, respectively, on the 4 monitor wells. Similar to the active well results (Fig. 2.13 and Fig. 2.14), the monitor well drawdown results are reasonably consistent, but the predicted buildup pressure shows a substantially larger spread (uncertainty) when rerun from the final estimated ensemble.

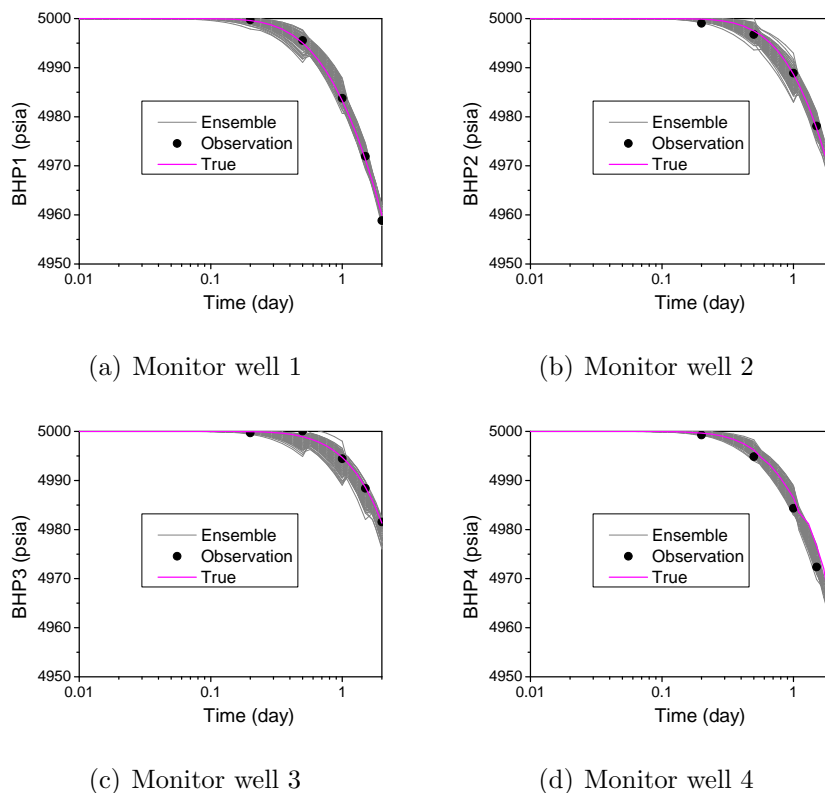


Figure 2.15: Monitor well drawdown pressure data match during data assimilation, case 2 of single layer example

2.2.4 Case 3: assimilating pressure data with wrong prior mean

In the previous case, the initial ensemble of model parameters are generated using the same statistical parameters (Table 2.2) used to generate the true reservoir properties. Here, we consider the case where the estimated prior means of the rock property fields are far from the true means. In this case, the initial ensemble of reservoir porosity and log-permeability fields are generated using different prior means than those used to generate the true reservoir property fields. We will investigate the impact of wrong prior means on data assimilation using EnKF. The initial ensemble of porosity and log-permeability fields are generated using means of 0.35 and 6.5, respectively. Other statistical parameters of the prior model are the same as the ones used to generate the truth (Table 2.2). This means that the initial ensemble of porosity and log-permeability used in this case are generated by adding 0.15 and 1.5, respectively to the initial ensemble of realizations used in the previous case. The same initial ensemble of skin factors are used as in the previous

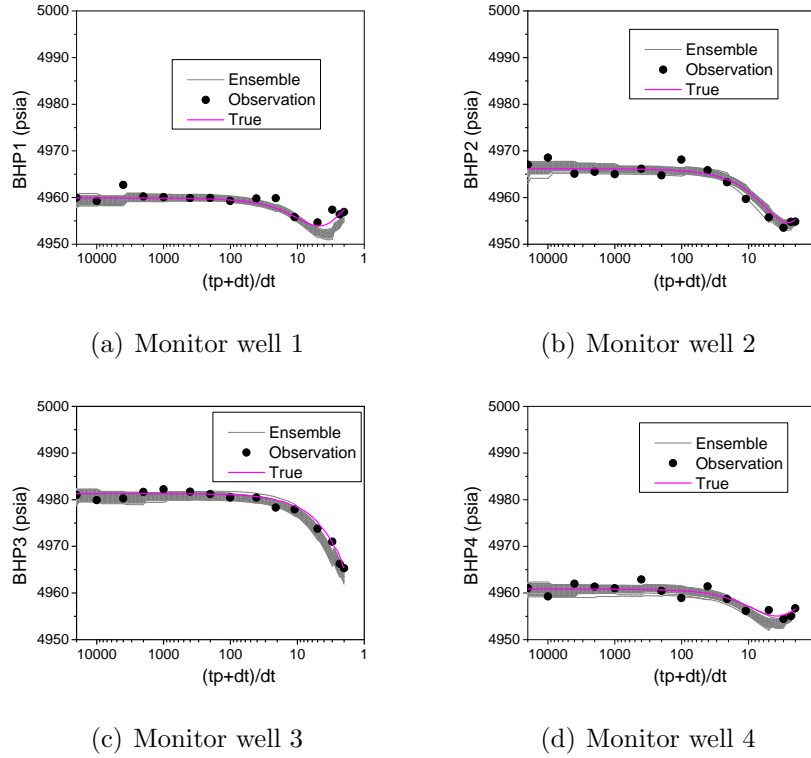


Figure 2.16: Monitor well buildup pressure data match during data assimilation, case 2 of single layer example

cases.

Fig. 2.19 shows the estimated mean log-permeability distribution after assimilating the drawdown data (Fig. 2.19(a)) and then the buildup data (Fig. 2.19(b)) from all wells. Although as in the truth (Fig. 2.1(a)), a high permeability channel running through the active well and monitor well M4 is exhibited by the estimate of Fig. 2.19, values of the log-permeability are much higher than that of the truth in the overshooting area shown as white. The maximum value in the estimated log-permeability field after assimilating drawdown test data is 8.6 (5442 md) and 7.89 (2671 md) after further assimilating pressure buildup test data, whereas the maximum value in the true log-permeability distribution is only 7 (1097 md). In addition to the overshooting problem, the channel is much wider than the truth and also there is an additional high permeability channel generated passing through monitor well M1, whereas the permeability in this area is supposed to be low in value according to the truth. Overall, the permeability fields of Fig. 2.19 clearly provide a poor estimate of the truth than was obtained

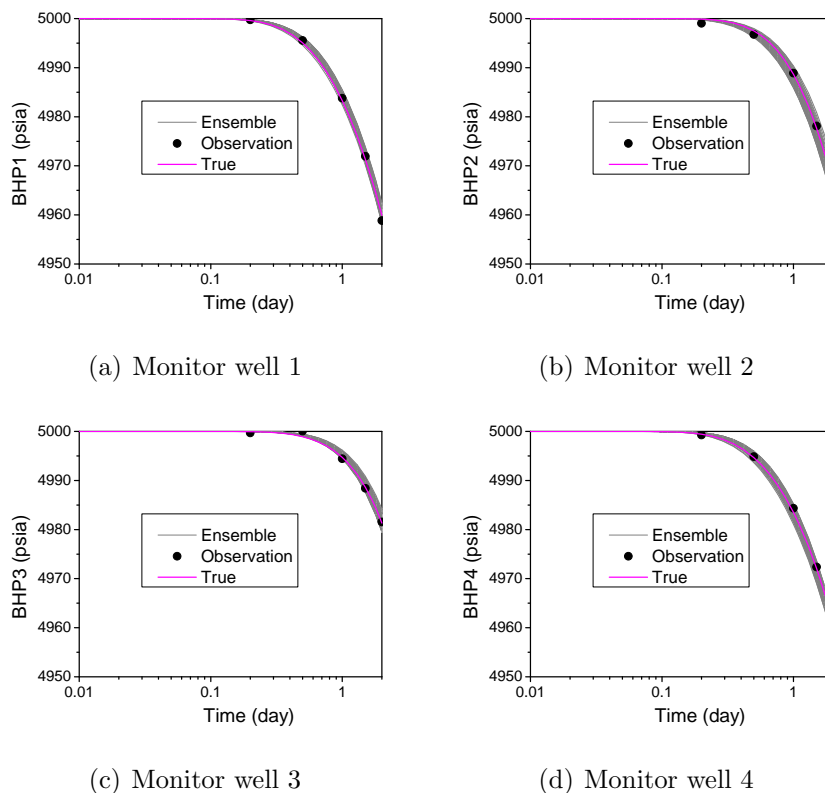


Figure 2.17: Monitor well drawdown pressure data match rerun from time 0, case 2 of single layer example

where the correct means are used to generate the initial ensemble in Fig. 2.9. After further data assimilation of pressure buildup data, it seems the overshooting is reduced, but the log-permeability distribution is still much rougher than the truth and the unwanted high permeability channel through M1 still remains. Fig. 2.20 shows estimated porosity fields after assimilating the drawdown and buildup pressure data. Similarly to the overshooting problem in the log-permeability field, after assimilating drawdown and buildup data (Fig. 2.20(b)), the top left corner is underestimated and the right bottom is overestimated. The overall estimation of porosity field is not good.

Although the estimated log-permeability fields are far from the truth, the estimates of the skin zone log-permeability (4.53) is reasonable compared to the truth (4.62) as is estimated well gridblock log-permeability (5.41) compared to the truth (5.24) as shown in Fig. 2.21. However, the true skin factor is out of range of the estimated ensemble of skin factor as shown in Fig. 2.21(c).

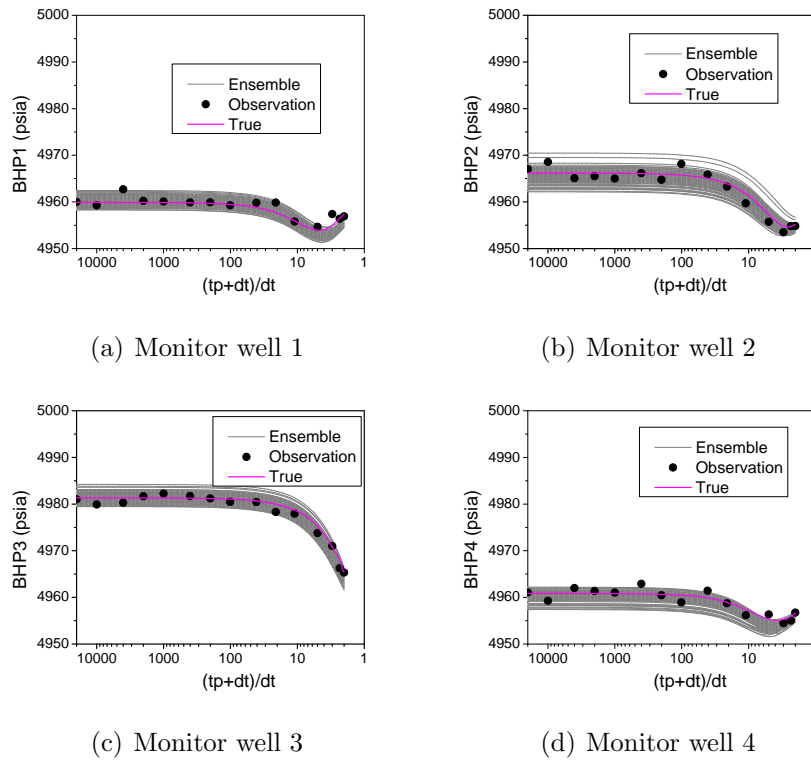


Figure 2.18: Monitor well buildup pressure data match rerun from time 0, case 2 of single layer example

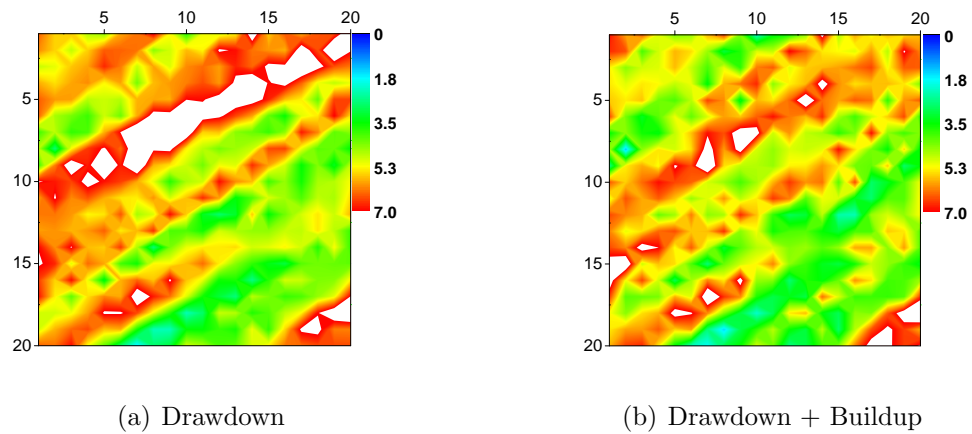
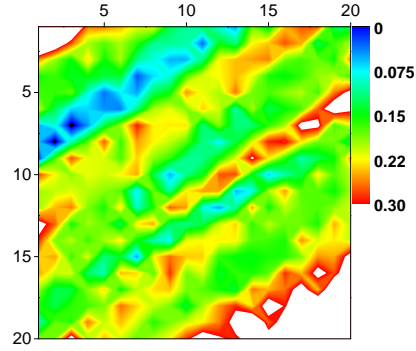
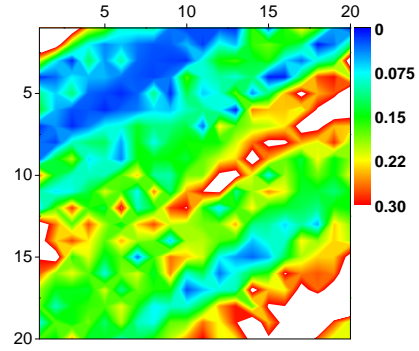


Figure 2.19: The updated ensemble mean of log-permeability field, case 3 of single layer example

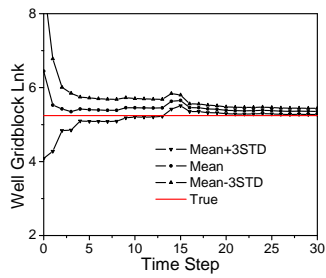


(a) Drawdown

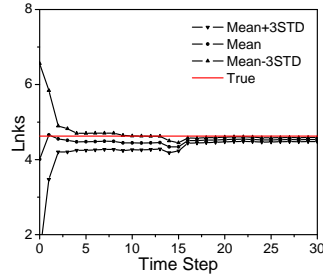


(b) Drawdown + Buildup

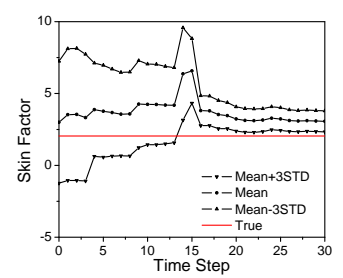
Figure 2.20: The updated ensemble mean of porosity field, case 3 of single layer example



(a) Well gridblock $\ln k$



(b) Skin zone $\ln k$



(c) Skin factor

Figure 2.21: Skin after assimilating drawdown and buildup data, case 3 of single layer example

As shown in Fig. 2.22 and Fig. 2.23, EnKF managed to obtain a relatively good match on the active well pressure data during data assimilation and during rerun from time 0. However, the derivative of pressure change match is not as good during the late time of drawdown and buildup tests. Fig. 2.24 and Fig. 2.25 show the data match at all monitor wells during data assimilation for the 2-day pressure drawdown and 2-day buildup tests. The data match at well M1 is poor and the data matches at the other monitor wells are relatively better. The drawdown pressure on monitor well 1 is overestimated indicates that permeability region around monitor well 1 is overestimated.

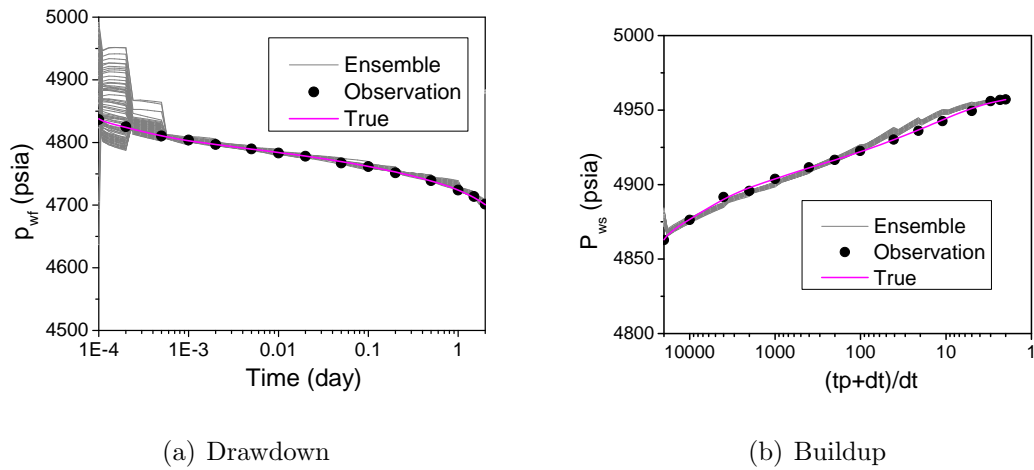


Figure 2.22: Active well pressure match, case 3 of single layer example

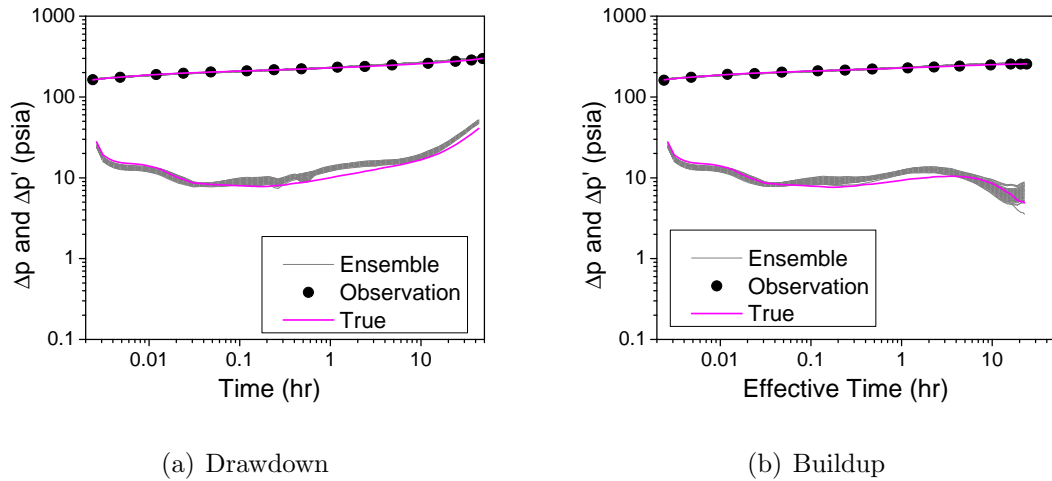


Figure 2.23: : Log-log diagnostic plots of the active well pressure data, case 3 of single layer example

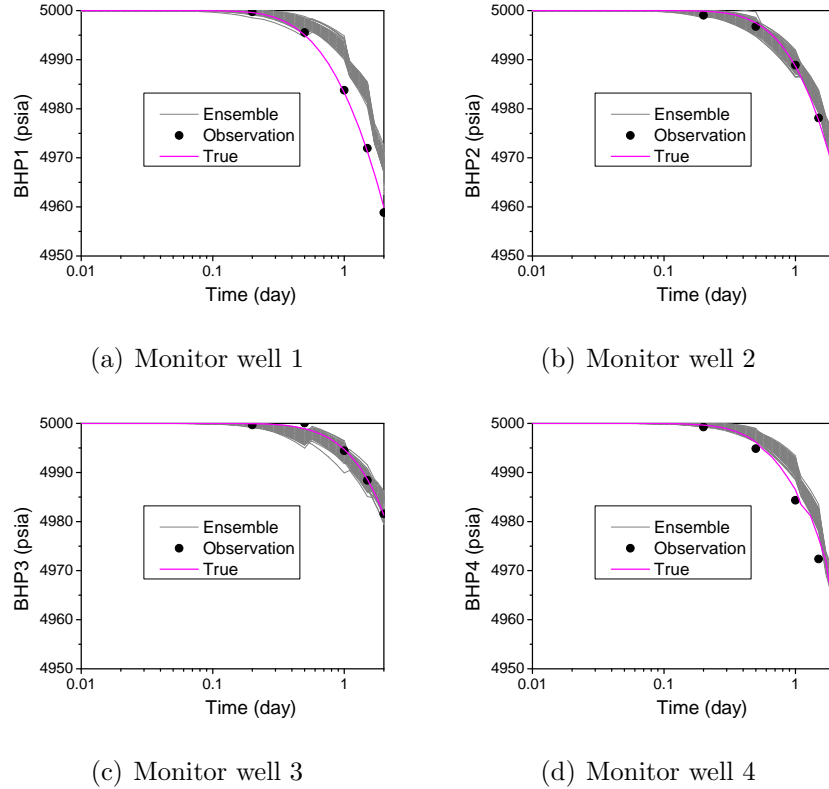


Figure 2.24: Monitor well drawdown pressure data match during data assimilation, case 3 of single layer example

2.2.5 Case 4: doubly stochastic data assimilation

In the previous case, we showed that when the initial ensemble of model parameters are generated using incorrect prior means far from the true means, EnKF fails to yield a reasonable estimate of the rock property fields. In case 4, we apply a partially doubly-stochastic process which includes uncertainty in the prior means, and thus allows us to make corrections to the “wrong” prior means. In this case, we generate the initial ensemble of porosity and log-permeability fields by adding corrections to the set of realizations used in case 3. Given a particular realization of $(m_{\ln k}^T, m_{\phi}^T)^T$, we add a realization of $\theta_{\ln k}$ to each entry of $m_{\ln k}$ and a realization of θ_{ϕ} to each entry of m_{ϕ} , where $\theta_{\ln k}$ is Gaussian with mean zero and variance 2 and θ_{ϕ} is Gaussian with mean zero and variance equal to 0.01. From this process, we generate an initial ensemble of the log-permeability and porosity fields. Because of the uncertainty in the prior means, the initial variations in gridblock porosities and log-permeabilities are much higher than when using the en-

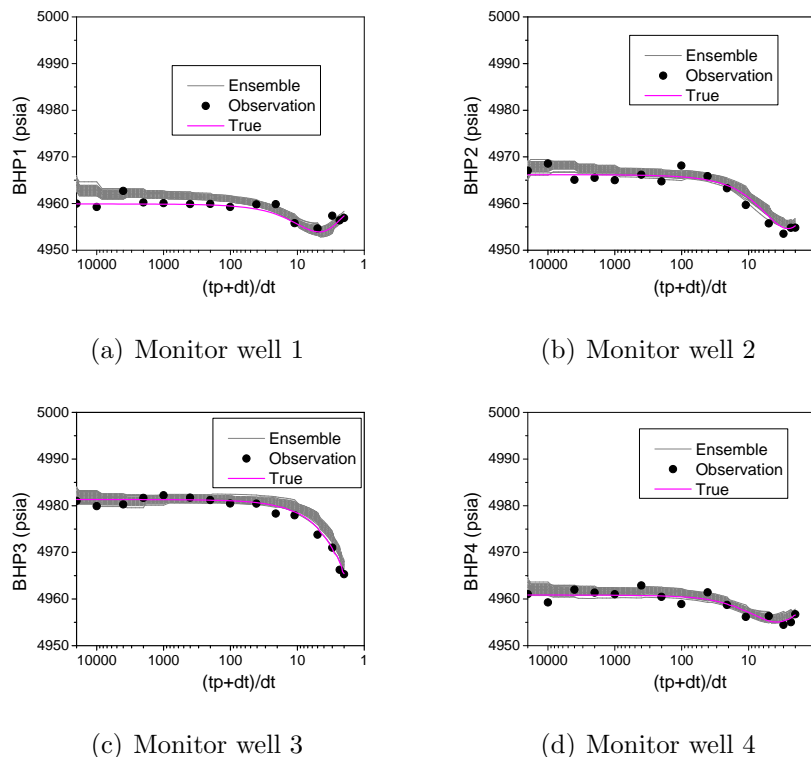


Figure 2.25: Monitor well buildup pressure data match during data assimilation, case 3 of single layer example

semble of initial models generated from the “wrong” prior mean in case 3. The same initial ensemble of skin factors is used.

The estimated ensemble means of the log-permeability and porosity fields in the doubly-stochastic case are shown in Fig. 2.26 and Fig. 2.27, and the estimates of the rock property fields are of very similar quality to those obtained using correct prior means in case 2; see Fig. 2.9 and Fig. 2.10.

Fig. 2.28(a) and Fig. 2.28(b) show the evolution of the estimated mean log-permeability and porosity, which is the prior mean plus the estimated correction to the mean at each data assimilation step. The true prior mean for the log-permeability is 5 as shown in Fig. 2.28(a) in red. After assimilating the 2-day pressure drawdown data (the first 15 steps of data assimilation), the estimated mean of log-permeability gets reasonably close to its true value of 5 and the uncertainty decreases during data assimilation. When we assimilate the pressure buildup data (the second 15 data assimilation steps), estimates of the mean of $\ln k$ and the mean of ϕ do not change appreciably. However, as

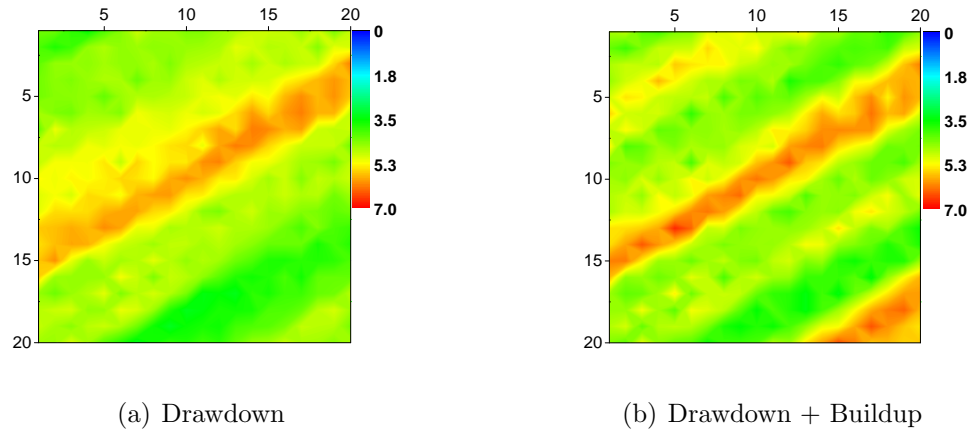


Figure 2.26: The updated ensemble mean of log-permeability field, case 4 of single layer example

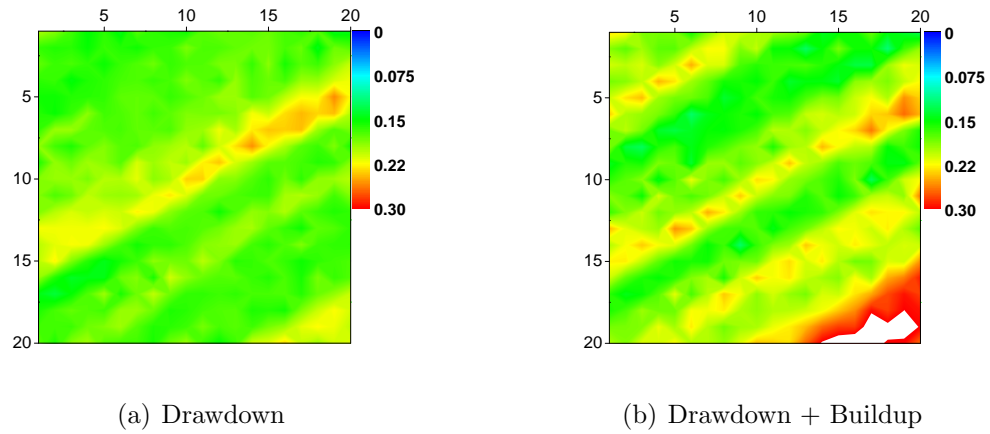
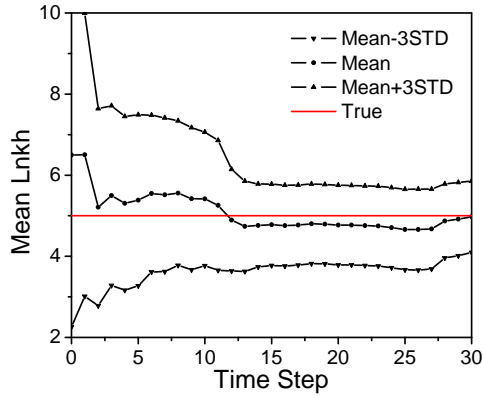
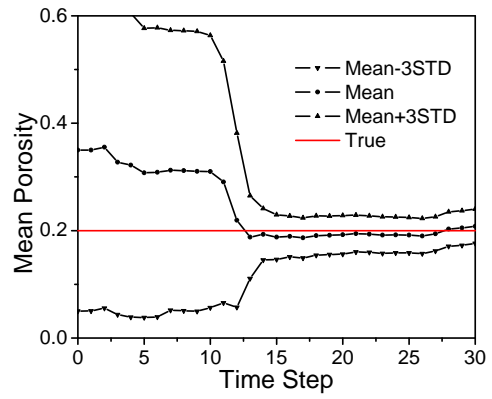


Figure 2.27: The updated ensemble mean of porosity field, case 4 of single layer example shown in Fig. 2.29, the skin estimate is improved by assimilating early time buildup data as in case 2.

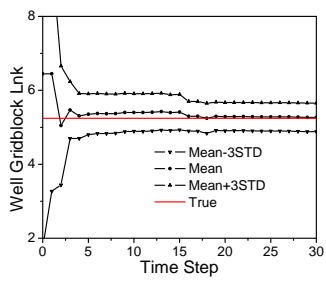


(a) Log-permeability

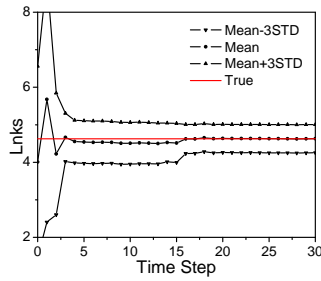


(b) Porosity

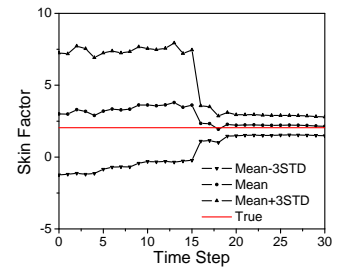
Figure 2.28: Ensemble mean of log-permeability and porosity after assimilating drawdown and buildup data, case 4 of single layer example



(a) Well gridblock $\ln k$



(b) Skin zone $\ln k$



(c) Skin factor

Figure 2.29: Skin after assimilating drawdown and buildup data, case 4 of single layer example

Fig. 2.30 shows the pressure data match at the active well during data assimilation which shows a better data match in late buildup (Fig. 2.30(b)) than in case 3 (Fig. 2.22(b)). Fig. 2.31 shows the ensemble predictions of active wellbore pressure and corresponding pressure derivatives obtained when rerunning from time zero using the final ensemble of model parameters. Note that even though we do not assimilate pressure derivative “data”, the derivatives of the ensemble predictions match the true prediction. A much better data match in the prediction of the monitor well pressure data, especially of monitor well 1, is obtained by the doubly stochastic process (Fig. 2.32 and Fig. 2.33) than that from case 3 where the “wrong” prior means were used but we did not include uncertainty in these means (Fig. 2.24 and Fig. 2.25).

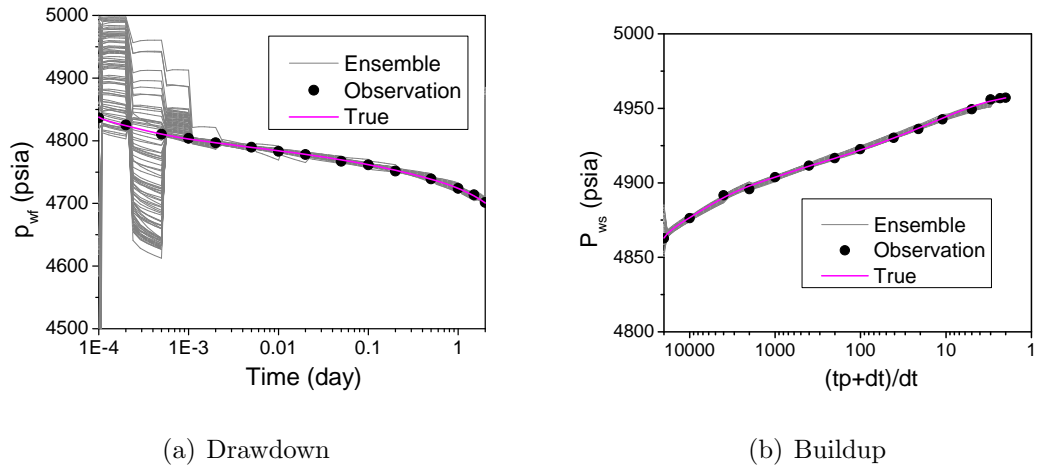
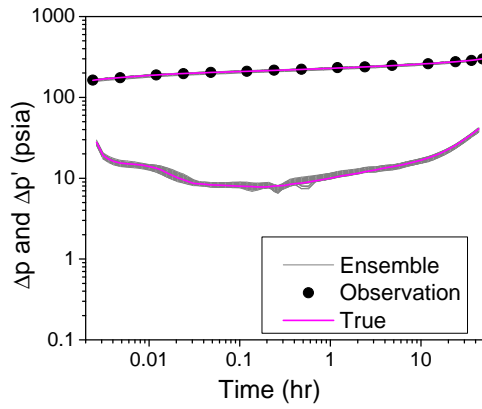
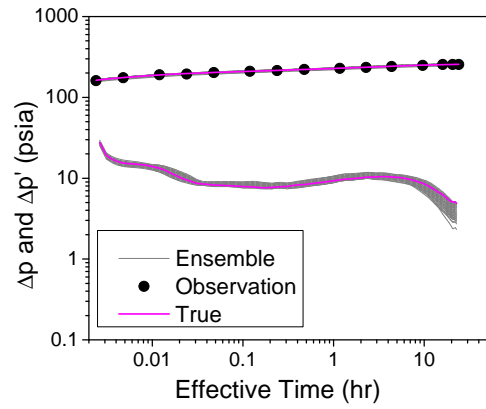


Figure 2.30: Active well pressure match, case 4 of single layer example

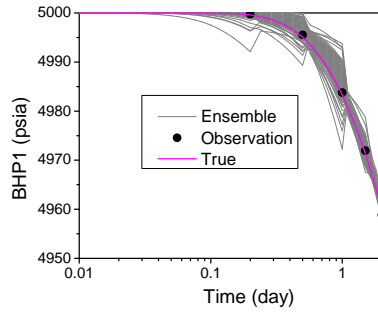


(a) Drawdown

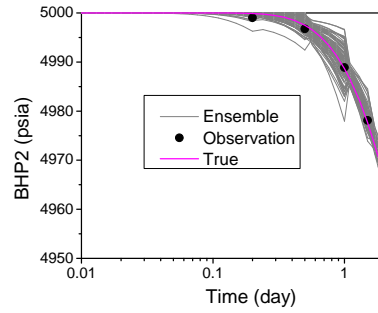


(b) Buildup

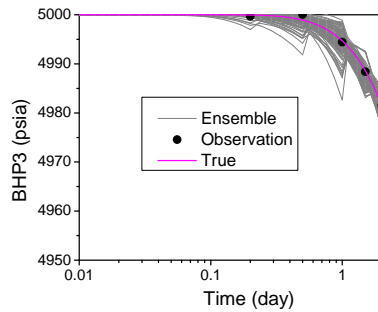
Figure 2.31: Log-log diagnostic plots of the active well pressure data, case 4 of single layer example



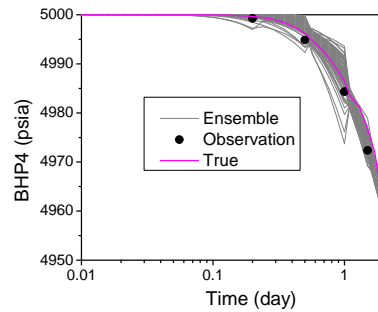
(a) Monitor well 1



(b) Monitor well 2

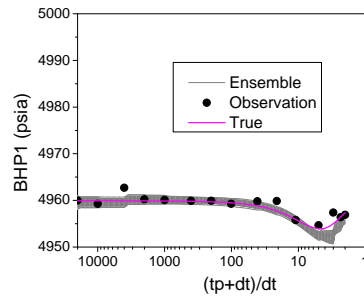


(c) Monitor well 3

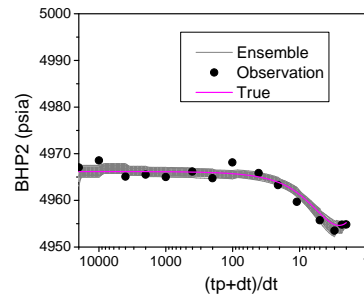


(d) Monitor well 4

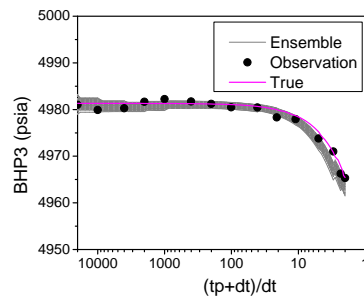
Figure 2.32: Monitor well drawdown pressure data match during data assimilation, case 4 of single layer example



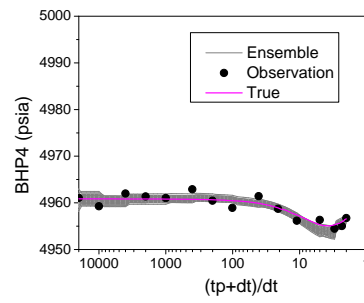
(a) Monitor well 1



(b) Monitor well 2



(c) Monitor well 3



(d) Monitor well 4

Figure 2.33: Monitor well buildup pressure data match during data assimilation, case 4 of single layer example

In summary, EnKF is applied to assimilate pressure transient data in a one-layer heterogeneous reservoir example of different scenarios. In the 1st case, assuming the prior information of the log-permeability and porosity fields are known, the pressure data at the active well are assimilated. In the 2nd case, we place 4 monitor wells in the reservoir and assimilate the interference pressure data observed at the monitor wells together with that from the active well. In both cases, reasonable data matches are obtained. The estimate of the property fields (log-permeability and porosity) obtained after assimilating the pressure transient data (drawdown and buildup) using EnKF captures the true geological structure and spatial geological features. However, matching interference pressure data, the geological feature in the regions that are far from the active well is improved.

In the 3rd case, where we use incorrect prior means and do not consider the uncertainty in these means, we obtain erroneous estimate of log-permeability and porosity fields with serious overshooting problems. The estimated skin factor is biased compared the truth. Even though EnKF managed to obtain a relatively good match on the active well pressure data, the match on the derivative of pressure change on the active well and pressure of monitor well 1 is not good. In the 4th case that the prior means of the rock property fields are erroneous as in 3rd case, we have applied a partially doubly stochastic model in the EnKF methodology, which results in significantly better estimate of the rock property fields and good data matches.

2.3 Two-layer heterogeneous examples

2.3.1 Case description

In this section, we consider a two-layer reservoir example. The grid system is $20 \times 20 \times 2$ and the size of each gridblock is the same as the single layer case. The thickness of each layer is 20 ft. The true log-permeability and porosity fields are shown in Fig. 2.34 and Fig. 2.35. The prior mean and variance of porosity are 0.2 and 0.0025, respectively for both layers. The prior mean and variance of log-permeability are 6 and 1 for layer 1, and 4 and 1 for layer 2. The direction of long correlation range for layer

1 is the same as in the single layer case in the previous section and the direction of long correlation range of layer 2 is perpendicular to that of layer 1. All other statistical parameters are the same as in the single layer case; see Table 2.2. The true initial reservoir pressure is 5000 psi and the initial water saturation is 0.1 which is equal to the irreducible water saturation. As in the single layer case, one active well is located at the center and four monitor wells are at the corners. All wells fully penetrate both layers. Although the reservoir has a vertical permeability of zero, the two layers can communicate through the monitor wells. We have applied local grid refinement around the active well in the same way as in the single layer case. The true skin factors of the first and second layer are 2 and 8, respectively. In this case, we added uncertainty to the initial reservoir pressure, i.e., we generated samples of white noise with mean of zero and standard deviation of 5 psi and added it to the true initial pressure to obtain an ensemble of initial pressures.

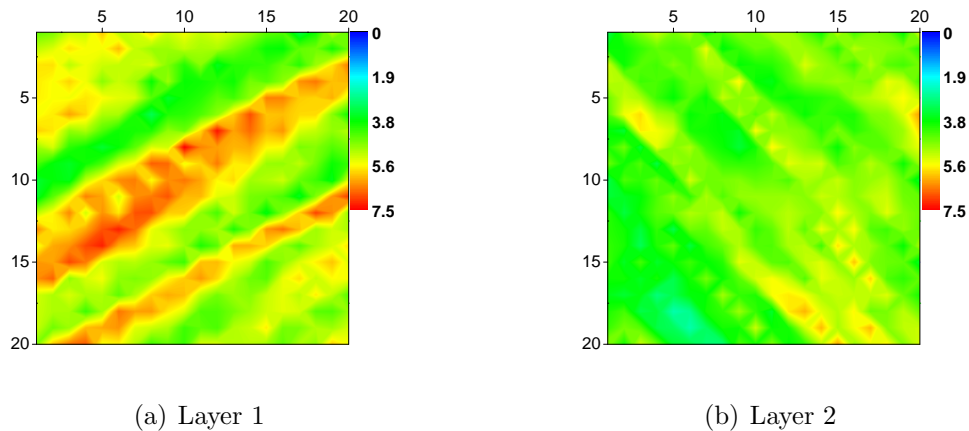


Figure 2.34: True horizontal log-permeability field, two-layer heterogenous example

The active well at the center of the reservoir produces at a constant oil rate of 600 STB/D for the first two days (referred to as drawdown 1) and 300 STB/D for the next two-day period (referred to as drawdown 2), i.e., we consider a two-step drawdown test. The bottomhole pressure of the active well and monitor wells are recorded and assimilated using EnKF.

Our objective is to show that the assimilation of layer rate production logging data, specifically individual layer flow rates, improves estimates of layer properties and

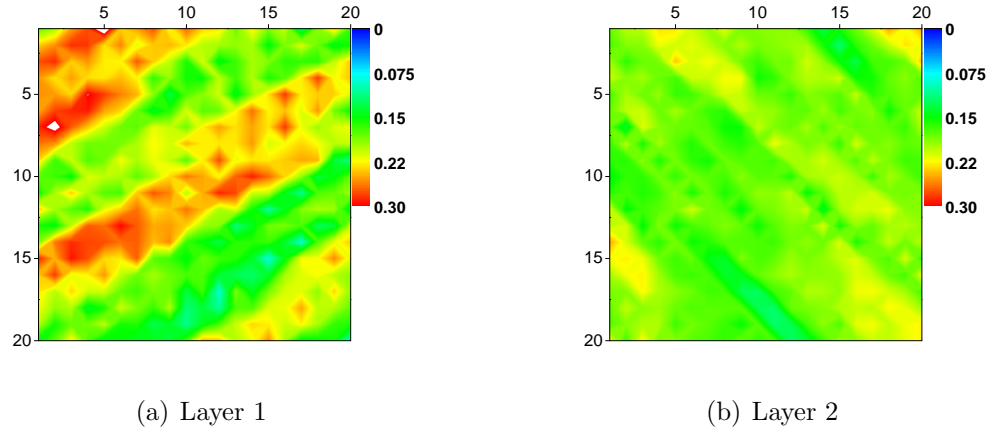
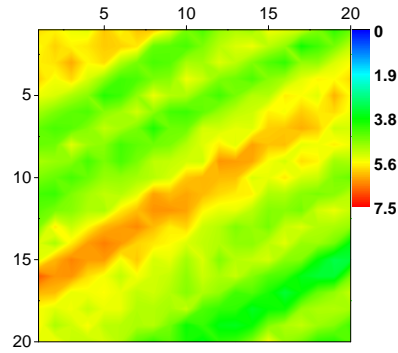


Figure 2.35: True porosity field, two-layer heterogenous example

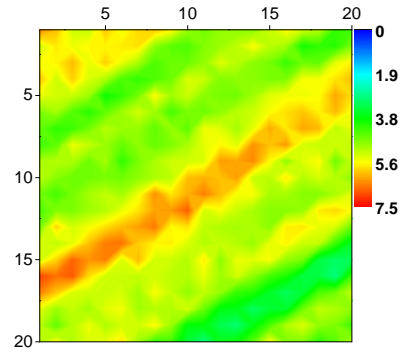
well skin factors. The initial realizations for the layer skin factors are generated with prior means of 6 and 4, respectively for the first and second layer with a variance of 2 for both layers. The realizations of initial pressure are drawn from a Gaussian distribution with mean 5,000 psi and a standard deviation of 5 psi. There are 60 data assimilation time steps, 30 steps in the first 48 hours when the production rate is 600 STB/D and 30 steps in the next 48 hours when the production rate is 300 STB/D. The measurement error for pressure and layer rate data are 1 psi and 5 STB/D, respectively.

2.3.2 Case 1: assimilating pressure data only

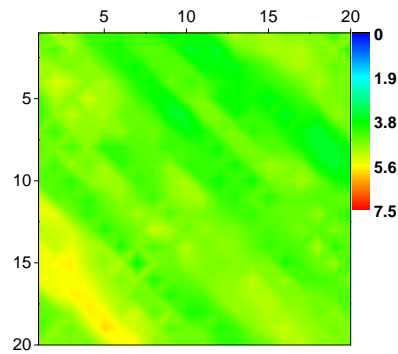
In the first case, the property fields and skin parameters are updated by assimilating pressure data from the active and monitor wells. Fig. 2.36 shows the ensemble mean log-permeability fields obtained by assimilating the BHP data of the active and monitor wells with EnKF but without assimilating layer rate data. The major geological features of the truth (high permeability channels) of layer 1 are captured in the estimated ensemble mean, but the estimated log-permeability field for layer 2 differs fairly significantly from the truth. Estimates of roughly similar quality are obtained for the porosity fields of both layers, as shown in Fig. 2.37.



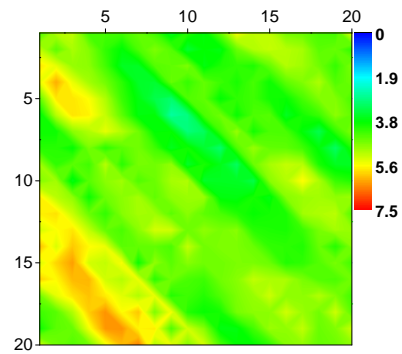
(a) Layer 1, Drawdown 1



(b) Layer 1, Drawdown 2

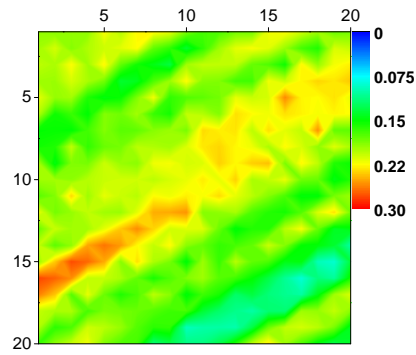


(c) Layer 2, Drawdown 1

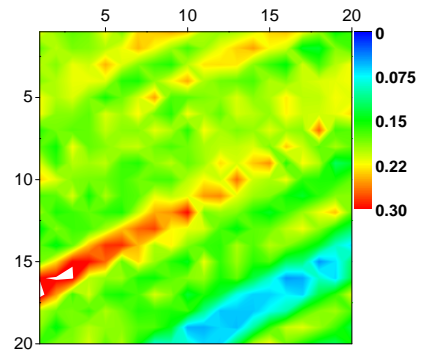


(d) Layer 2, Drawdown 2

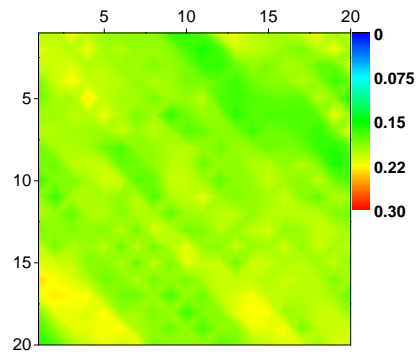
Figure 2.36: The updated ensemble mean of log-permeability field, case 1 of two-layer heterogeneous example



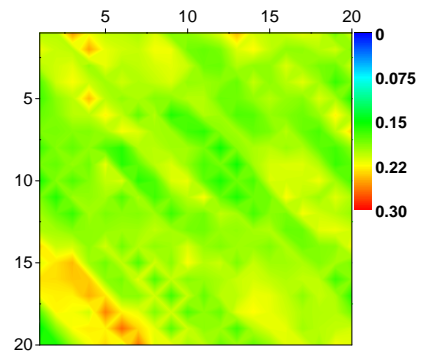
(a) Layer 1, Drawdown 1



(b) Layer 1, Drawdown 2



(c) Layer 2, Drawdown 1



(d) Layer 2, Drawdown 2

Figure 2.37: The updated ensemble mean of porosity field, case 1 of two-layer heterogeneous example

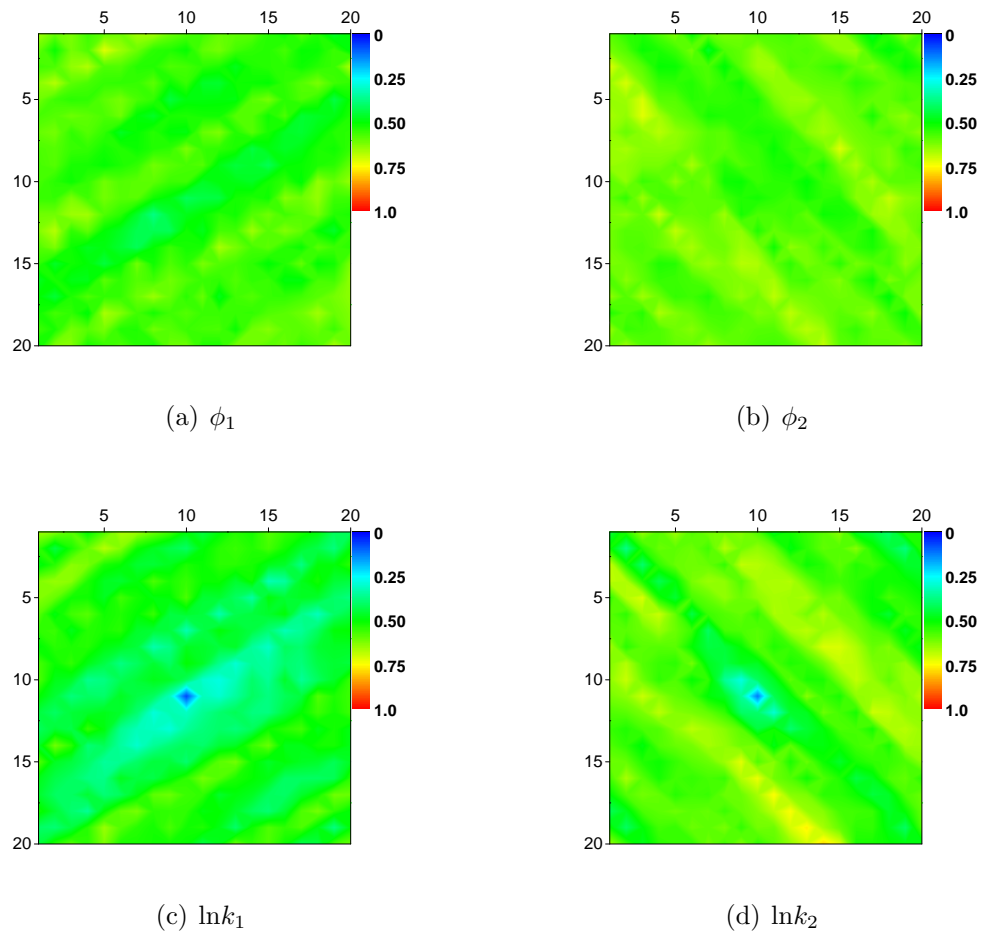


Figure 2.38: Ratio of posterior to prior STD of porosity and log-permeability, case 1 of two-layer heterogeneous example

Fig. 2.39 and Fig. 2.40 show the estimated well gridblock log-permeability, skin zone log-permeability and skin factor with uncertainty for layer 1 and 2, respectively. It can be seen that for both layers, the true well gridblock log-permeability stays within the uncertainty bound; skin zone log-permeability is somewhat biased; the true skin factors are totally outside the uncertainty bound. However, the well “effective skin factor” stays within the uncertainty bound as shown in Fig. 2.41. Here the well effective skin factor is defined by using the thickness-averaged permeability in the skin zone and the thickness-averaged well gridblock permeability using Hawkin’s formula (Eq. 2.31). The results show that pressure transient data alone cannot resolve individual layer skin factors in a multi-layer reservoir, even though the pressure data match is reasonably good (Fig. 2.42 and Fig. 2.43). Fig. 2.42 and Fig. 2.43 show only the data match of the active well for the first 48-hour drawdown during data assimilation and the associated data match when rerunning from time zero using the final estimated rock property fields and skin factors. The monitor well pressure data match during data assimilation are shown in Fig. 2.44 and Fig. 2.45 and the corresponding pressure data match when rerunning from time 0 are shown in Fig. 2.46 and Fig. 2.47. Rerunning from time zero with final ensemble yields a substantially larger spread (uncertainty) in the predicted pressure, which may be due to the fact that we did not adjust the initial pressure during data assimilation. As indicated in Fig. 2.42(b) and similar plots, a few realizations failed during simulation run; the failure is indicated by a sudden drop in pressure to zero.

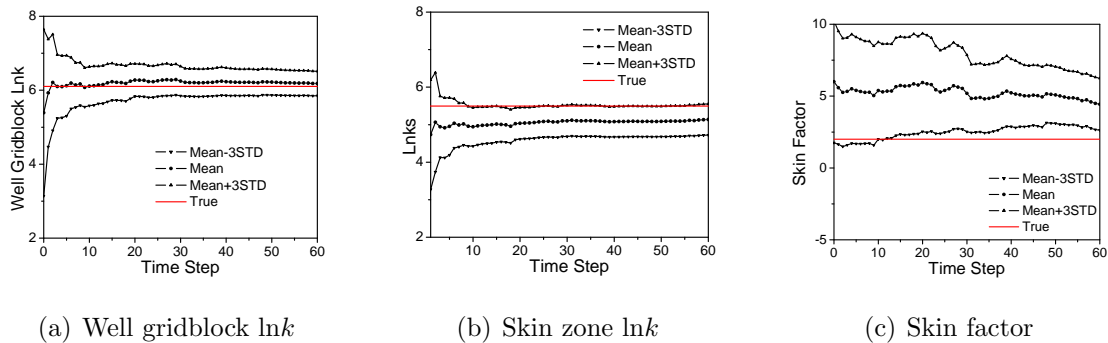


Figure 2.39: Skin of layer 1 when assimilating multi-rate drawdown data, case 1 of two-layer heterogeneous example

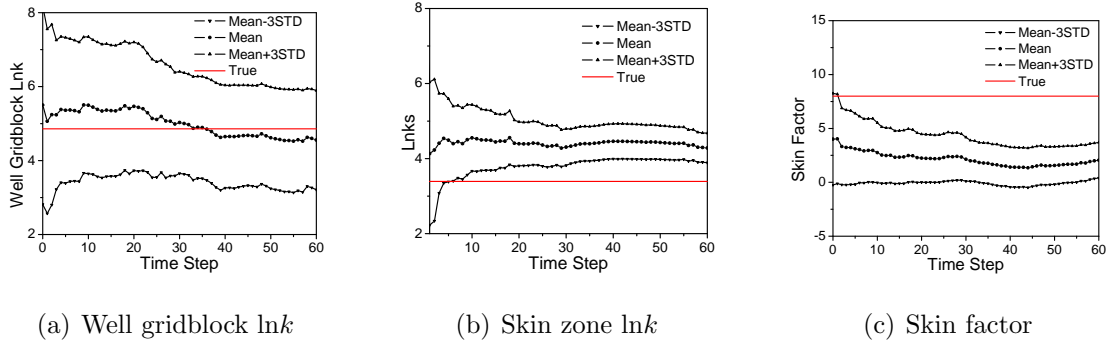


Figure 2.40: Skin of layer 2 when assimilating multi-rate drawdown data, case 1 of two-layer heterogeneous example

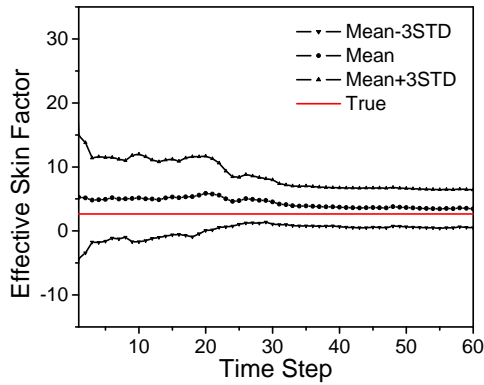


Figure 2.41: Effective skin when assimilating multi-rate drawdown data, case 1 of two-layer heterogeneous example

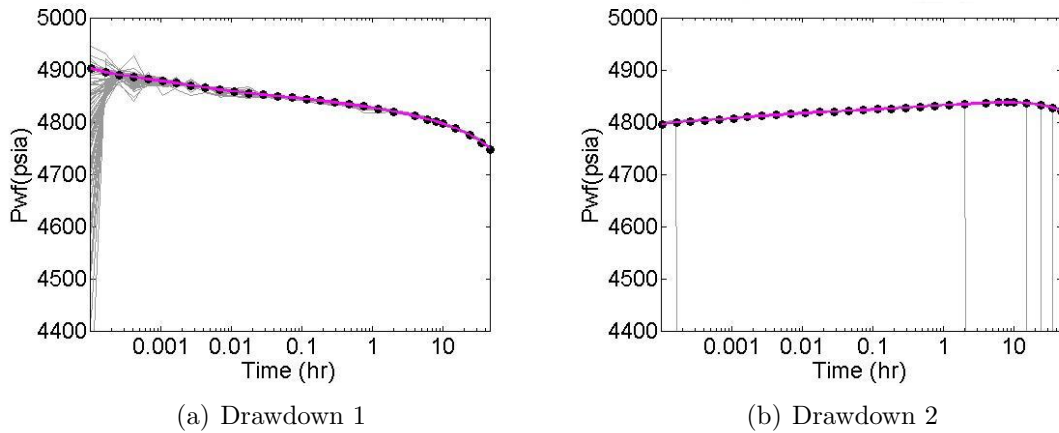


Figure 2.42: Active well drawdown pressure match during data assimilation, case 1 of two-layer heterogeneous example

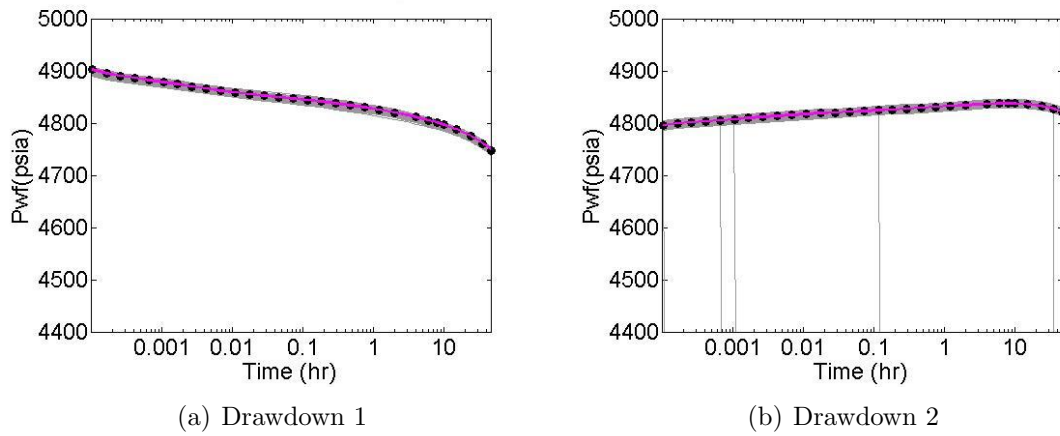


Figure 2.43: Active well drawdown pressure match rerun from time 0, case 1 of two-layer heterogeneous example

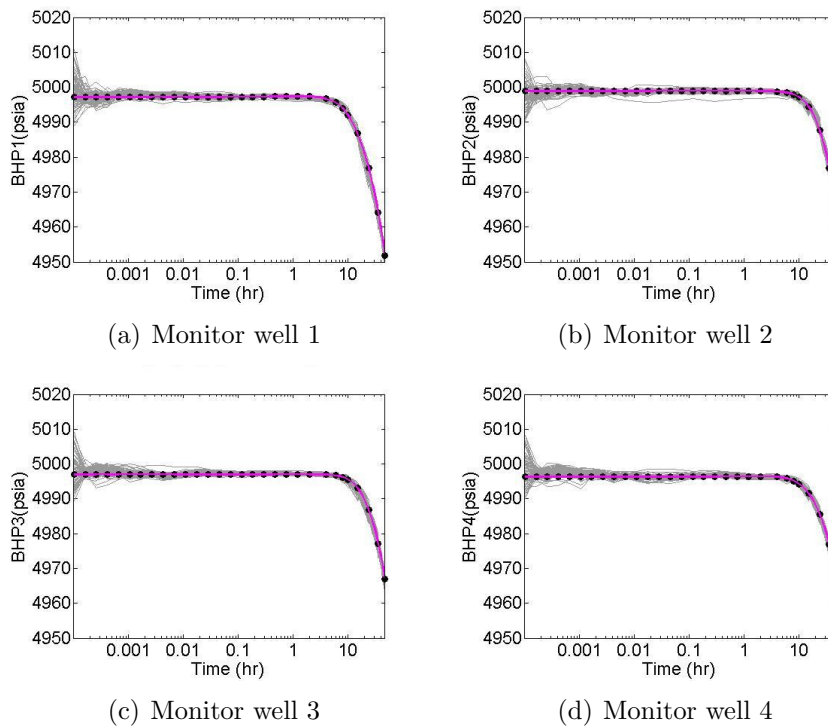


Figure 2.44: Monitor well pressure data match during drawdown 1 data assimilation, case 1 of two-layer heterogeneous example

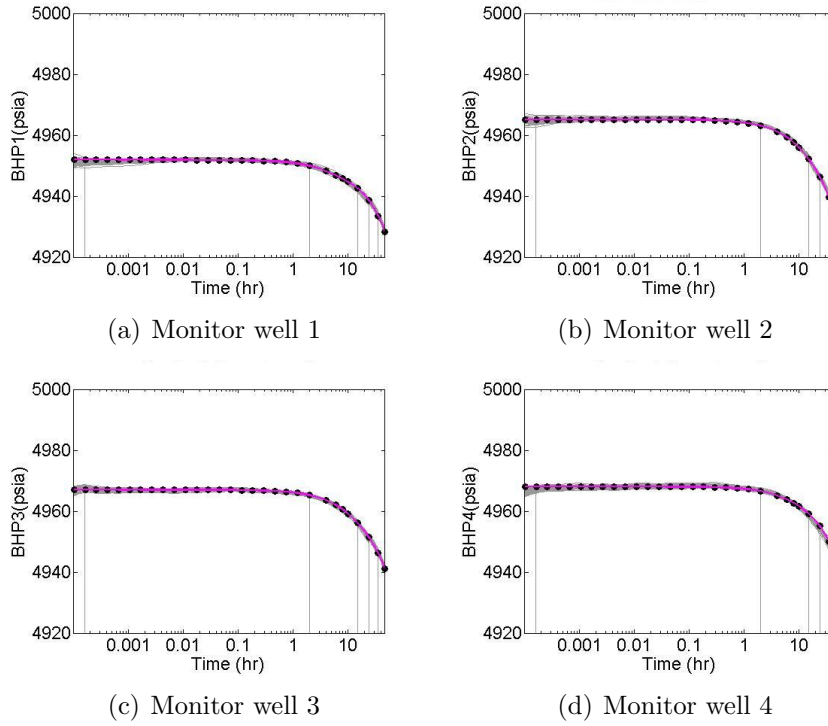


Figure 2.45: Monitor well pressure data match during drawdown 2 data assimilation, case 1 of two-layer heterogeneous example

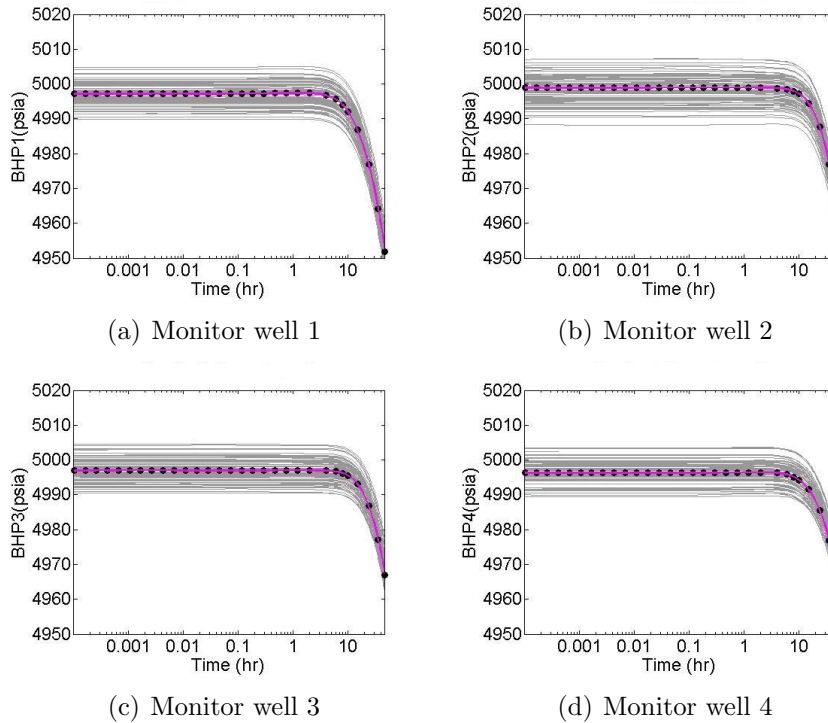


Figure 2.46: Monitor well drawdown 1 pressure data match rerun from time 0, case 1 of two-layer heterogeneous example

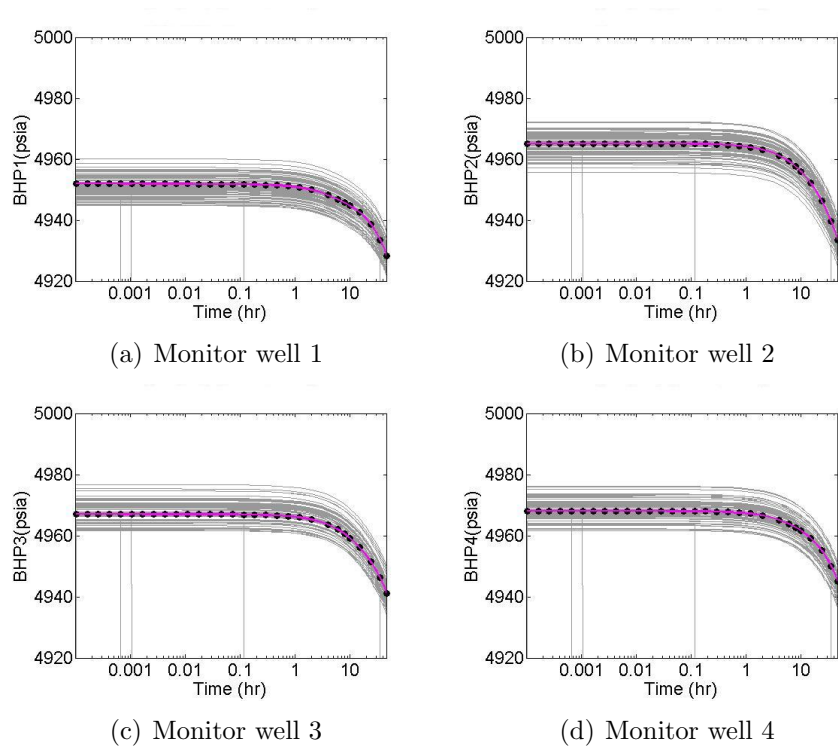


Figure 2.47: Monitor well drawdown 2 pressure data match rerun from time 0, case 1 of two-layer heterogeneous example

Fig. 2.48 and Fig. 2.49 show the layer rate predictions during data assimilation and rerun from time 0, respectively, for layer 1. The pink curve shows the prediction with the true model and black circles are the observed layer rate data. Note that in this case, we do not assimilate layer rate data. The production rate from layer 1 tends to be underestimated especially during the first flow period. An erroneously low layer rate is consistent with an over estimate of the skin factor of layer 1. Although we do not assimilate the layer rate data, the uncertainty of the ensemble predictions decreases as we assimilate more and more pressure data due to the fact that uncertainty in the skin factors and rock property fields decreases. The layer rate predictions from layer 2 are complementary to that of layer 1 because the total production rate is constant during each flow period.

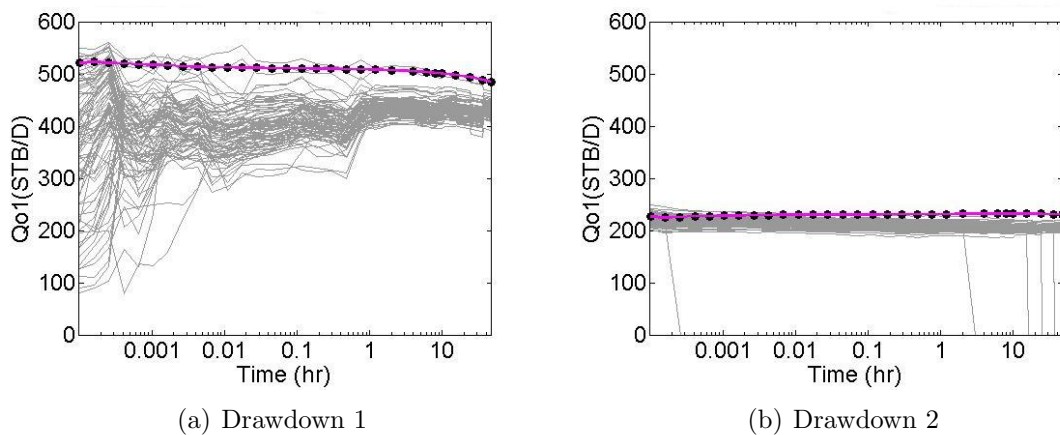


Figure 2.48: Layer rate of layer 1 data match during data assimilation, case 1 of two-layer heterogeneous example

2.3.3 Case 2: assimilating pressure and layer rate data

In this case, both the pressure data from the active well and monitor wells and the layer rate data are assimilated to update the property fields and skin zone log-permeability. Fig. 2.50 shows the ensemble mean of the estimated log-permeability fields for both layers for the case where we assimilate both pressure data and layer rate data. Note in this case, a more geologically reasonable estimate of the log-permeability for layer 2 is obtained but the main channel of layer 1 is wider than in the true case as the

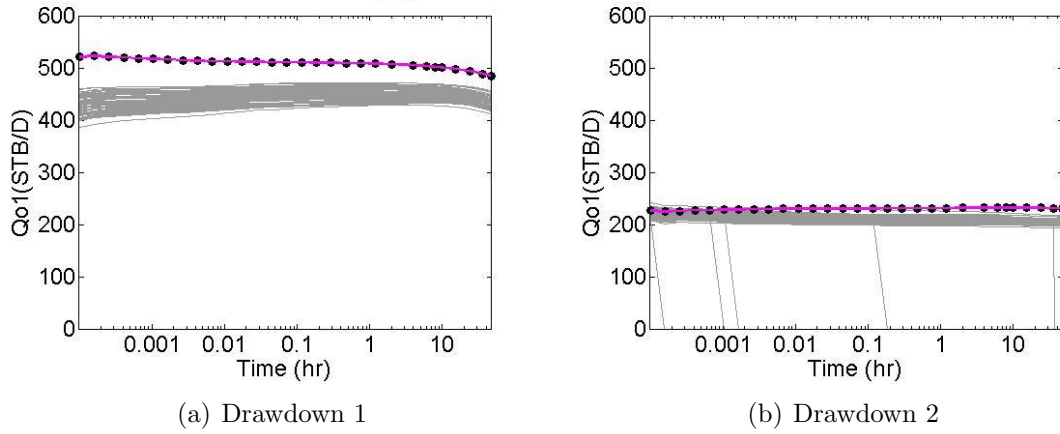
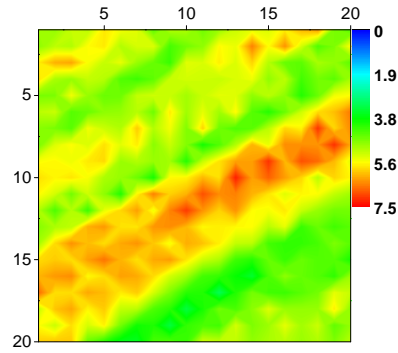
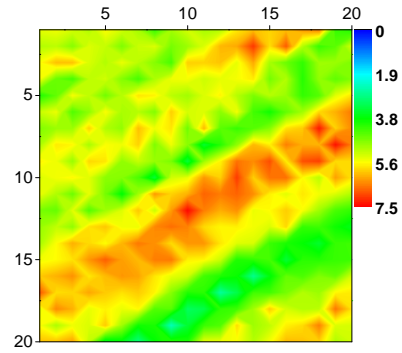


Figure 2.49: Layer rate of layer 1 data match rerun from time 0, case 1 of two-layer heterogeneous example

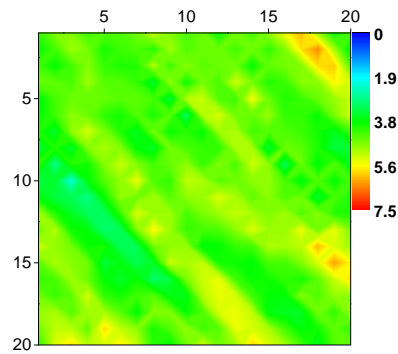
estimate is essentially a combination of the two high permeability channels in layer 1 of the truth. Similar to the log-permeability field, reasonable estimate on the porosity field are obtained as shown in Fig. 2.51. Comparing Fig. 2.52 to Fig. 2.38, we obtained overall more uncertainty reduction by integrating layer rate data.



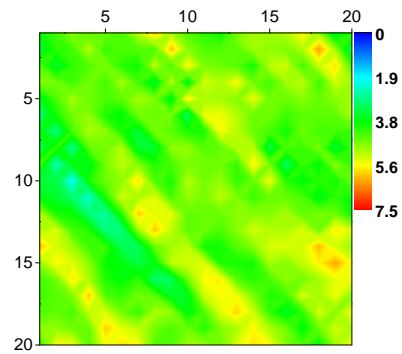
(a) Layer 1, Drawdown 1



(b) Layer 1, Drawdown 2

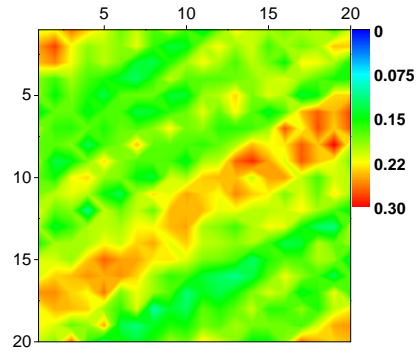


(c) Layer 2, Drawdown 1

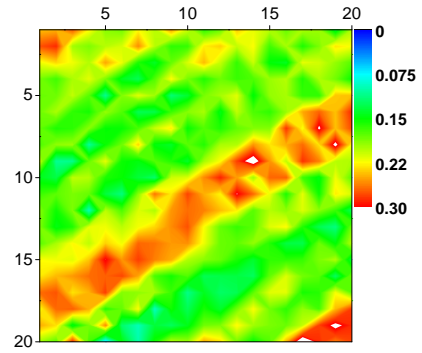


(d) Layer 2, Drawdown 2

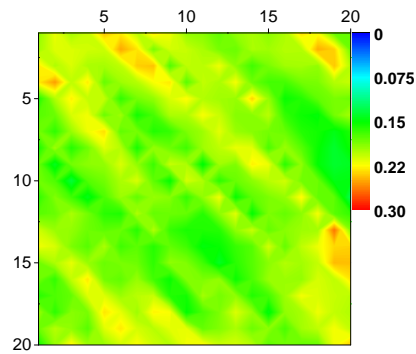
Figure 2.50: The updated ensemble mean of log-permeability field, case 2 of two-layer heterogeneous example



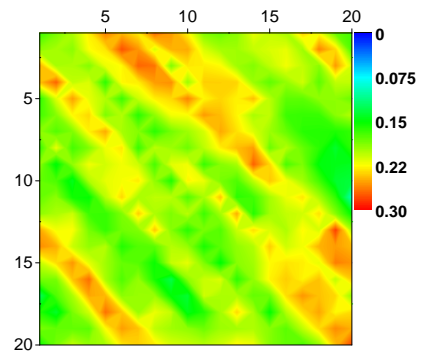
(a) Layer 1, Drawdown 1



(b) Layer 1, Drawdown 2



(c) Layer 2, Drawdown 1



(d) Layer 2, Drawdown 2

Figure 2.51: The updated ensemble mean of porosity field, case 2 of two-layer heterogeneous example

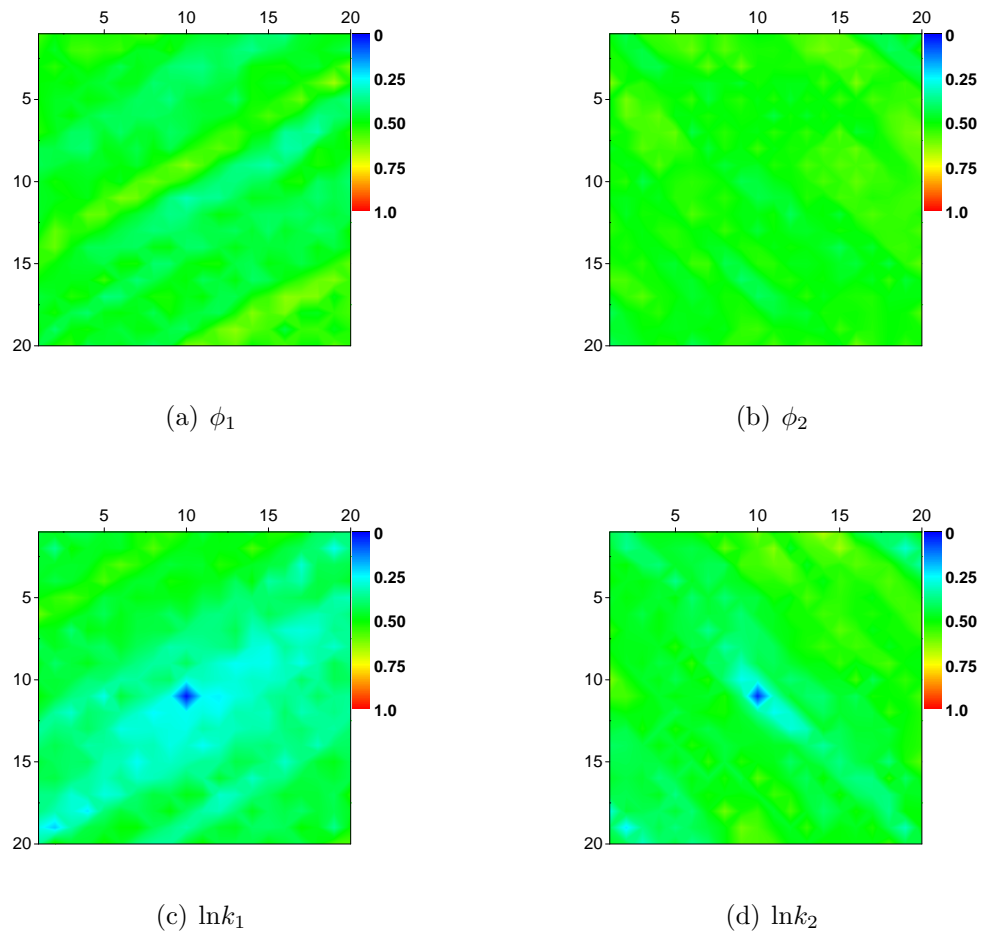


Figure 2.52: Ratio of posterior to prior STD of porosity and log-permeability, case 2 of two-layer heterogeneous example

Fig. 2.53 and Fig. 2.54 show the evolution of the skin parameters during data assimilation in the case where we assimilate not only pressure data but also layer rate data. In both layers, the well gridblock and skin zone log-permeability changed drastically in the first few time steps and remain relatively constant in the later time steps, except for layer 2 well gridblock log-permeability, the uncertainty keep fluctuating and decreasing and the mean is getting close to true in first 30 time steps. The skin factor of the first layer had a dramatic change and shift towards the truth in the first 8 data assimilation time steps and then remains relatively constant. The second layer skin factor gradually increases towards the truth in the first 30 data assimilation steps, which corresponds to the first 48 hours (drawdown 1). At the end of drawdown 1, the mean estimate of layer 2 skin factor is close to the truth. During drawdown 2, it remains relatively constant. Compared to the case where we did not assimilate layer rate data (Fig. 2.39 and Fig. 2.40), we obtain a much better estimate on the individual layer skin factor when the layer rates are assimilated (Fig. 2.53 and Fig. 2.54). However, the estimate of the well effective skin factor in Fig. 2.55 is of similar quality to that obtained assimilating no layer rates in Fig. 2.41, and the uncertainty bounds the truth for all data assimilation steps.

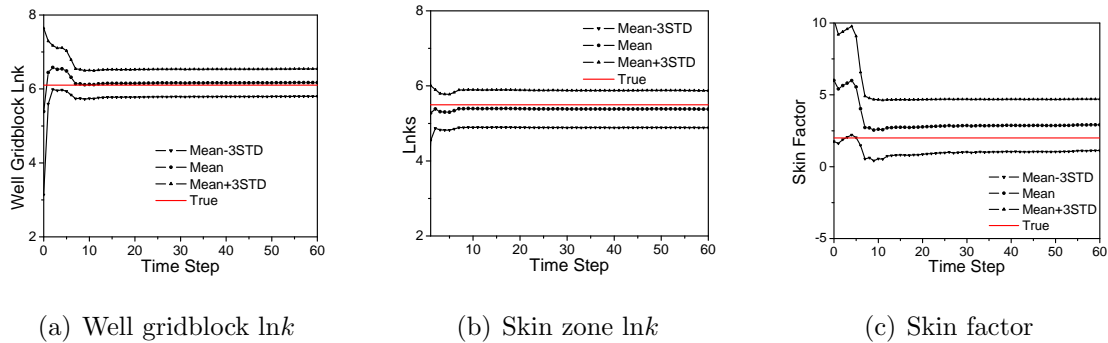


Figure 2.53: Skin of layer 1 when assimilating multi-rate drawdown data, case 2 of two-layer heterogeneous example

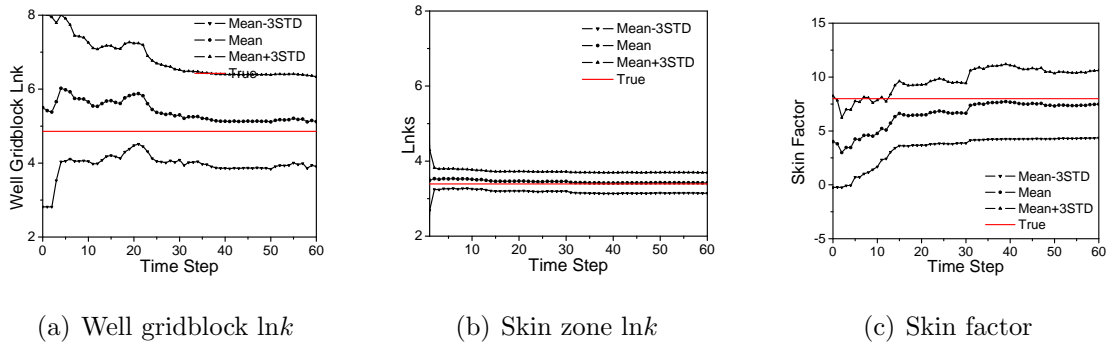


Figure 2.54: Skin of layer 2 when assimilating multi-rate drawdown data, case 2 of two-layer heterogeneous example

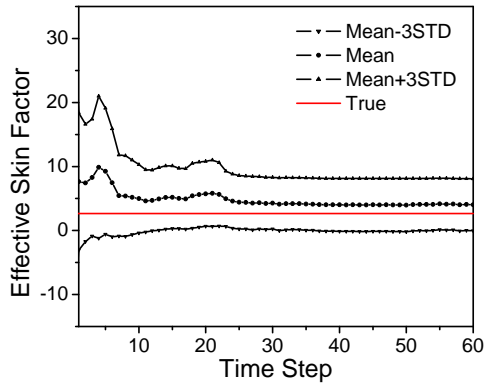


Figure 2.55: Effective skin when assimilating multi-rate drawdown data, case 2 of two-layer heterogeneous example

The pressure data match of the active and monitor wells during data assimilation are shown in Fig. 2.56, Fig. 2.58 and Fig. 2.59. The pressure data matches is reasonably well as in the previous cases. The layer rate data match for the first layer during data assimilation is shown in Fig. 2.57. The ensemble predictions (grey curves) start with a large uncertainty shown as a big spread (from 80 to 550 STB/D) compared to the true layer 1 rate of about 500 STB/D. This large uncertainty is reduced dramatically in the first 3 data assimilation steps and all the realizations give layer rate prediction close to the truth during the rest of data assimilation steps. Rerun from time 0, the layer rates match the true very well as shown in Fig. 2.61. As shown in Fig. 2.60, Fig. 2.62 and Fig. 2.63, the data match when rerunning from time 0 are as good as the pressure data match in the previous case without assimilating the layer rates.

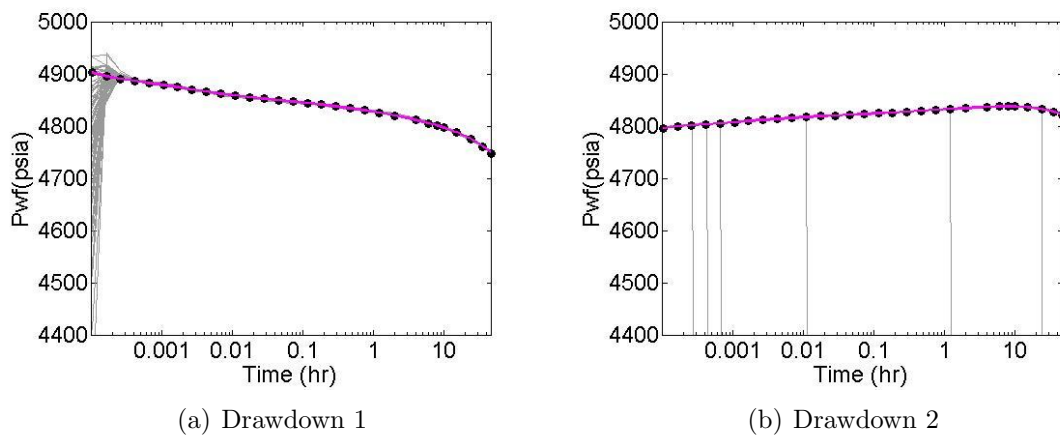
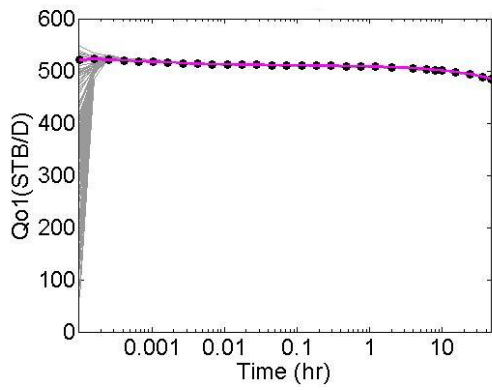
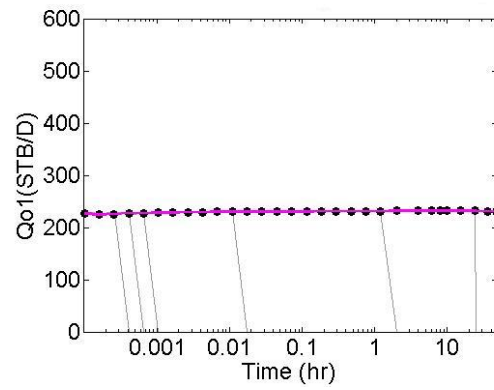


Figure 2.56: Active well drawdown pressure match during data assimilation, case 2 of two-layer heterogeneous example

In summary, for a two-layer reservoir, the pressure data alone cannot resolve the layer skin factors and log-permeability field. However, the pressure data alone is able to resolve effective skin factor. Assimilating both layer rate and pressure data gives good estimates of the individual layer skin factors as well as geologically reasonable estimates of the rock property fields.

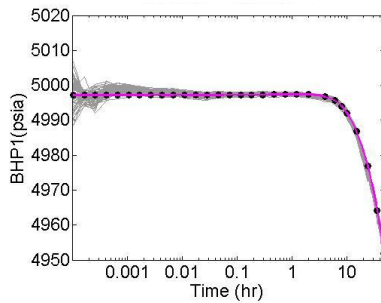


(a) Drawdown 1

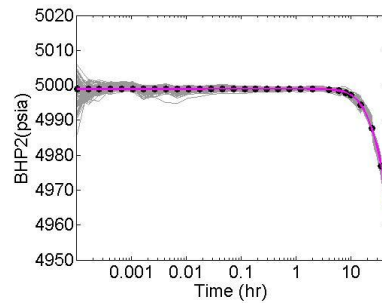


(b) Drawdown 2

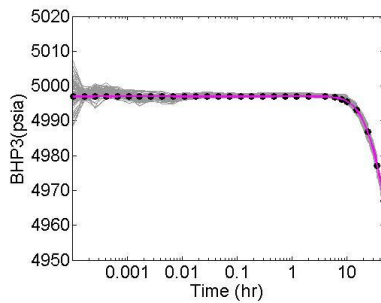
Figure 2.57: Layer rate of layer 1 data match during data assimilation, case 2 of two-layer heterogeneous example



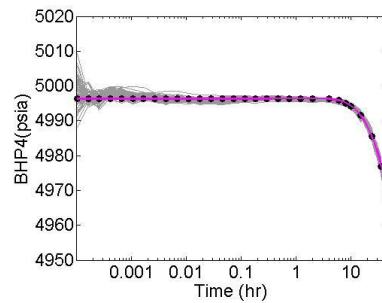
(a) Monitor well 1



(b) Monitor well 2



(c) Monitor well 3



(d) Monitor well 4

Figure 2.58: Monitor well pressure data match during drawdown 1 data assimilation, case 2 of two-layer heterogeneous example

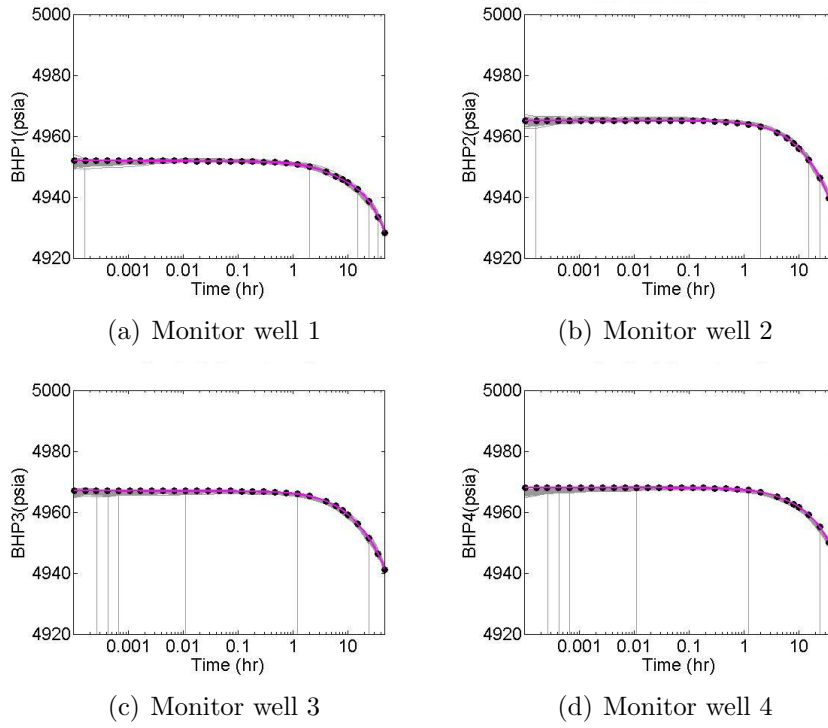


Figure 2.59: Monitor well pressure data match during drawdown 2 data assimilation, case 2 of two-layer heterogeneous example

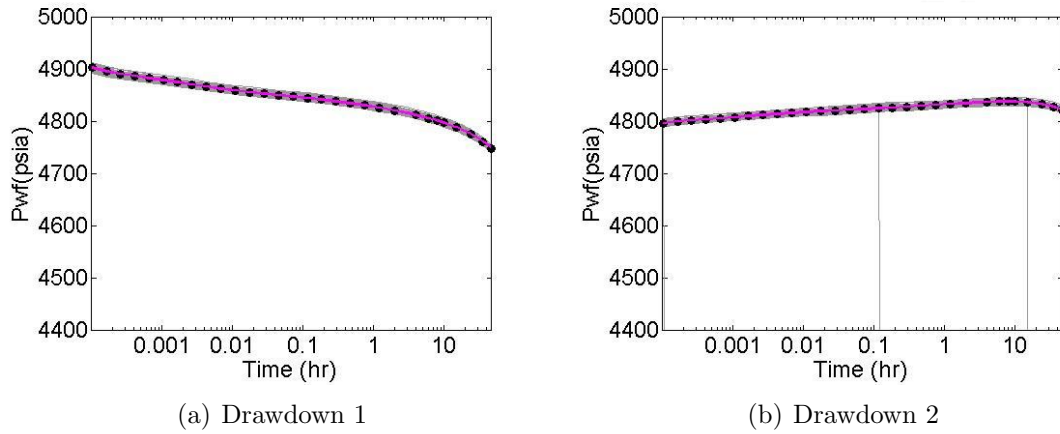
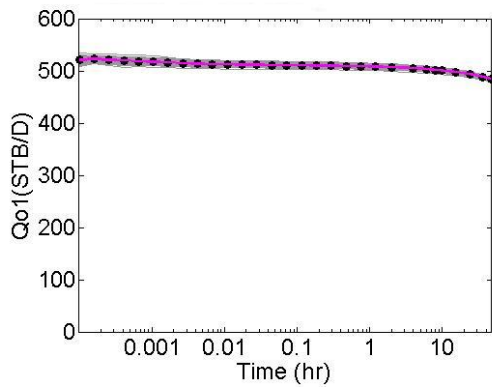
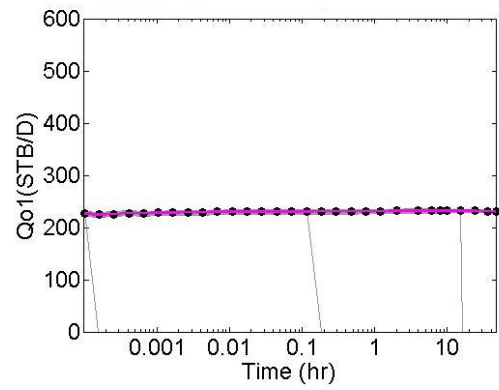


Figure 2.60: Active well drawdown pressure match rerun from time 0, case 2 of two-layer heterogeneous example

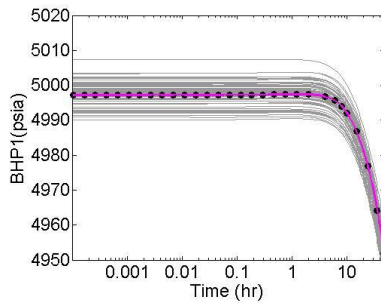


(a) Drawdown 1

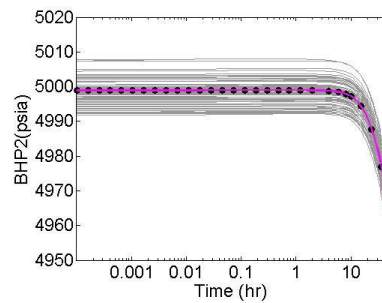


(b) Drawdown 2

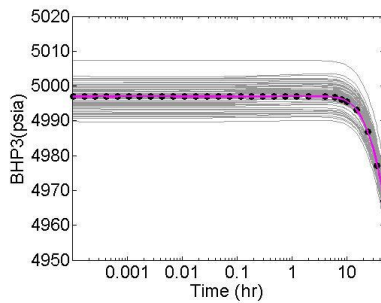
Figure 2.61: Layer rate of layer 1 data match during data assimilation, case 2 of two-layer heterogeneous example



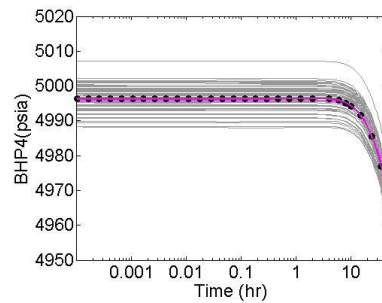
(a) Monitor well 1



(b) Monitor well 2



(c) Monitor well 3



(d) Monitor well 4

Figure 2.62: Monitor well drawdown 1 pressure data match rerun from time 0, case 2 of two-layer heterogeneous example

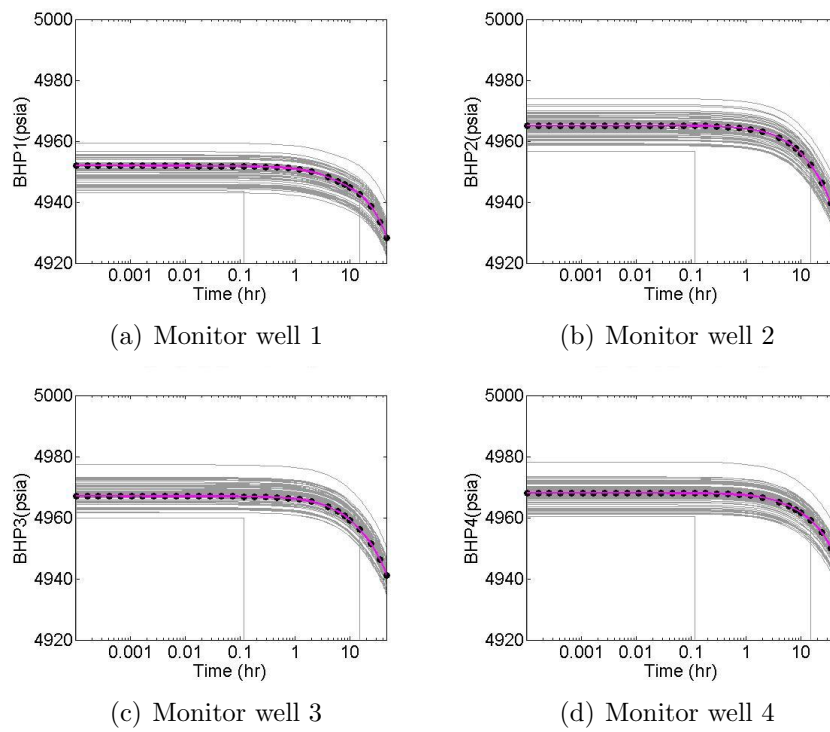


Figure 2.63: Monitor well drawdown 2 pressure data match rerun from time 0, case 2 of two-layer heterogeneous example

CHAPTER 3
ASSIMILATING WELLTEST/MICROSEISMIC
DATA FOR LAYERED RESERVOIRS

3.1 Microseismic data

3.1.1 Overview

During hydraulic fracturing of a hydrocarbon well, many microseismic events occur along the propagating fracture. The first arrival times of the microseismic wave are picked up at the geophones placed in nearby wells as a common microseismic monitoring practice to characterize the distribution, orientation and extent of hydraulic fractures in tight/shale gas reservoirs. The first arrival time depends on the location of the microseismic events as well as the velocity of the formation in its path. The current application of the microseismic measurements is mostly limited to qualitative characterization of the hydraulic fracture by evaluating the microseismic spatial event distribution. The velocity structure that is used in event location inversion is either estimated directly from sonic logs or calibrated from perforation timing microseismic measurements. In the perforation timing procedure, the velocity structure is calibrated by assimilating the arrival time of microseism caused by the perforation shots where the event location is known. As sonic logs reflect the vertical velocity while microseismic wave travel is heavily affected by horizontal velocity, Warpinski et al. [67] suggested that the estimated velocity structure from perforation timing inversion is more accurate in an anisotropic environment and it yielded more reasonable fracture locations when this velocity structure is applied to invert the fracture locations from the microseismic data obtained during fracture stimulation. The velocity structure of the formation can be related to the reservoir rock properties through rock physical models. The travel velocity of microseismic waves can

be calculated as a function of porosity and rock elastic properties. Normally porosity is assumed to be correlated with log-permeability. Hence the microseismic data can be used to improve the formation characterization and reduce the uncertainty of the rock properties.

3.1.2 Forward model for first arrival time calculation

Seismic traveltimes through different media have been calculated in a variety of ways, but raytracing and finite-difference solution to the Eikonal equation are most commonly used. Raytracing is better suited to homogenous or layered velocity fields, while the Eikonal method can be applied to a more complex heterogeneous field. Thus, the Eikonal method is used in this study with heterogeneous model in reservoir characterization.

The propagation of two-dimensional geometric rays and therefore the propagation of two-dimensional wavefronts is guided by the Eikonal equation in 2D isotropic media that is described by

$$\left(\frac{\partial t}{\partial x}\right)^2 + \left(\frac{\partial t}{\partial z}\right)^2 = s(x, z)^2 \quad (3.1)$$

where t is traveltimes, s denotes slowness which is the inverse of velocity, x and z are the coordinate axes [64]. For the ease of explanation, we use the 2D Eikonal equation in the plane as shown in Fig. 3.1, where t_0 , t_1 and t_2 are known arrival times at left bottom, left top and right bottom grid point in the square cell, respectively, h is the uniform grid spacing, s is the slowness in the block.

The two differential terms in Eq. 3.1 can be approximated with the finite difference form as

$$\frac{\partial t}{\partial x} = \frac{1}{2h}(t_1 + t_3 - t_0 - t_2), \quad (3.2)$$

$$\frac{\partial t}{\partial z} = \frac{1}{2h}(t_2 + t_3 - t_0 - t_1). \quad (3.3)$$

Substituting Eq. 3.2 and Eq. 3.3 into Eq. 3.1, we obtain t_3 with superscript “(1)”

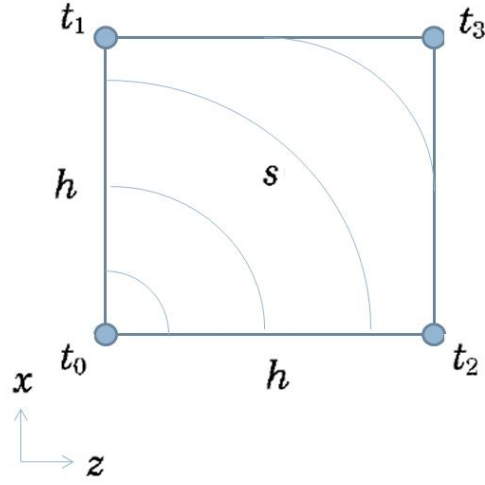


Figure 3.1: 2D Eikonal equation model

representing the calculated travel time in one way, which is,

$$t_3^{(1)} = t_0 + \sqrt{2(hs)^2 - (t_2 - t_1)^2}. \quad (3.4)$$

As shown in Fig. 3.2, the travel time can also be calculated using Eq. 3.5 and Eq. 3.6 considering waves can be transmitted from left top and right bottom grid point as head waves [77]. The scattering wave from left bottom point are considered in Eq. 3.7. The first arrival time is the minimum of travel times among all possible mechanisms (directions) as shown in Eq. 3.8.

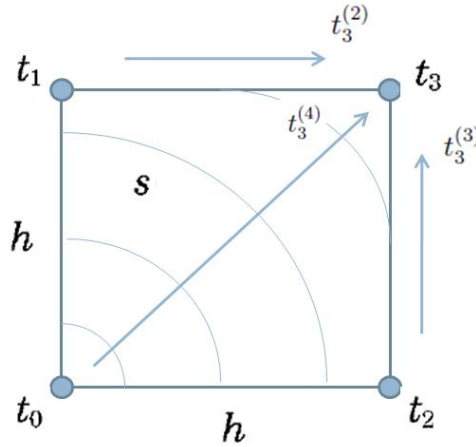


Figure 3.2: Travel time calculation in the 2D Eikonal equation model

$$t_3^{(2)} = t_1 + hs \quad (3.5)$$

$$t_3^{(3)} = t_2 + hs \quad (3.6)$$

$$t_3^{(4)} = t_0 + \sqrt{2}hs \quad (3.7)$$

$$t_3 = \min(t_3^{(1)}, t_3^{(2)}, t_3^{(3)}, t_3^{(4)}) \quad (3.8)$$

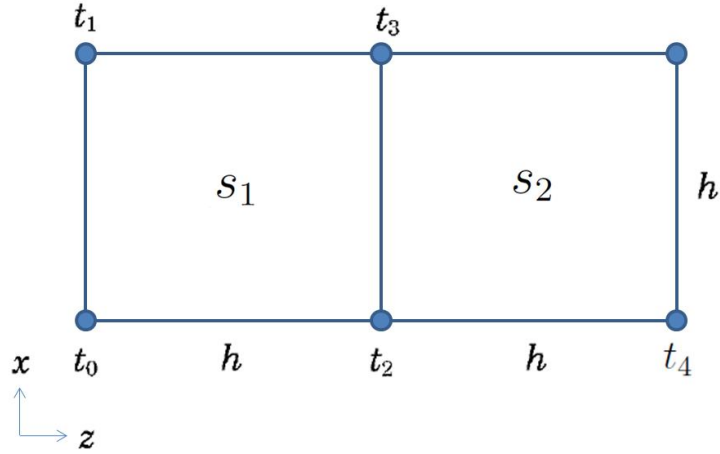


Figure 3.3: 2D Eikonal equation model of local minimum

As shown in Fig. 3.3, when $t_2 < t_0$ and $t_2 < t_4$, t_2 is considered as the local minimum among t_0 , t_2 and t_4 . The two differential terms in Eq. 3.1 can be approximated with the finite difference form as

$$\frac{\partial t}{\partial x} = \frac{1}{h}(t_3 - t_2), \quad (3.9)$$

$$\frac{\partial t}{\partial z} = \frac{1}{2h}(t_4 - t_0). \quad (3.10)$$

Substituting Eq. 3.9 and Eq. 3.10 into Eq. 3.1, we obtain $t_3^{(1)}$ using Eq. 3.11 as,

$$t_3^{(1)} = t_2 + \sqrt{(h\bar{s})^2 - 0.25(t_4 - t_0)^2}, \quad (3.11)$$

where

$$\bar{s} = \frac{s_1 + s_2}{2}. \quad (3.12)$$

When calculating $t_3^{(1)}$, Eq. 3.11 is only used when $t_2 < t_0$ and $t_2 < t_4$, otherwise Eq. 3.4 is used.

The following steps are used to obtain the minimum traveltimes (first arrival time) at each point of the whole computational domain from the source.

- First, we calculate the traveltimes of all grid points on the same row and column as the source using the velocity at each grid block assuming a straight raypath using equations such as Eq. 3.5 and Eq. 3.6. These traveltimes are considered as initial values of first arrival time.
- Second, we calculate the traveltimes for the points on the left side of the source, column by column, from right to left. For each column, the traveltimes at each grid point is calculated from bottom to top grid point by grid point using the above mentioned stencils (Eq. 3.4-Eq. 3.11), and then we recalculate the grid points from top to bottom in the same column using the stencils.
- Third, we calculate the traveltimes for the points on the right side of the source, column by column, from left to right. For each column, the traveltimes at each grid point is calculated from bottom to top using the above mentioned stencils (Eq. 3.4-Eq. 3.11), and then recalculate the grid points from top to bottom in the same column. At this point, all grid points are assigned with first arrival time in the whole domain.
- Fourth, the first arrival time at each grid point is calculated again, column by column from left to right, from bottom to top in each column, for the whole com-

putational domain.

- Fifth, the first arrival time at each grid point is calculated using reversal direction mentioned in fourth step, which is column by column from right to left, from top to bottom in each column.

For steps 2-5, after calculation of each grid point, the new first arrival time is compared with the previous value and the smaller value will be saved and used for calculation of other grid points.

Fig. 3.4 shows an example of the 2D traveltimes calculation scheme with source at the left bottom corner. The arrowed lines illustrate the sequence of grids that are going to be calculated. The blue gridblock represents the gridblock that has been calculated and assigned an arrival time while the white gridblock represents the gridblock that has not been calculated. The top left subfigure represents step 1 when grid points on the same row and column are calculated first assuming direct wave raypath. As there is no grid points on the left of source, step 2 is skipped. The top right and bottom left subfigures represent step 3 when the grid points on the right side of the source are calculated column by column. The bottom right subfigure represents the step 4-5 that each grid point is recalculated using the forward and backward directions after all grid points are calculated.

The method is outlined in 2D for ease of illustration. The Eikonal equation of ray tracing in 3D isotropic media is described by

$$\left(\frac{\partial t}{\partial x}\right)^2 + \left(\frac{\partial t}{\partial y}\right)^2 + \left(\frac{\partial t}{\partial z}\right)^2 = s(x, y, z)^2. \quad (3.13)$$

Similar to a 2D first arrival time calculation, the calculation of 3D begins with calculation of traveltimes to grid points that are nearest to the source assuming a straight raypath. The next step is to calculate the traveltimes in a bigger box by applying finite difference to Eq. 3.13 in three different schemes [65]. The iterative process which is directly analogous to the process for 2D is continued until all the grid points are calculated. More details of

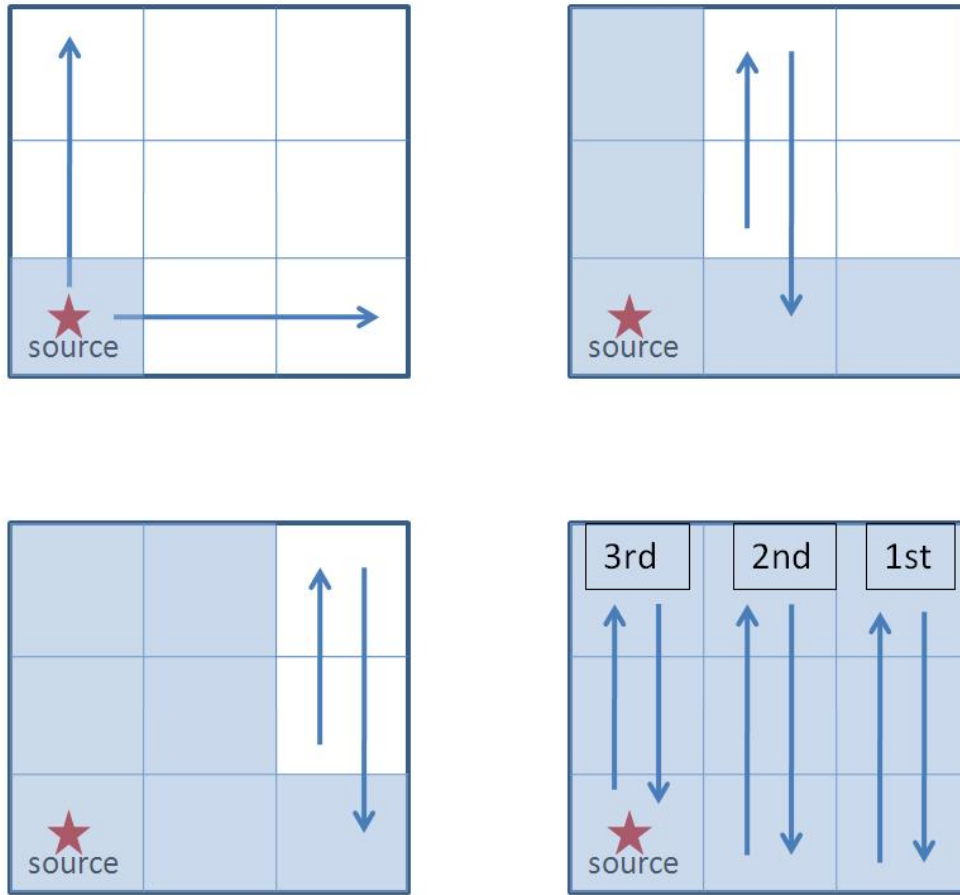


Figure 3.4: 2D traveltimes calculation scheme

the finite difference calculation of traveltimes in 3D are shown in Vidale [65]. The details of the forward model can be found in the open source program [73].

3.1.3 Assimilating microseismic and welltest data

In this study, we hypothesize that the dynamic hydrocarbon reservoir production/welltest data are available and complementary to the microseismic data. If this is verified to be true, the perforation timing measurement together with the production/welltest data will yield a better velocity structure and hence more accurate characterization of the fracture development from microseismic inversion. On the other hand, the microseismic data will help the production/welltest data to resolve or quantify the rock property fields far from wells.

The pressure data during pressure transient test are sensitive to the thickness-

weighted average permeability. As log-permeability is used as the model parameter instead of the absolute permeability, the pressure data are more sensitive to the permeability in the high permeability layer in a multi-layer reservoir when the layer thicknesses are approximately equal and much smaller than the horizontal distance between microseismic event source and receivers. According to Snell’s law, the seismic raypath is longer in the low porosity/high velocity layer, the first arrival time is more sensitive to porosity in the low porosity layer. Due to the fact that the production/welltest data are more sensitive to the high productive (high porosity, high permeability) layers and the microseismic data are more sensitive to the high velocity (low porosity, low permeability) layers, these two types of data are complimentary to each other in resolving the reservoir rock properties.

We will first apply microseismic and welltest data assimilation to a two-layer homogenous reservoir example and then to a two-layer heterogenous reservoir example. Since EnKF is a stochastic process, we run each case with 10 different ensembles generated using the same mean and covariance. At the end, we will apply the microseismic and welltest data assimilation to a ten-layer homogenous reservoir model. Detailed information for each case will be listed in the case description of each section.

3.2 Two-layer homogeneous case

3.2.1 Case description

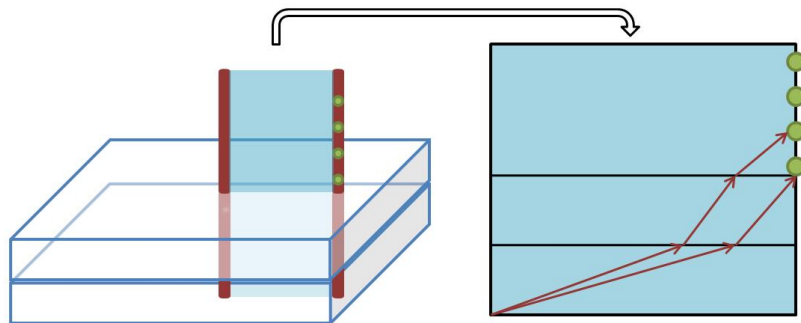


Figure 3.5: Microseismic measurement diagram

We first consider a two-layer homogeneous reservoir in this example. As shown in

Fig. 3.5, the reservoir consists of a $21 \times 21 \times 2$ grid system with a grid size of $200 \text{ ft} \times 200 \text{ ft} \times 50 \text{ ft}$. The bottom layer is denoted as layer 1, the top reservoir layer is denoted as layer 2. The cap rock above the reservoir is 200 ft thick. The reservoir fluid properties is the same as the ones in Chapter 2 (Table 2.1). The initial reservoir pressure is 5000 psi. The initial water saturation is equal to irreducible water saturation, $S_{iw} = 0.1$, so we have single-phase oil flow in the reservoir during the well test. The skin factor is set as zero and will not be considered here, because microseismic data are not expected to improve the estimation of permeability near the wellbore very well.

There is an active well in the middle of reservoir at grid (11,11) and perforated in both layers. Local grid refinement is applied around the active well to capture the early time pressure transient with 20 rings, but we did not put any skinzone. A monitor well is drilled (3000 ft away from the active well). Twelve microseismic receivers are set in the monitor well and they are 20 ft apart from each other. Since each layer is homogenous, the model for calculating the first arrival time is a 2D cross section between the active well and the monitor well, which consists of 300×3000 gridblocks with a grid size of $1 \text{ ft} \times 1 \text{ ft}$ for first arrival time calculation using the Eikonal equation.

The cap rock is assumed to be homogenous. The seismic velocity of the cap rock is $3000 \text{ m}\cdot\text{s}^{-1}$ for P-wave and $2000 \text{ m}\cdot\text{s}^{-1}$ for S-wave. The Raymer model [53, 45] is used to calculate the velocity for a medium composed of a porous dry matrix filled with fluids:

$$V_p = (1 - \phi)^2 \cdot V_{solid} + \phi \cdot V_{fluid} \quad (3.14)$$

with

$$V_{solid} = \sqrt{\frac{K_{solid} + \frac{4}{3} \cdot \mu_{solid}}{\rho_{solid}}} \quad \text{for P-wave,} \quad (3.15)$$

$$V_{solid} = \sqrt{\frac{\mu_{solid}}{\rho_{solid}}} \quad \text{for S-wave,} \quad (3.16)$$

$$V_{fluid} = \sqrt{\frac{K_{fluid}}{\rho_{fluid}}}, \quad (3.17)$$

$$K_{fluid} = K_w \cdot S_w + K_o \cdot S_o + K_g \cdot S_g, \quad K_{solid} = \sum_{i=1}^{N_{solid}} f_i \cdot K_i, \quad \mu_{solid} = \sum_{i=1}^{N_{solid}} f_i \cdot \mu_i, \quad (3.18)$$

$$\rho_{solid} = \sum_{i=1}^{N_{solid}} f_i \cdot \rho_i, \quad \rho_{fluid} = \rho_w \cdot S_w + \rho_o \cdot S_o + \rho_g \cdot S_g. \quad (3.19)$$

Throughout, ϕ is porosity, K is bulk modulus (pa), μ is shear modulus (pa), ρ is density (kg/m^3), f_i is the fractional volume of the i th solid component, and S_m is the fluid saturation of phase m . The subscript i refers to the i th solid component, o to oil, w to water, and g to gas. The difference in P- and S-wave velocity calculation is only in the calculation of V_{solid} .

In the example, we assume there is only one solid component (sandstone) and two liquid phases, water and oil. The physical properties of liquid and sandstone are listed in Table 3.1 and Table 3.2.

Table 3.1: Fluid Properties

$K_o(Pa)$	$K_w(Pa)$	$\rho_o (kg/m^3)$	$\rho_w (kg/m^3)$
6.71×10^8	2.39×10^9	800	1000

Table 3.2: Sandstone Properties

$K_s(Pa)$	$\mu_s(Pa)$	$\rho_s (kg/m^3)$
3.80×10^{10}	4.40×10^{10}	2.65×10^3

Once the velocity structure is calculated using Eq. 3.14 to Eq. ?? with the poros-

ity distribution, the first arrival time at each receiver can be obtained by solving the Eikonal equation [65], which was discussed in section 3.1.2. The true porosity and log-permeability of the two reservoir layers are shown in Table 3.3. The velocity profile of the P-wave and S-wave are shown in Fig. 3.6 for both the reservoir rock and the cap rock. As shown in Fig. 3.6, the bottom layer has smaller porosity and higher velocity value. Lower porosity indicates more solid content and because solid velocity is much higher than liquid velocity, the overall velocity in a low porosity layer is higher than in a high porosity layer. The first arrival time maps from perforation shots in both layers are shown in Fig. 3.7 and Fig. 3.8. The perforation coordinates in layer 1 and layer 2 are (0, 25) and (0, 75), respectively. As shown in Fig. 3.7 and Fig. 3.8, the P-wave first arrival time is smaller than the S-wave first arrival time as P-wave velocity is much higher than S-wave velocity. The wave path is perpendicular to arrival time contour lines. The wave path can be calculated using reversibility of the wave travel [77]. As wave propagates into a different media, the raypath follows Snell’s law and it bends as it goes into another layer. As the P-wave and S-wave are strongly related (Eq. 3.14), the P-wave and S-wave wave paths are very similar. Since seismic wave travels fastest in the high velocity layer, the waves are transmitted mostly in the high velocity layer, layer 1, from both perforation shots, as shown in Fig. 3.7(a) and Fig. 3.8(a) where the black line represent the raypath to one of the receivers.

Table 3.3: True porosity and log-permeability

	Layer 1	Layer 2
Porosity	0.125	0.235
log-permeability	2.403	5.501

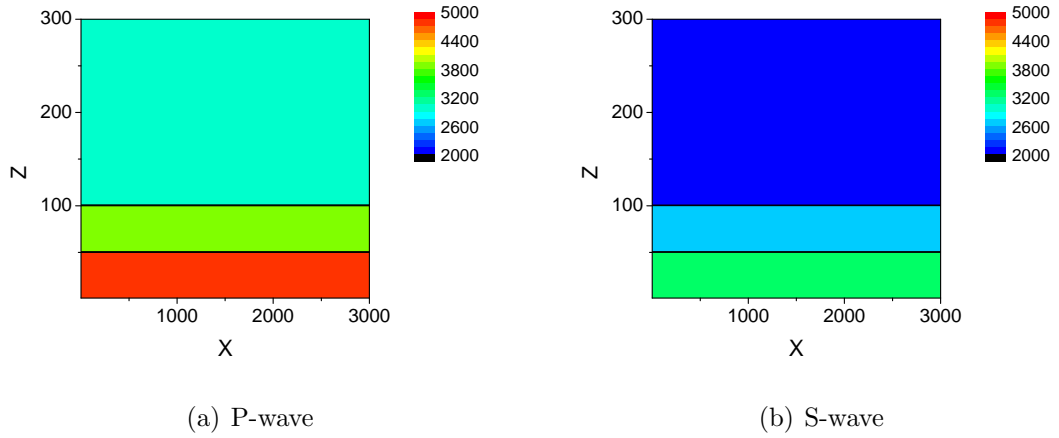


Figure 3.6: Velocity structure of the two-layer homogeneous example

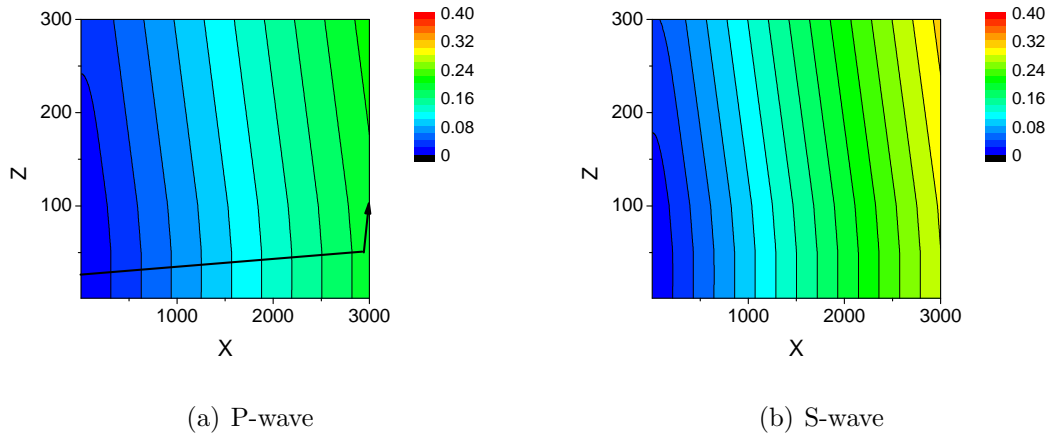


Figure 3.7: Simulated first arrival time map from perforation shot at the bottom reservoir layer, two-layer homogeneous example

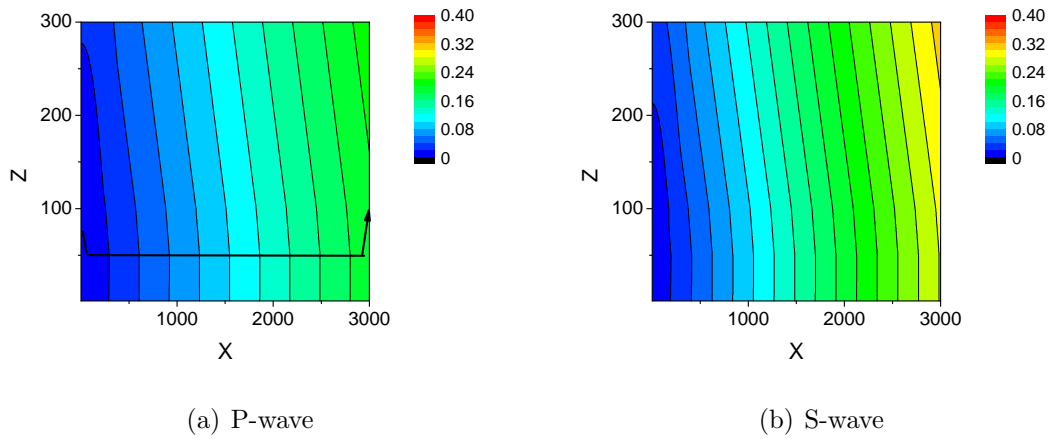


Figure 3.8: Simulated first arrival time map from perforation shot at the top reservoir layer, two-layer homogeneous example

The porosity and permeability are assumed to be Gaussian with the geostatistical parameters listed in Table 3.4. The initial ensemble of porosity and log-permeability is generated using Eq. 3.20, where z_i is a random normal deviate.

$$\begin{pmatrix} \phi \\ \ln k \end{pmatrix} = \begin{pmatrix} \bar{\phi} \\ \overline{\ln k} \end{pmatrix} + \begin{pmatrix} C_\phi & C_{\phi \ln k} \\ C_{\phi \ln k} & C_{\ln k} \end{pmatrix}^{\frac{1}{2}} \begin{pmatrix} z_1 \\ z_2 \end{pmatrix}, \quad (3.20)$$

where $C_\phi = \sigma_\phi^2$, $C_{\ln k} = \sigma_{\ln k}^2$ and $C_{\phi \ln k} = \rho \sigma_\phi \sigma_{\ln k}$. Fig. 3.9 shows the log-permeability vs. porosity of the initial ensemble members. The black stars represent the true log-permeability and porosity of the two layers. The red and lavender dots represent ensemble members of layer 1 and layer 2, respectively. There are totally 100 ensemble members. As shown in Fig. 3.9, the log-permeability and porosity are correlated with a correlation coefficient of 0.8. The porosity and log-permeability in these two layers are distinct in values, and they have minimal overlap in the initial ensemble. The microseismic data (first arrival times) are directly related to the layer porosities through Eq. 3.14. not log-permeability, The log-permeabilities are updated during data assimilation using EnKF through correlation.

Table 3.4: Porosity and log-permeability

	Layer 1	Layer 2
Porosity		
True	0.125	0.235
Mean, $\bar{\phi}$	0.15	0.25
STD, σ_ϕ	0.025	0.025
$\ln k$		
True	2.403	5.501
Mean, $\overline{\ln k}$	3	5
STD, $\sigma_{\ln k}$	0.6	0.6
Correlation coefficient, ρ	0.8	0.8

The synthetic microseismic data (first arrival times at 12 receivers) are generated by assuming the perforation at each layer is shot in the middle of the layer (25 ft from the base of the layer.) Once the well is completed, it is put on production at 1500 STB/D

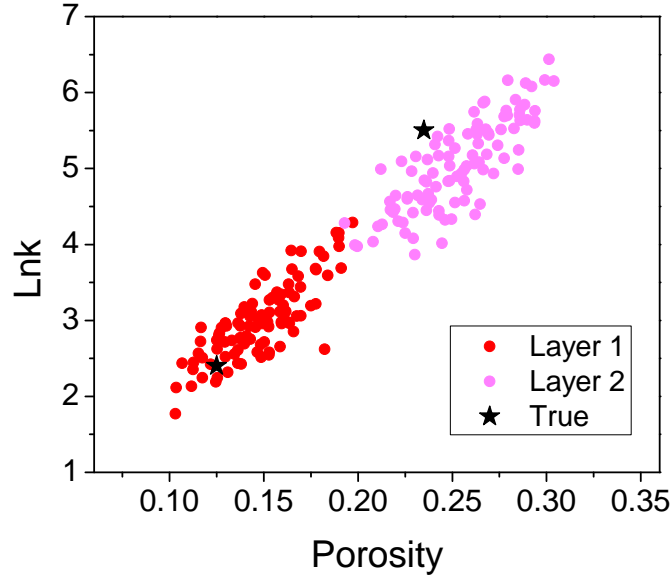


Figure 3.9: Prior $\ln k$ vs. ϕ , two-layer homogeneous example

liquid rate for 2 days and shut in for another 2 days for buildup. The measurement error for pressure, microseismic and layer rate data are 1 psi, 1 ms and 5 STB/D, respectively.

In this chapter, we consider 4 scenarios:

1. Porosity and log-permeability fields are updated by assimilating pressure transient data only. In the pressure transient test, there are 10 drawdown and 10 buildup pressure data which are logarithmically spaced in time. In the heterogeneous case, interference pressure data measured at the monitor wells are also assimilated.
2. Porosity and log-permeability fields are updated by assimilating microseismic data only. The microseismic data are the P- and S-wave first arrival times at the receivers of a nearby monitor well for homogeneous case or receivers of 4 monitor wells for heterogeneous case.
3. Porosity and log-permeability fields are updated using both pressure and microseismic data.
4. The porosity and log-permeability fields are updated by assimilating the pressure transient data and layer rate data as in the previous chapter.

3.2.2 Assimilating pressure transient data only

In this case, we assimilate pressure transient data with only 10 drawdown and 10 buildup data points. Fig. 3.10 shows the estimated log-permeability vs. porosity of all ensemble members after assimilating pressure data. Log-permeability in layer 2 (higher permeability layer) is well resolved by assimilating pressure transient data only. The final estimated log-permeability is around the true (5.5), as indicated by the fact that all points of layer 2 on a relatively horizontal line. Uncertainties of other parameters, porosity of both layers and log-permeability of layer 1, are reduced compared to the prior in Fig. 3.9. Fig. 3.11 shows the estimated porosity and log-permeability of two layers at each assimilation step. In this and similar plots, the red line represents the true, the top, middle and bottom black lines represent mean plus 3 times standard deviation, mean and mean minus 3 times standard deviation of the ensemble, respectively. The first 10 steps are drawdown and the second 10 steps are buildup. Similar conclusions can be drawn from Fig. 3.11 as from Fig. 3.10. Large uncertainty decrease is observed for the log-permeability in layer 2 - the high permeability layer. The porosity of layer 2 has some uncertainty reduction after assimilating the first few data points during drawdown and buildup. The uncertainty decreased for layer 1 is minimal during assimilating drawdown data, but more significant with buildup data.

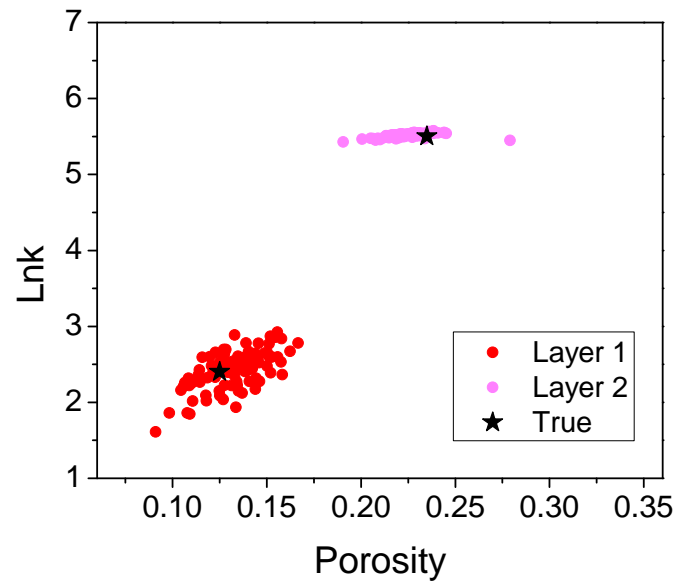
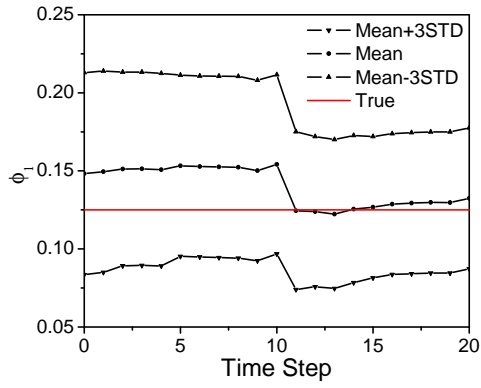
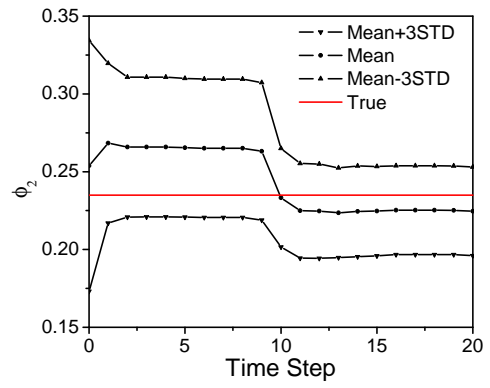


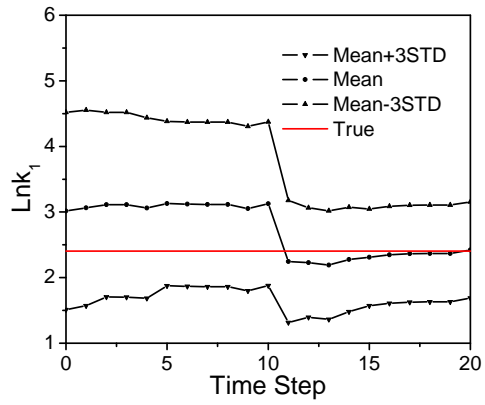
Figure 3.10: $\ln k$ vs. ϕ , after assimilating pressure data only, two layer homogeneous example



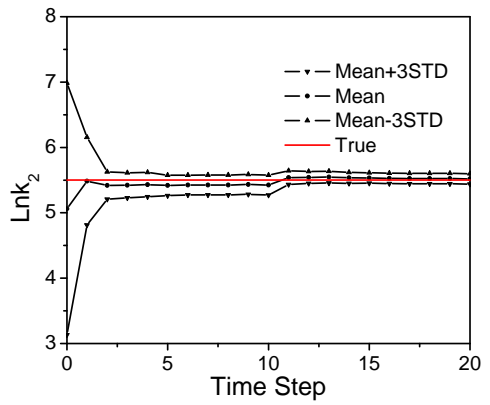
(a) ϕ_1



(b) ϕ_2



(c) $\ln k_1$



(d) $\ln k_2$

Figure 3.11: Porosity and log-permeability in layer 1 and layer 2 during pressure data assimilation, two layer homogeneous example

The pressure data match during data assimilation and rerun from time zero are shown in Fig. 3.12. Similar to results shown in Chapter 2, the uncertainty of data prediction decreases significantly in the first several data assimilation steps and remains small for the rest of the data assimilation steps. The pressure and its derivative match the true after rerunning from time zero. Note that during data assimilation, we match pressure data only, not the pressure derivatives.

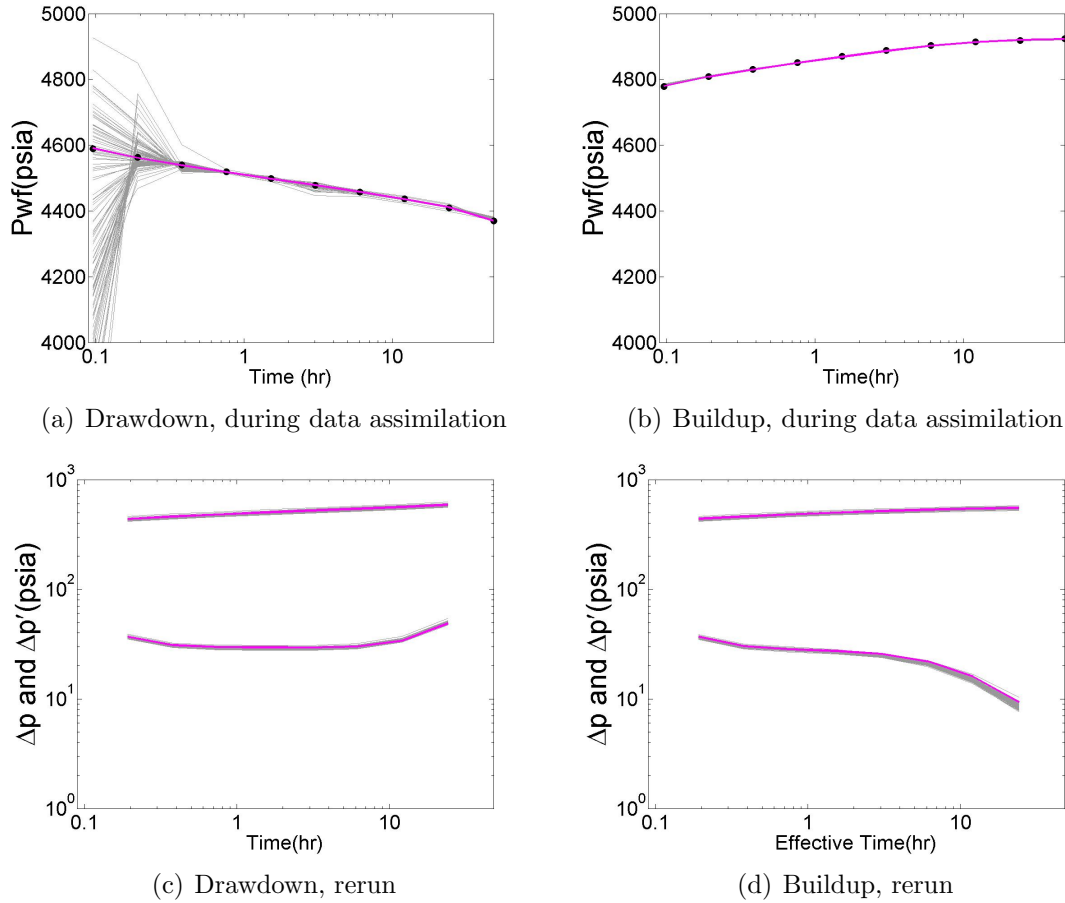


Figure 3.12: Active well pressure data match assimilating pressure data only, two layer homogeneous example

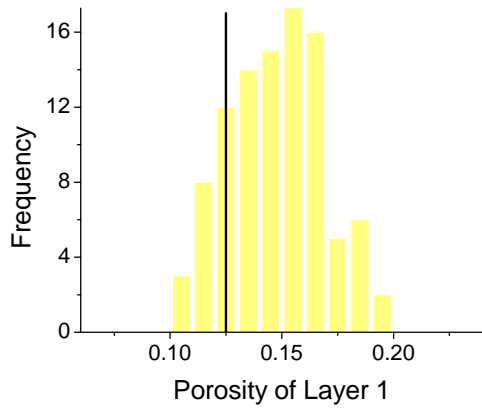
3.2.3 Assimilating microseismic data only

In this case, the ensemble of porosity and log-permeability in both reservoir layers are updated by assimilating the first arrival times of P-wave and S-wave at 12 receivers on the top of reservoir layer using EnKF. We first assimilate the 12 first arrival times of P-wave and 12 first arrival times of S-wave from the perforation shot of layer 1 which is

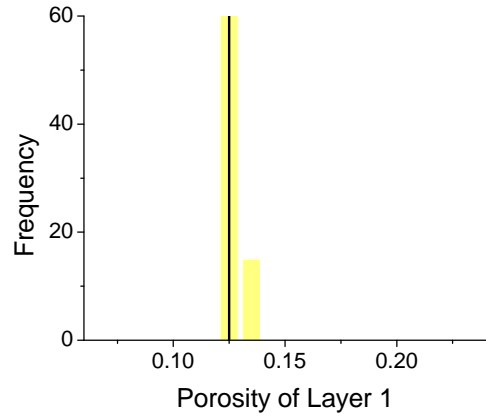
located in the center of layer 1; then assimilate the 12 first arrival times of P-wave and S-wave from the perforation shot at layer 2 which is located in the center of layer 2.

Fig. 3.13 and Fig. 3.14 show the histogram of the initial ensemble and final estimates of porosity and log-permeability after assimilating the microseismic data of the perforation shot of layer 1. The black vertical line in the figure is the true. Comparing Fig. 3.13(a) and Fig. 3.13(b) indicates that a large uncertainty decrease in layer 1 porosity. In contrast, the uncertainty reduction for layer 2 porosity is insignificant (Fig. 3.13(c), Fig. 3.13(d)). As shown in Fig. 3.14(b) and Fig. 3.14(d), the uncertainty in log-permeability of layer 1 is reduced, however the mean of ensemble is slightly larger than the true; the estimate of log-permeability of layer 2 is not improved.

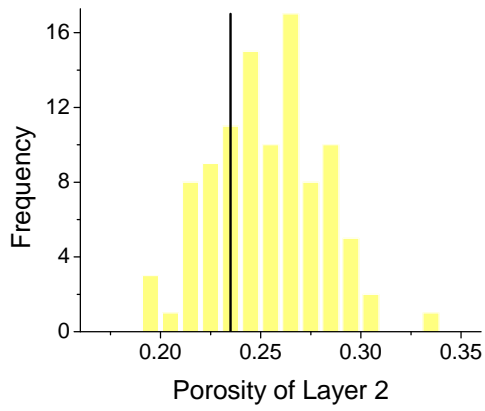
Both porosity and log-permeability are updated by assimilating microseismic data. However, only porosity is related to the first arrival time in a functional form and reflected in the model. The permeability is updated by EnKF through correlation in the cross-covariance matrix. Due to the fact that the raypath of P- and S-wave between the source and receiver has a large proportion in the low porosity layer (high velocity) to satisfy minimum travel time, the first arrival time are more sensitive to the low permeability/porosity layer. Thus, the uncertainty reduction in the low porosity/permeability layer is larger compared to the high porosity/permeability layer.



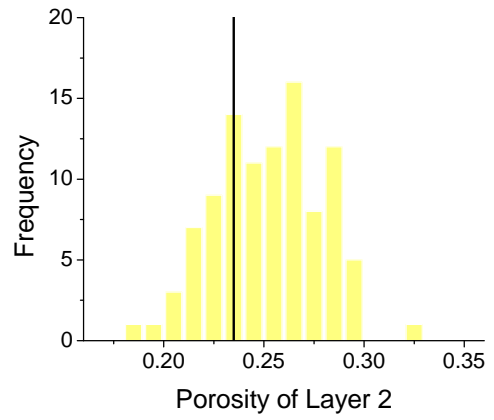
(a) ϕ_1 , Prior



(b) ϕ_1 , Posterior

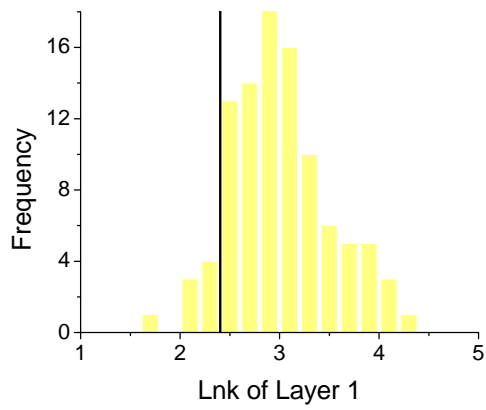


(c) ϕ_2 , Prior

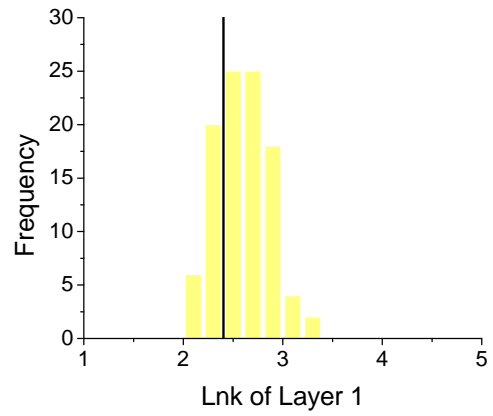


(d) ϕ_2 , Posterior

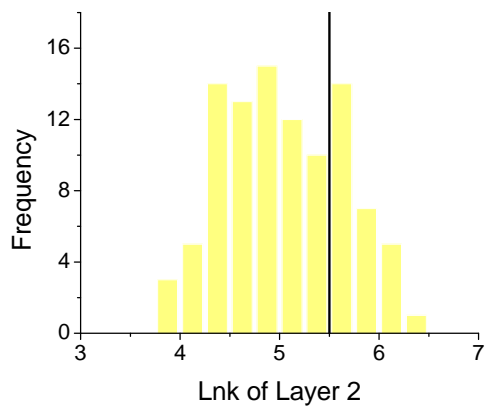
Figure 3.13: Prior and posterior porosity in layer 1 and layer 2 after assimilating first arrival time of perforation shot of layer 1, two layer homogeneous example



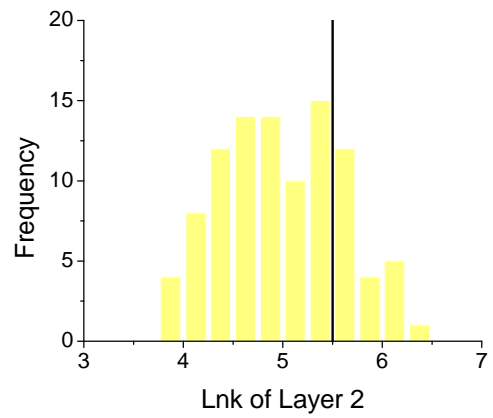
(a) $\ln k_1$, Prior



(b) $\ln k_1$, Posterior



(c) $\ln k_2$, Prior



(d) $\ln k_2$, Posterior

Figure 3.14: Prior and posterior $\ln k$ in layer 1 and layer 2 after assimilating first arrival time of perforation shot in layer 1, two layer homogeneous example

Fig. 3.15(a) and Fig. 3.15(b) show the predicted first arrival times recorded at the 12 receivers using the initial ensemble and final ensemble after assimilating first arrival time data using EnKF. Note that R1-R12 on the x-axis are P-wave first arrival times and R13-R24 are the S-wave first arrival times in a box plot. The black dots are the observed data. Fig. 3.16 explains the box plot. The prior prediction has a big uncertainty and also the mean is larger than the observed data as shown in Fig. 3.15(a). The posterior prediction after assimilating microseismic data has very small uncertainty and matches the observed data as shown in Fig. 3.15(b).

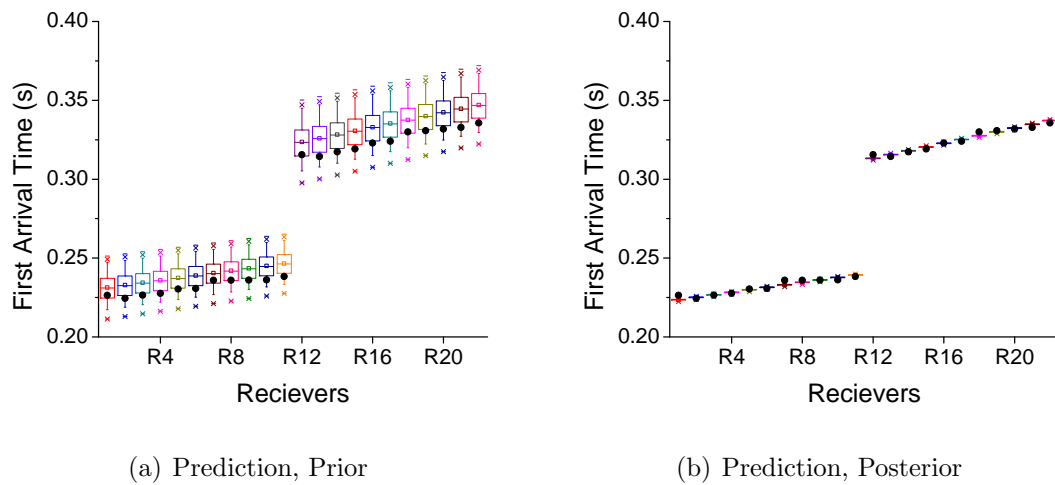


Figure 3.15: Prediction assimilating first arrival time of perforation shot in layer 1, two layer homogeneous example

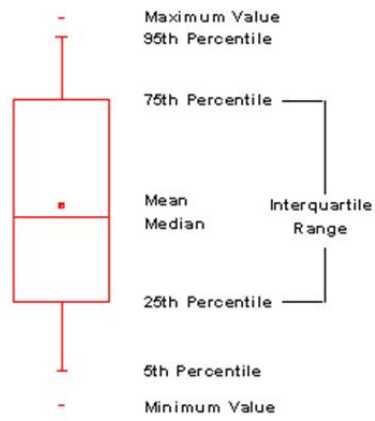


Figure 3.16: Box plot schematic

The crossplot of the updated permeability vs. porosity is shown in Fig. 3.17. As indicated in Fig. 3.13 and Fig. 3.14, the uncertainty of porosity in the low porosity layer (layer 1) decreased significantly and the estimated porosity is almost the same as the truth as all points for layer 1 are on a vertical line close to the truth. The uncertainty of permeability in layer 1 has also decreased due to its strong correlation with porosity. The final ensemble of porosity and log-permeability for in layer 2 is similar to the prior ensemble (Fig. 3.9), i.e., conditioning to microseismic data has not reduced the uncertainty in porosity and log-permeability for layer 2.

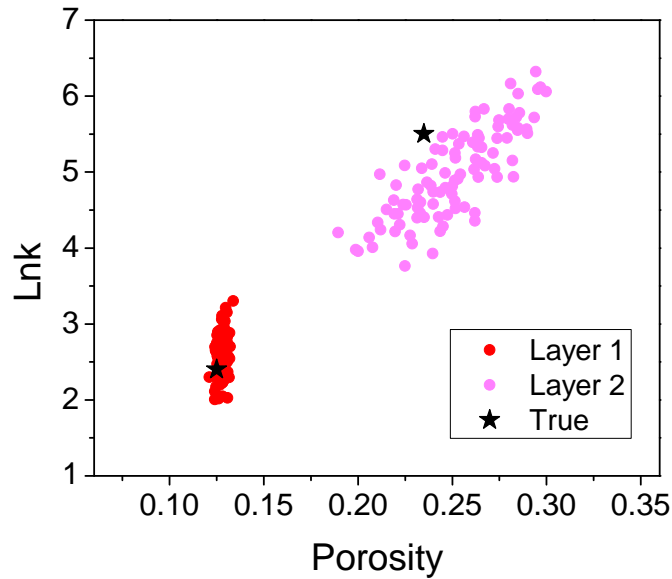


Figure 3.17: $\ln k$ vs. ϕ , after assimilating first arrival times from perforation shot at layer 1, two layer homogeneous example

Fig. 3.18 and Fig. 3.19 show the histograms of the final estimated porosity and log-permeability after assimilating the microseismic data from the perforation shot of both layers. The posterior ensemble after assimilating perforation shot of layer 1 is used as the prior for assimilating first arrival time of the wave from the perforation shot of layer 2. Fig. 3.20 is the cross-plot of the final estimated porosity and log-permeability. Due to large velocity contrast between the two layers, the raypath from the perforation shots in both layers has the largest proportion in the low porosity (high velocity) layer (Fig. 3.8(a)). Therefore, the first arrival times from both perforation shots are more sensitive to the properties in the low porosity layer (layer 1). Therefore, the porosity of layer 1 is accurately estimated and the log-permeability of layer 1 also has significant uncertainty reduction because it is correlated with layer 1 porosity. Due to low sensitivity, matching the first arrival times yields insignificant uncertainty reduction in layer 2 porosity and log-permeability. As porosity in lower porosity layer is already resolved after assimilating perforation shot of layer 1, assimilating perforation shot of layer 2 has not further improved porosity and permeability estimation as shown in Fig. 3.18, Fig. 3.19 and Fig. 3.20. Fig. 3.21 shows reasonable first-arrival data match from the perforation shot of layer 2.

3.2.4 Assimilating both microseismic and pressure data

In this section, the porosity and log-permeability fields are updated by assimilating both microseismic and pressure transient data using EnKF. The pressure transient data are the same as that in section 3.2.2 with 10 pressure points during drawdown and 10 pressure points during buildup. The microseismic data are the same as the ones used in section 3.2.3.

The results of assimilating microseismic data are shown in the previous section. Fig. 3.22 shows the evolution of layer porosity and log-permeability values during assimilating the pressure transient data. Note that the initial ensemble are the final estimate after assimilating the microseismic data in the previous section. The estimate of porosity in layer 1 is accurate after assimilating microseismic data and does not change when

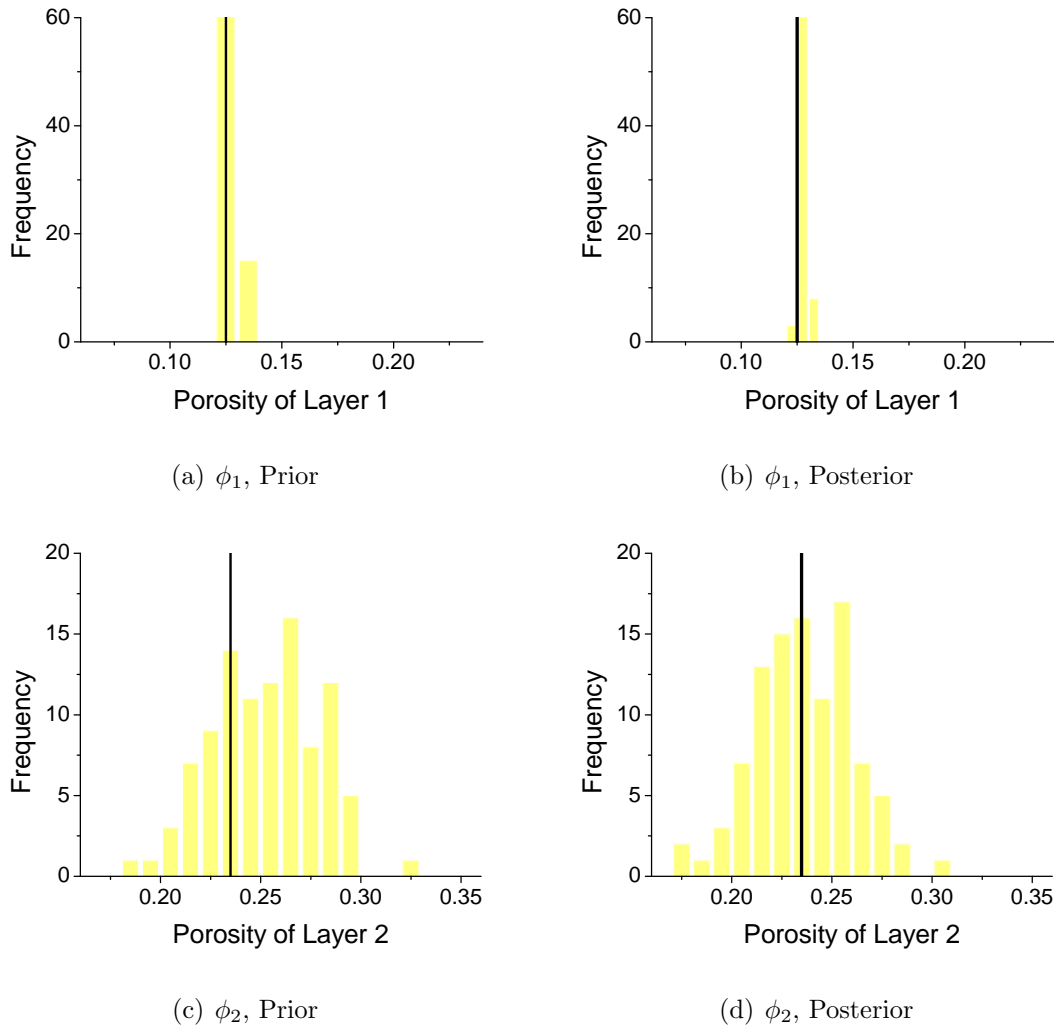


Figure 3.18: Porosity in layer 1 and layer 2 after assimilating first arrival time of both perforation shots, two-layer homogeneous example

assimilating pressure data as shown in Fig. 3.22(a). As shown in Fig. 3.22(c), the estimated log-permeability in layer 1 changes gradually during drawdown pressure data assimilation and remains about the same in the buildup assimilation steps. The mean of final ensemble of log-permeability in layer 1 is around 2.54, which is slightly higher than the true 2.4. The uncertainty in the log-permeability of the high permeability layer (layer 2) is reduced significantly by assimilating the pressure transient data as shown in Fig. 3.22(d) and the uncertainty in porosity from the same layer is reduced somewhat as shown in Fig. 3.22(b). The true values of the layer porosities and log-permeabilities are within the uncertainty bounds of the final estimates.

Same conclusions can be drawn from the crossplot of log-permeability vs. poros-

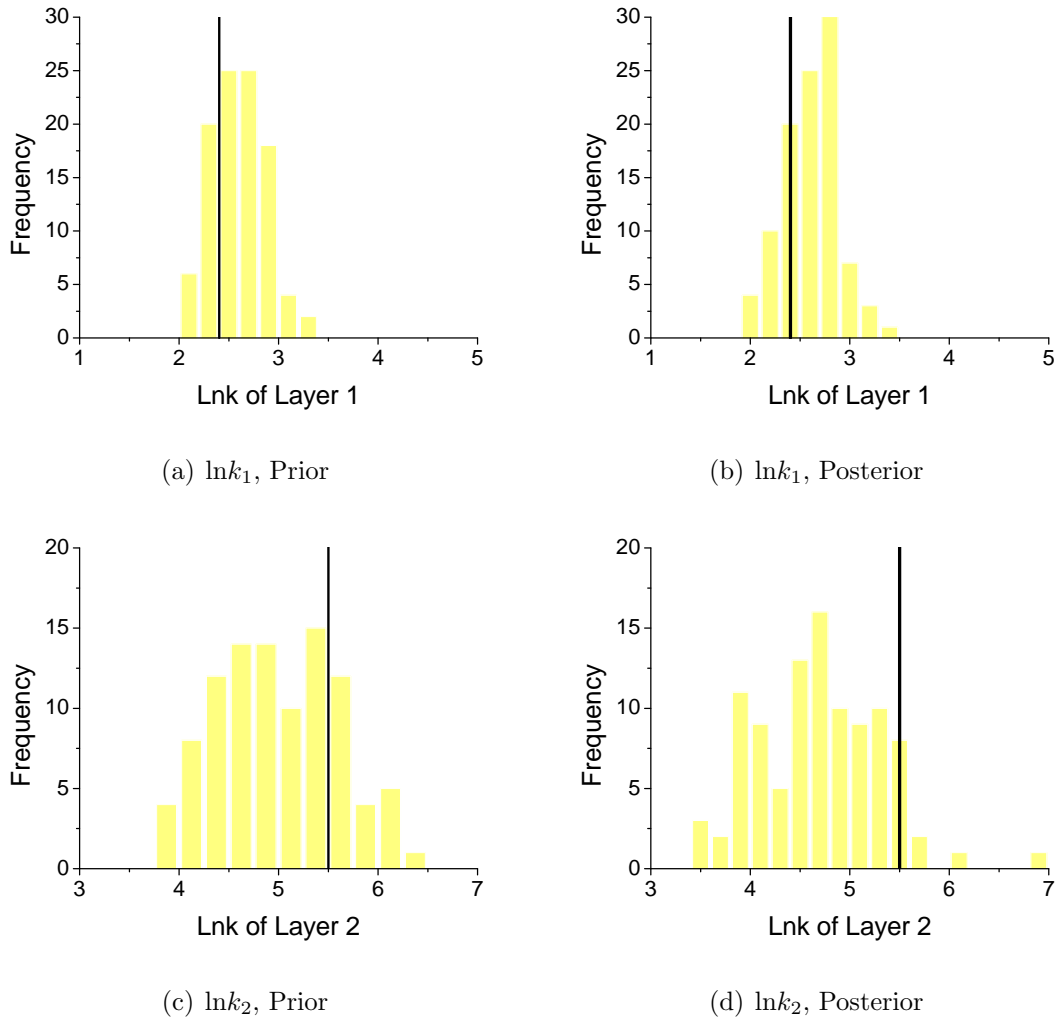


Figure 3.19: $\ln k$ in layer 1 and layer 2 after assimilating first arrival time of both perforation shots, two-layer homogeneous example

ity after assimilating both microseismic data and pressure transient data as shown in Fig. 3.23. The uncertainty in log-permeability of the high permeability layer decreased significantly, while the uncertainties in the log-permeability of the low permeability layer and the porosity in high porosity layer are reduced somewhat compared to Fig. 3.20 after further data assimilation on the microseismic data. After assimilating both microseismic and pressure data, the porosity in low porosity layer and log-permeability in high permeability layer are resolved, while uncertainty of the porosity in high porosity layer and log-permeability in low permeability layer is reduced.

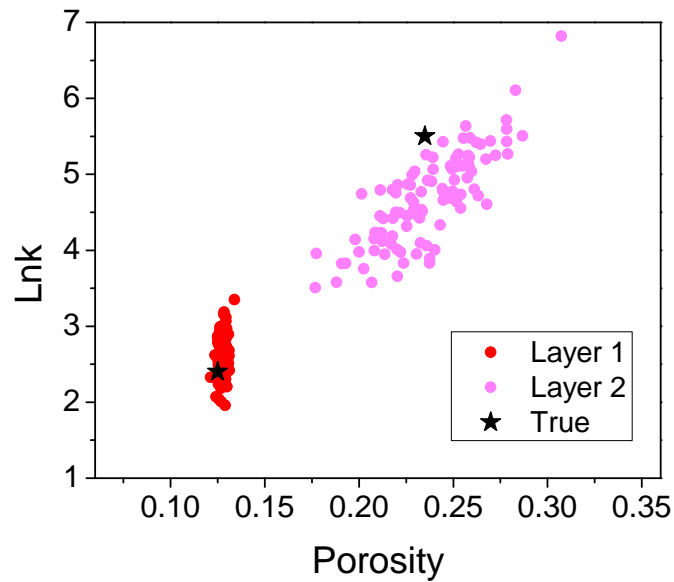


Figure 3.20: Lnk vs. ϕ , after assimilating microseismic data, two-layer homogeneous example

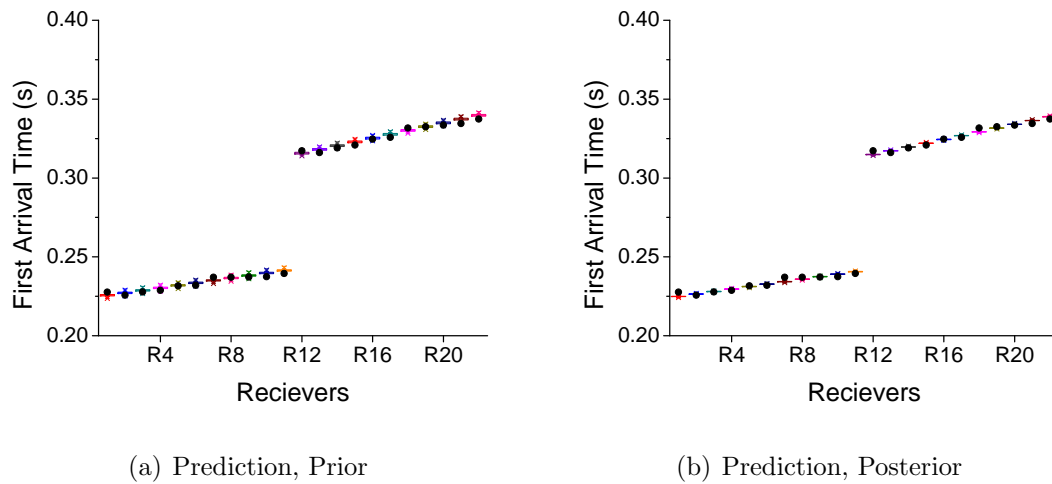
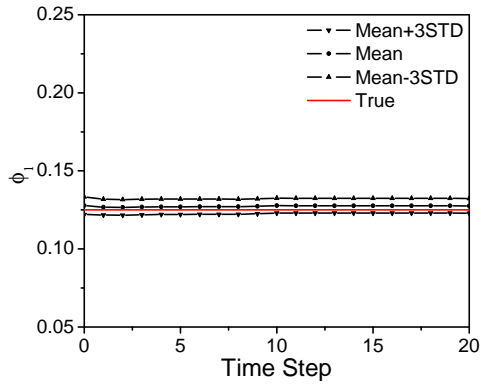
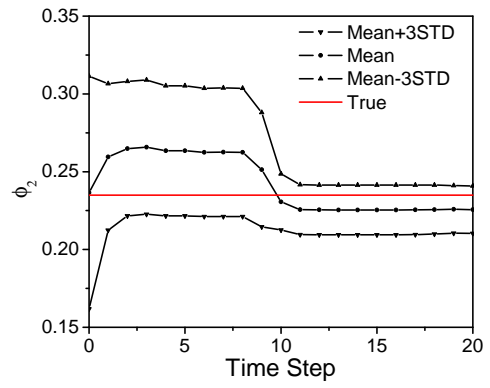


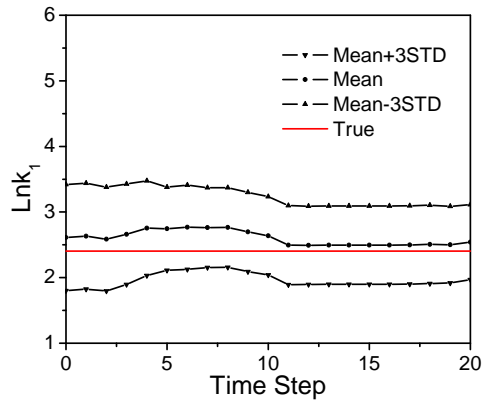
Figure 3.21: First arrival time data match from perforation shot at layer 2, two-layer homogeneous example



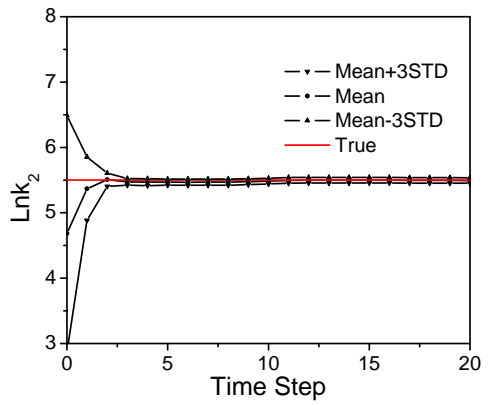
(a) ϕ_1



(b) ϕ_2



(c) $\ln k_1$



(d) $\ln k_2$

Figure 3.22: Porosity and log-permeability in layer 1 and layer 2 during pressure data assimilation after assimilating microseismic data, two-layer homogeneous example

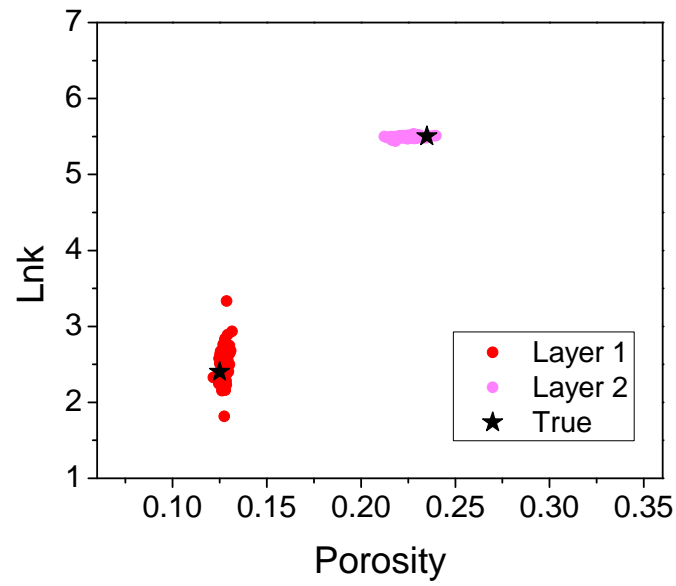


Figure 3.23: $\ln k$ vs. ϕ , after assimilating microseismic and pressure data, two-layer homogeneous example

The pressure and its derivative data match is shown in Fig. 3.24. Due to the fact that uncertainty in log-permeability of the high permeability layer did not decrease much from microseismic data assimilation, the predicted p_{wf} during early pressure data assimilation steps show a large spread, i.e., behave similar to the corresponding predicts obtained without assimilating microseismic data (Fig. 3.12(a)). After assimilating both microseismic and pressure transient data, we rerun both dynamic reservoir simulator and microseismic forward model (Eikonal equation) with the final estimated rock properties. The predicted pressure transient data and its derivatives during drawdown and buildup as shown in Fig. 3.24(c) and Fig. 3.24(d). Compared to Fig. 3.12 (assimilating pressure data only), the predicted pressure and the corresponding microseismic data result in lower uncertainty. Fig. 3.25 shows the predicted first arrival times predicted by the final estimates after assimilating both pressure and microseismic data.

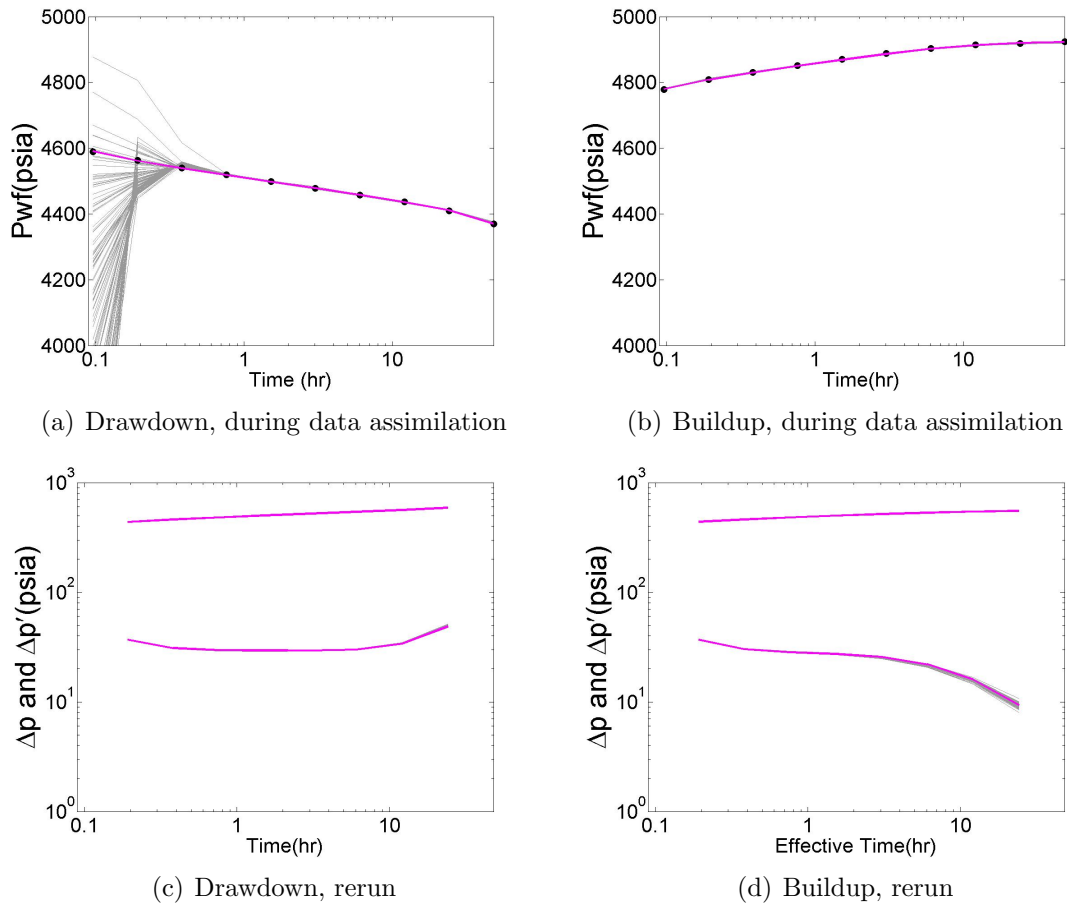


Figure 3.24: Pressure data match during data assimilation and rerun from time zero, microseismic + pressure data, two-layer homogeneous example

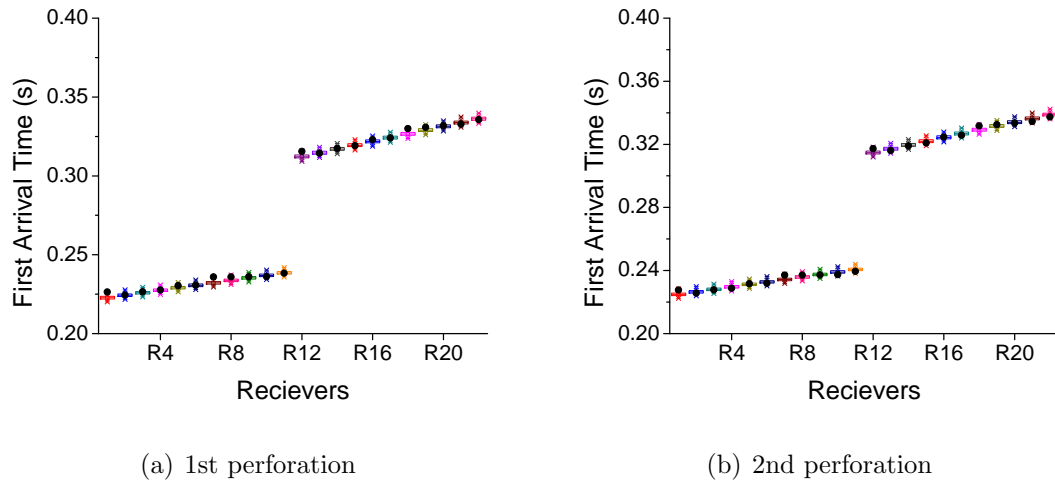
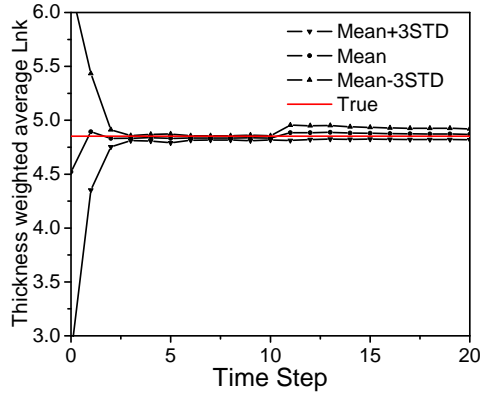
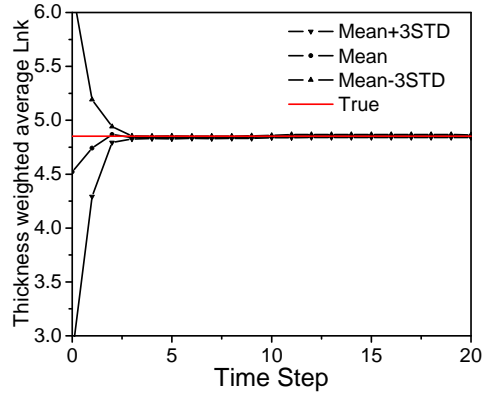


Figure 3.25: First arrival time data match after assimilating microseismic and pressure data, two-layer homogeneous example

Fig. 3.26 shows the evolution of the thickness-weighted average permeability during pressure transient data assimilation for two cases: a) assimilating pressure data only, b) assimilating microseismic data first before assimilating pressure transient data. Comparing Fig. 3.26(a) and Fig. 3.26(b) indicates that assimilating microseismic data did not yield significant uncertainty reduction in the thickness-weighted average permeability due to the fact that it is more sensitive to the tighter low permeability/porosity layer. In both cases, there is a significant decrease in the uncertainty for the thickness-weighted permeability average in the first few data assimilation steps. After the 5th data assimilation steps, the change in the uncertainty is negligible for the case which assimilates both microseismic and pressure data. However, there is a slight uncertainty increase after assimilating pressure buildup data without assimilating microseismic data.



(a) pressure



(b) microseismic+pressure

Figure 3.26: Thickness-weighted average permeability

As EnKF is a stochastic process, we run the data assimilation with 10 different initial ensembles which are generated using the same mean and covariance for testing. Fig. 3.27 and Fig. 3.28 show the final estimates of log-permeability in layer 1 and layer 2 for 10 different ensembles by assimilating pressure data only and by assimilating both microseismic and pressure data, respectively. The black horizontal line represents the true value. As shown in Fig. 3.27(a), by assimilating pressure data only, the estimated log-permeability in the low permeability layer is quite different for different ensembles. Most of ensembles have an estimated mean higher than the truth and several of them have biased estimates with the truth falling below the 5th percentile. The uncertainty of most final ensembles is quite large and different from each other. By assimilating both microseismic and pressure data as shown in Fig. 3.27(b), the ensemble mean and variance are relatively close to each other. The majority of the posterior means are close to the truth and the uncertainty is smaller than when assimilating only pressure data in most of the cases. The 1st ensemble happened to be good log-permeability estimate by assimilating pressure data only. If we judge the results by only looking at the first ensemble, wrong conclusions may be made. As the pressure data are more sensitive to the log-permeability of the high permeability layer, the log-permeability in the higher permeability layer is well resolved in both cases as shown in Fig. 3.28, though assimilating both pressure and microseismic data yields more accurate log-permeability estimates than the case assimilating pressure data only. Similar results are obtained for the predicted layer rate of layer 2 at the end time day 2, when we rerun the final estimated ensembles from time 0 comparing assimilating only pressure data in Fig. 3.29(b) and assimilating both pressure and microseismic data in Fig. 3.29(c). Prediction in both cases are improved compared to the prediction with the initial ensembles (Fig. 3.29(a)). Prediction after assimilating both microseismic and pressure data is overall better than assimilating pressure data only. In general, including information of microseismic data in data assimilation improves permeability field estimate and production data prediction in the 2-layer homogenous case.

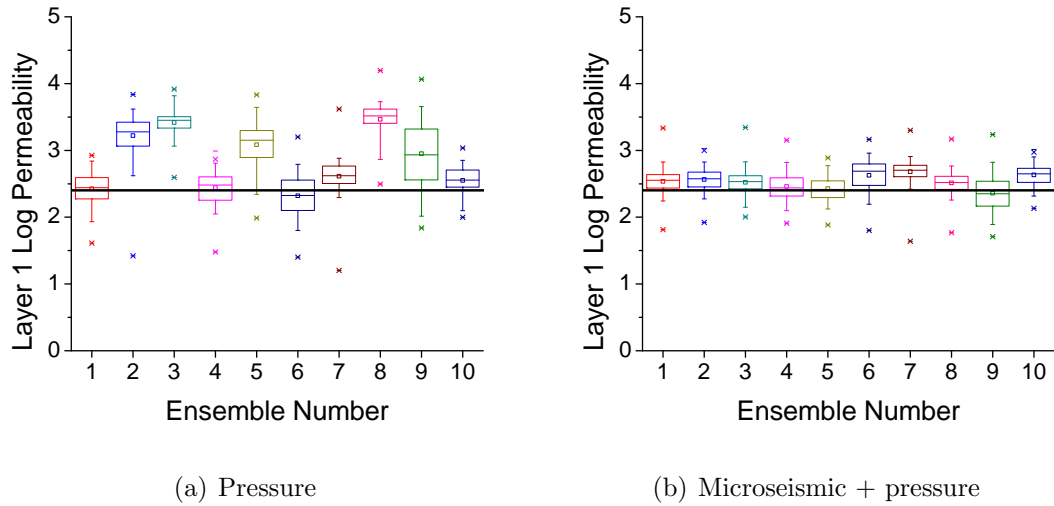
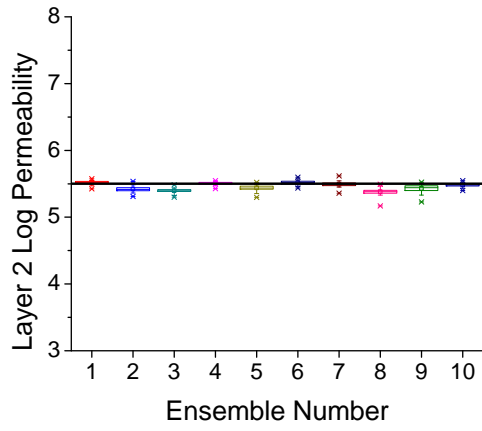


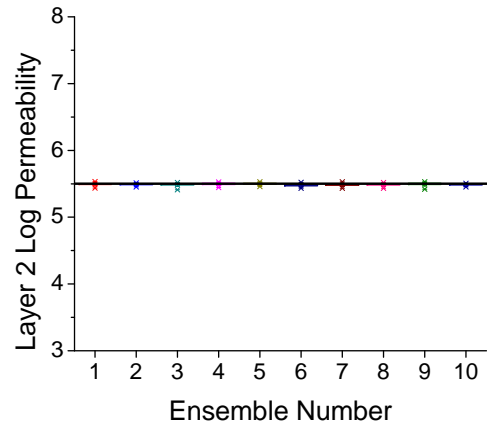
Figure 3.27: Layer 1 log-permeability of 10 different ensembles, two-layer homogeneous example

3.2.5 Assimilating pressure and layer rate data

As shown in Chapter 2, assimilating both layer rates and pressure data gives accurate estimates of the individual layer skin factors and rock property fields (porosity and log-permeability). Results after assimilating pressure and layer rate data are shown in this section for comparison with assimilating microseismic and pressure data. As shown in Fig. 3.30 and Fig. 3.31, the log-permeability of both layers are well resolved after assimilating the layer rate and pressure data. The porosity in layer 1 did not change much after initial uncertainty reduction in the first several data assimilation steps. The uncertainty reduction of porosity in layer 2 is similar to layer 1 during assimilating drawdown pressure data, then changes significantly when assimilating pressure buildup data. Note that the pressure drawdown test reaches pseudo-steady state at the end of the drawdown test as indicated by a unit slope in the derivative plot (Fig. 3.32). There is a slight uncertainty reduction when assimilating the last few drawdown pressure data points corresponding to pseudo-steady state, as the pressure at pseudo-steady state is most sensitive to porosity. The predicted pressure during data assimilation (Fig. 3.32(a) and Fig. 3.32(b)) shows a good data match. Rerunning with final estimated rock properties resulted in a very good data match as shown in the log-log diagnostic plot (Fig. 3.32(c) and Fig. 3.32(d)). Although we do not assimilate the pressure derivative data, the match is almost perfect.



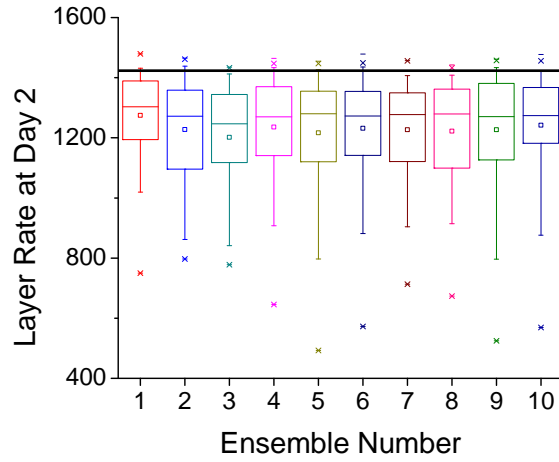
(a) Pressure



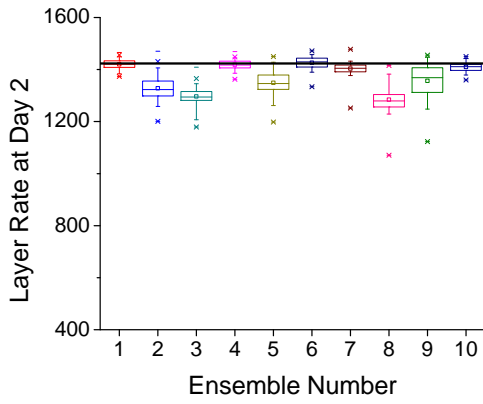
(b) Microseismic + pressure

Figure 3.28: Layer 2 log-permeability of 10 different ensembles, two-layer homogeneous example

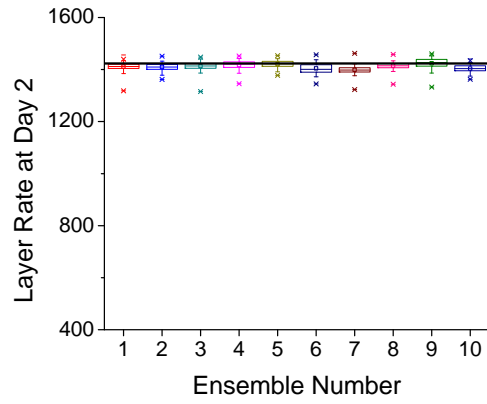
Fig. 3.33 shows the predicted layer rate data during data assimilation and rerun from time zero with the final estimated properties and a good match is obtained.



(a) Prior

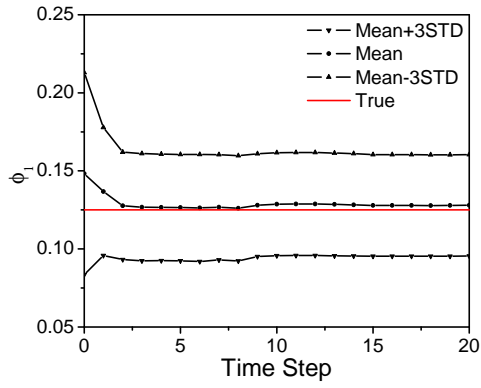


(b) Pressure

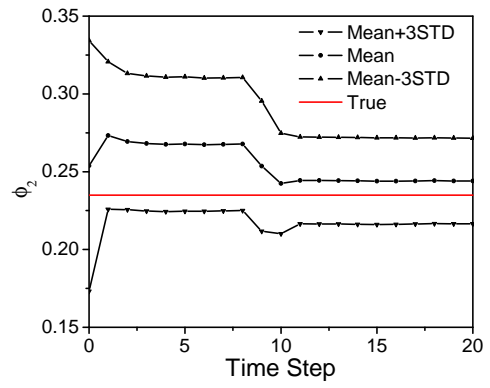


(c) Microseismic + pressure

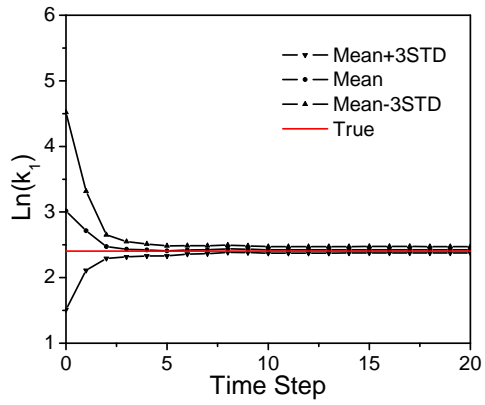
Figure 3.29: Prediction of Layer rate in layer 1 at time day 2 rerunning from time 0 of all ensembles, two-layer homogeneous example



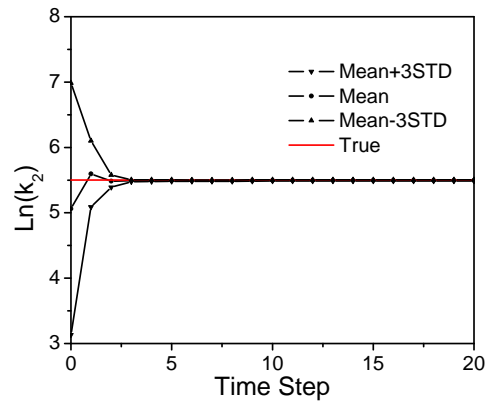
(a) ϕ_1



(b) ϕ_2



(c) $\ln k_1$



(d) $\ln k_2$

Figure 3.30: Porosity and log-permeability when assimilating pressure and layer rate data, two-layer homogeneous example

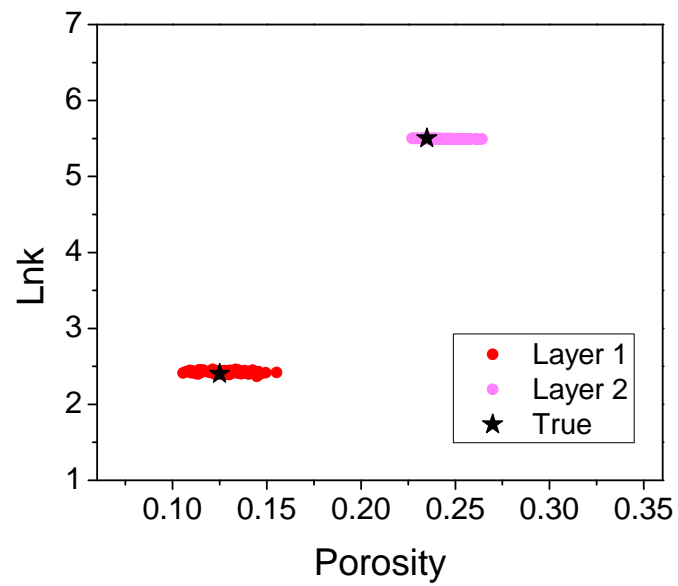


Figure 3.31: $\ln k$ vs. ϕ , after assimilating pressure and layer rate data, two-layer homogeneous example

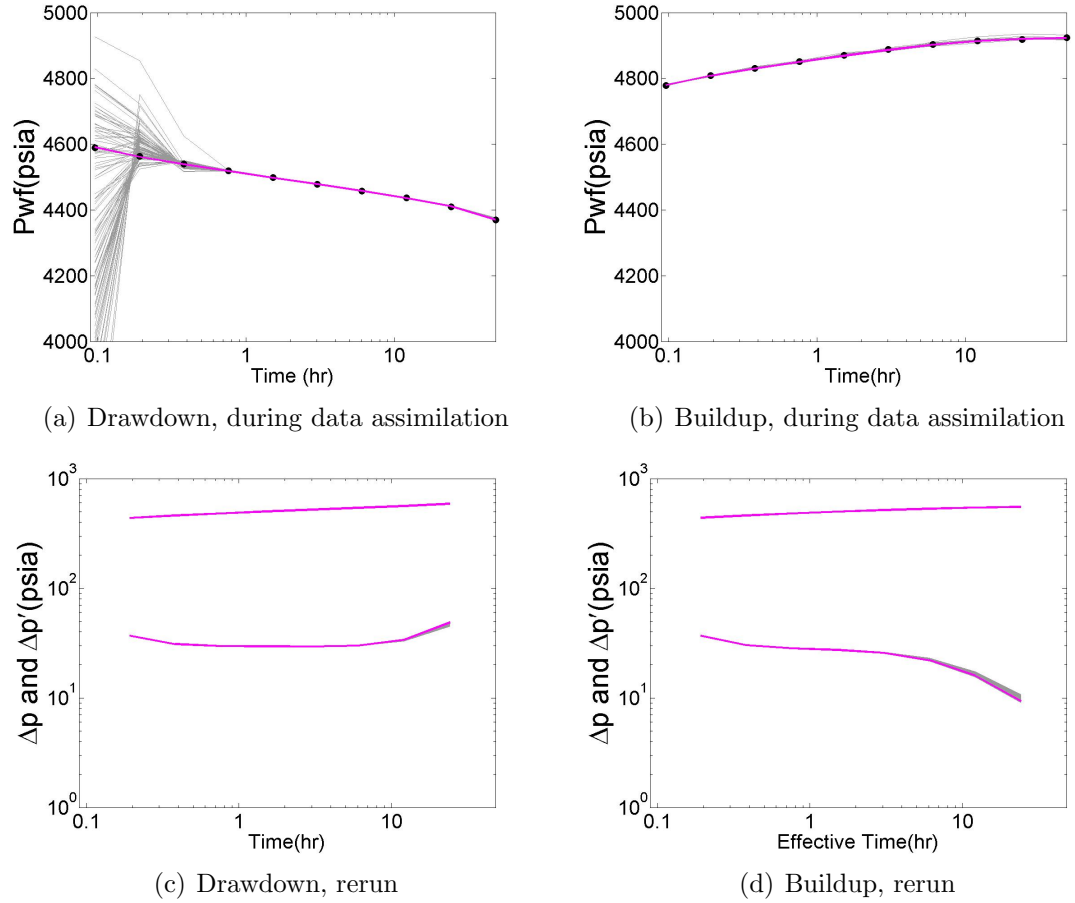


Figure 3.32: pressure prediction after assimilating microseismic and pressure data, two-layer homogeneous example

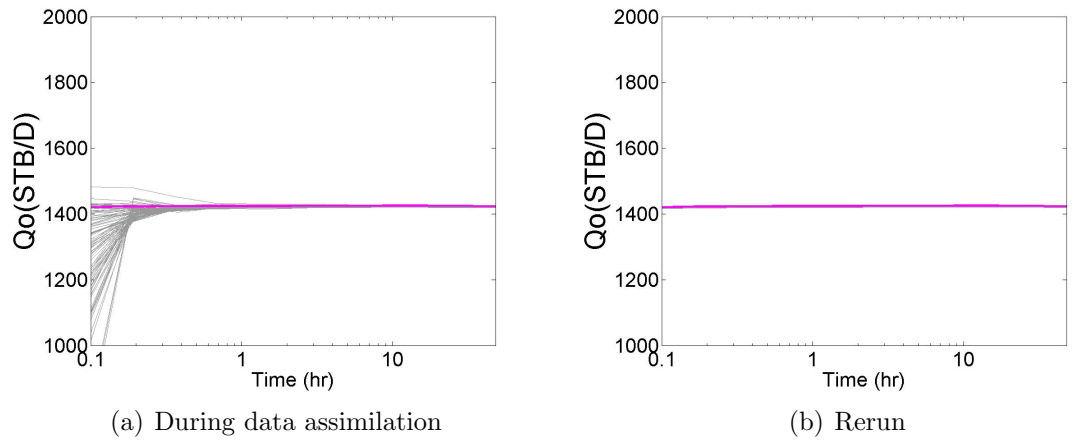


Figure 3.33: Layer rate prediction after assimilating microseismic and pressure data, two-layer homogeneous example

3.3 Two-layer heterogeneous case

3.3.1 Case description

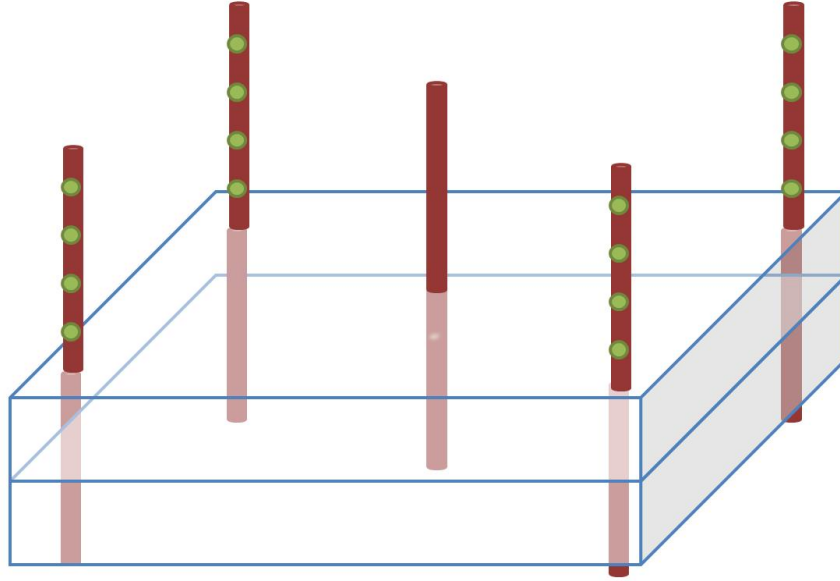


Figure 3.34: Reservoir and well schematic, two-layer heterogeneous example

In this section, we consider a synthetic two-layer heterogeneous example. As shown in Fig. 3.34, we have $20 \times 20 \times 2$ grid system with grid size of $200 \text{ ft} \times 200 \text{ ft} \times 50 \text{ ft}$. The active well is in the middle of the reservoir at grid $(10, 10)$ and perforated in both layers. Cap rock is on top of the reservoir layers and its velocity is assumed known. The reservoir fluid properties and other model parameters are the same as in the homogeneous case. Four monitor wells that are located at the corner gridblocks $(2, 2)$, $(2, 19)$, $(19, 2)$ and $(19, 19)$. Each monitor well has 11 microseismic receivers above the reservoir and 20 ft apart from each other with the first receiver right on the top of the reservoir. The model for calculating the first arrival time is $400 \times 400 \times 40$ 3-D grid with $5 \text{ ft} \times 5 \text{ ft} \times 5 \text{ ft}$ as the grid size.

Similar to the two-layer homogeneous case, perforations are shot in the middle of both layers and the first arrival time data of P-wave and S-wave are recorded at receivers in the 4 monitor wells. The well is produced at 1500 STB/D liquid rate for 2 days and shut in for another 2 days. The pressure data are recorded during the 2-day drawdown

and 2-day buildup at the active well and the four monitor wells. In the following cases, 4×11 first arrival time data of P-wave and S-wave, 10 pressure drawdown and 10 pressure buildup data (logarithmically spaced) at the active and monitor wells, and layer rate data are assimilated to update porosity and log-permeability fields.

The true case is a realization generated using GCOSIM3D [23] with the geostatistical parameters listed in Table 3.5 and Fig. 3.35 shows the true porosity and permeability distribution of two layers. Layer 1 has lower porosity and permeability than layer 2. The active well and 2 monitor wells are located in a high permeability channel in layer 1. The high permeability channel in layer 1 has a trend from the lower left corner to the upper right corner.

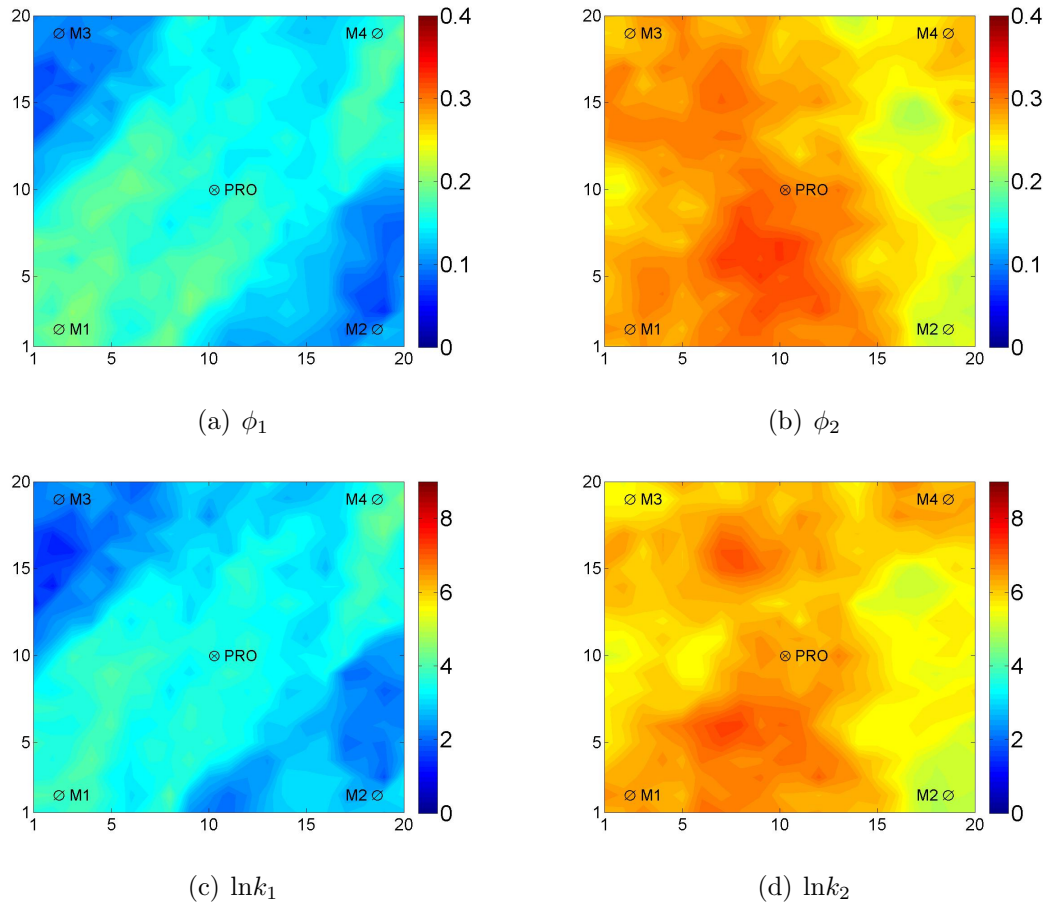


Figure 3.35: True porosity and log-permeability distributions, two-layer heterogeneous example

The cross section of velocity structure between the active well and the monitor well at the lower left corner is shown in Fig. 3.36. The black line approximates a ray

path from the perforation to the receiver just above the top reservoir layer. As layer 2 (top layer) has higher travel velocity (lower porosity) than layer 1, the ray path stays mostly in layer 2 to satisfy the minimum travel time requirement.

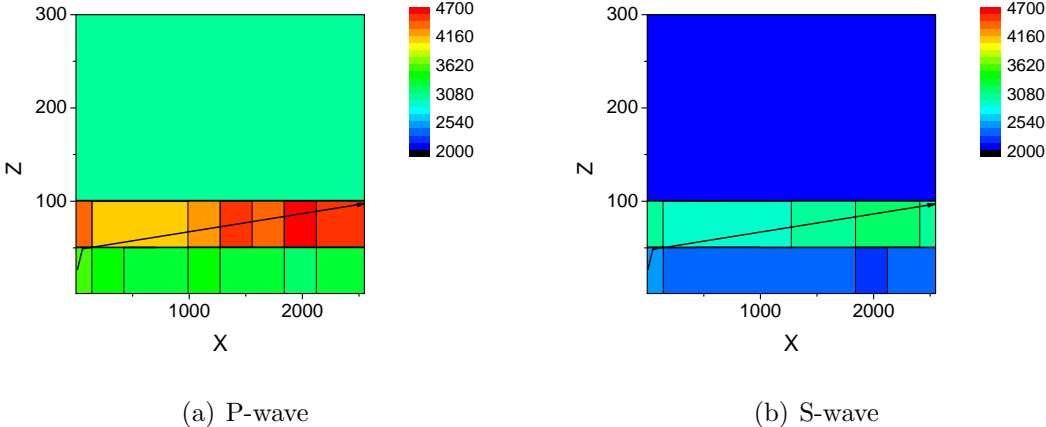


Figure 3.36: A cross-section of the velocity structure, two-layer heterogeneous example

Porosity and permeability of prior ensemble members are generated by GSCOSIM3D using parameters in Table 3.5. Prior mean and standard deviation of 100 ensemble members are shown in Fig. 3.37 and Fig. 3.38.

Table 3.5: Prior geostatistical parameters, two-layer heterogeneous example

	Layer 1	Layer 2
$\bar{\phi}$	0.10	0.25
$\overline{\ln k}$	2	5
σ_{ϕ}	0.025	0.025
$\sigma_{\ln k}$	0.6	0.6
$\rho_{\phi, \ln k}$	0.8	
Angle α	30°	0°
Long range, r_1 (ft)	3800	1112
short range, r_2 (ft)	2800	2800

3.3.2 Assimilating pressure data only

The porosity and log-permeability fields are first updated by assimilating pressure transient data of the active and monitor wells during drawdown and buildup test. The updated ensemble mean of porosity and log-permeability after assimilating pressure data only are shown in Fig. 3.39. As shown in Fig. 3.39(a) and Fig. 3.39(c), the mean porosity and log-permeability in the low permeability layer (layer 1) are increased compared to the initial (Fig. 3.37). Compared to the true rock property field (Fig. 3.35), the estimated mean porosity and log-permeability are lower than the true values and the long high permeability/porosity channel is not captured. The mean of estimated porosity and log-permeability for high-permeability layer (layer 2) is increased by matching the pressure data compared to the prior mean (Fig. 3.37). Fig. 3.40 shows the standard deviation of the porosity and log-permeability fields calculated using 100 final estimated ensemble members. As can be seen from the figure, significant uncertainty reduction in the high permeability layer (layer 2) is observed around the active well when it is compared to the prior STD distribution in Fig. 3.38. The uncertainty reduction in layer 1 and other area of layer 2 close to monitor wells are also observed but not significant. This observation

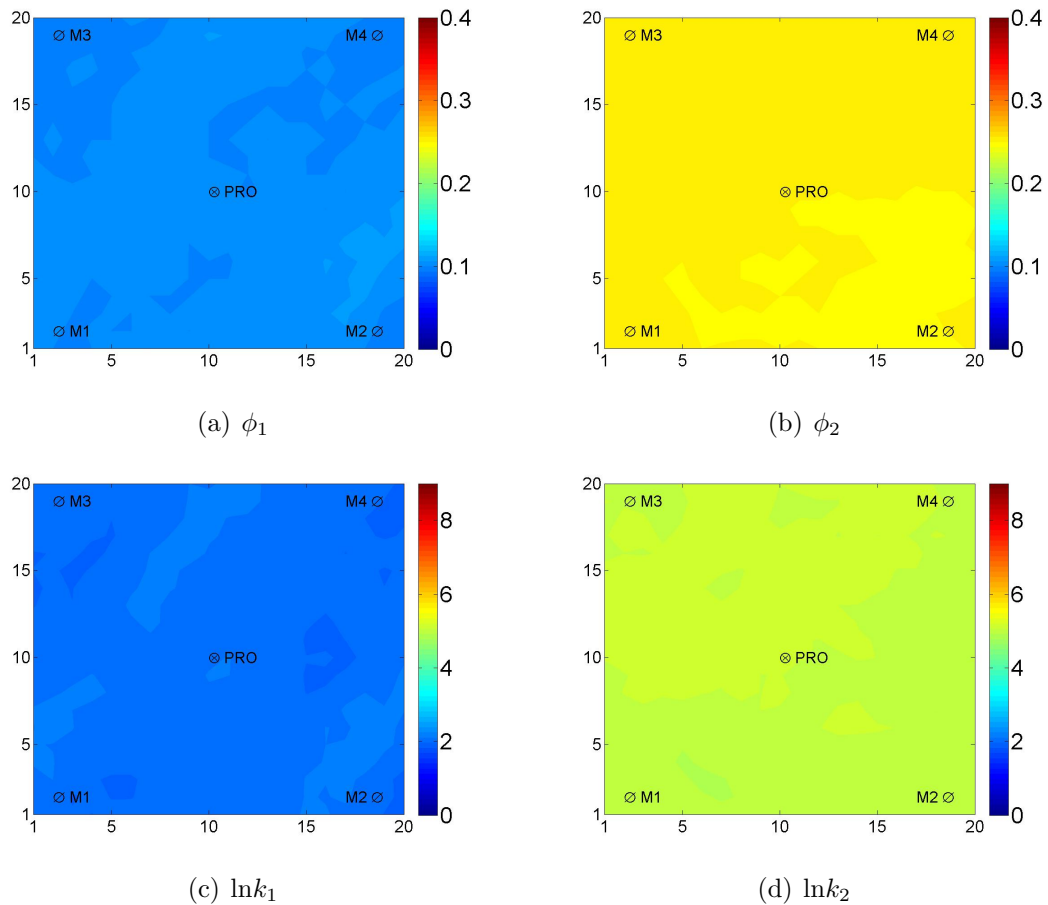


Figure 3.37: Prior mean of porosity and log-permeability fields calculated from the 100 initial ensemble members, two-layer heterogeneous example

can also be seen in Fig. 3.41, which shows the ratio of the standard deviation between the final and initial ensemble. In the figure, the red color (close to a value of 1) indicates low uncertainty reduction, while the blue color (a value close to 0) indicates large uncertainty reduction. Fig. 3.42 to Fig. 3.45 are examples of porosity and log-permeability fields of individual ensemble member before and after assimilating pressure transient data.

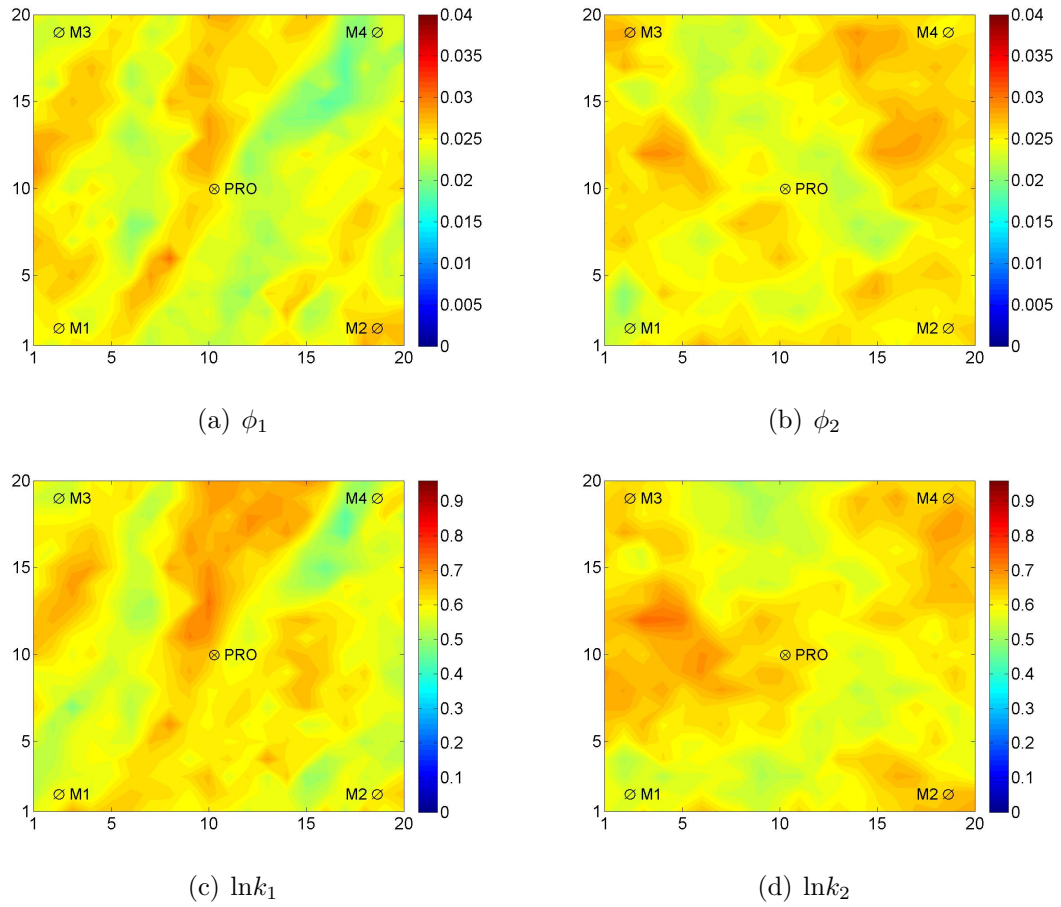


Figure 3.38: Prior STD of porosity and log-permeability calculated from the 100 initial ensemble members, two-layer heterogeneous example

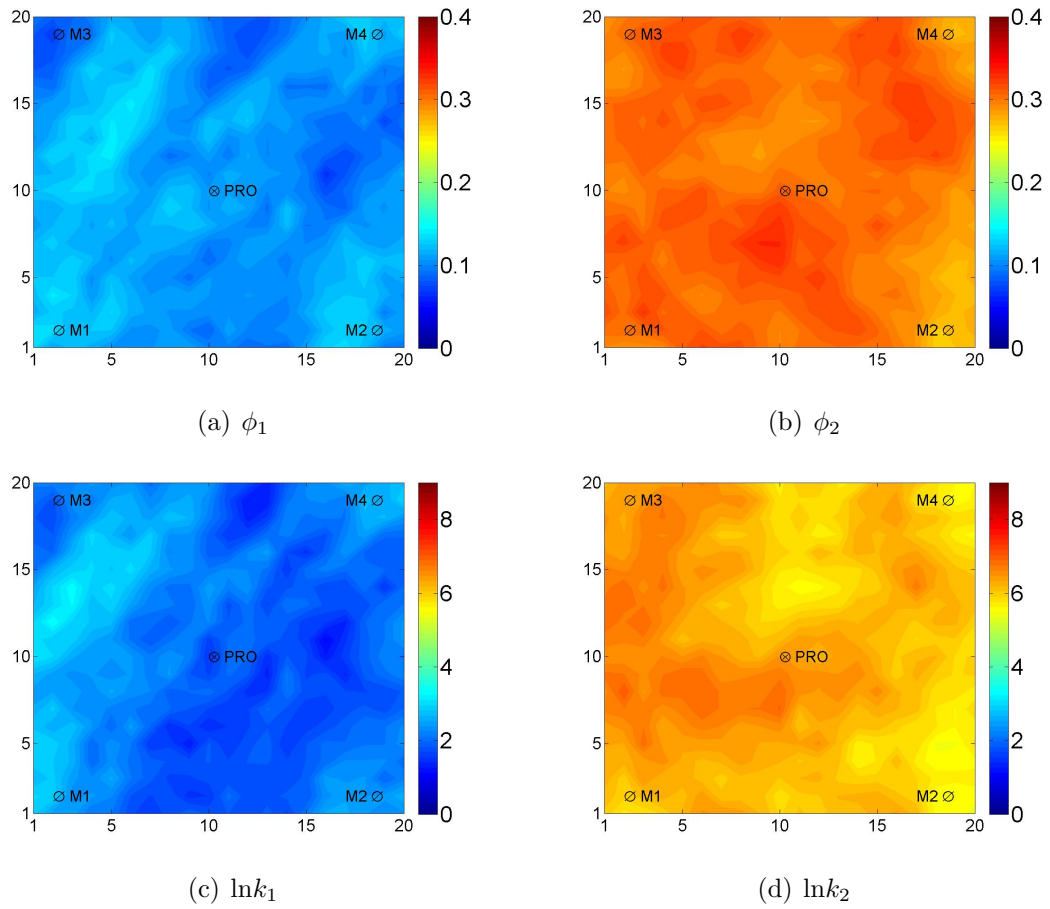


Figure 3.39: Porosity and log-permeability posterior mean after assimilating pressure data only, two-layer heterogeneous example

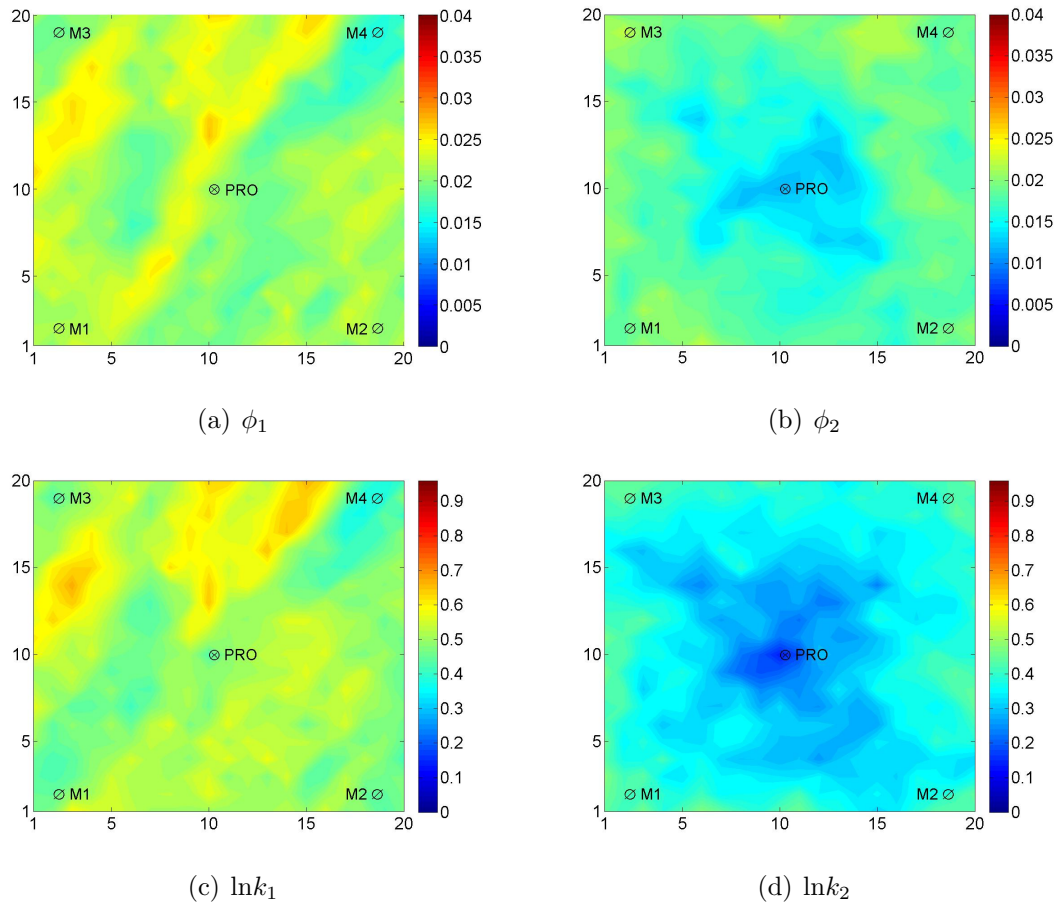


Figure 3.40: Porosity and log-permeability posterior STD after assimilating pressure data only, two-layer heterogeneous example

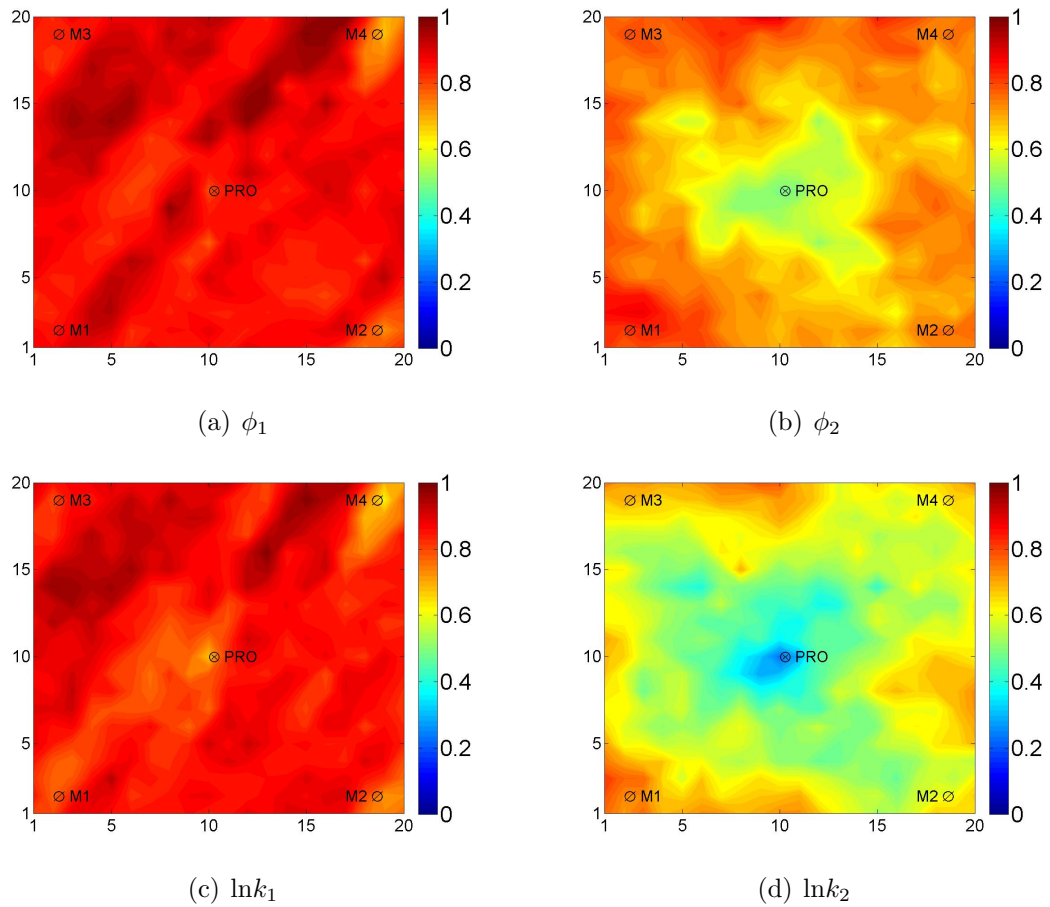


Figure 3.41: Posterior to prior STD ratio of porosity and log-permeability assimilating pressure data only, two-layer heterogeneous example

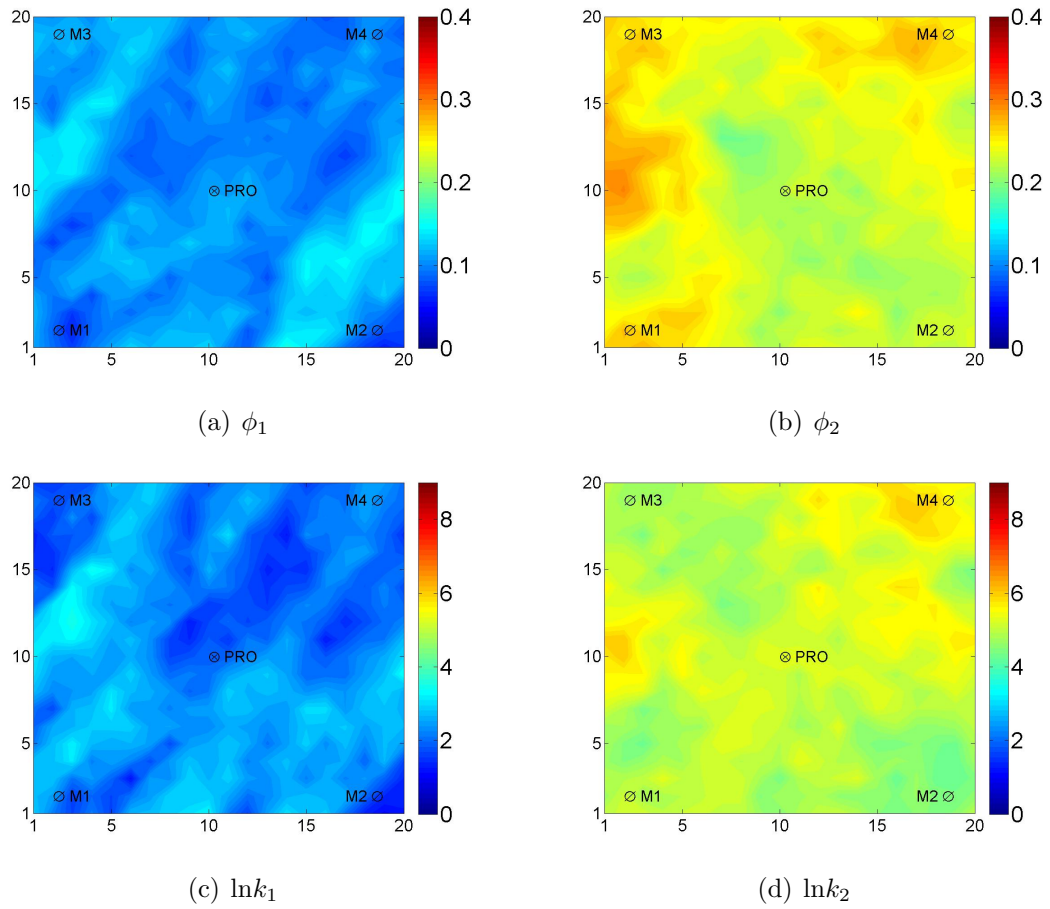


Figure 3.42: Porosity and log-permeability field of the 43rd initial ensemble member, two-layer heterogeneous example

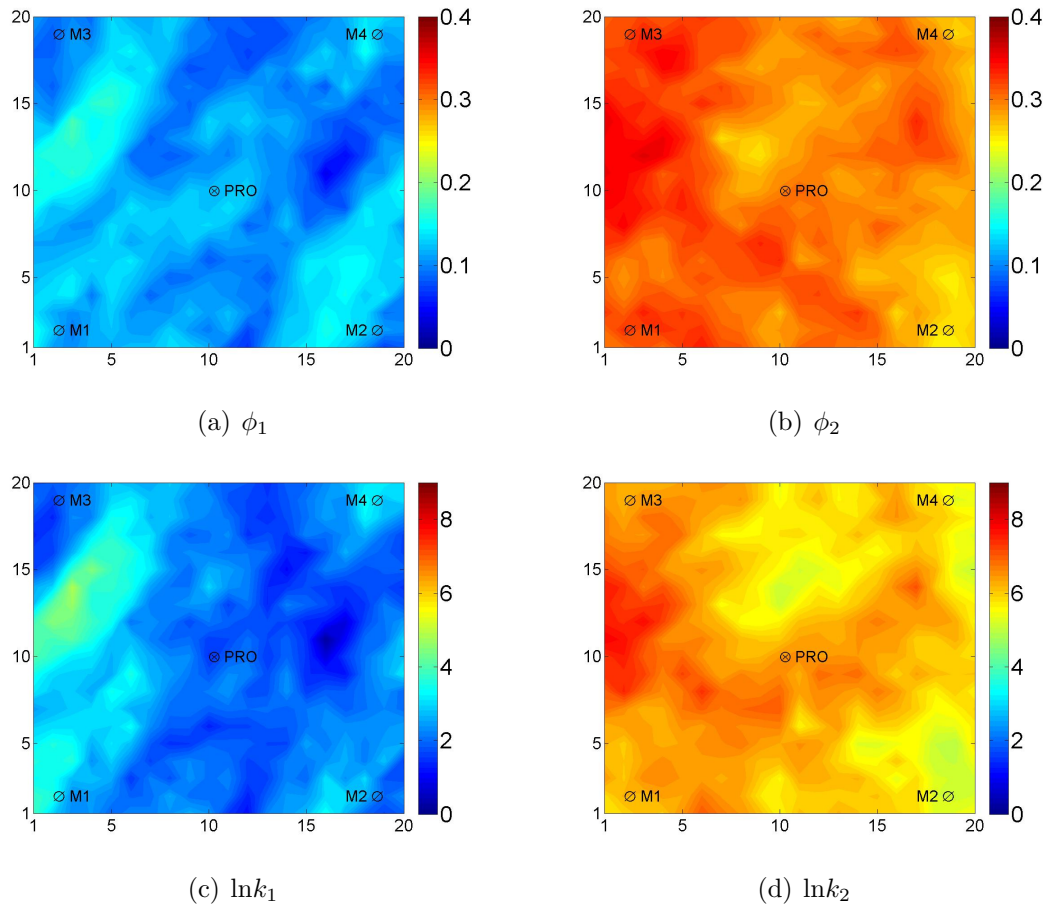


Figure 3.43: Porosity and log-permeability field of the 43rd ensemble member after assimilating pressure data only, two-layer heterogeneous example

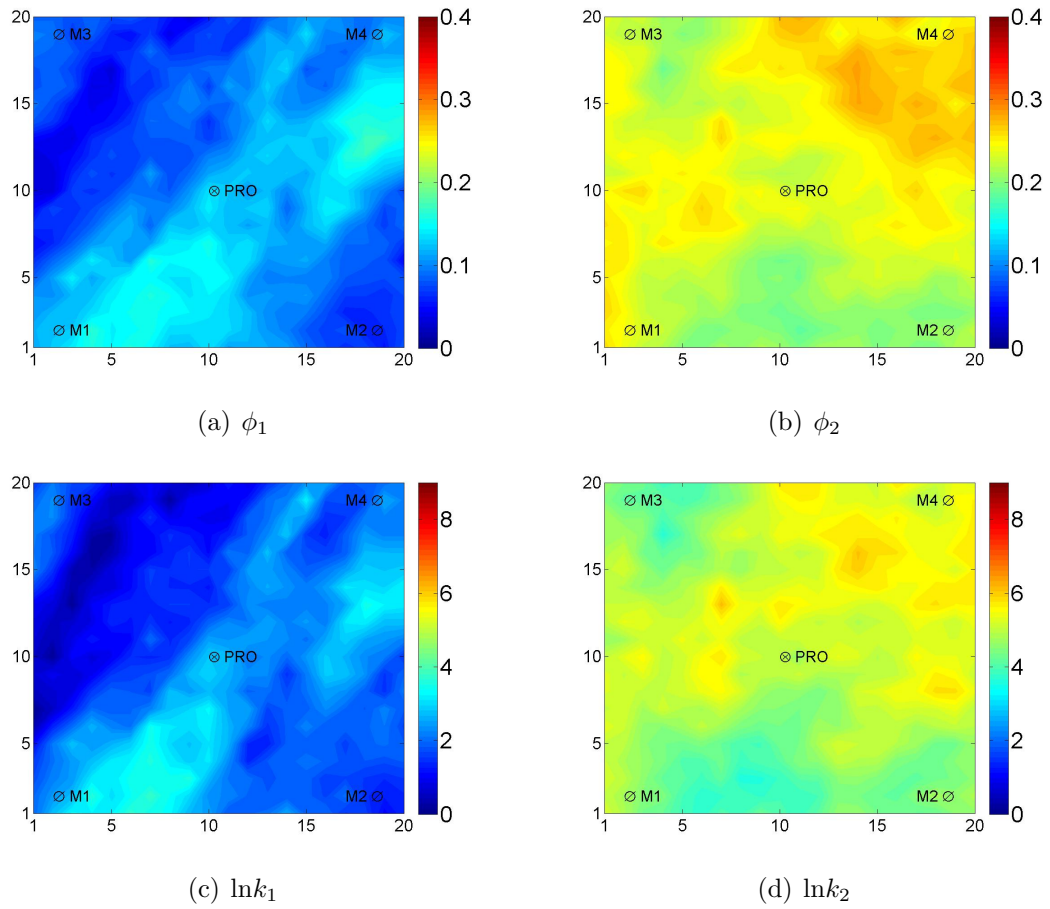


Figure 3.44: Porosity and log-permeability field of the 78th initial ensemble member, two-layer heterogeneous example

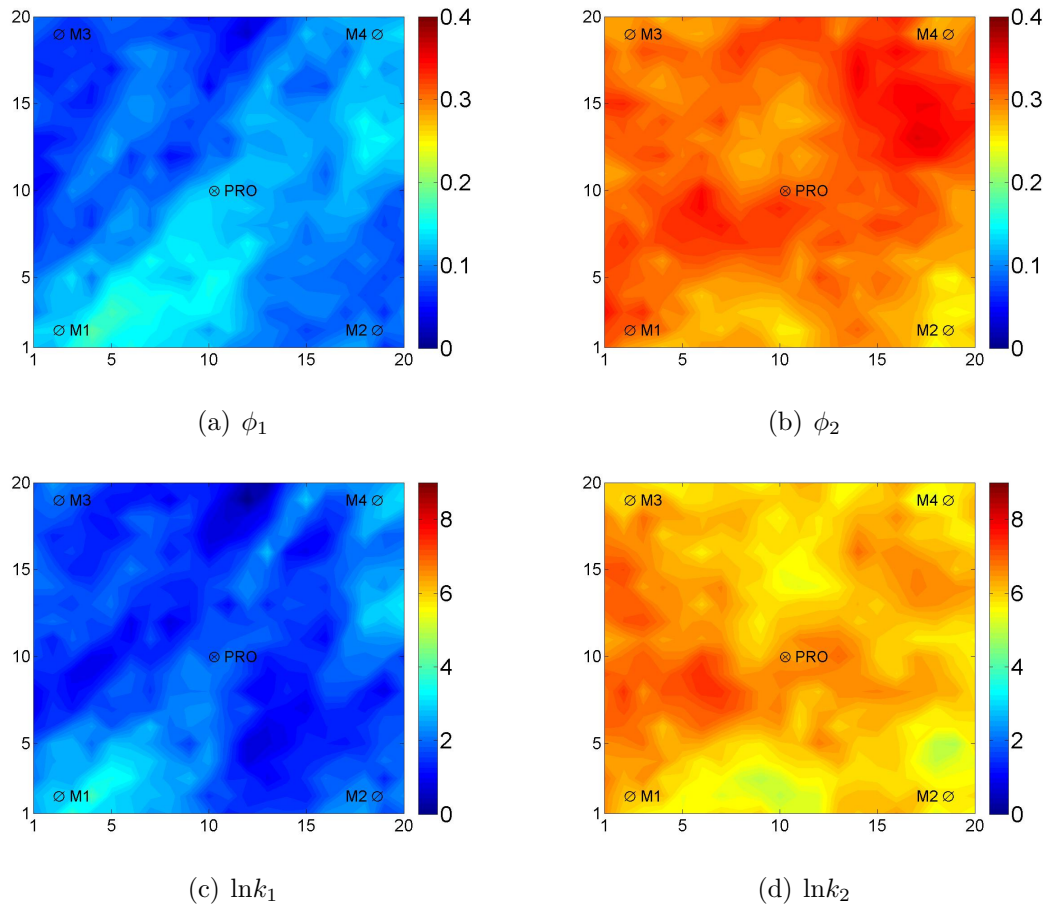


Figure 3.45: Porosity and log-permeability field of the 78th ensemble member after assimilating pressure data only, two-layer heterogeneous example

The data match of the active well is shown in Fig. 3.46. Fig. 3.46(a) and Fig. 3.46(b) show the pressure data match during assimilating the pressure drawdown and buildup data, respectively. Fig. 3.46(c) and Fig. 3.46(d) are the log-log diagnostic plots of pressure and pressure derivative obtained after rerunning the updated ensemble from time 0 for drawdown and buildup, respectively. All the ensemble members after assimilating pressure data predict pressure close to the truth with very small spread (uncertainty). The data match of monitor well 1 is shown in Fig. 3.47. Other monitor wells have similar data matches. Fig. 3.47(a) and Fig. 3.47(b) show the pressure match during data assimilation for drawdown and buildup, and Fig. 3.47(c) and Fig. 3.47(d) shows the data match at this monitor well when rerunning the estimated ensemble from time 0. Note that no significant change is observed in the predicted pressure at the monitor well during data assimilation and rerun from time zero. In Fig. 3.46(b) and Fig. 3.47(b), the predicted pressure dropped to zero due to simulator license failure. During rerun, these two ensemble members were removed.

3.3.3 *Assimilating microseismic data only*

In this section, the porosity and log-permeability fields are updated by assimilating the first arrival time data recorded at the receivers placed in the four monitor wells during perforation of the bottom and top reservoir layers. Fig. 3.48 shows the updated ensemble mean of porosity and permeability distribution after assimilating microseismic data from the perforation shot in the bottom layer using standard EnKF. Since the first arrival time is sensitive the porosity along the ray path between source and receivers, the high porosity and permeability channel in layer 1 between the active well and monitor well 1 and 4 is captured by assimilating microseismic data as shown in Fig. 3.48. However, the high permeability/porosity channel is narrower than the truth (Fig. 3.35), due to the fact that microseismic data only resolves the average porosity along its path. The angle of the channel is also different from the truth. Porosity and log-permeability in layer 2 was increased after assimilating the microseismic data as shown in Fig. 3.48(b) and Fig. 3.48(d). Fig. 3.49 shows the standard deviation of the final estimated ensemble

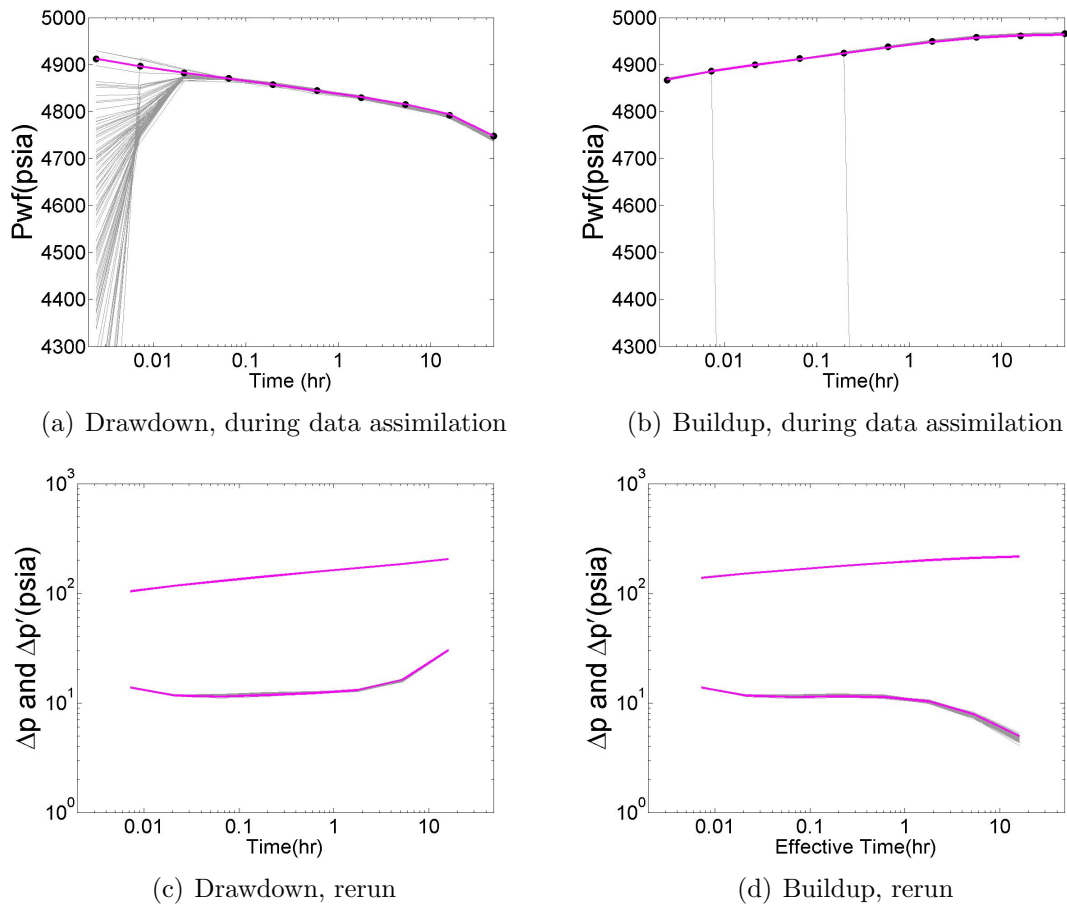
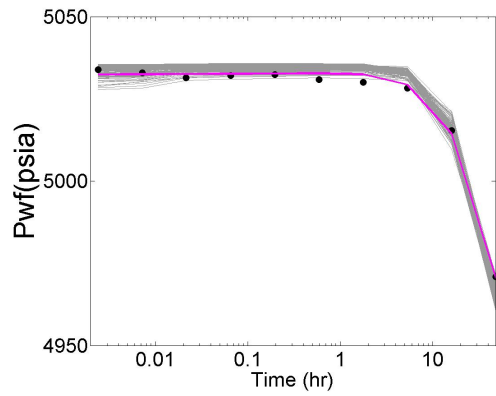
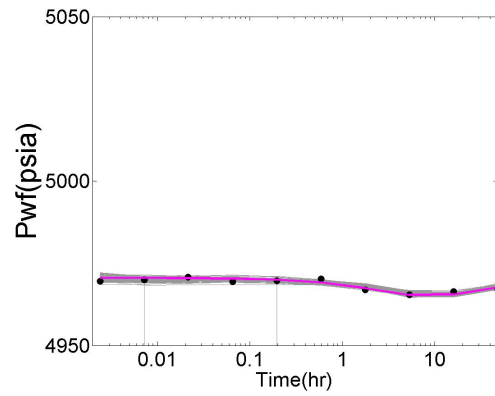


Figure 3.46: Pressure data match of the active well after assimilating pressure data only, two-layer heterogeneous example

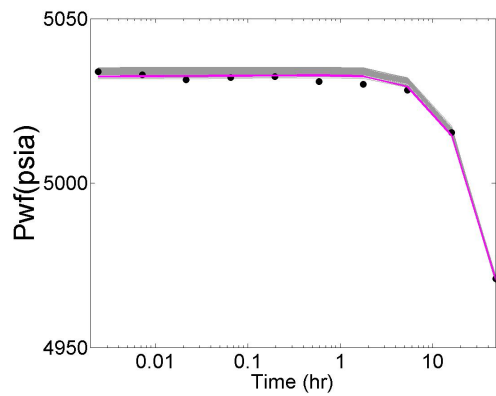
after assimilating the microseismic data. Fig. 3.50 shows the ratio of the standard deviation between the final and initial ensemble. Large uncertainty reduction (as indicated by lighter color) is observed in layer 1 between monitor wells 1 and 4. Virtually no uncertainty reduction is observed for layer 2.



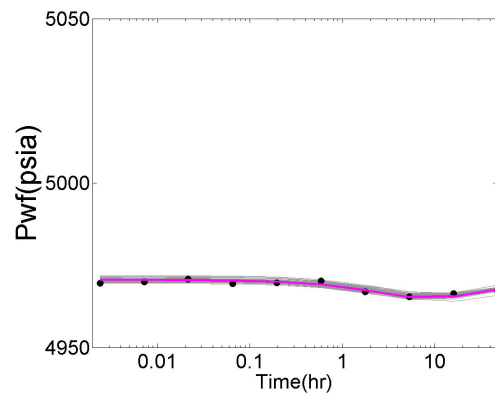
(a) Drawdown, during data assimilation



(b) Buildup, during data assimilation



(c) Drawdown, rerun



(d) Buildup, rerun

Figure 3.47: Pressure data match of monitor well 1 after assimilating pressure data only, two-layer heterogeneous example

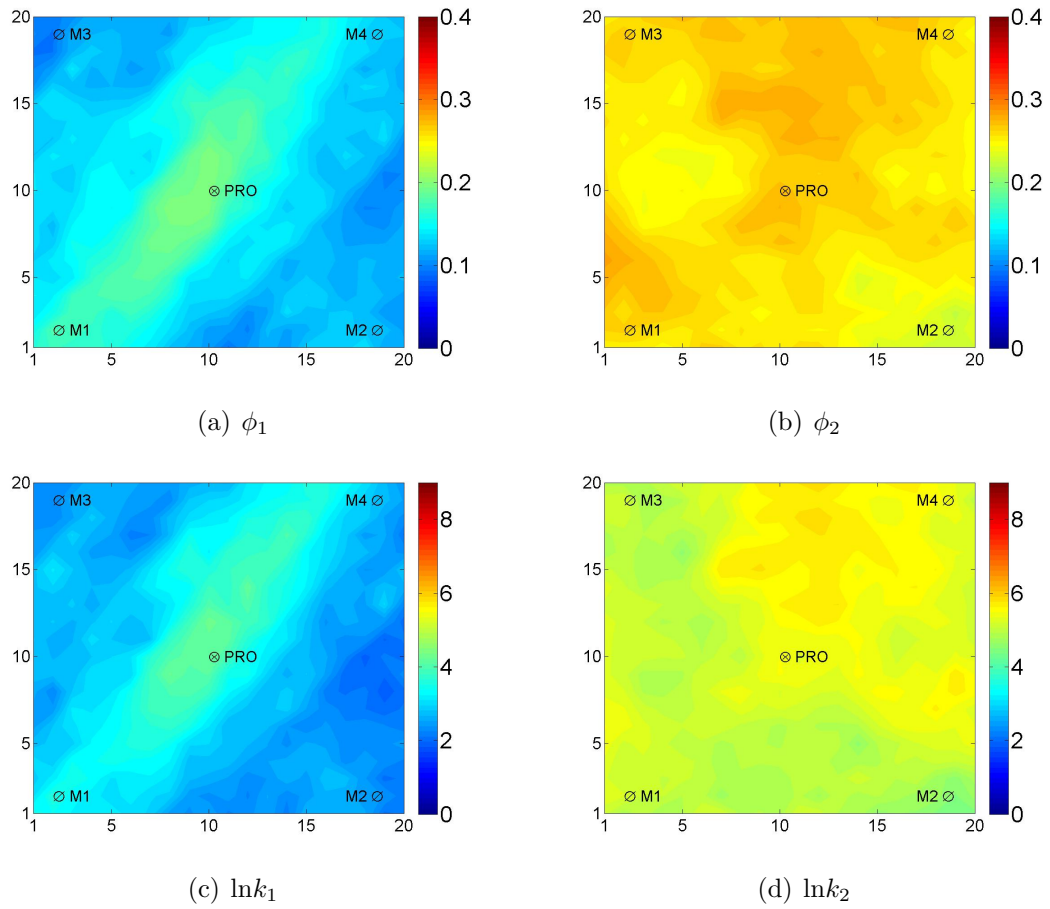


Figure 3.48: Porosity and log-permeability posterior mean after assimilating microseismic data from perforation shot of layer 1, two-layer heterogeneous example

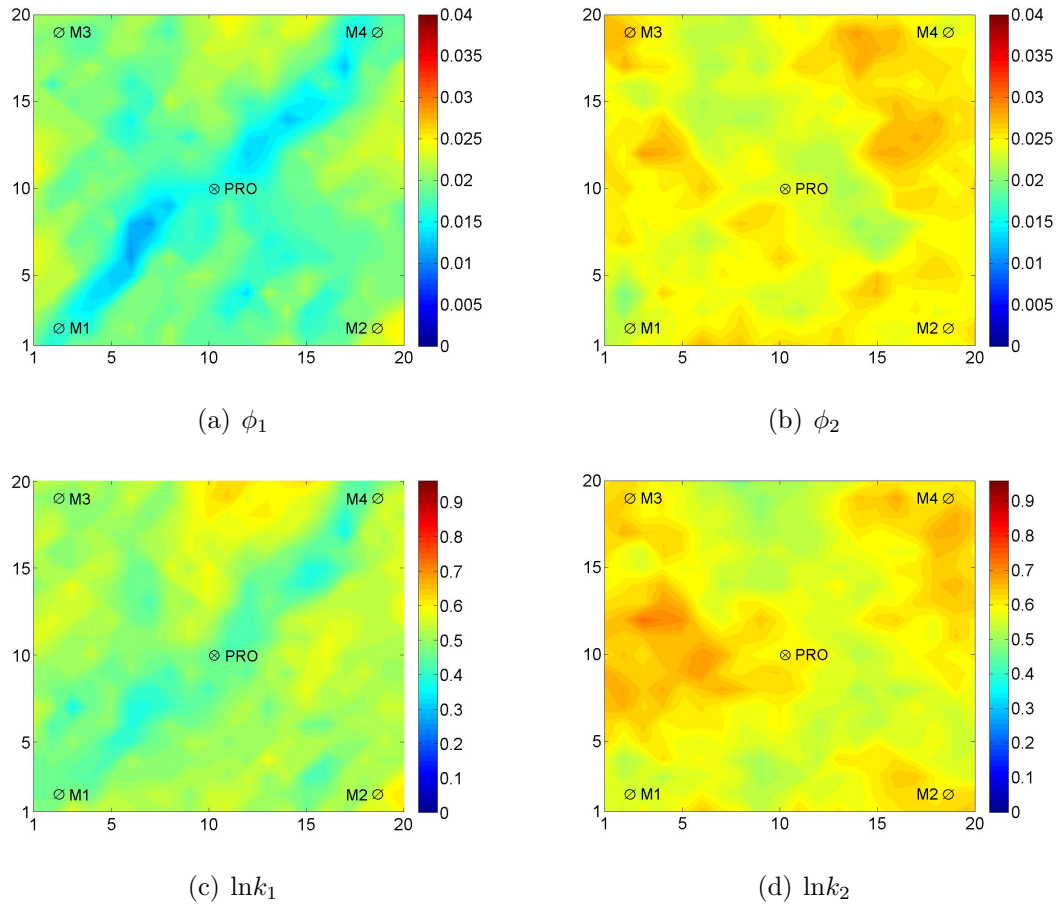


Figure 3.49: Porosity and log-permeability posterior STD after assimilating microseismic data from perforation shot of layer 1, two-layer heterogeneous example

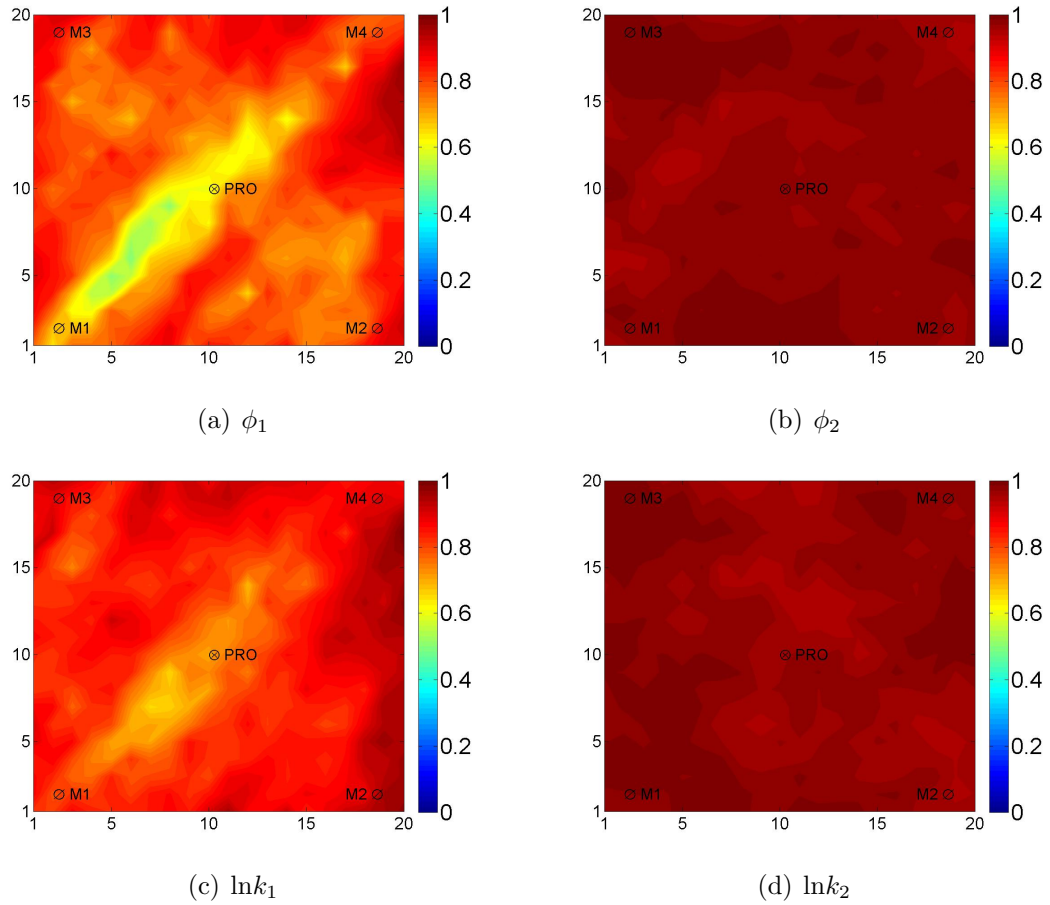


Figure 3.50: Posterior /prior STD ratio of porosity and log-permeability after assimilating microseismic data from perforation shot of layer 1, two-layer heterogeneous example

Fig. 3.51 shows the prediction of first arrival times from the perforation shot of layer 1 at receivers placed in monitor well 1. The black dots are the prediction with the true rock property fields while the box plots represent the prediction from the initial and final ensemble. As indicated in Fig. 3.51(a), the truth prediction falls out the uncertainty range of the initial ensemble. This indicates that all initial ensemble members have lower porosity (higher velocity) between the active well and monitor well 1 than the truth. After data assimilation, the predicted first arrival times match the truth as shown in Fig. 3.51(b).

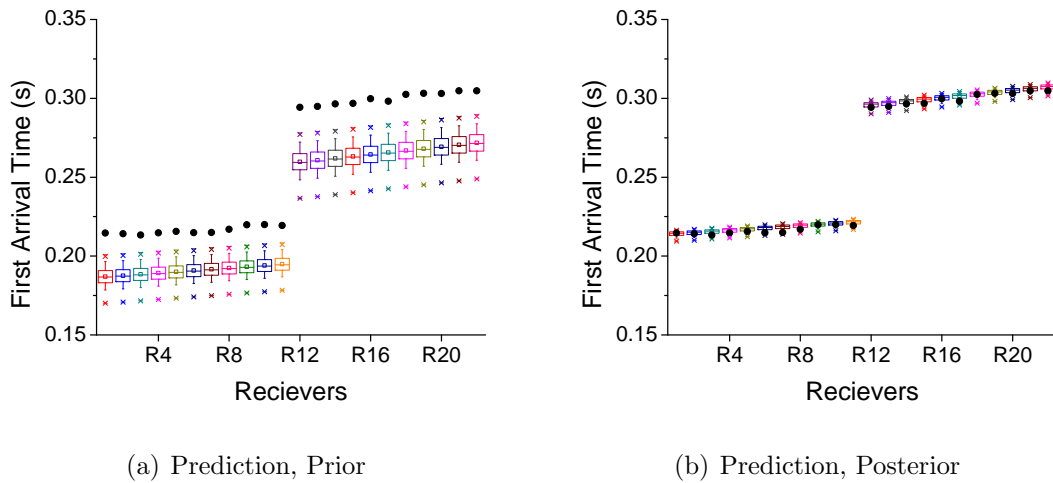


Figure 3.51: The first arrival time data match at receivers in monitor well 1 from perforation shot of layer 1, two-layer heterogeneous example

Since the porosity in the low porosity layer has already been adjusted to match first arrival time data after assimilating the microseismic data from perforation shot of layer 1 (bottom layer), the mean and standard deviation of the porosity and permeability has not changed much when assimilating microseismic data from the top layer perforation shot as shown in Fig. 3.52 and Fig. 3.53 compared to Fig. 3.48 and Fig. 3.49. Assimilating microseismic data from the perforation shot of layer 2 did not result in much further uncertainty reduction comparing Fig. 3.54 and Fig. 3.55 to Fig. 3.49 and Fig. 3.50. In summary, assimilating the first arrival time data improves reservoir characterization in the region in the wave travel path.

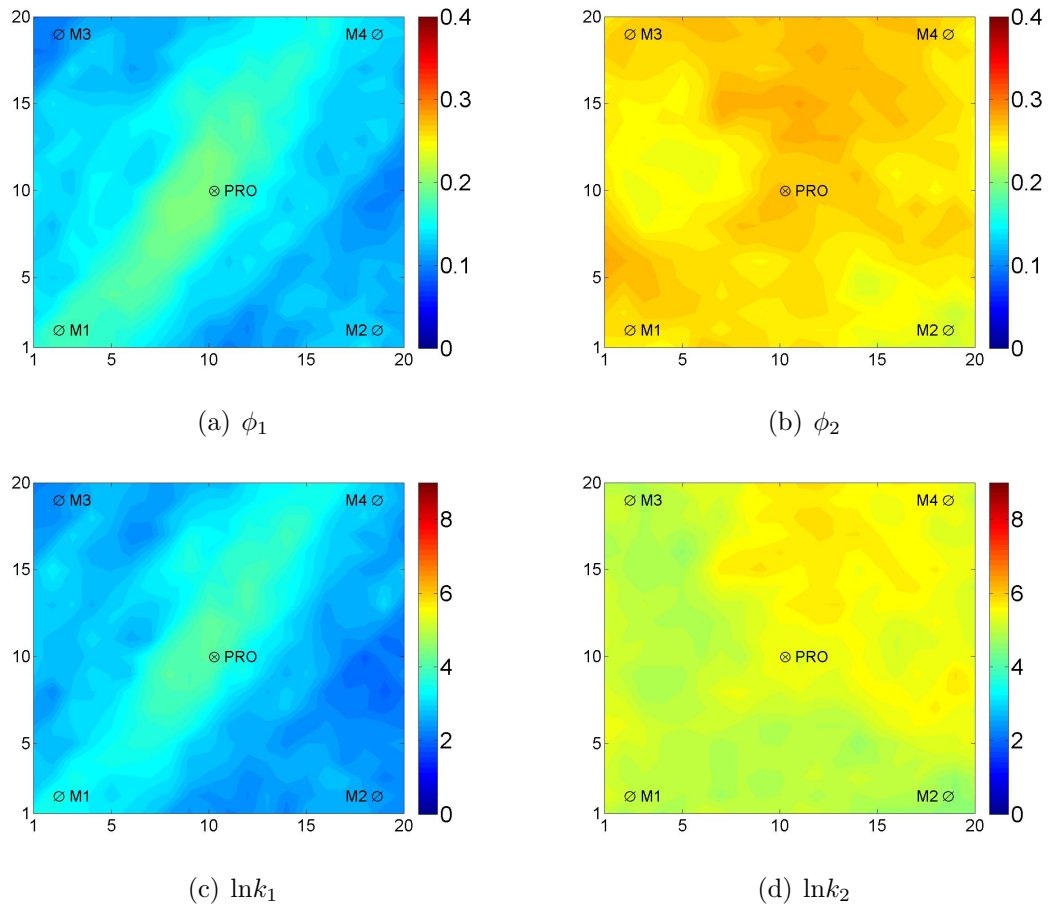


Figure 3.52: Porosity and log-permeability posterior mean after assimilating microseismic data from perforation shot of layer 2, two-layer heterogeneous example

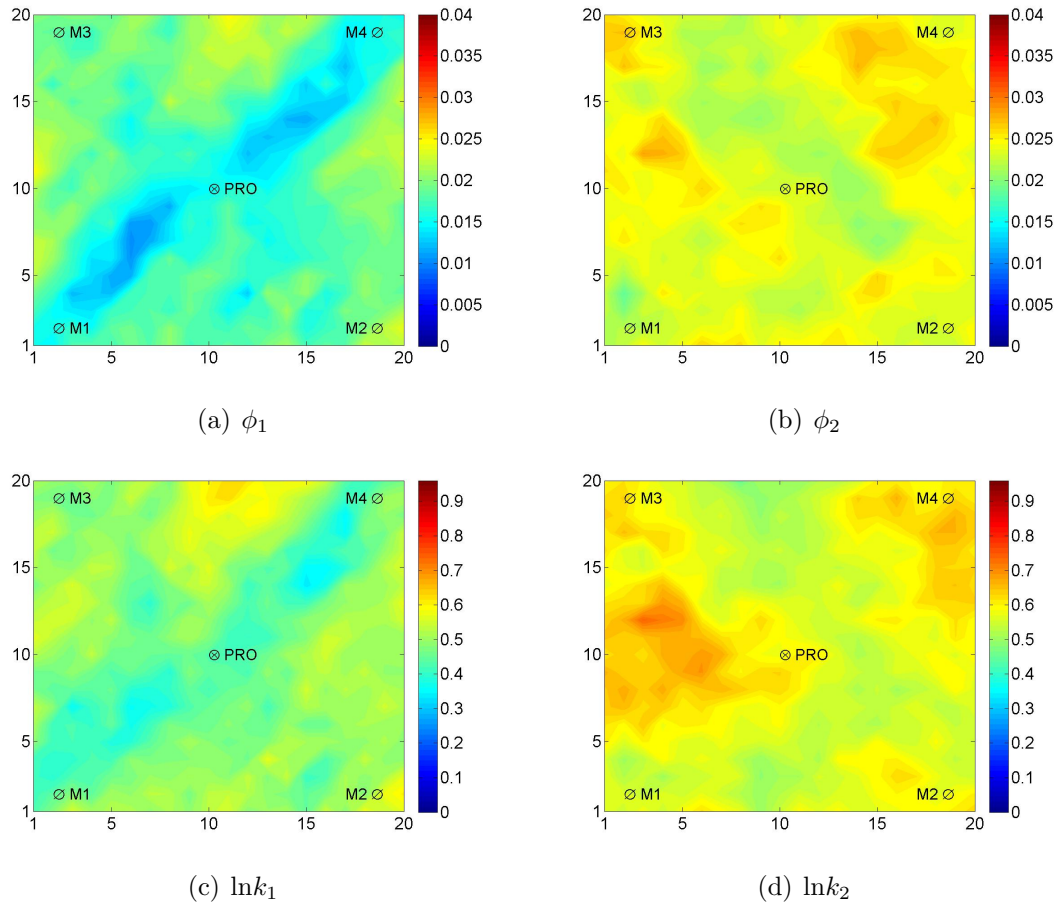


Figure 3.53: Porosity and log-permeability posterior STD of layer 1 and 2 after assimilating microseismic data from perforation shot of layer 2, two-layer heterogeneous example

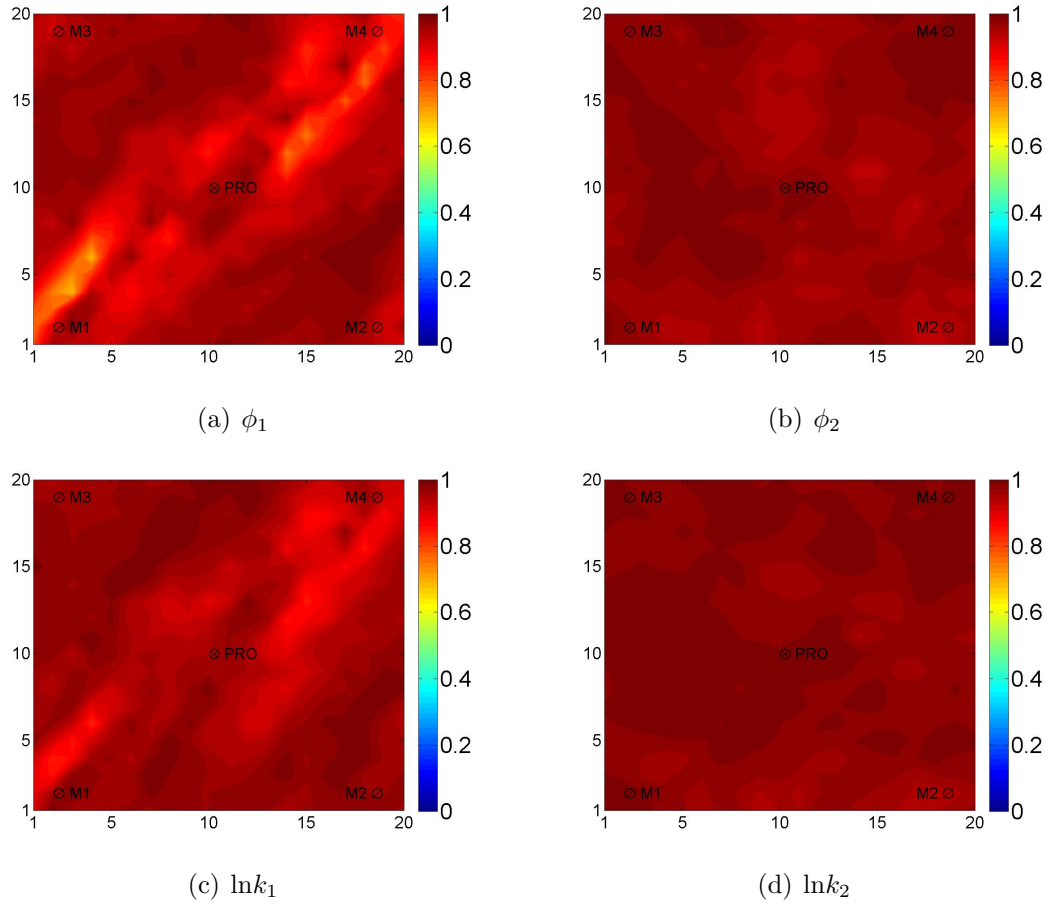


Figure 3.54: Posterior STD ratio of porosity and log-permeability before and after assimilating the microseismic data from the perforation shot of layer 2, two-layer heterogeneous example

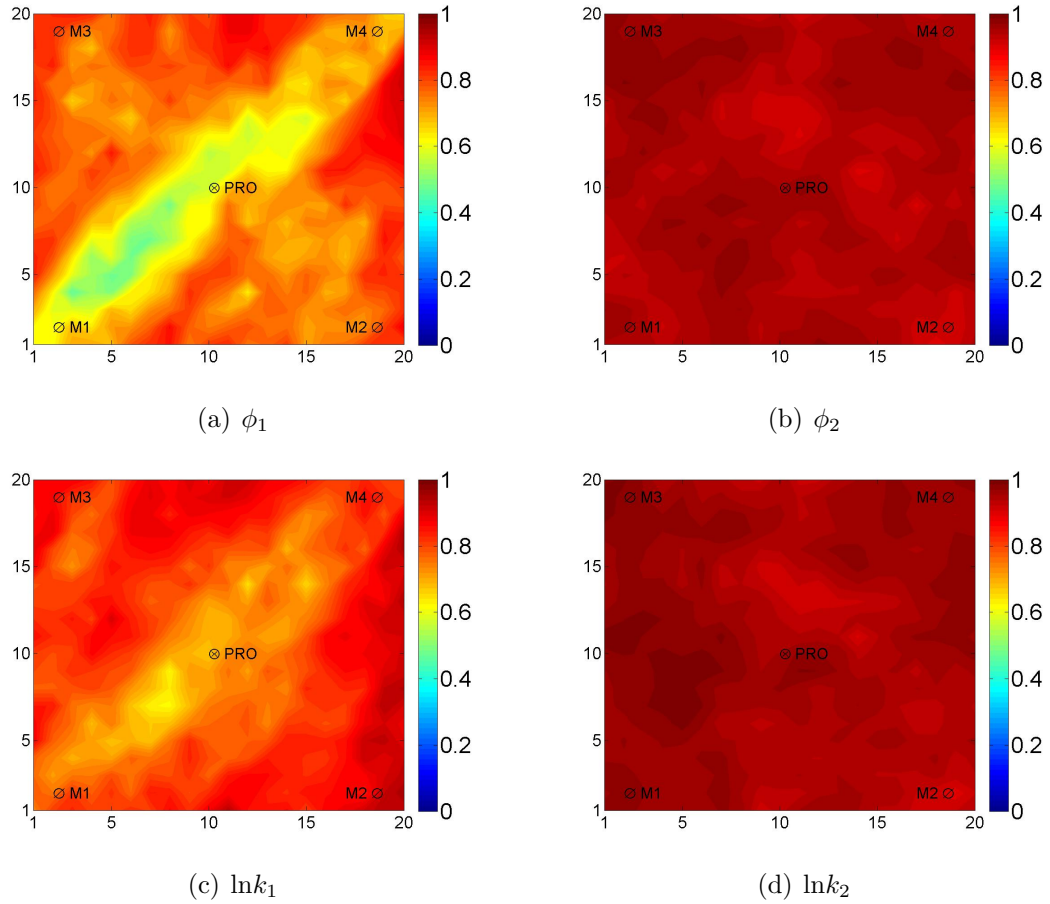


Figure 3.55: Posterior to prior STD ratio of porosity and log-permeability after assimilating the microseismic data from perforation shots of both layers, two-layer heterogeneous example

Fig. 3.56 shows the prediction of the first arrival times obtained at receivers in monitor well 1 after assimilating the microseismic data from perforation shots of both layers. Note that first group of 11 first arrival times are from P-wave and the other 11 are from S-wave. Since the porosity along the wave path has already been corrected after assimilating microseismic data from the perforation shot of layer 1, the predicted prior ensemble before assimilating the microseismic data from the perforation shot of layer 1 matches the observed data with very small uncertainty as shown in Fig. 3.56(a). After data assimilation, the uncertainty in the prediction is further decreased as shown in Fig. 3.56(b). The data match of the first arrival times at other monitor wells is similar to monitor well 1 and not shown here.

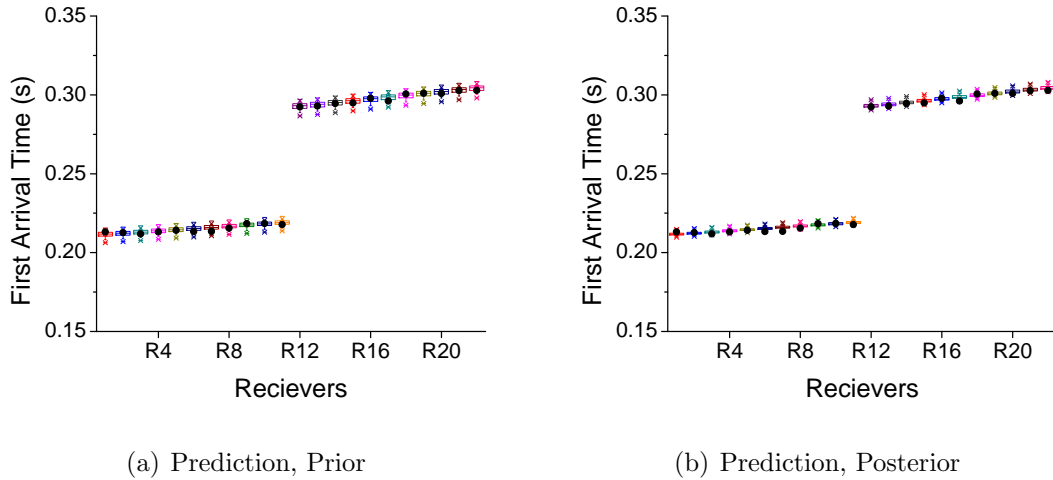


Figure 3.56: First arrival time data match at receivers in monitor well 1 when assimilating microseismic data from perforation shot of layer 2, two-layer heterogeneous example

3.3.4 Assimilating both microseismic and pressure data

As shown in the previous two sections, the pressure transient data resolves properties in the high porosity and permeability layer while the microseismic data help resolve properties in the low porosity and permeability layer. In this case, we assume both microseismic and pressure data are available and they are complementary to each other in data assimilation. We assimilate the microseismic data first and then the pressure transient data. As shown in section 3.3.3, the porosity and log-permeability fields in layer

1 (low porosity and log-permeability layer) is improved by assimilating the microseismic data while that of layer 2 did not change much from the initial ensemble. The ensemble of updated porosity and log-permeability fields after assimilating microseismic data are used as the initial ensemble in assimilating pressure transient data in this section. After assimilating the microseismic and pressure data, the estimated mean porosity and log-permeability fields are significantly improved as shown in Fig. 3.57 compared to Fig. 3.52 and the truth (Fig. 3.35). The uncertainty in layer 1 and layer 2 (especially around the active well) is further reduced as shown in Fig. 3.58 compared to Fig. 3.53 after assimilating microseismic data only. This is verified by the standard deviation ratio plots in Fig. 3.59, which shows the standard deviation ratio between assimilating both microseismic and well test data and assimilating microseismic data only. As clearly shown in Fig. 3.59, the uncertainty of log-permeability in the region around the active well has some reduction in layer 1 and significant reduction in layer 2. The average uncertainty reduction in layer 2 log-permeability field is around 50% (Fig. 3.59(d)). Fig. 3.60 shows the overall uncertainty reduction after assimilating both microseismic and well test data by plotting the standard deviation ratio of the final ensemble after assimilating both microseismic and well test to the prior standard deviation. As shown in Fig. 3.60, the uncertainty in both layer 1 and layer 2 is greatly reduced. Assimilating both pressure and microseismic data yields lower uncertainty in layer 1 (Fig. 3.60(a) and Fig. 3.60(c)) than the one from assimilating microseismic data only (Fig. 3.55(a) and Fig. 3.55(c)); and lower uncertainty in layer 2 (Fig. 3.60(b) and Fig. 3.60(d)) than the one from assimilating pressure data only (Fig. 3.41(b) and Fig. 3.41(d)).

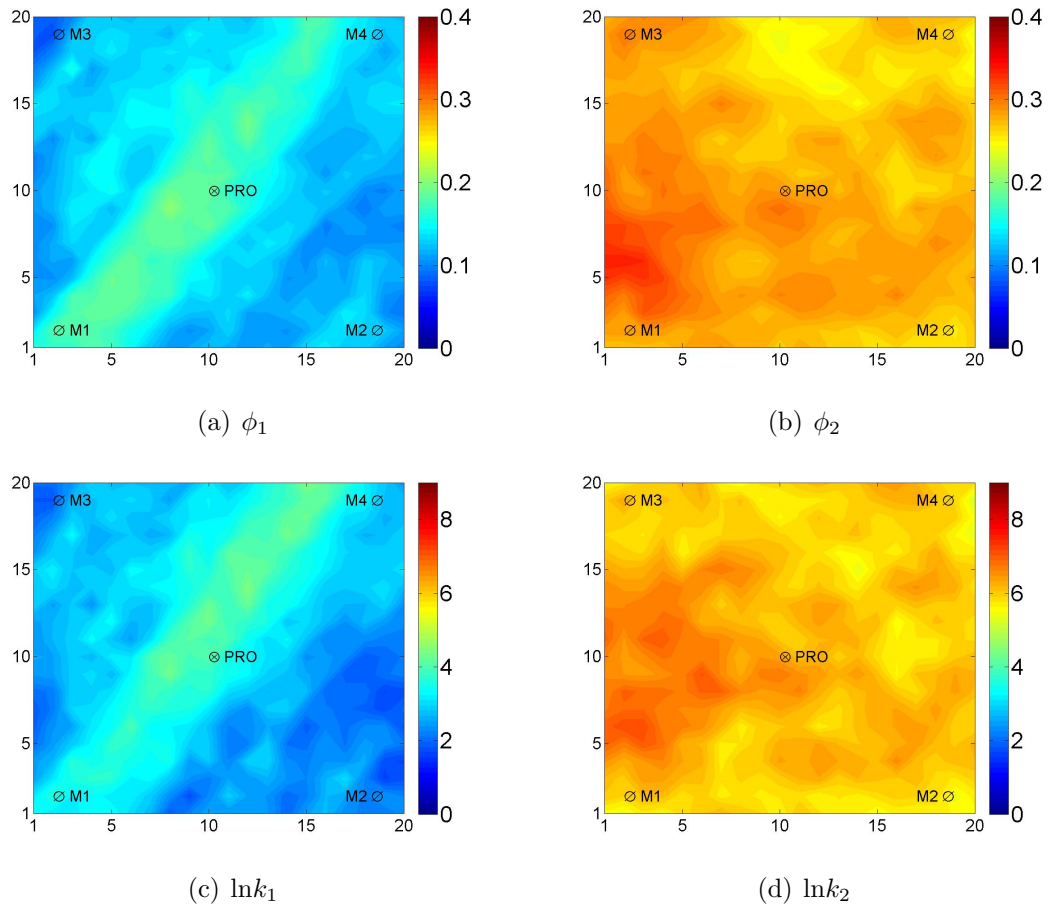


Figure 3.57: Porosity and log-permeability posterior mean after assimilating microseismic and pressure data, two-layer heterogeneous example

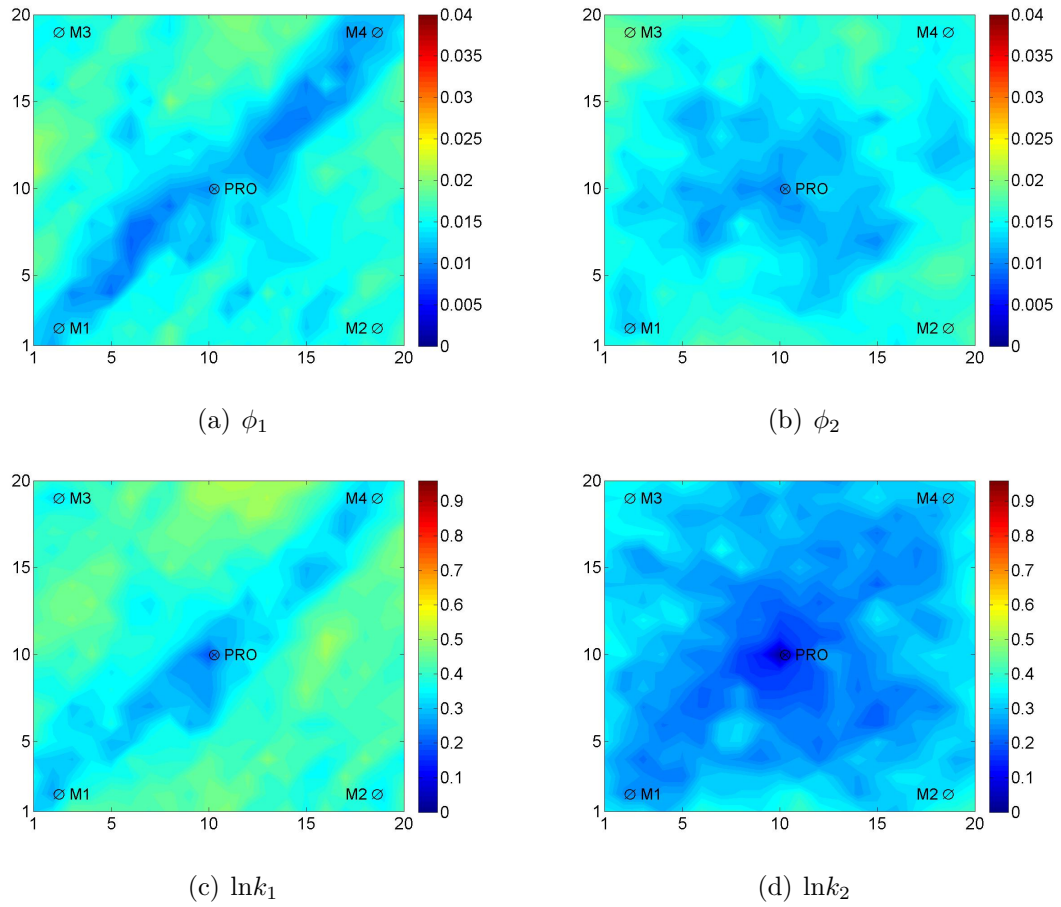


Figure 3.58: Porosity and log-permeability posterior STD after assimilating microseismic and pressure data, two-layer heterogeneous example

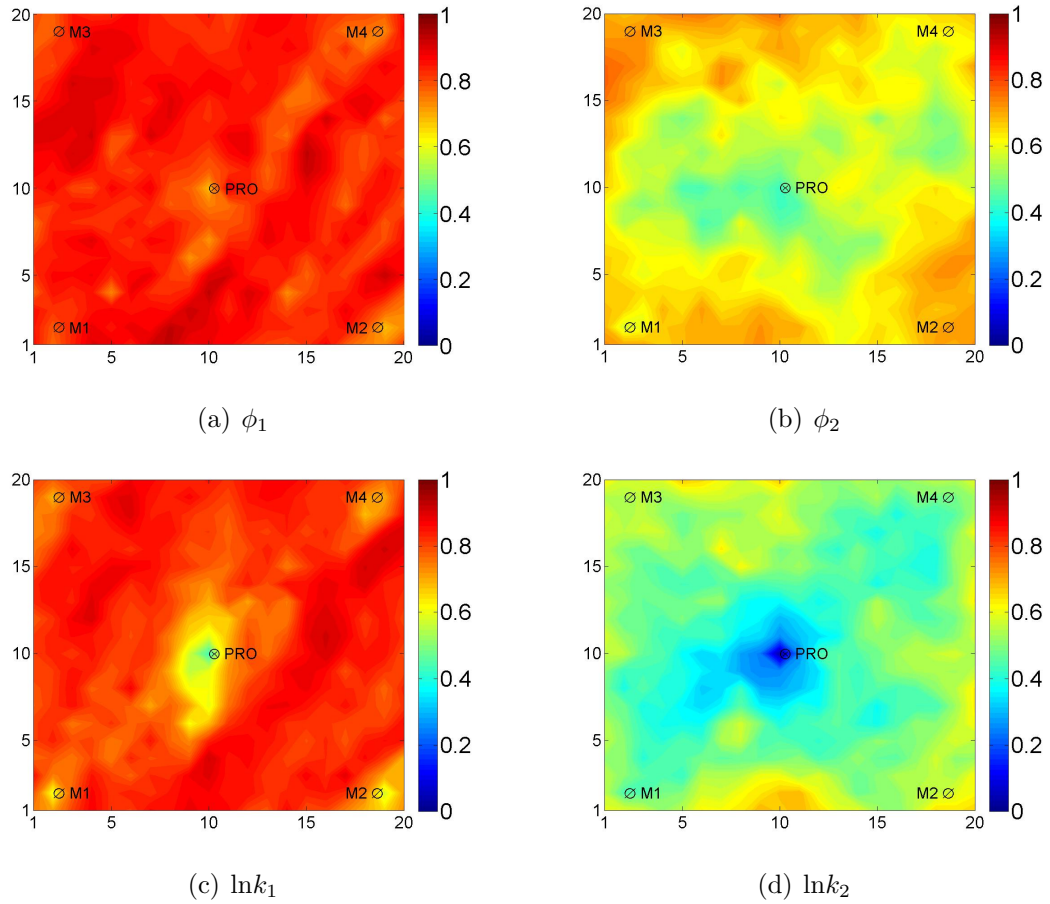


Figure 3.59: Posterior STD ratio of porosity and log-permeability between assimilating both pressure and microseismic data and assimilating microseismic data only, two-layer heterogeneous example

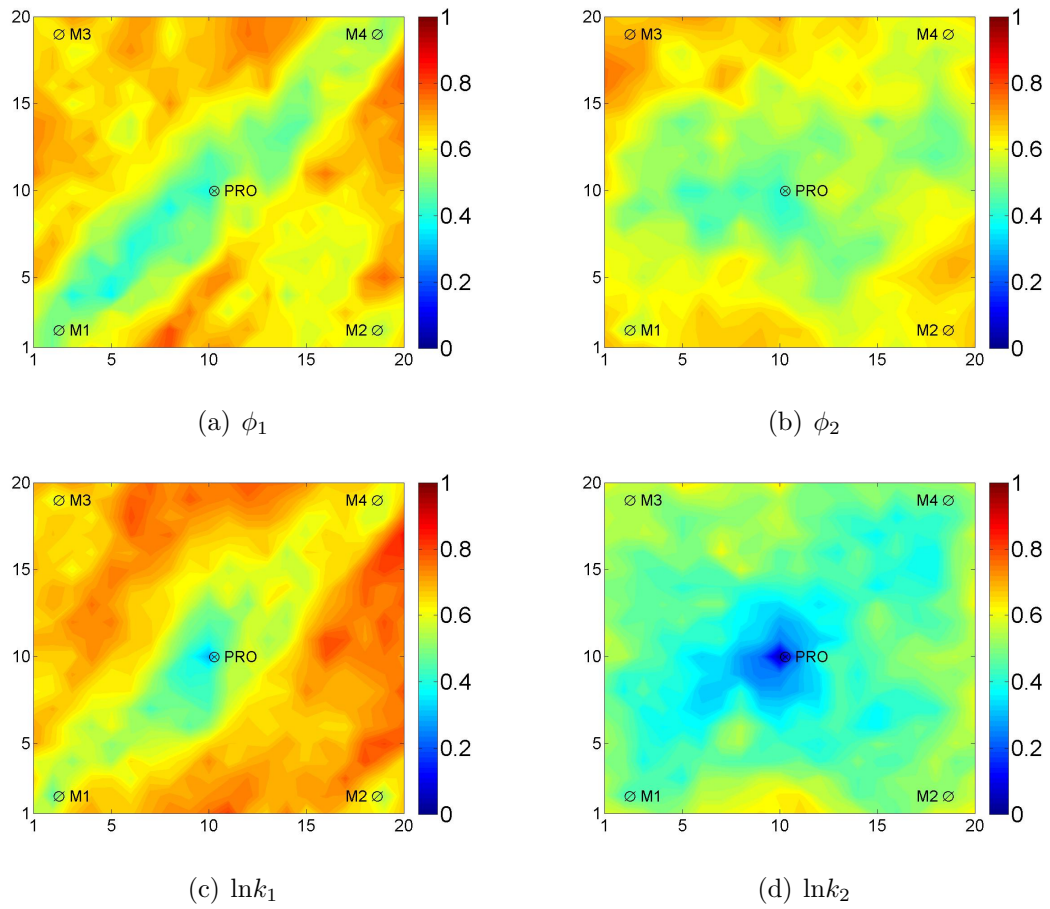


Figure 3.60: Posterior to prior STD ratio of porosity and log-permeability after assimilating both microseismic and pressure data, two-layer heterogeneous example

Fig. 3.61 and Fig. 3.62 show the pressure data match at the active and monitor wells during data assimilation and rerun from time zero. The large spread during early data assimilation time steps indicates large uncertainty in the ensemble even after assimilating the microseismic data. However, this is lower than the prior uncertainty in Fig. 3.46(a) before assimilating the microseismic data. This also confirms that microseismic data help on reservoir characterization.

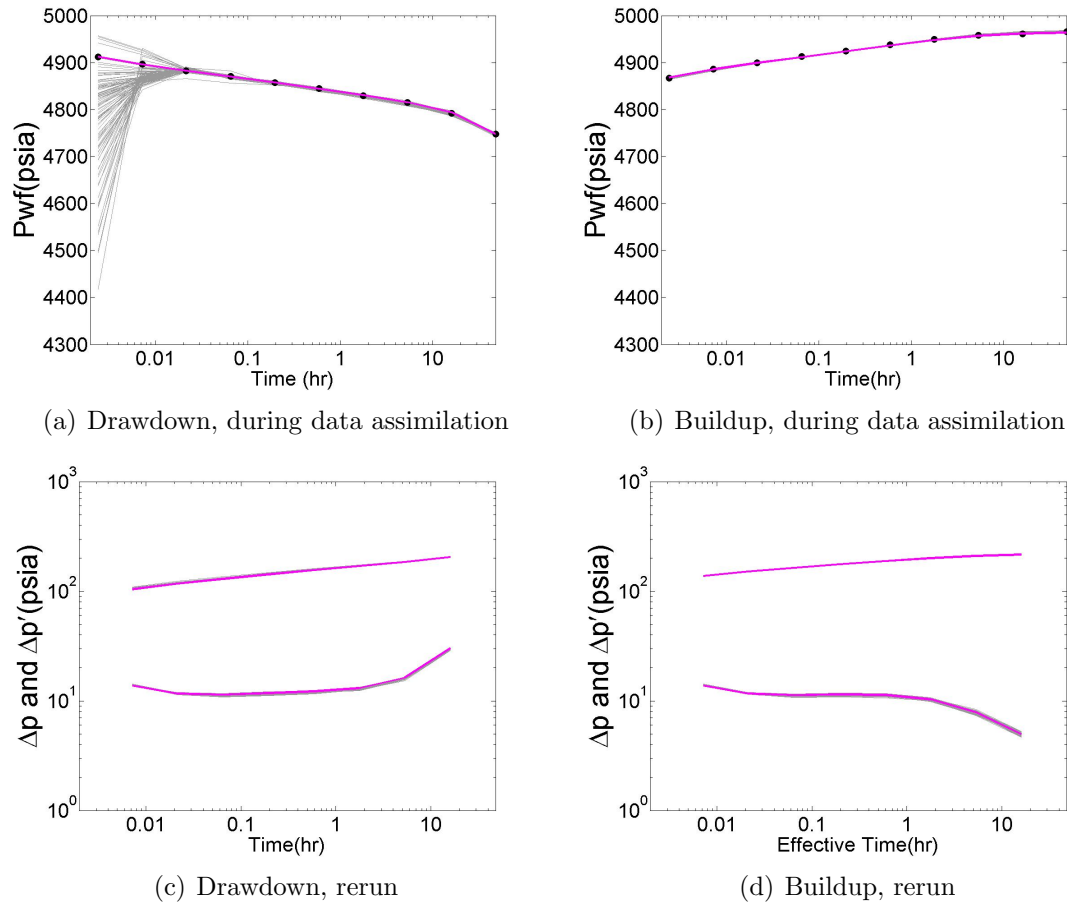


Figure 3.61: Active well pressure data match after assimilating microseismic and pressure data during data assimilation and rerun from time 0, two-layer heterogeneous example

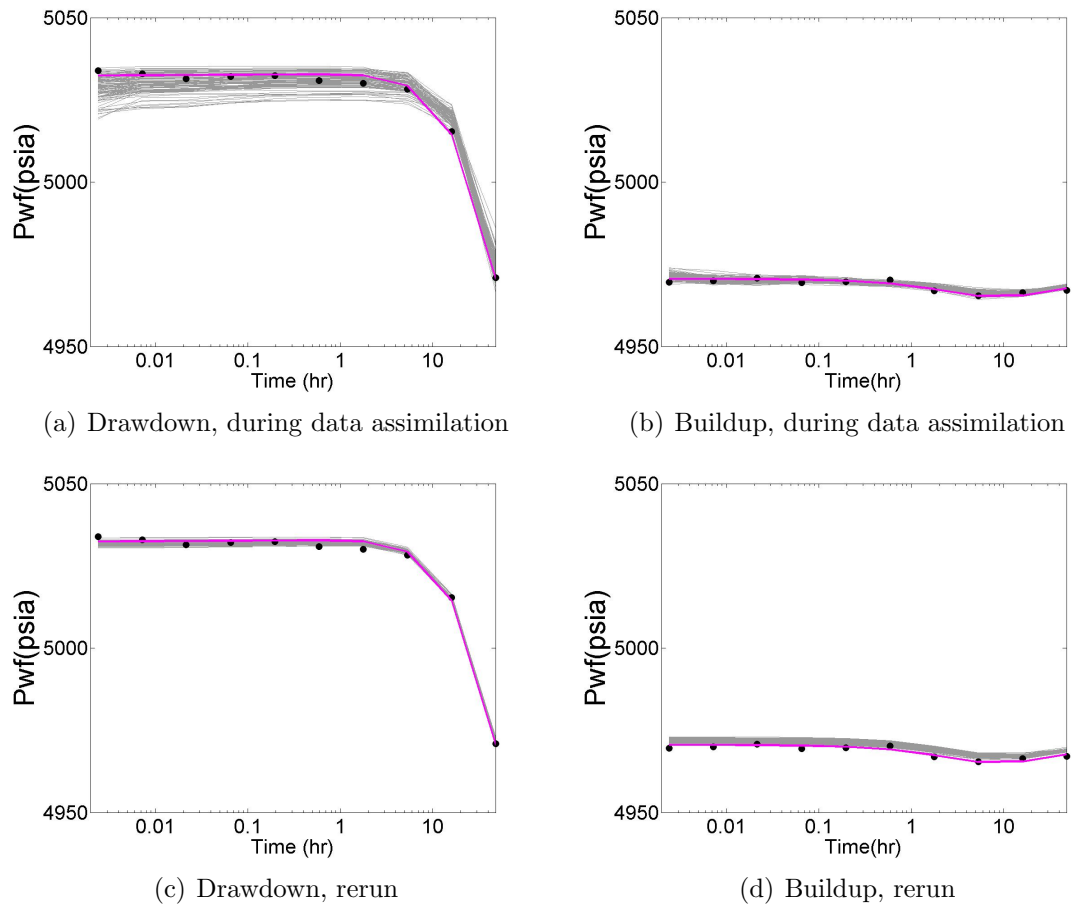


Figure 3.62: Monitor well 1 pressure data match after assimilating microseismic and pressure data during data assimilation and rerun from time 0, two-layer heterogeneous example

Fig. 3.63 compares the predicted layer rate in layer 2 with the final ensemble after assimilating both microseismic and pressure data and assimilating pressure data only. The well was producing at a constant liquid rate of 1500 STB/D during drawdown test and the calculated layer rate for the high permeability layer (layer 2) is around 1420 STB/D from the truth model. Note that the layer rates are not assimilated in the two cases. By assimilating pressure data only, the permeability in the high permeability layer (layer 2) is well resolved while the permeability in the low permeability layer (layer 1) is not resolved. The estimated permeability values in layer 1 is lower than the truth, which results in lower layer production rate in layer 1 and high layer production rate in layer 2 from the ensemble as shown in Fig. 3.63(a). The truth layer rate prediction is out of the uncertainty bound of the ensemble. It is hoped that assimilating both pressure and microseismic data would result in better layer rate prediction. However, the predicted layer rates from the final ensemble after assimilating both pressure and microseismic data underpredict the layer production rate for layer 2 as shown in Fig. 3.63(b), but with a larger uncertainty later, we will show the results from 9 other ensembles, which indicates that assimilating both microseismic and pressure data results in better layer rate prediction than assimilating pressure data only.

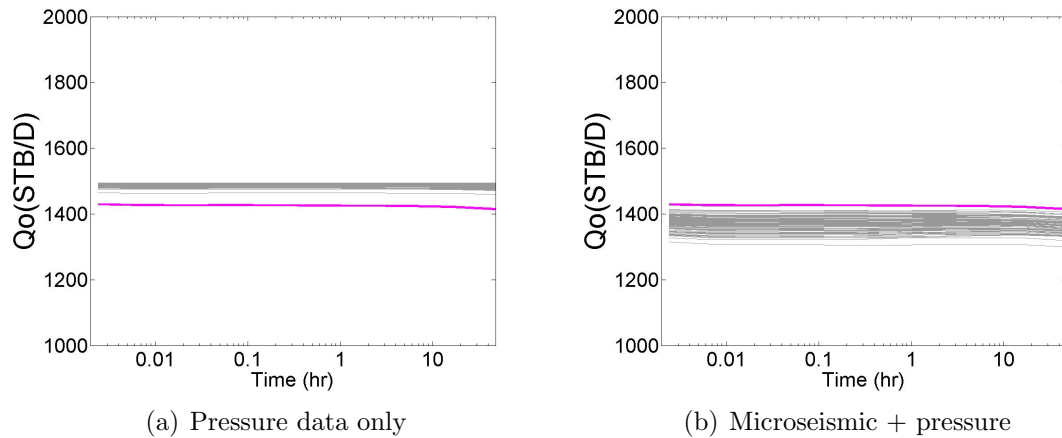


Figure 3.63: Prediction of rate of layer 2 with/without assimilating microseismic data, two-layer heterogeneous example

As EnKF is a stochastic process, we evaluate its the performance with 10 different initial ensembles generated using the same prior information given in Table 3.5. The ensemble mean of log-permeability field in both layers after assimilating pressure data only and after assimilating both microseismic and pressure data are shown from Fig. 3.64- Fig. 3.67. The updated ensemble mean varies from ensemble to ensemble. Comparing Fig. 3.64 and Fig. 3.65, we see that assimilating microseismic data improved the estimation of the log-permeability field and helps resolve the high permeability channel in layer 1. There is not much difference in layer 2 log-permeability field after assimilating pressure data only (Fig. 3.66) and after assimilating both microseismic and pressure data (Fig. 3.67).

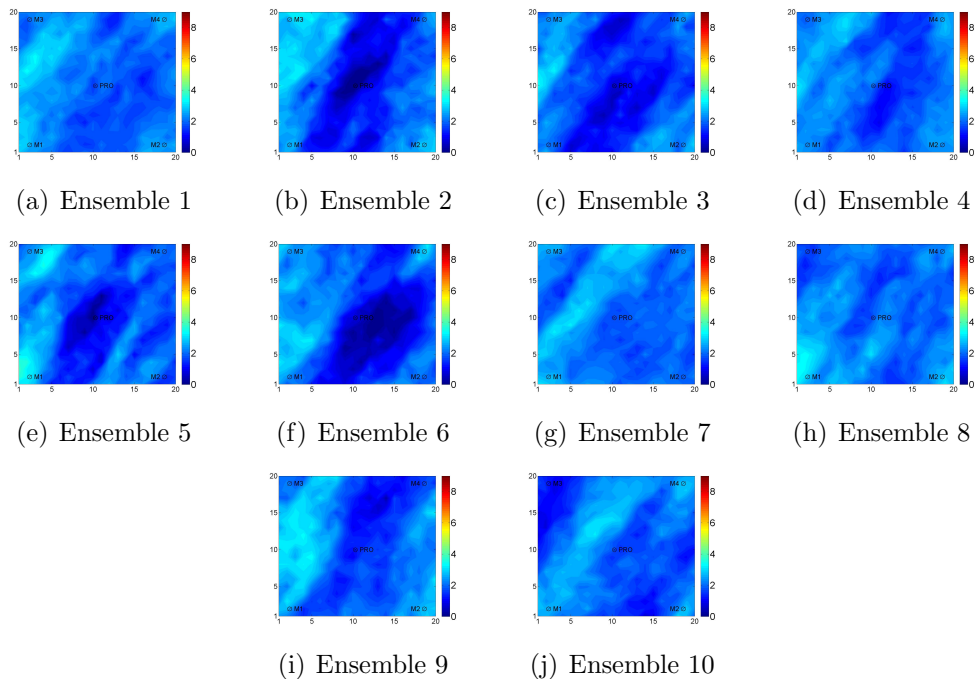


Figure 3.64: Ensemble mean of log-permeability field in layer 1 after assimilating pressure data only

The prior well gridblock log-permeability of 10 ensembles in both layers is shown in Fig. 3.68. The figure shows that the prior well gridblock log-permeability of most realizations in the 10 ensembles is lower than the true, even though they all have large uncertainty. Fig. 3.69 and Fig. 3.70 show the estimated of well gridblock log-permeability in layer 1 and layer 2, respectively. Assimilating the pressure transient data resolved only

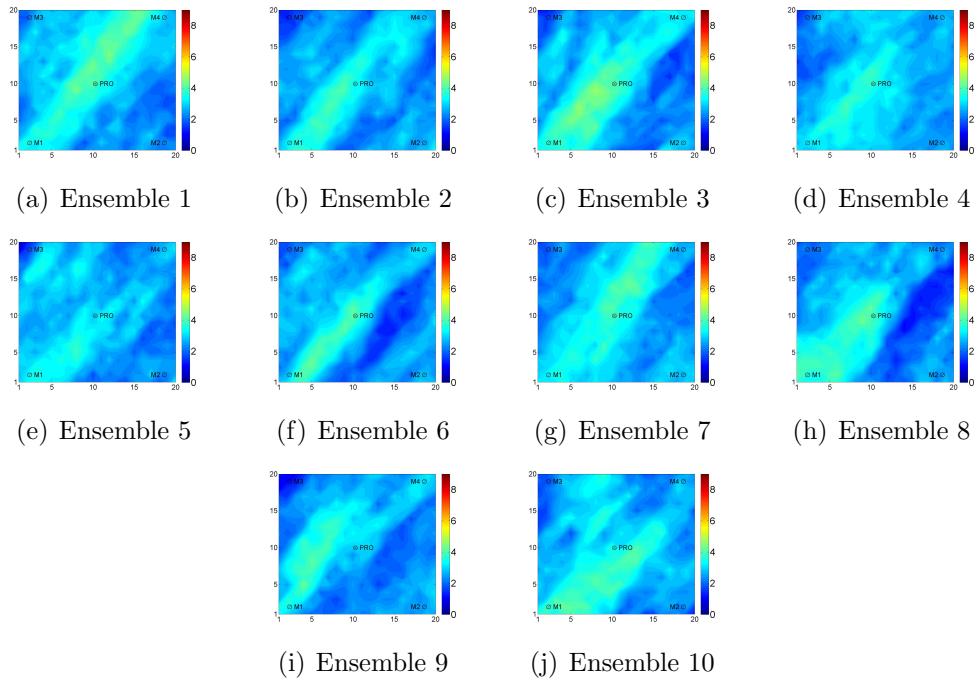


Figure 3.65: Ensemble mean of log-permeability field in layer 1 after assimilating micro-seismic and pressure data

the well gridblock permeability for layer 2 (the high permeability layer) as indicated in Fig. 3.70(a), with small final uncertainty, although a few realizations have very low log-permeability values as indicated in the plot. However, the pressure transient data are not able to resolve the well gridblock permeability for layer 1 (the low permeability layer) as indicated in Fig. 3.69(a). Compared to the prior, some estimated ensembles are even further away from the true value (Fig. 3.68(a) and Fig. 3.69(a)). After assimilating microseismic and pressure data, the estimated well gridblock permeability for layer 2 is slightly better than that obtained by assimilating the pressure data only. This is indicated by the fact that some ensemble means are above the truth and some are below with smaller uncertainty, while all the ensemble means after assimilating pressure data only are above the true (Fig. 3.70(a)). The well gridblock log-permeability for layer 1 after assimilating the microseismic and pressure data has large uncertainty, but they bound the true (Fig. 3.69(b)), which indicates that the mean estimate of well gridblock permeability in the low permeability layer after assimilating both microseismic and pressure data is better than assimilating pressure data only.

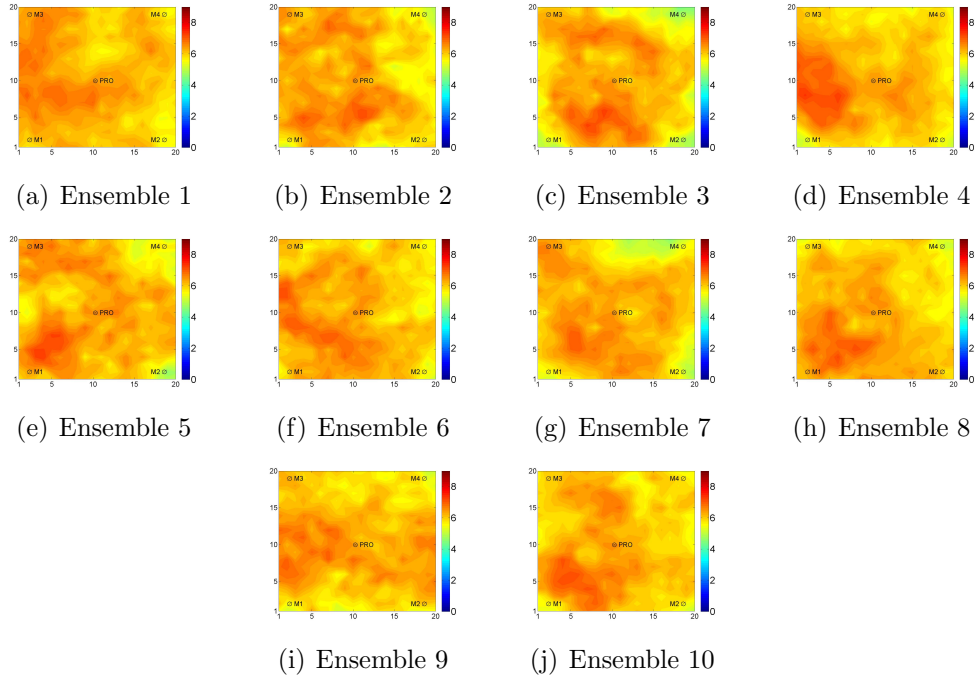


Figure 3.66: Ensemble mean of log-permeability field in layer 2 after assimilating pressure data only

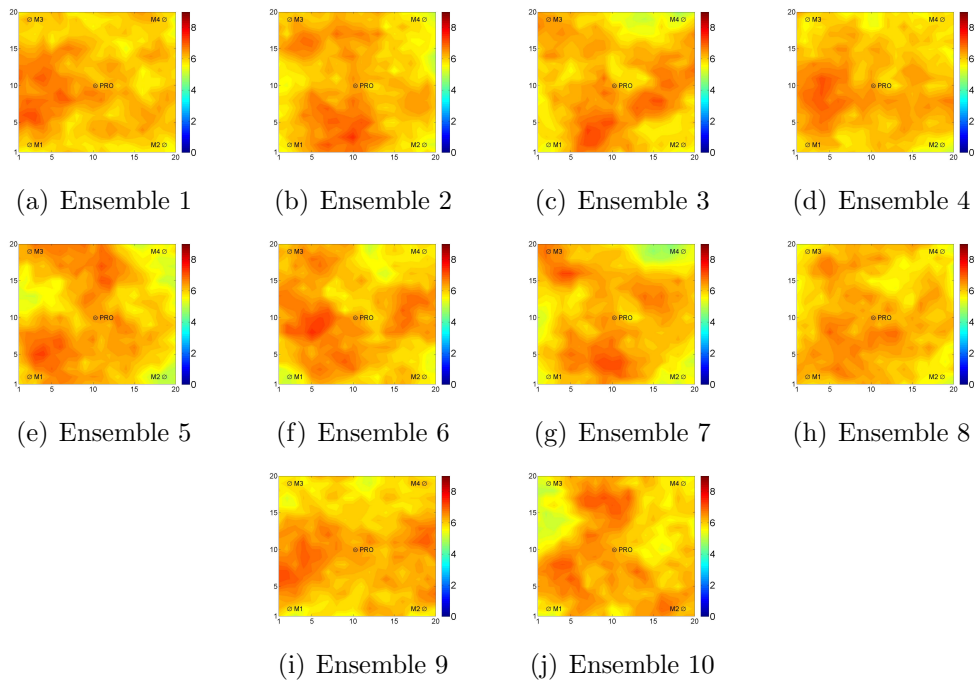
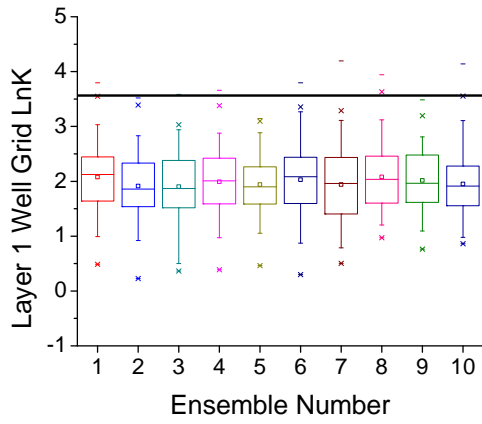
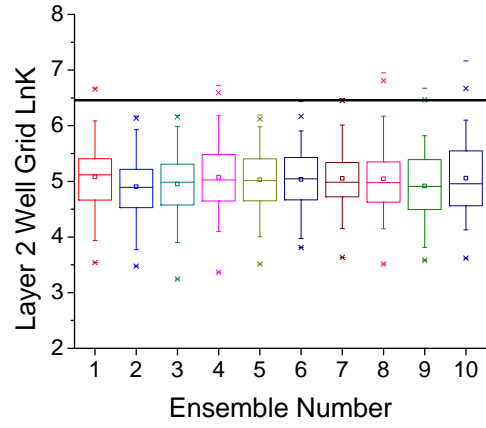


Figure 3.67: Ensemble mean of log-permeability field in layer 2 after assimilating micro-seismic and pressure data

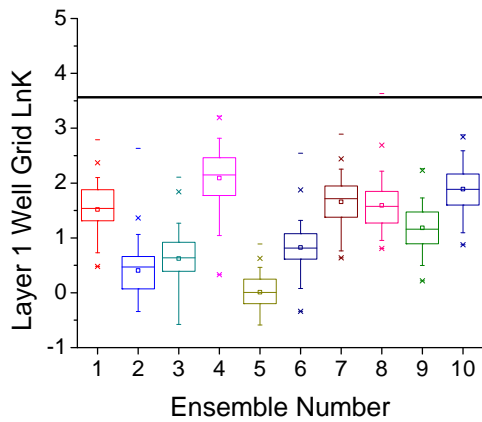


(a) Layer 1

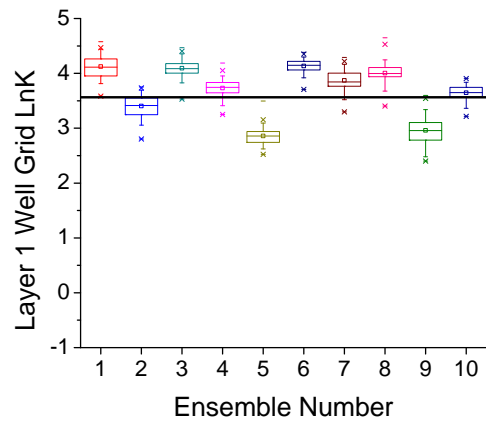


(b) Layer 2

Figure 3.68: Prior well gridblock log-permeability of all ensembles, two-layer heterogeneous example

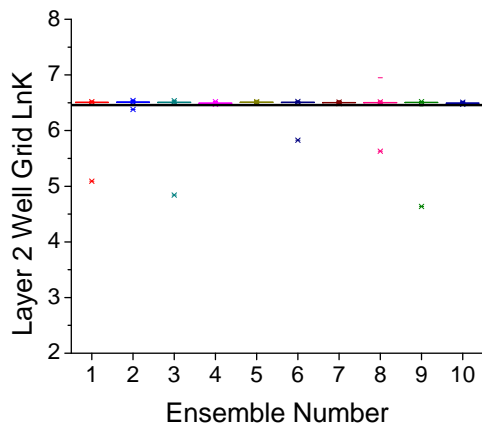


(a) Pressure

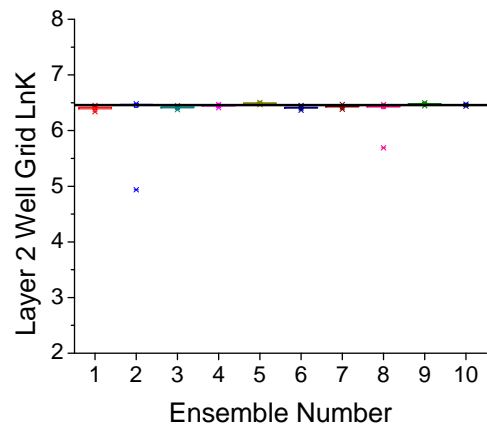


(b) Microseismic + pressure

Figure 3.69: Layer 1 well gridblock log-permeability of all ensembles after data assimilation, two-layer heterogeneous example



(a) Pressure



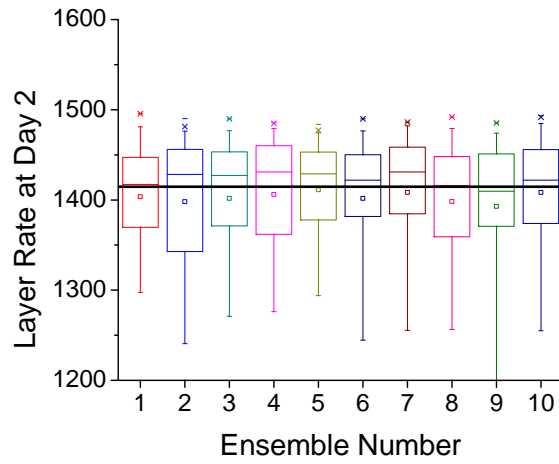
(b) Microseismic + pressure

Figure 3.70: Layer 2 well griddblock log-permeability of all ensembles after data assimilation, two-layer heterogeneous example

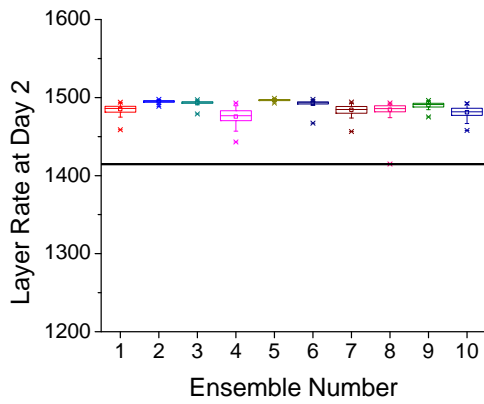
Fig. 3.71 shows the predicted layer rate in layer 2 at the end of day 2 running from time 0 using the prior ensembles, ensembles after assimilating pressure data only, ensembles after assimilating both microseismic and pressure data. As shown in Fig. 3.63, the layer rate remains almost constant during the drawdown test, so the layer rate at the end of day 2 is representative of layer rates during the entire drawdown test. As shown in Fig. 3.71(a), the predicted layer rate from the prior ensembles has large uncertainty. Although the prior well gridblock log-permeability in both layers are lower than the true, the well gridblock permeability ratio between the two layers is close to the true, so the average layer rate prediction is actually close to the true. By assimilating pressure data only (Fig. 3.71(b)), the log-permeability in layer 1 is underestimated while the estimated log-permeability in layer 2 is close to the truth, so the layer rate in layer 1 is overestimated. By assimilating both microseismic and pressure data, the predicted layer rate from all ensembles has more uncertainty compared to the case assimilating pressure data only. However, the true prediction is within the uncertainty bound characterized by different ensembles (Fig. 3.71(c)). This figure indicates that predictions from EnKF results based on single ensemble can overpredict or underpredict the layer rates.

3.3.5 Assimilating pressure and layer rate data

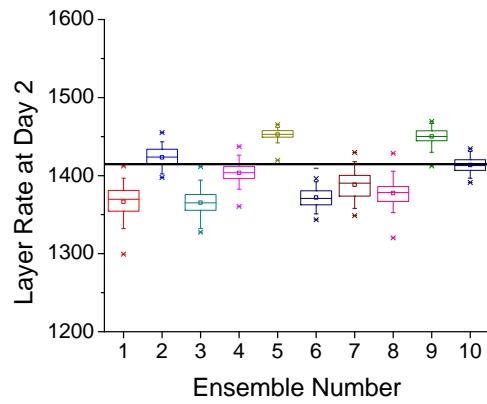
This section presents the results of assimilating the pressure and layer rate for the heterogeneous case. The results are compared with the cases in the previous section that assimilate both microseismic data and pressure data. As shown in Fig. 3.72, by assimilating both pressure and layer rate data, the high permeability region around the well in layer 1 is well captured. However, the long high permeability channel connecting monitor well 1 to monitor well 4 is not continuous as in the case of assimilating microseismic and pressure data in Fig. 3.57. As shown in Fig. 3.73 and Fig. 3.74, the uncertainty is reduced mainly in the near wellbore region in layer 1. Data match on the active well pressure, monitor well pressure and layer rate in layer 1 during data assimilation and rerun from time zero are reasonable as shown in Fig. 3.75, Fig. 3.76 and Fig. 3.77.



(a) Prior



(b) Pressure



(c) Microseismic + pressure

Figure 3.71: Predicted layer rate of layer 1 at end of day 2 rerunning from time 0 of all ensembles after data assimilation, two-layer heterogeneous example

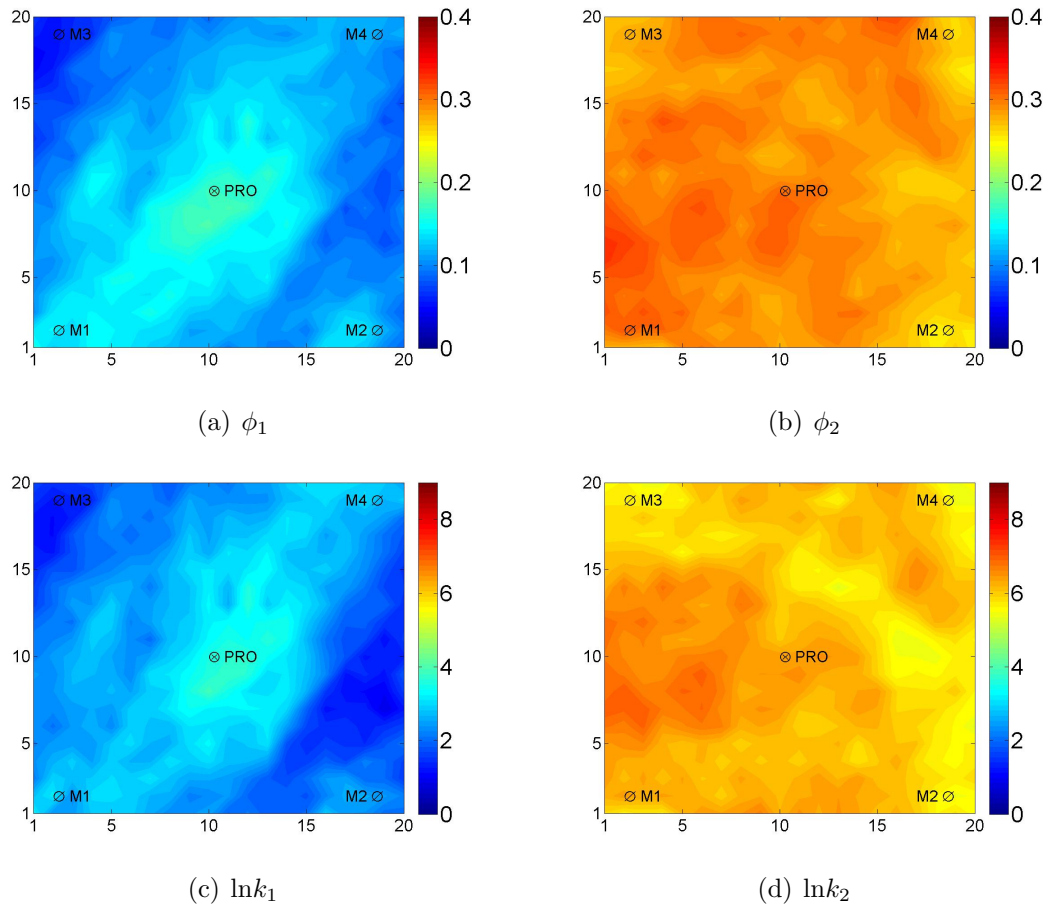


Figure 3.72: Porosity and log-permeability posterior mean after assimilating pressure and layer rate data, two-layer heterogeneous example

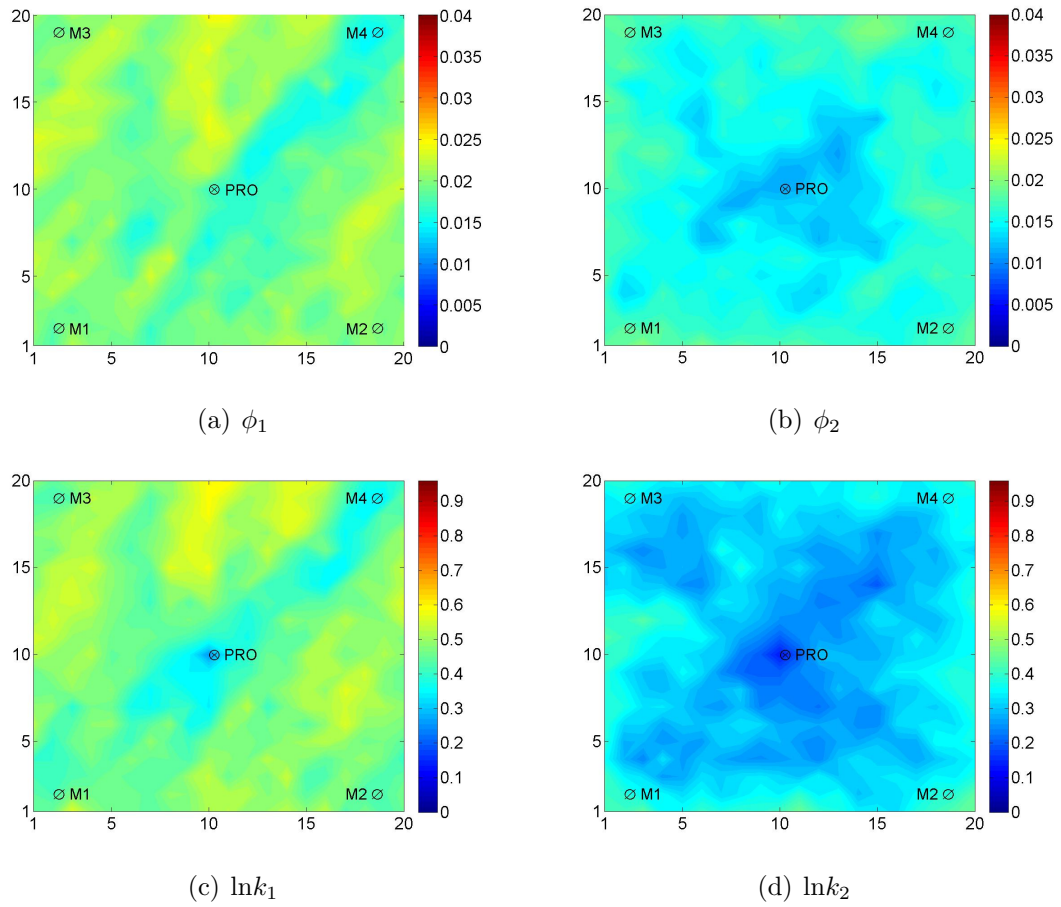


Figure 3.73: Porosity and log-permeability posterior STD after assimilating pressure and layer rate data, two-layer heterogeneous example

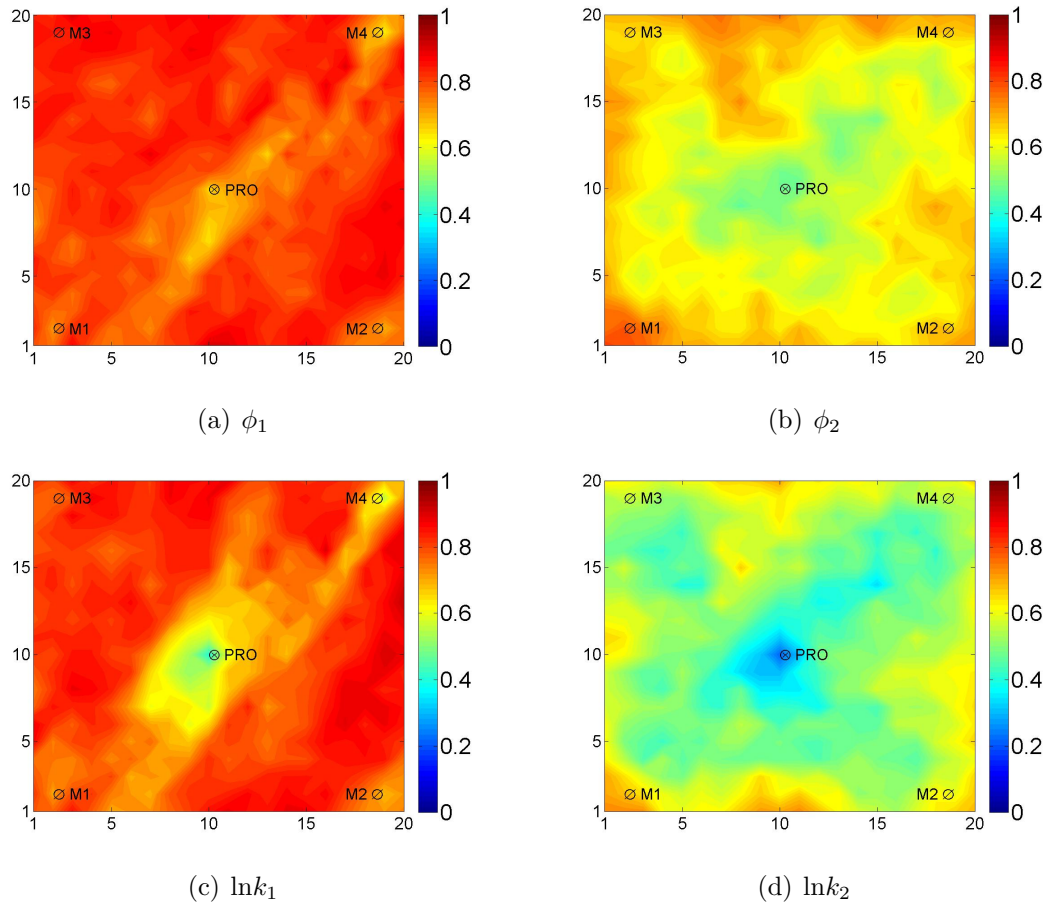
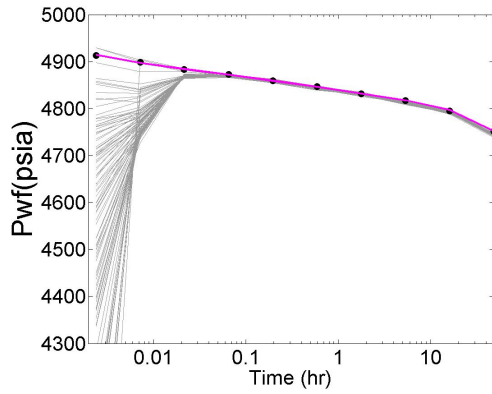
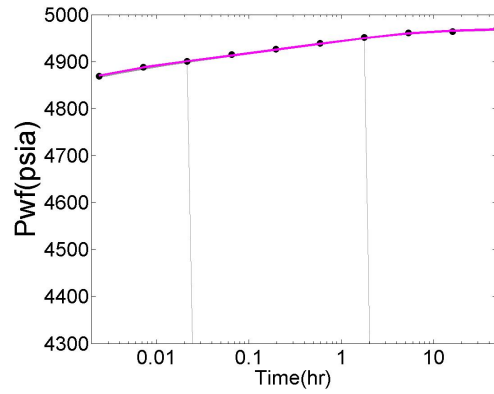


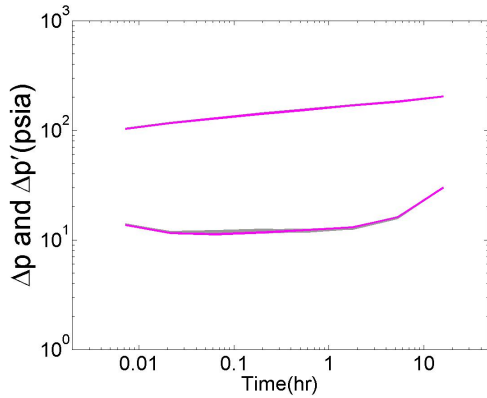
Figure 3.74: Posterior to prior STD ratio of porosity and log-permeability after assimilating pressure and layer rate data, two-layer heterogeneous example



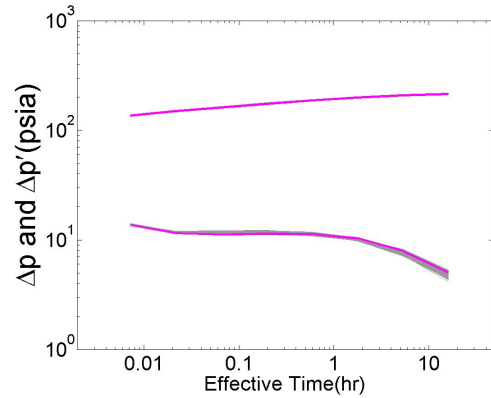
(a) Drawdown, during data assimilation



(b) Buildup, during data assimilation



(c) Drawdown, rerun



(d) Buildup, rerun

Figure 3.75: Active well pressure data match after assimilating pressure and layer rate data, two-layer heterogeneous example

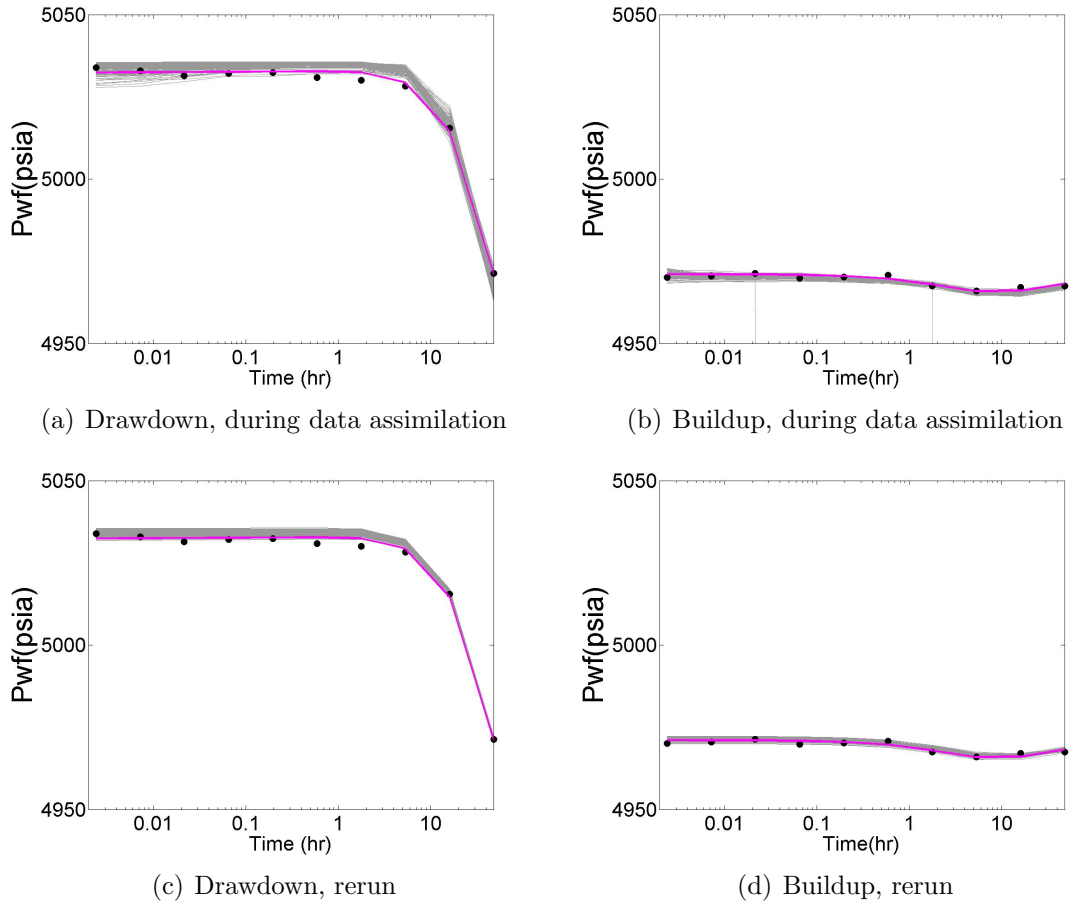


Figure 3.76: Pressure data match at monitor well 1 after assimilating pressure and layer rate data, two-layer heterogeneous example

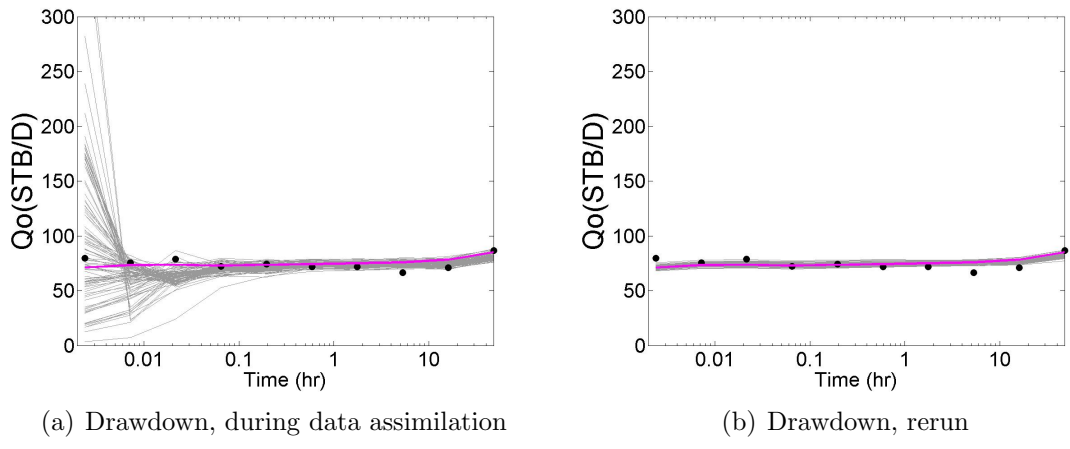


Figure 3.77: Layer rate data match in layer 1 after assimilating pressure and layer rate data, two-layer heterogeneous example

The same 10 initial ensembles used to assimilate microseismic and pressure data are run to assimilate pressure and layer rate data. The prior well gridblock log-permeability in layer 1 which are lower than the true is shown in Fig. 3.68(a). Fig. 3.78 shows well gridblock log permeability estimates in layer 1 of all ensembles. Well gridblock log-permeability are better resolved by assimilating the layer rate data than assimilating pressure and microseismic data.

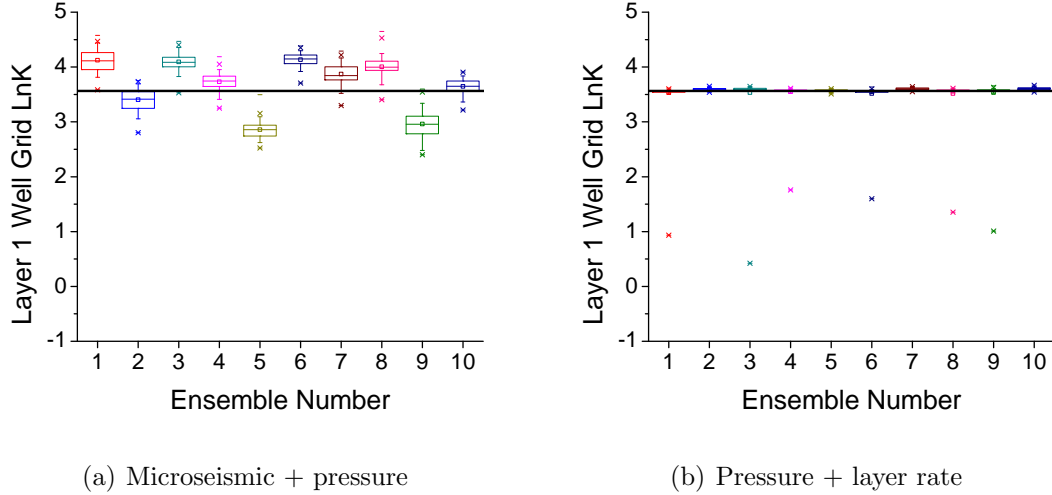


Figure 3.78: Layer 1 well gridblock log-permeability of all ensembles after data assimilation, two-layer heterogeneous example

Here, we quantify the data assimilation performance using mean square error between the true and estimated porosity and log-permeability with different types of data. The mean square error E is defined in Eq. 3.21, where N_m is the total number of model parameters. This is calculated for each ensemble and the average value of all 10 ensemble is listed in Table 4.8. Overall, assimilating pressure and layer rate data and pressure plus microseismic data give better estimates of the rock properties fields, i.e. microseismic and layer rate data improve the estimated rock property fields. As indicated earlier, layer rate data contains only near wellbore information while microseismic data contain information along its wave path, which covers more spatial area. Therefore, assimilating microseismic and pressure gives the overall best rock properties estimate as indicated by the smallest mean square error of all cases.

$$E = \frac{1}{N_m} \sum_{i=1}^{N_m} \frac{(m_{i,est} - m_{i,true})^2}{\sigma_{m,prior}^2} \quad (3.21)$$

Table 3.6: Mean square error between estimated and true, two-layer heterogeneous example

	Layer 1		Layer 2	
	ϕ	$\ln k$	ϕ	$\ln k$
prior	4.73	4.32	2.06	3.73
pressure	5.62	5.64	2.27	0.84
microseismic	1.21	1.36	2.38	3.84
microseismic+pressure	1.41	1.60	1.46	0.90
pressure+layer rate	3.13	2.57	1.73	1.02

3.4 Ten-layer homogeneous case

Here, we test the same scheme on a 10-layer case with each homogenous. We perforate in the middle of each layer and the receivers are located on the top of reservoir. The true, prior mean and prior standard deviation are shown in Table 3.7. The first arrival time data of the P-wave and S-wave of all 12 receivers of each perforation shot are assimilated sequentially by EnKF. The P-wave and S-wave velocity structures are shown Fig. 3.79. The approximate raypaths from each perforation to the lowest receiver are shown in Fig. 3.79(a). As in a two layer homogenous case, the first arrival waves travel mostly in high velocity layers, especially in layer 6, in this ten layer homogenous case. The measurement error for first arrival time data is 1 ms.

Table 3.7: True and prior of porosity and permeability

	True		Prior Mean		Prior STD		Correlation
	ϕ	$\ln k$	ϕ	$\ln k$	ϕ	$\ln k$	
Layer 1	0.1718	3.15	0.15	3	0.025	0.5	0.8
Layer 2	0.1787	4.29	0.20	5	0.025	0.5	0.8
Layer 3	0.1534	3.46	0.15	3	0.025	0.5	0.8
Layer 4	0.2672	5.46	0.25	5.5	0.025	0.5	0.8
Layer 5	0.2284	5.25	0.25	5.5	0.025	0.5	0.8
Layer 6	0.1527	3.31	0.15	3	0.025	0.5	0.8
Layer 7	0.2207	5.61	0.20	5	0.025	0.5	0.8
Layer 8	0.2398	5.22	0.25	5.5	0.025	0.5	0.8
Layer 9	0.2392	5.90	0.20	5	0.025	0.5	0.8
Layer 10	0.2667	6.06	0.25	5.5	0.025	0.5	0.8

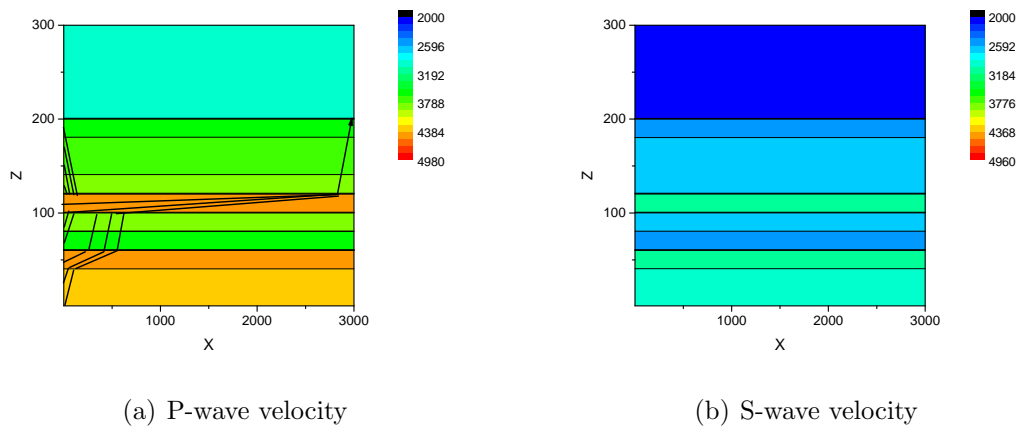


Figure 3.79: first arrival time and velocity

As shown in Fig. 3.80, by assimilating microseismic data, uncertainties of the porosities in the layers of lower porosity, e.g. layers 1, 3, 6 are reduced significantly. The uncertainty in permeability decreases some correspondingly to its layer porosity uncertainty reduction. The black dots in Fig. 3.80 and Fig. 3.81 represent the true porosity or log-permeability values.

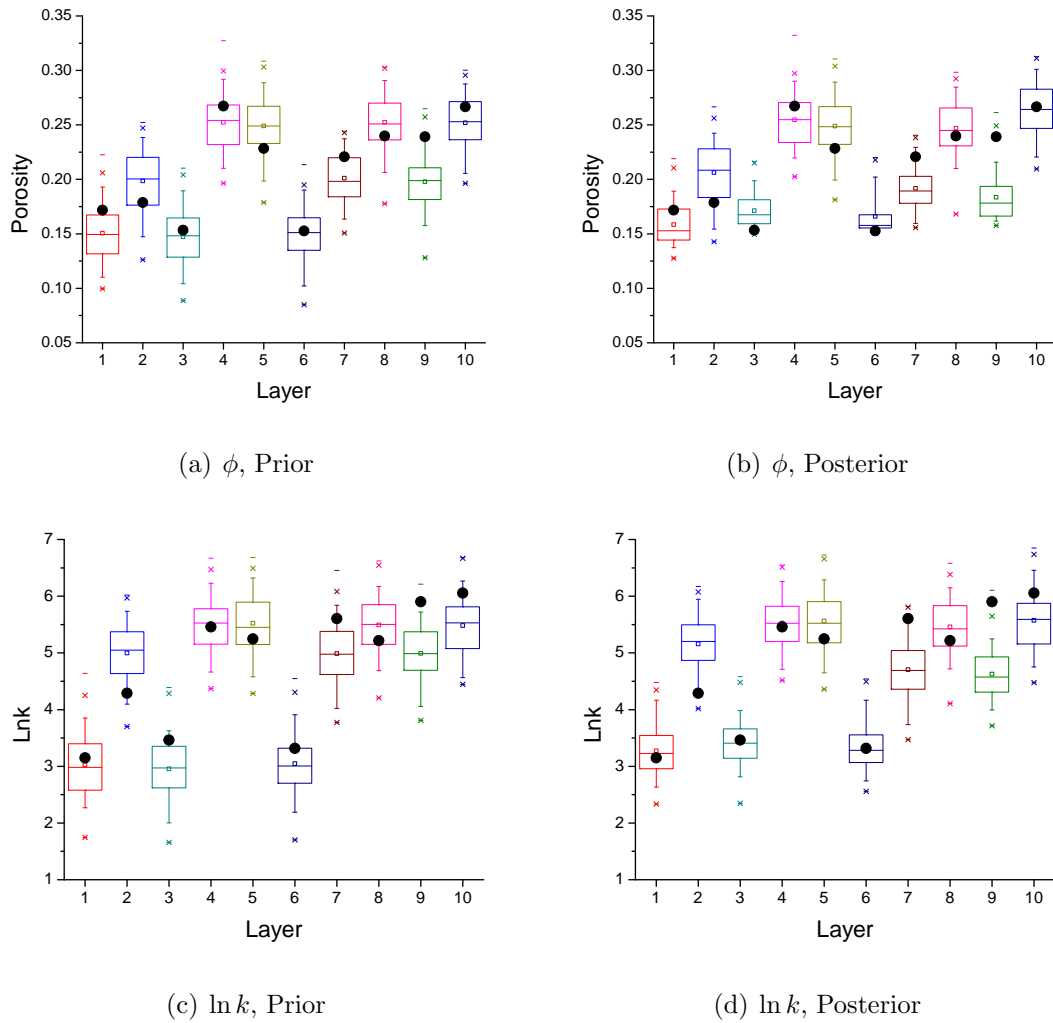


Figure 3.80: Prior and posterior porosity and $\ln k$ distribution before and after assimilating microseismic data

Fig. 3.81 compares the posterior porosity and permeability after assimilating both microseismic and pressure data to the posterior after assimilating only pressure data. Including microseismic data helps reduce the uncertainty in true porosity and permeability of some layers.

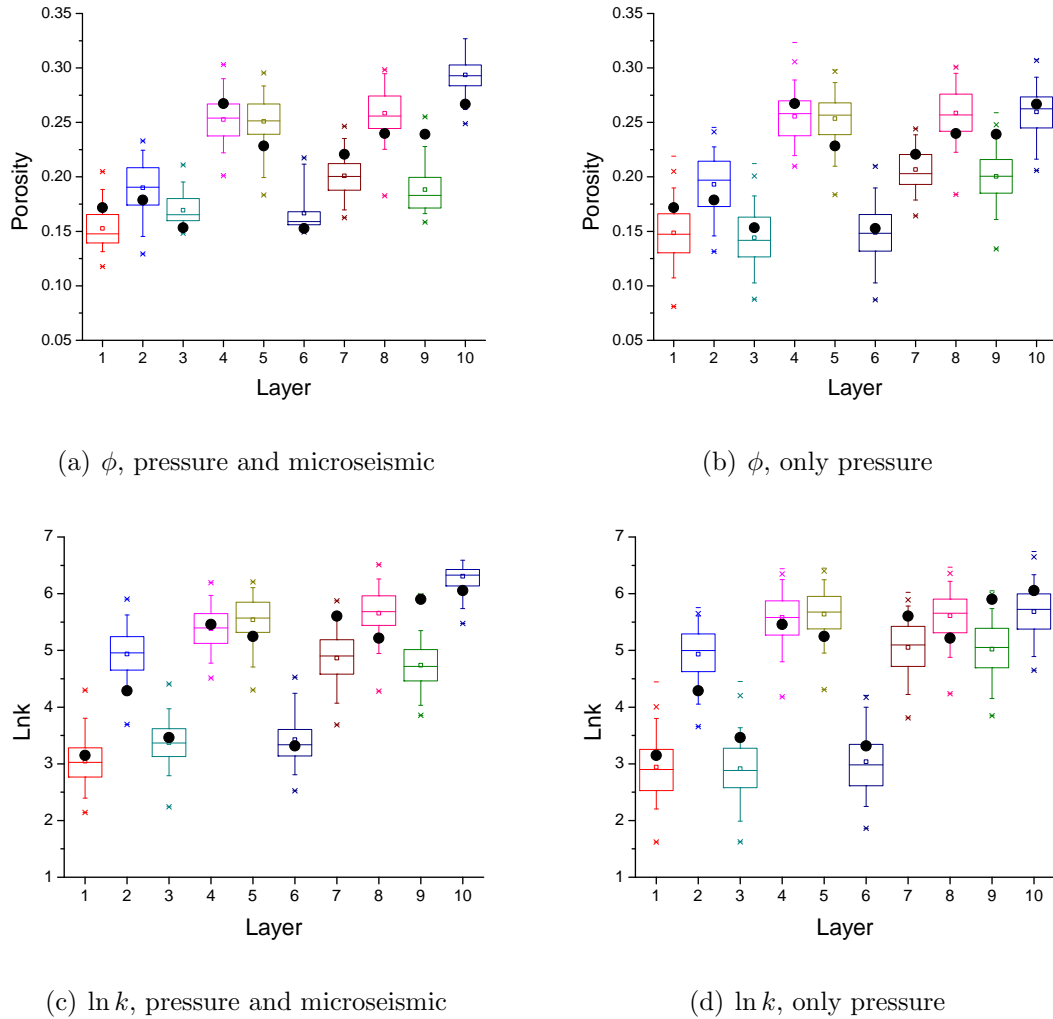
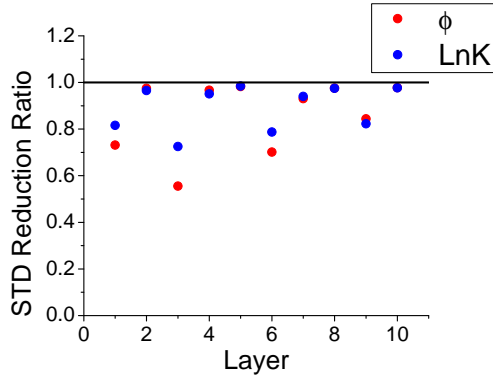


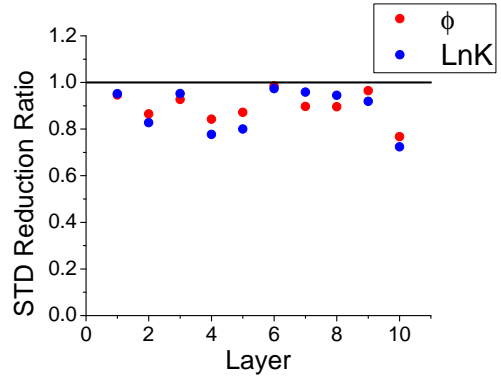
Figure 3.81: Posterior porosity and $\ln k$ by assimilating pressure data and/or microseismic data

Fig. 3.82 shows the standard deviation reduction ratio calculated by dividing posterior standard deviation by the prior standard deviation of each layer, with red dots as porosity and blue dots as log permeability. For instance, Fig. 3.82(a) shows the values of standard deviation after assimilating microseismic data divided by standard deviation of prior; Fig. 3.82(b) shows the values of standard deviation after assimilating microseismic and well test data sequentially divided by standard deviation after assimilating

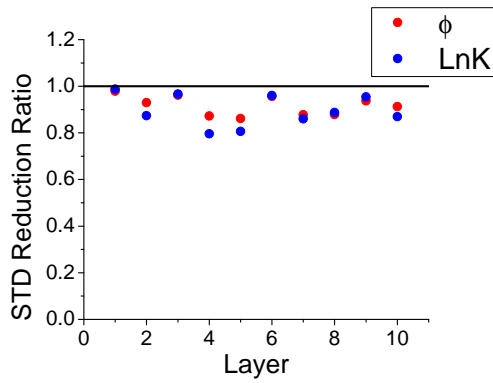
only microseismic data. So Fig. 3.82(a) shows the uncertainty reduction by assimilating microseismic data from prior and Fig. 3.82(b) shows the uncertainty reduction by assimilating well test data after microseismic data are assimilated. Fig. 3.82(c) and Fig. 3.82(d) show the uncertainty reduction by assimilating well test data first and then microseismic data. The black line in the plots represents reduction ratio equal to 1 which means uncertainty is not changing; and the lower the value, the more uncertainty reduction is achieved. As shown in Fig. 3.82(a), the same conclusions are drawn as from previous plots, by assimilating microseismic data, uncertainty of the porosity in lower porosity layers, e.g., layer 1, 3, 6, is reduced a lot and the uncertainty in permeability decreases some correspondingly within the same layer. As shown in Fig. 3.82(b), by assimilating well test data, uncertainty of the permeability in higher permeability layers, e.g., layer 4, 5, 10, is reduced more than permeability in lower permeability layers, and porosity are reduce correspondingly due to the correlation between porosity and log-permeability. Reversibly, similar phenomenon are observed by assimilating well test data first and then microseismic data as shown in Fig. 3.82(c) and Fig. 3.82(d).



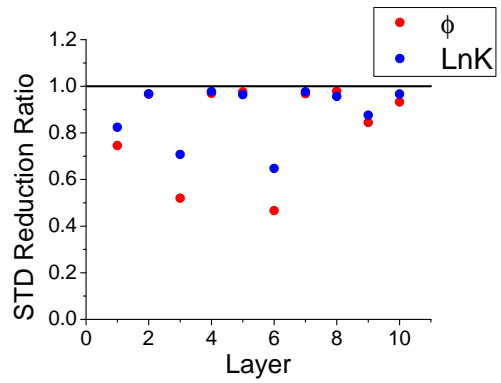
(a) microseismic/prior



(b) microseismic+well test/microseismic



(c) well test/prior



(d) well test+microseismic/well test

Figure 3.82: Posterior porosity and $\ln k$ uncertainty reduction by assimilating pressure data and/or microseismic data

As shown in Fig. 3.83(a), by assimilating only well test data, the uncertainty in the thickness averaged permeability is greatly reduced even though the uncertainty in the permeability of each layer has not changed significantly as shown in Fig. 3.82(c). By assimilating both microseismic and well test data, the uncertainty in thickness averaged permeability increased after assimilating buildup data which may be due to the non-linearity of the problem.

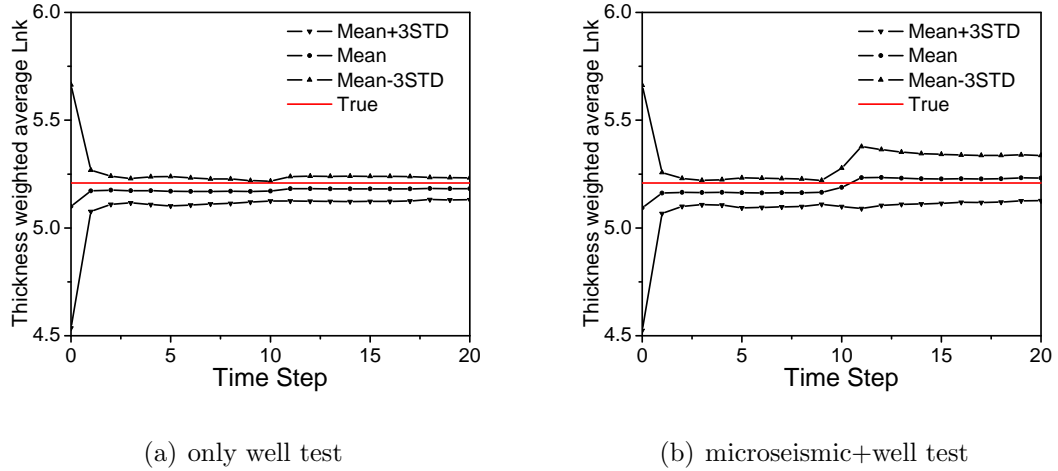
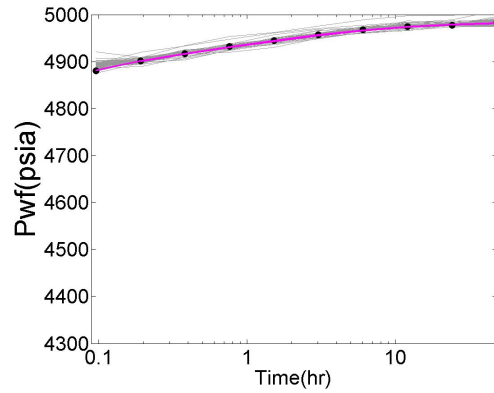
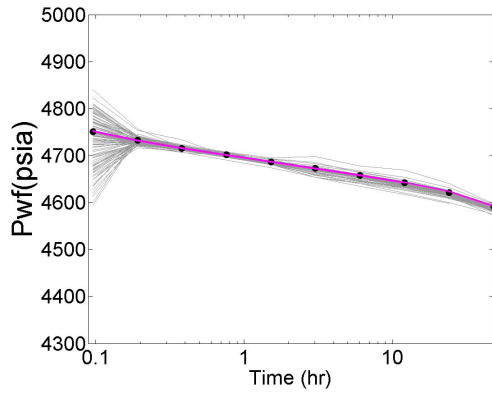
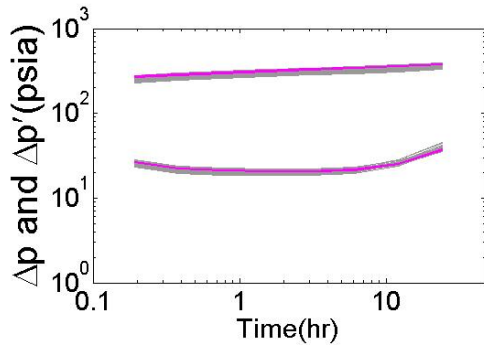


Figure 3.83: Thickness average permeability

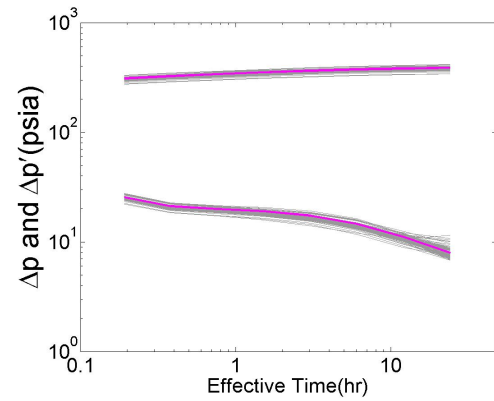
Data prediction during assimilation and rerun from time 0 with and without assimilating microseismic data are shown in Figs. 3.84 and Figs. 3.85 respectively. Data matches are reasonably good in both cases.



(a) Drawdown, Prediction during data assimilation (b) Buildup, Prediction during data assimilation

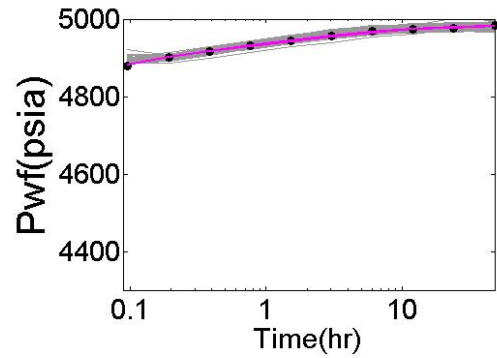
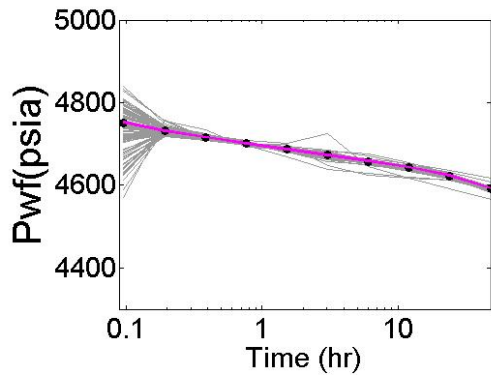


(c) Drawdown, Rerun

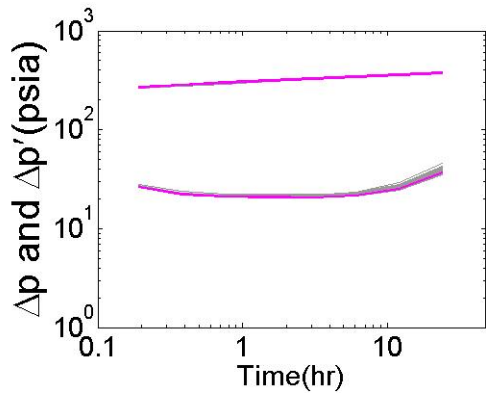


(d) Buildup, Rerun

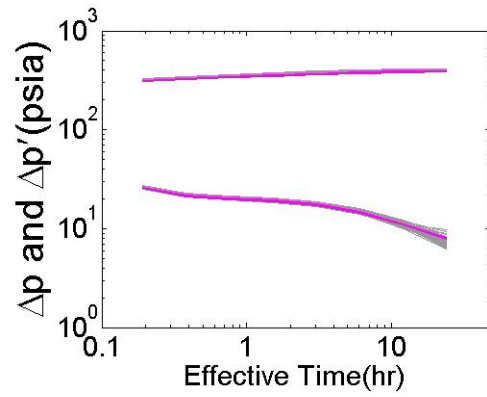
Figure 3.84: Prediction after assimilating microseismic and pressure data



(a) Drawdown, Prediction during data assimilation (b) Buildup, Prediction during data assimilation



(c) Drawdown, Rerun



(d) Buildup, Rerun

Figure 3.85: Prediction after assimilating pressure data only

CHAPTER 4
MICROSEISMIC EVENT LOCATION

4.1 Overview

From the microseismic data collected during multi-stage hydraulic fracturing, we may pick out the first arrival times for both P- and S-waves for each event and at each geophone. The P- and S-wave arrival times contain the distance information from the event location to the geophones as well as the event initiating time. Inverting these interpreted microseismic data yields the event location parameters, which can be used to characterize the hydraulic fractures for reservoir modeling. An efficient gradient-based and an ensemble-based microseismic event location inversion method are presented in this Chapter. A novel method is devised to obtain the gradient of the first arrival times to the event location parameters in addition to the first arrival times in one forward model run in the gradient-based method. The forward model that is used to calculate the first arrival times is the finite-difference solution to the Eikonal equation. The method is applied to a multi-layer reservoir with a vertical well and one hydraulic fracture. Application to a more realistic multi-layer shale gas reservoir with a horizontal well and several stages of hydraulic fractures is presented in [41], and will not be shown here.

4.2 Event location inversion methodology

4.2.1 Gauss-Newton algorithm

The Gauss-Newton algorithm is a gradient-based method used to solve non-linear least squares problems. It can be viewed as a modification to the Newton's method for finding a minimum of a function. However, the Gauss-Newton algorithm avoids the calculation of second-order derivatives.

The parameters to be determined are the event location (x, y, z) and the event occurrence time (t_0) . The current code solves for the event locations one at a time. Therefore, the parameter vector is $X = [x, y, z, t_0]^T$. Here we use the vector d_{obs} to represent the measurement data vector, which includes the noisy first arrival times for each event at each receiver (geophone) for both P- and S-wave. Therefore for each event, the maximum number of measurements at each geophone is 2. The objective function of the optimization problem is defined as

$$O(X) = \frac{1}{2}(X - X^P)^T C_X^{-1}(X - X^P) + \frac{1}{2}(d_{obs} - d_{calc})^T C_D^{-1}(d_{obs} - d_{calc}). \quad (4.1)$$

The first term in Eq. 4.1 is a regularization term based on the prior information where X^P is the prior mean and the C_X is the prior covariance matrix. The second term in Eq. 4.1 is the mismatch of the observed (d_{obs}) and calculated (d_{calc}) data and C_D is the measurement error covariance matrix, which provides the weight to different data entries in the objective function.

To minimize the objective function of Eq. 4.1, the gradient and Hessian of the objective function are given, respectively, by

$$\nabla O(X) = C_X^{-1}(X - X^P) + G^T C_D^{-1}(d_{calc} - d_{obs}) \quad (4.2)$$

and

$$H = C_X^{-1} + G^T C_D^{-1} G + (\nabla G^T) C_D^{-1} (d_{calc} - d_{obs}). \quad (4.3)$$

Here, G is the sensitivity matrix defined by

$$G = \begin{bmatrix} (\nabla_X d_{calc,1})^T \\ (\nabla_X d_{calc,2})^T \\ \vdots \\ (\nabla_X d_{calc,N_d})^T \end{bmatrix} = (\nabla_X d_{calc}^T)^T \quad (4.4)$$

or

$$G^T = [\nabla_X d_{calc,1} \ \nabla_X d_{calc,1} \ \cdots \ \nabla_X d_{calc,N_d}] = \nabla_X (d_{calc}^T). \quad (4.5)$$

The (i, j) element of the sensitivity matrix is

$$d_{ij}(X) = \frac{\partial d_i}{\partial X_j}, \quad (4.6)$$

for $i = 1, 2, \dots, N_d$ and $j = 1, 2, \dots, N_X$. The $d_{ij}(X)$'s are referred to as the sensitivities or sensitivity coefficients. Note from the first-order Taylor expansion, $d_{ij}(X)$ gives the sensitivity of the i th (predicted or calculated) data $d_{calc,i}$, to the j th model parameter X_j at a particular X and gives a measure of the change in the i th predicted data that results from a unit change in X_j keeping all other entries of X fixed.

In Gauss-Newton method, we simply ignore the term involving the second derivatives in Eq. 4.3 and replace the Hessian matrix with

$$H = C_X^{-1} + G^T C_D^{-1} G. \quad (4.7)$$

At each iteration l , we solve the following linear system of equations:

$$(C_X^{-1} + G_l^T C_D^{-1} G_l) \delta X^{l+1} = -C_X^{-1} (X^l - X^P) - G_l^T C_D^{-1} (d_{calc}^l - d_{obs}), \quad (4.8)$$

where the term in the parenthesis on left hand side is the Gauss-Newton Hessian matrix and the right hand side is the negative gradient of the objective function of Eq. 4.2.

After solving the linear system of equations for δX^{l+1} , we update the parameter vector X as

$$X^{l+1} = X^l + \alpha^{l+1} \delta X^{l+1}, \quad (4.9)$$

where α is the step size. We set the step size to 1.0 and if the objective function does not decrease, we cut it by half and re-evaluate the objective function. We stop cutting the step size once a smaller objective function is reached.

The convergence criteria for the algorithm are:

$$\frac{\|X^{l+1} - X^l\|}{\|X^l\| + 10^{-5}} = \varepsilon_x, \quad (4.10)$$

$$\frac{\|O(X^{l+1}) - O(X^l)\|}{\|O(X^l)\| + 10^{-5}} = \varepsilon_o. \quad (4.11)$$

ε_x and ε_o are prescribed values given in the input file. $\varepsilon_x = 10^{-3}$ and $\varepsilon_o = 10^{-5}$ is used in the example. We also limit the number iteration to a maximum number (5 used in the example).

4.2.2 Sensitivity matrix calculation

One of the key steps in the Gauss-Newton algorithm is to efficiently obtain the sensitivity matrix G , which is either derived analytically or calculated using the finite-difference method. With the numerical solution to the Eikonal equation, it is not easy to obtain an analytical form of the sensitivity. Therefore, we have to rely on the finite-difference method to calculate the sensitivity. With finite-difference method, we would have to perturb one parameter at a time to obtain the gradient. Fig. 4.1 shows a simple 2D grid in the x-y direction, in which the source location is at (i, j) and the receiver location is at (m, n) . To calculate the derivative of the first arrival time t from source to receiver with respect to x and y , we need three forward Eikonal solution runs with the source locations at (i, j) , $(i + 1, j)$ and $(i, j + 1)$. The first arrival times from these three different source locations are $t_{i,j}$, $t_{i+1,j}$ and $t_{i,j+1}$. The derivatives of the first arrival time with respect to x and y are then calculated as

$$\frac{\partial t}{\partial x} = \frac{t_{i+1,j} - t_{i,j}}{h}, \quad (4.12)$$

$$\frac{\partial t}{\partial y} = \frac{t_{i,j+1} - t_{i,j}}{h}. \quad (4.13)$$

In the 3D setting, we calculate the derivative with respect to z in a similar way, so we need 4 forward runs to calculate all the derivatives for one event. This can be time-

consuming when there are many events. Here, we devise a more efficient finite-difference method to calculate all the derivatives for one event location in one forward simulation run [41]. Note that in each forward run when the Eikonal equation is solved, it calculates the first arrival time from source to all other grid points, but only the first arrival time to the receiver location is used. In the new method, we treat the receiver as the source and the source as the receiver. With point R as the source location, we may calculate the first arrival time from $R(m, n)$ to grid point $S(i, j)$ and its two neighbour points $(i + 1, j)$ and $(i, j + 1)$. Due to its reversibility, these first arrival times are $t_{i,j}$, $t_{i+1,j}$ and $t_{i,j+1}$. Applying Eq. 4.12 and Eq. 4.13 yields the derivatives.

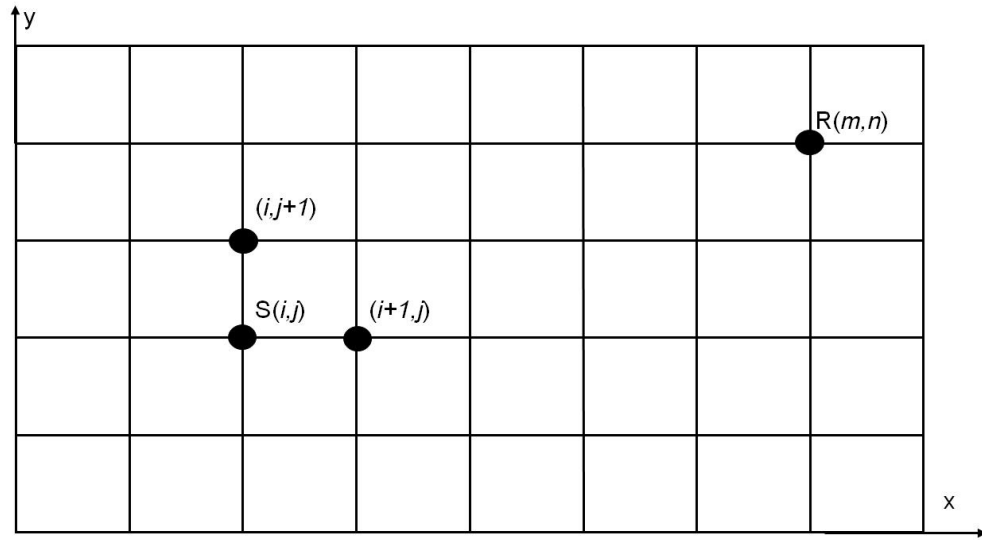


Figure 4.1: Schematic of the first arrival time gradient calculation using Eikonal equation

4.3 Case study

4.3.1 Case description

In this case, we have a vertical well with one hydraulic fracture in the middle of the reservoir and four monitor wells at the corners. The reservoir has a thickness of 160 ft. The velocity structure of the reservoir is shown in Table 4.1. Layer 1 is the cap rock. The fracture dimension is listed in Table 4.2. The perforation location is in layer 6 at (1000, 1000, 4328) as shown in Table 4.3. There are 6 receivers placed in each

monitor well and the receiver locations are given in Table 4.4 to Table 4.7. There are totally 60 microseismic events. The location of the true microseismic events and receiver locations are shown in Fig. 4.2 in 3D, X-Y and X-Z crossplots. As shown in these plots, the blue line is the trajectory of the vertical well, the red dots are receivers and the black circles are microseismic events. The receivers are intentionally set at four corners and at different depths to capture as much event location information as possible. The distance between events and receivers is around 1000 ft in the x and y direction and, 100 to 500 ft in the z direction.

In the following applications, the first arrival times obtained at the receivers are assimilated to estimate the microseismic event location for each event. The parameters are the x , y and z coordinates (event location) and the time t_0 at which the event occurs. The origin time t_0 is included as a parameter because the arrival time measured at receivers is equal to the origin time t_0 plus the time it takes for the P- or S-wave to travel from the event location to the receiver. Both the Gauss-Newton and EnKF methods are tested to invert the microseismic event location. For the Gauss-Newton method, the initial guess of the location parameters is at the perforation location. For the EnKF method, the initial ensemble is generated using the perforation location as the prior mean and 1/3 of total fracture length as the standard deviation. For occurrence time, half of total fracture time is used as the prior mean and 1/3 of total fracture time is used as the standard deviation. For both inversion methods, we test the impact of receiver location on the microseismic event location inversion by adding the receivers from one monitor well at a time. The measurement error for first arrival time data is 1 ms.

Table 4.1: Velocity structure for microseismic event location inversion

Layer No.	Top depth (ft)	P-wave Velocity(ft/s)	S-wave Velocity(ft/s)
1	0	12500	8333
2	4236	11271	7967
3	4256	11702	8100
4	4276	12168	8238
5	4296	11555	8055
6	4316	12009	8192
7	4336	11853	8145
8	4356	11412	8011
9	4376	12009	8192
10	4396	12500	8333

Table 4.2: Fracture dimension

Length (x)	Width(y)	Height(z)	time
600 ft	200 ft	200 ft	600 s

Table 4.3: Perforation location

x	y	z
1000	1000	4328

Table 4.4: Receiver location in monitor well 1

receiver	x	y	z
1	2000	2000	4100
2	2000	2000	4120
3	2000	2000	4140
4	2000	2000	4160
5	2000	2000	4180
6	2000	2000	4200

Table 4.5: Receiver location in monitor well 2

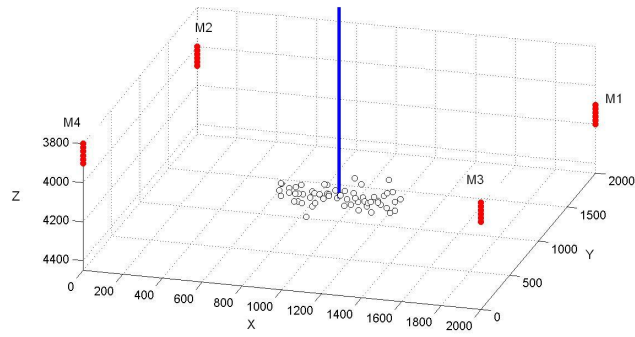
receiver	x	y	z
1	0	2000	4000
2	0	2000	4020
3	0	2000	4040
4	0	2000	4060
5	0	2000	4080
6	0	2000	4100

Table 4.6: Receiver location in monitor well 3

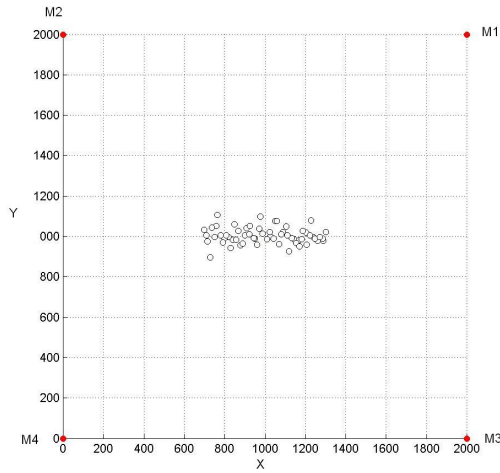
receiver	x	y	z
1	2000	0	3900
2	2000	0	3920
3	2000	0	3940
4	2000	0	3960
5	2000	0	3980
6	2000	0	4000

Table 4.7: Receiver location in monitor well 4

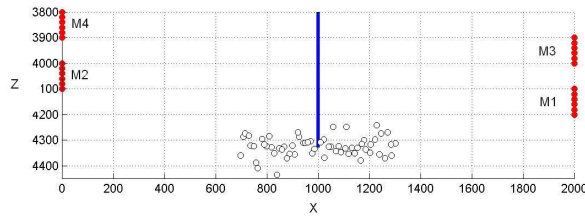
receiver	x	y	z
1	0	0	3800
2	0	0	3820
3	0	0	3840
4	0	0	3860
5	0	0	3880
6	0	0	3900



(a) 3D



(b) X-Y



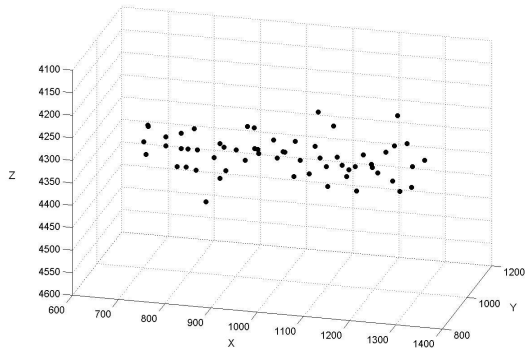
(c) X-Z

Figure 4.2: True microseismic event location in 3D, X-Y and X-Z plots

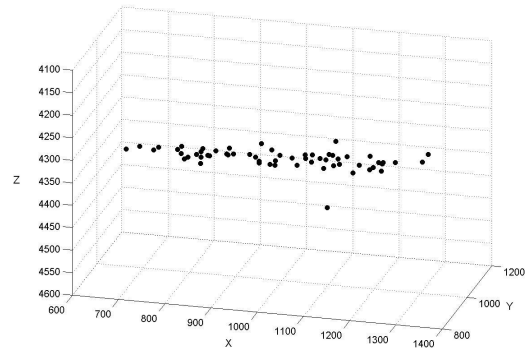
4.3.2 *Microseismic event location obtained with Gauss-Newton method*

This section presents the results of microseismic event location inversion using Gauss-Newton method by assimilating the first arrival times from the receivers placed in all 4 monitor wells. Fig. 4.3 compares the estimated event location on the right column to the true event location on the left column in 3D, X-Y and X-Z crossplots by assimilating the first arrival times from monitor well 1. The black dots represent microseismic events. By visual inspection, the estimated fracture width (y-direction) and height (z-direction) are much smaller than the true, but the estimated length along x-direction is close to the true. The Sensitivity of the first arrival times at monitor well 1 (2000, 2000) to x and y-coordinates are the same at the initial guess (1000,1000) (APPENDIX A). To show the quantitative comparison between the true and estimated event locations, the crossplots of the event location coordinates and origin time between the true and estimated are presented in Fig. 4.4. As shown in Fig. 4.4, the event origin time is the parameter that is estimated most accurately because the arrival times are more sensitive to the origin time than to the event location (APPENDIX A), in fact the estimated arrival time is almost exact; the x-coordinate of the event location is also well resolved by the data; but the y- and z-coordinates of the event are close to the initial guesses as the arrival time is relatively insensitive to these two parameters of the event location. By assimilating the first arrival times at two monitor wells (monitor wells 1 and 2), good width estimates are obtained and the height is slightly underestimated as shown in Fig. 4.5. As shown in Fig. 4.6, assimilating first arrival times from two monitor wells improves the estimates on x and y-coordinates of the microseismic event location while the estimated z-coordinates show almost no correlation with the true. By adding the 3rd monitor well, the estimated fracture length, width and height are further improved as shown in Fig. 4.7. Fig. 4.8 shows that the estimated y-coordinates are very close to the true and the estimated z-coordinates start showing some correlation with the true. There is not much difference in the x-, y-coordinates and origin time estimates by adding the 4th monitor well compared with the case using 3 monitor wells as shown in Fig. 4.9 and Fig. 4.10. However, the estimated z-coordinates are further improved by adding the

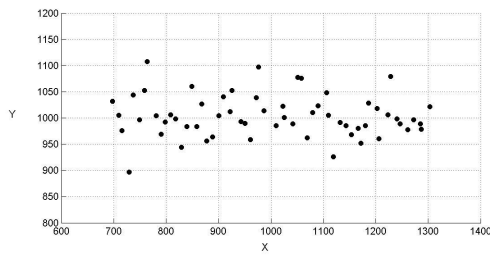
4th monitor well. As receivers are closer to the events in the vertical direction than in the horizontal direction, the arrival time is least sensitive to the z -coordinate in the event location, thus z -coordinate estimation is least accurate (Appendix A).



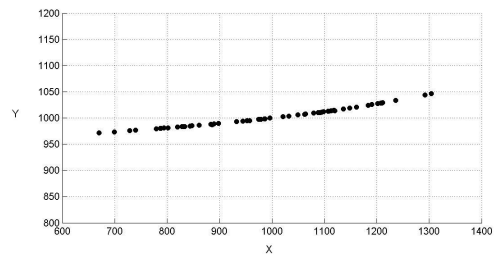
(a) True 3D



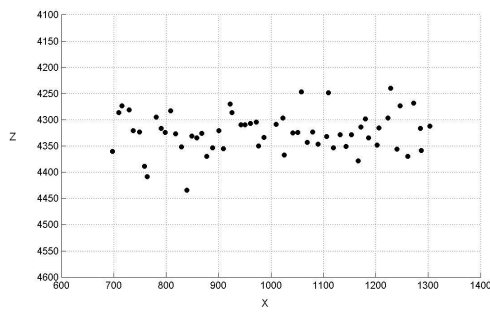
(b) 3D



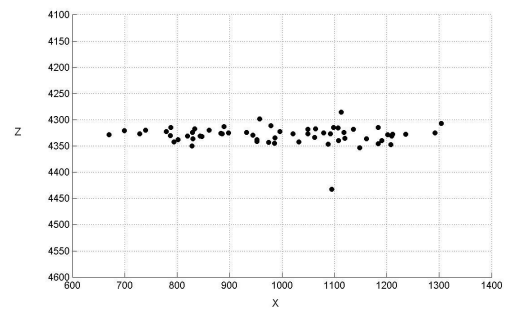
(c) True X-Y



(d) X-Y

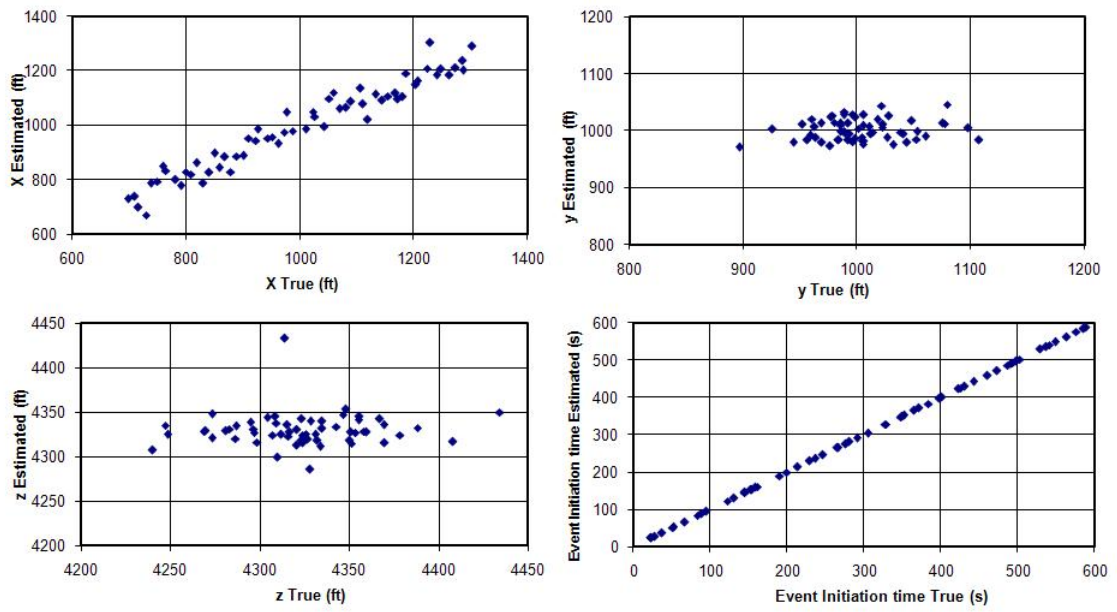


(e) True X-Z



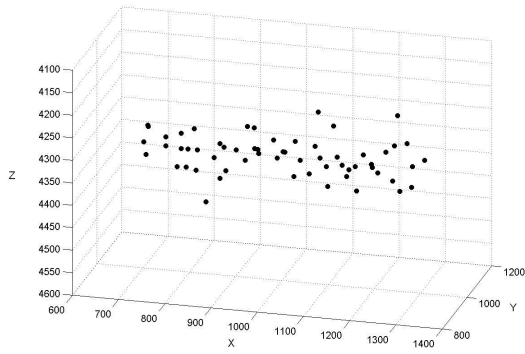
(f) X-Z

Figure 4.3: True vs estimated microseismic location after assimilating first arrival times from monitor well 1 (Gauss-Newton)

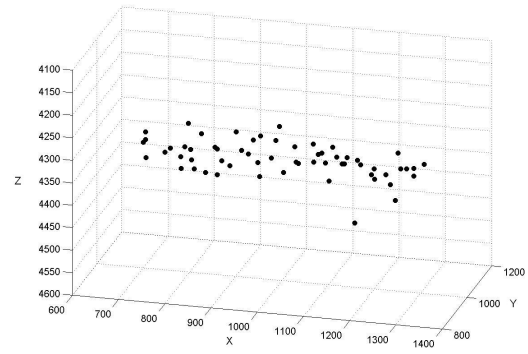


(a)

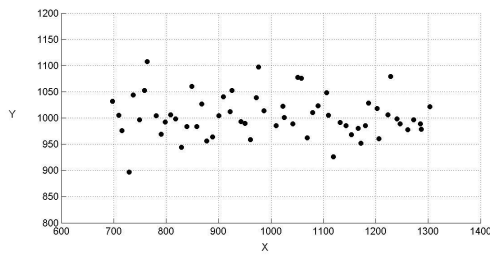
Figure 4.4: The cross-plot of the microseismic event location (x , y , z) and event occurrence time between the true and the estimated after assimilating first arrival times at monitor well 1 (Gauss-Newton)



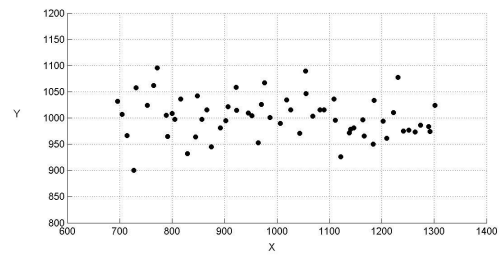
(a) True 3D



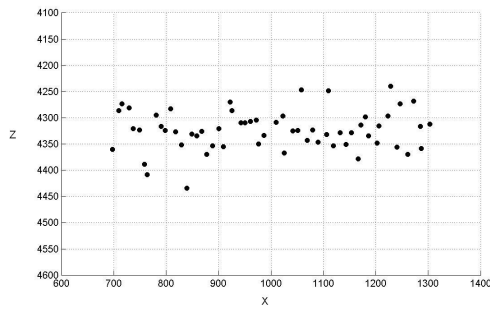
(b) 3D



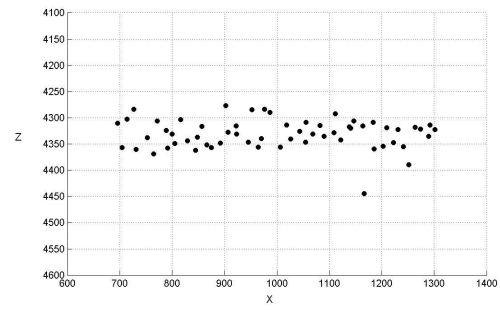
(c) True X-Y



(d) X-Y

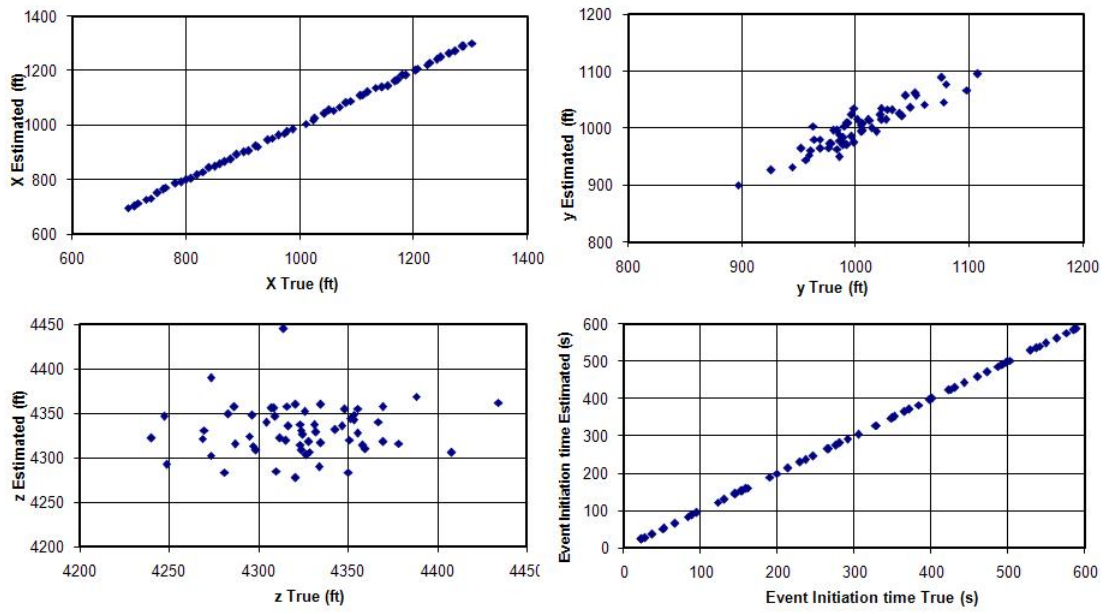


(e) True X-Z



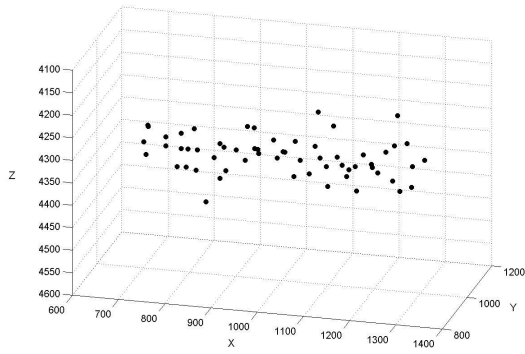
(f) X-Z

Figure 4.5: True vs estimated microseismic location after assimilating first arrival times from monitor wells 1 and 2 (Gauss-Newton)

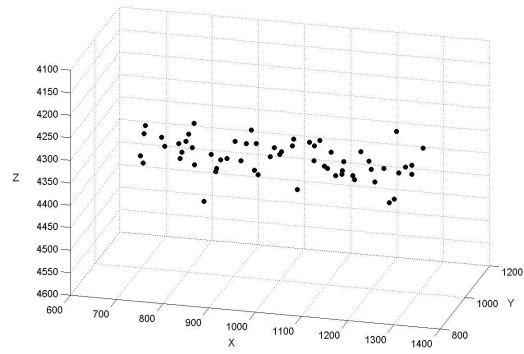


(a)

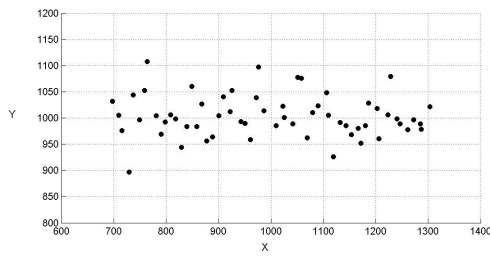
Figure 4.6: The cross-plot of the microseismic event location (x , y , z) and event occurrence time between the true and the estimated after assimilating first arrival times from monitor wells 1 and 2 (Gauss-Newton)



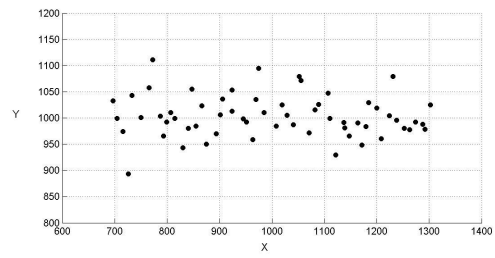
(a) True 3D



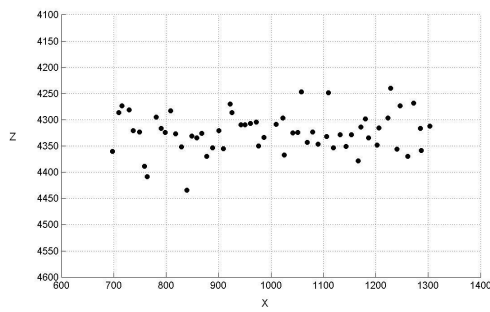
(b) 3D



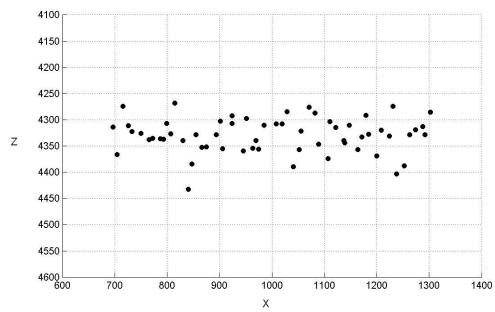
(c) True X-Y



(d) X-Y

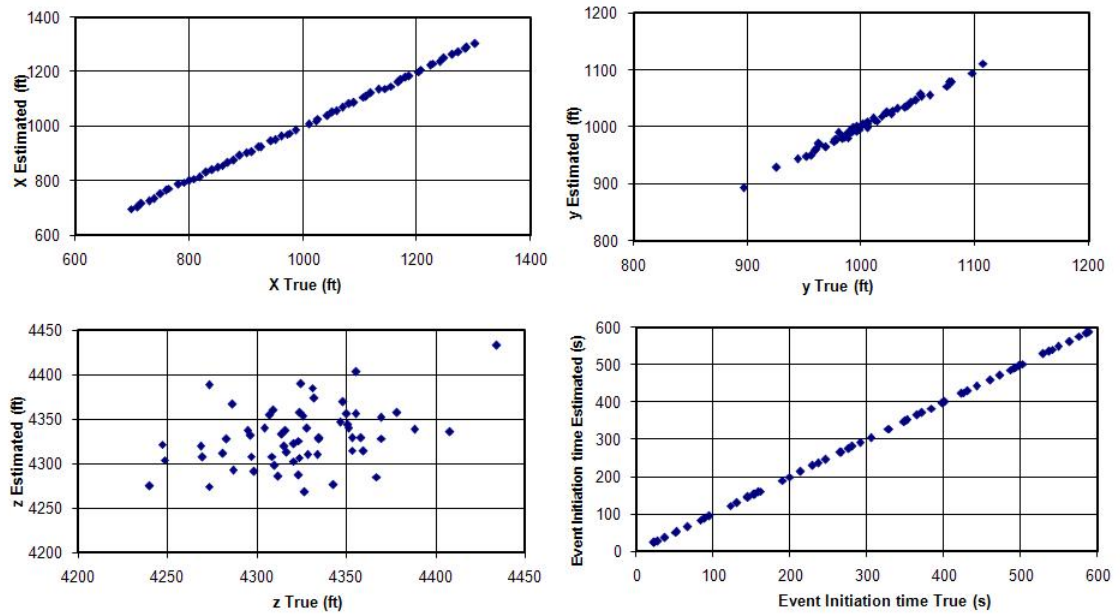


(e) True X-Z



(f) X-Z

Figure 4.7: True vs estimated microseismic location after assimilating first arrival times from monitor wells 1 to 3 (Gauss-Newton)



(a)

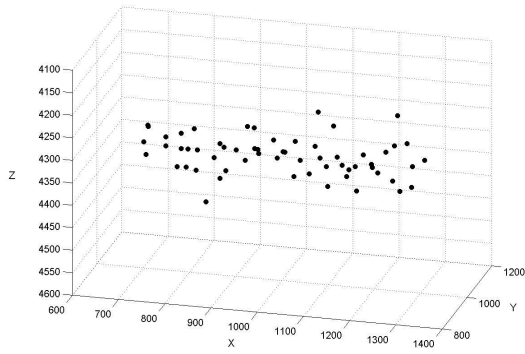
Figure 4.8: The cross-plot of the microseismic event location (x, y, z) and event occurrence time between the true and the estimated after assimilating first arrival times from monitor wells 1 to 3 (Gauss-Newton)

4.3.3 Microseismic event location obtained with EnKF method

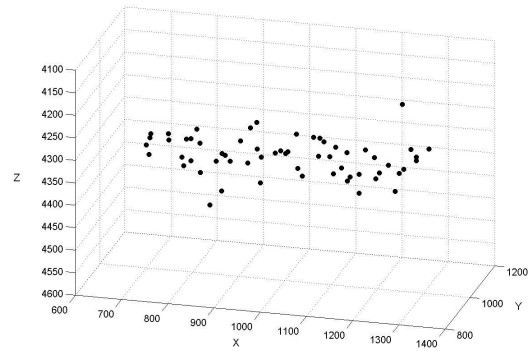
This section presents the event location results obtained using EnKF by adding one monitor well at a time. The number of ensemble members is 30. The mean of the updated ensemble is used to make analysis plots. By assimilating the first arrival times from monitor well 1 as shown in Fig. 4.11, the estimated fracture width and height obtained using EnKF look more reasonable than that from Gauss-Newton method shown in Fig. 4.3 by visual inspection. This is because we add noise to the initial ensemble. However the estimated event location parameters are not better than those obtained from the Gauss-Newton method in the crossplot between the estimated and true as shown in Fig. 4.12. We obtained results using EnKF very close to those obtained from Gauss-Newton when we use the first arrival times obtained from two, three or four monitor wells as shown from Fig. 4.13 to Fig. 4.18.

In summary, 1) The microseismic event occurring time is estimated with good accuracy; 2) The coordinate of event location along the fracture direction (x-coordinate

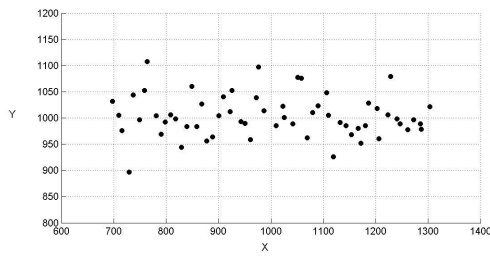
in this example) can be estimated with good accuracy even with first arrival times from one monitor well. However more first arrival times from other monitor wells further improve the estimate; 3) The coordinates perpendicular to the fracture direction (y-coordinate in this example) require first arrival times in wells from different directions to yield good estimates. 4) It is difficult to obtain a accurate estimate of the z-coordinate of the event location due to smaller sensitivity compared to other coordinates. This is mainly due to the fact that the distance between receiver and source in the z direction is much smaller than in the x and y directions when geophones are placed in the monitor wells.



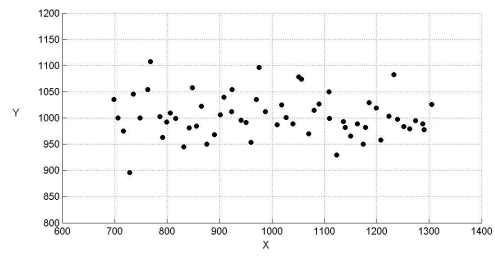
(a) True 3D



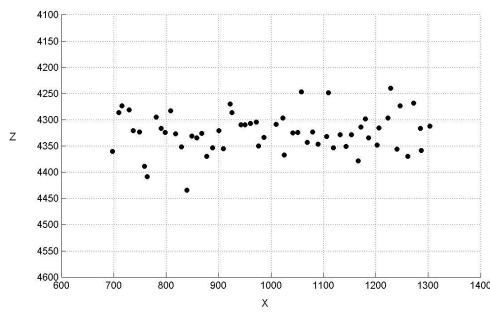
(b) 3D



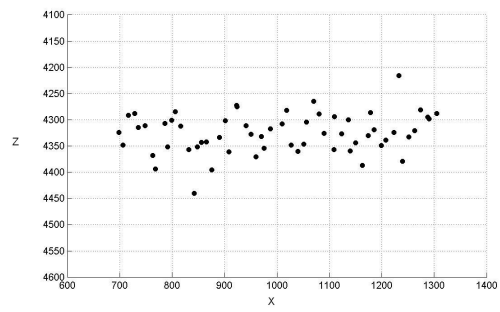
(c) True X-Y



(d) X-Y

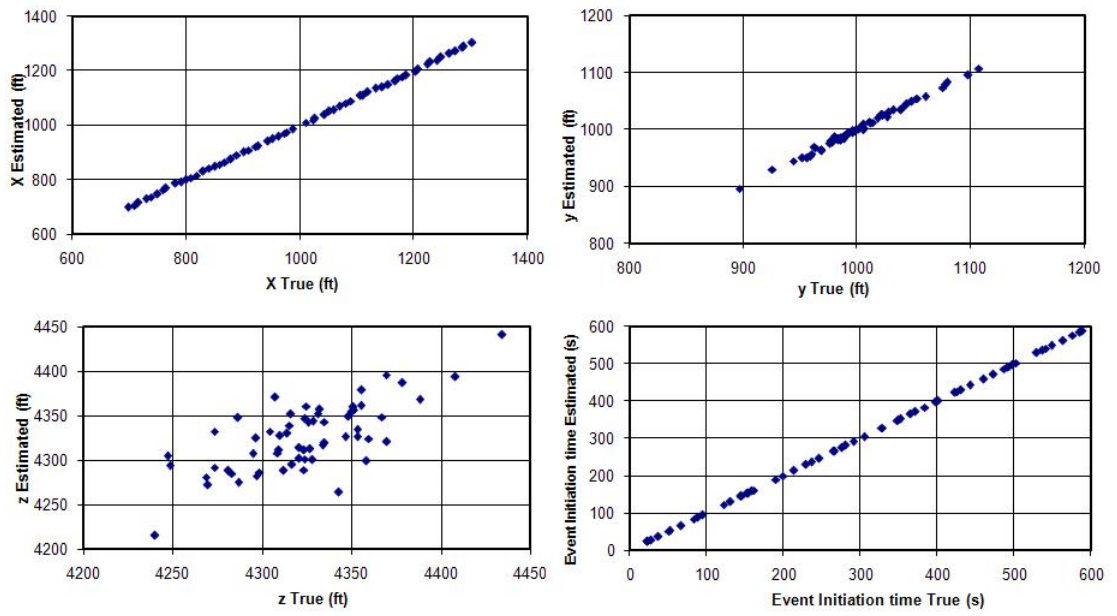


(e) True X-Z



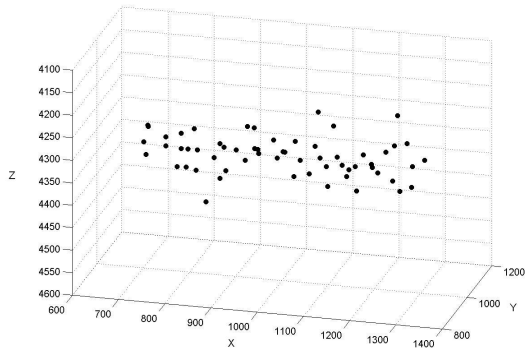
(f) X-Z

Figure 4.9: True vs estimated microseismic location after assimilating first arrival times from all 4 monitor wells (Gauss-Newton)

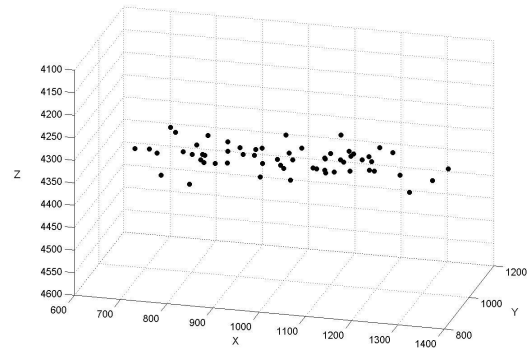


(a)

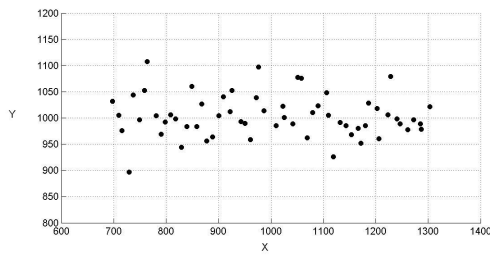
Figure 4.10: The cross-plot of the microseismic event location (x , y , z) and event occurrence time between the true and the estimated after assimilating first arrival times from all 4 monitor wells (Gauss-Newton)



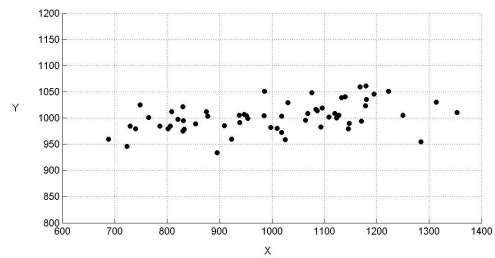
(a) True 3D



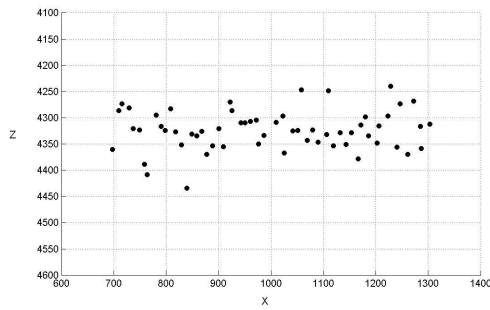
(b) 3D



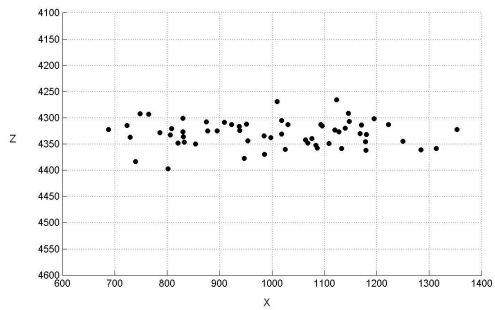
(c) True X-Y



(d) X-Y

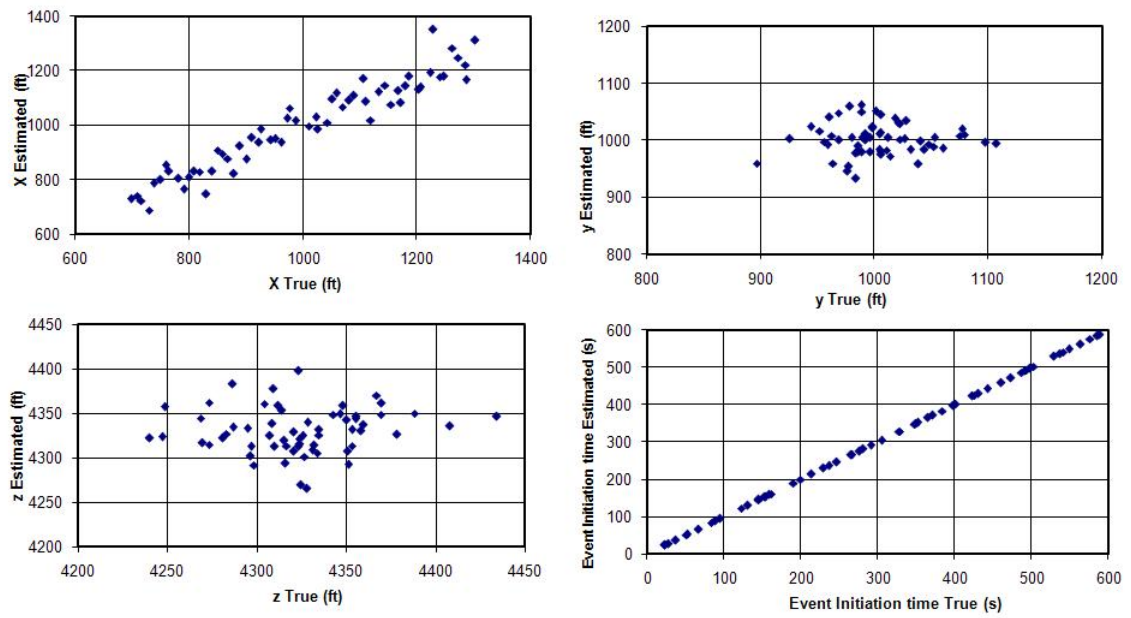


(e) True X-Z



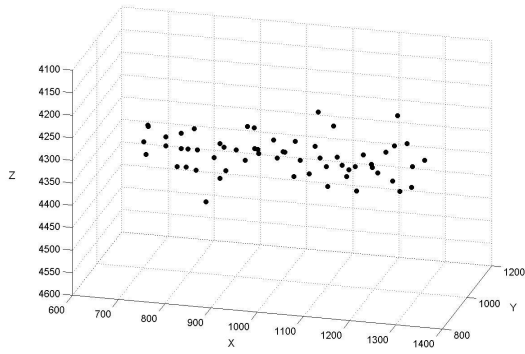
(f) X-Z

Figure 4.11: True vs estimated microseismic location after assimilating first arrival times from monitor well 1 (EnKF)

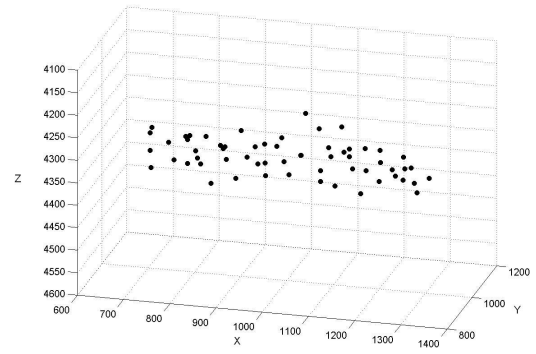


(a)

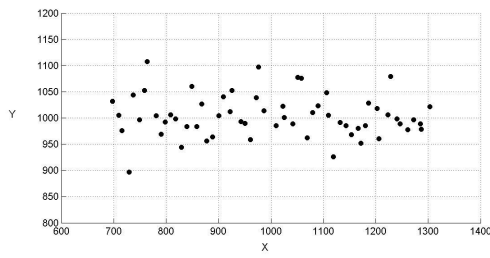
Figure 4.12: The cross-plot of the microseismic event location (x , y , z) and event occurrence time between the true and the estimated assimilating first arrival times from monitor well 1 (EnKF)



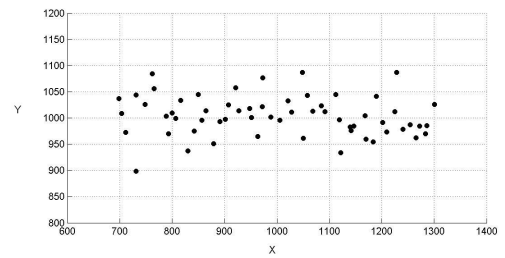
(a) True 3D



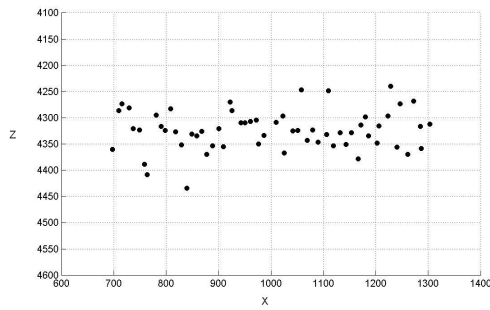
(b) 3D



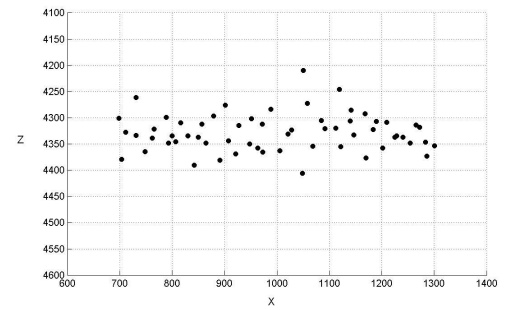
(c) True X-Y



(d) X-Y

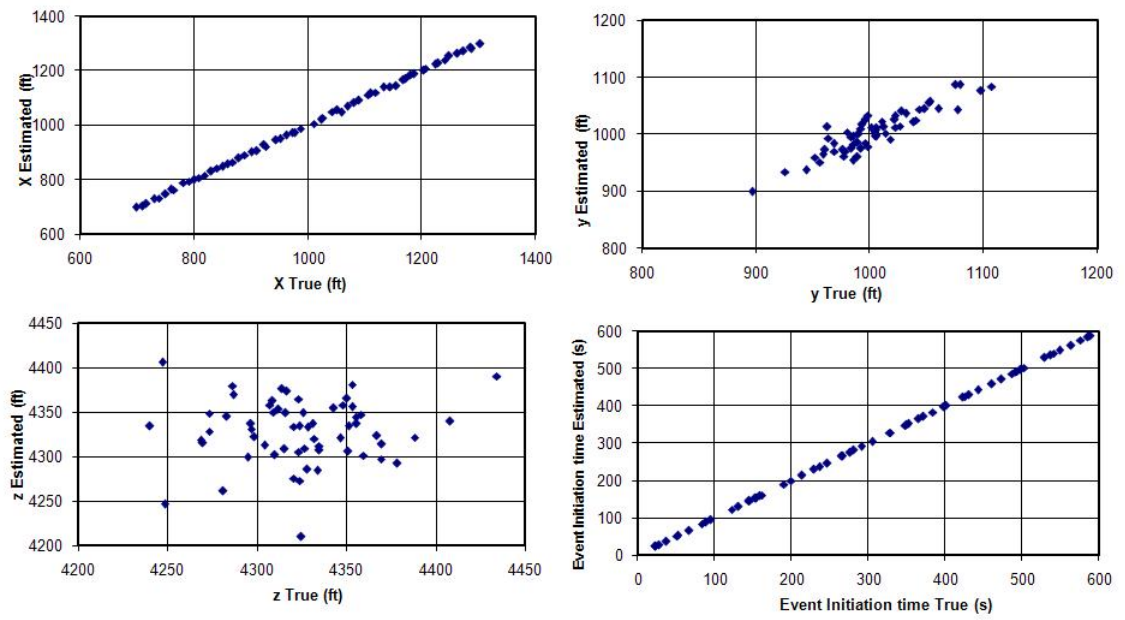


(e) True X-Z



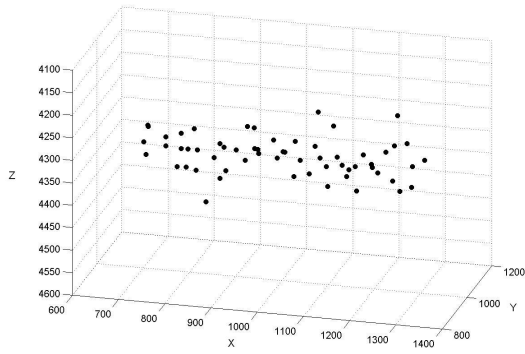
(f) X-Z

Figure 4.13: True vs estimated microseismic location after assimilating first arrival times from monitor wells 1 and 2 (EnKF)

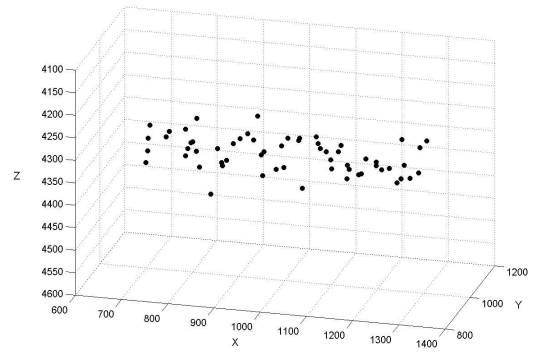


(a)

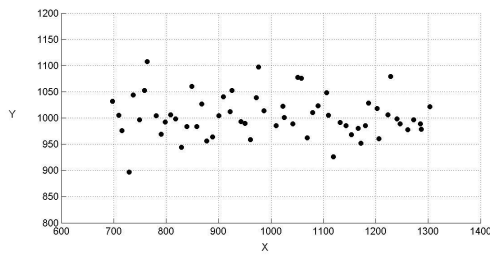
Figure 4.14: The cross-plot of the microseismic event location (x , y , z) and event occurrence time between the true and the estimated after assimilating first arrival times from monitor wells 1 and 2 (EnKF)



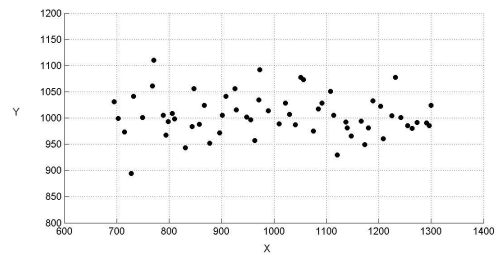
(a) True 3D



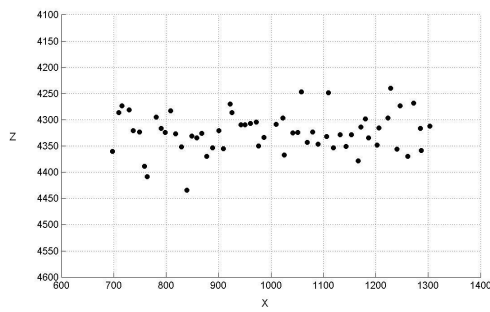
(b) 3D



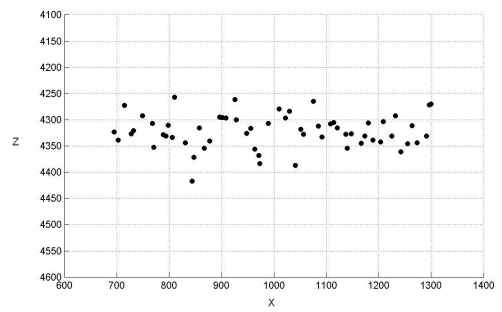
(c) True X-Y



(d) X-Y

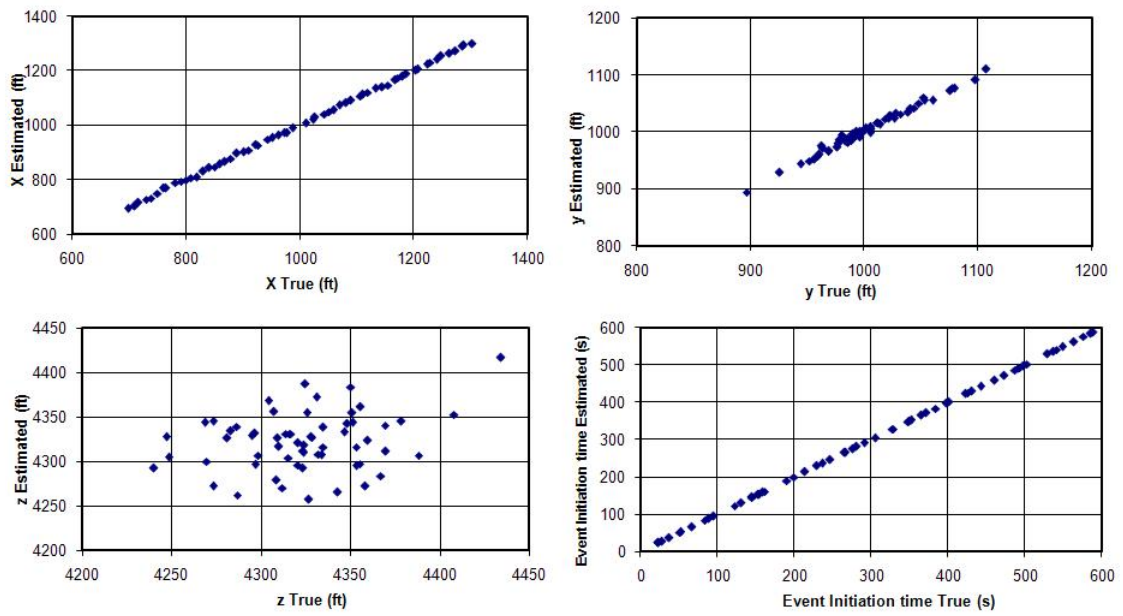


(e) True X-Z



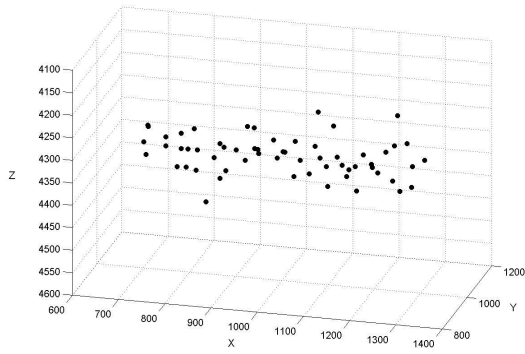
(f) X-Z

Figure 4.15: True vs estimated microseismic location with 3 monitor wells after assimilating first arrival times from monitor wells 1 to 3 (EnKF)

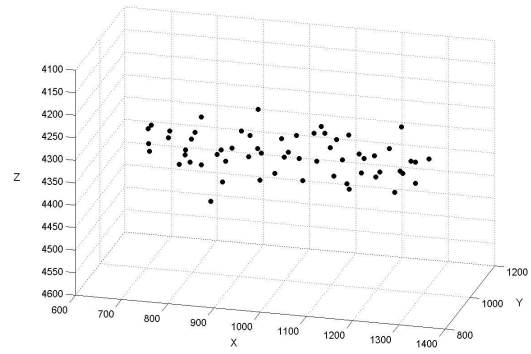


(a)

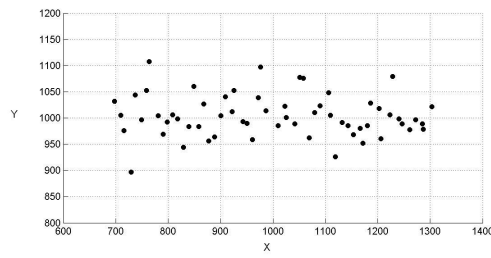
Figure 4.16: The cross-plot of the microseismic event location (x , y , z) and event occurrence time between the true and the estimated after assimilating first arrival times from monitor wells 1 to 3 (EnKF)



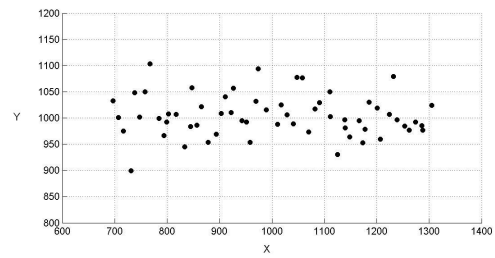
(a) True 3D



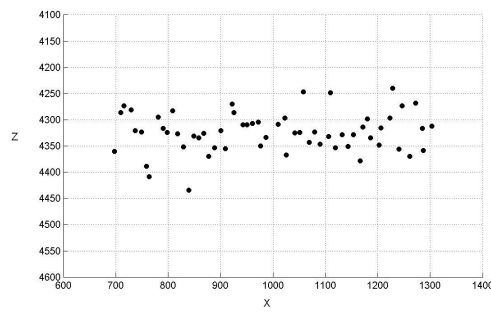
(b) 3D



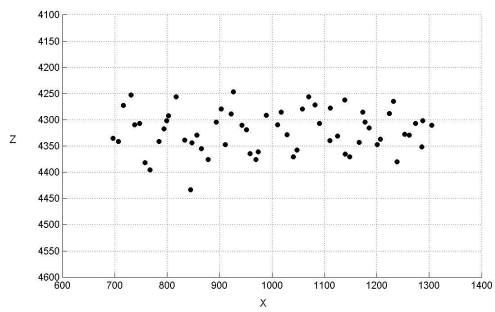
(c) True X-Y



(d) X-Y

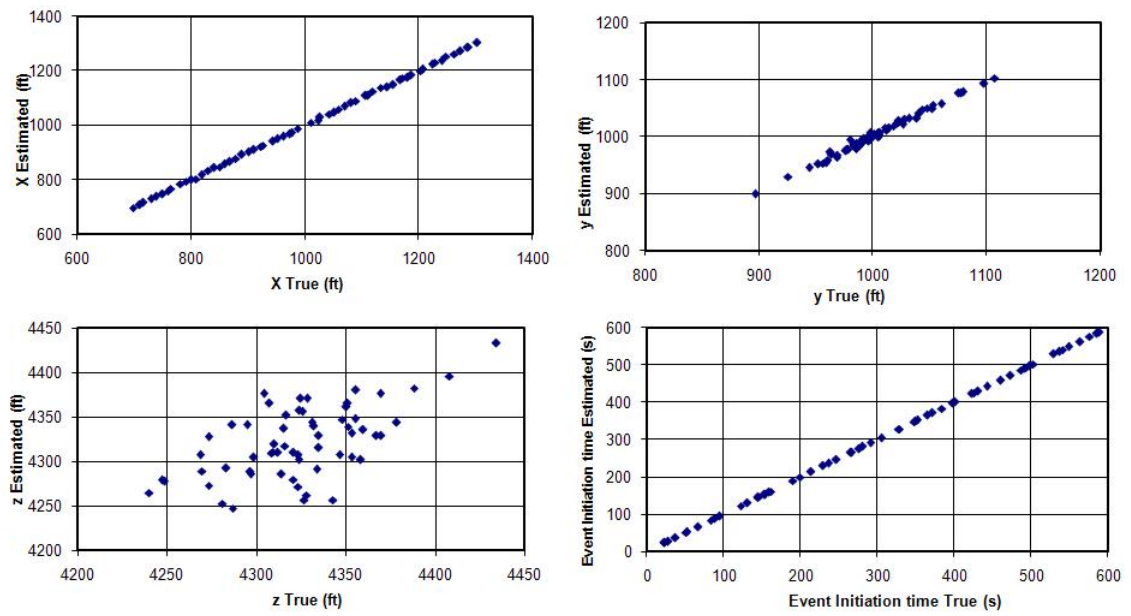


(e) True X-Z



(f) X-Z

Figure 4.17: True vs estimated microseismic location estimation after assimilating first arrival times from all 4 monitor wells (EnKF)



(a)

Figure 4.18: The cross-plot of the microseismic event location (x , y , z) and event occurrence time between the true and the estimated after assimilating first arrival times from all 4 monitor wells (EnKF)

4.4 Event location inversion with uncertain velocity structure

4.4.1 Case description

In this case, we have a vertical well with one hydraulic fracture in the bottom reservoir layer and three monitor wells in north, southwest and southeast directions. The reservoir has 10 layers. The true and initial ensemble of porosity is shown in Table 4.8. The true velocity structures of the P- and S-waves are shown in Fig. 4.19. The velocity and top depth are listed in Table 4.9. Note that the layers are numbered from bottom to top. The cap rock P- and S-wave velocities are 9842 ft/s and 6562 ft/s, respectively. The fracture dimension is the same as for the case considered in the previous section; see Table 4.2. The perforation location is (1000, 1000, 8128) which is at the bottom layer. There are 6 receivers placed in each monitor well and the receiver locations are given in Table 4.10 to Table 4.12. There are total 60 microseismic events. The location of true microseismic events and receivers location are shown in Fig. 4.20 in 3D, X-Y and X-Z crossplots. The measurement error for first arrival time data is 1 ms.

Table 4.8: True and prior of porosity and permeability

	True		Prior Mean		Prior STD		Correlation
	ϕ	$\ln k$	ϕ	$\ln k$	ϕ	$\ln k$	
Layer 1	0.1718	3.15	0.15	3	0.025	0.5	0.8
Layer 2	0.1787	4.29	0.20	5	0.025	0.5	0.8
Layer 3	0.1534	3.46	0.15	3	0.025	0.5	0.8
Layer 4	0.2672	5.46	0.25	5.5	0.025	0.5	0.8
Layer 5	0.2284	5.25	0.25	5.5	0.025	0.5	0.8
Layer 6	0.1527	3.31	0.15	3	0.025	0.5	0.8
Layer 7	0.2207	5.61	0.20	5	0.025	0.5	0.8
Layer 8	0.2398	5.22	0.25	5.5	0.025	0.5	0.8
Layer 9	0.2392	5.90	0.20	5	0.025	0.5	0.8
Layer 10	0.2667	6.06	0.25	5.5	0.025	0.5	0.8

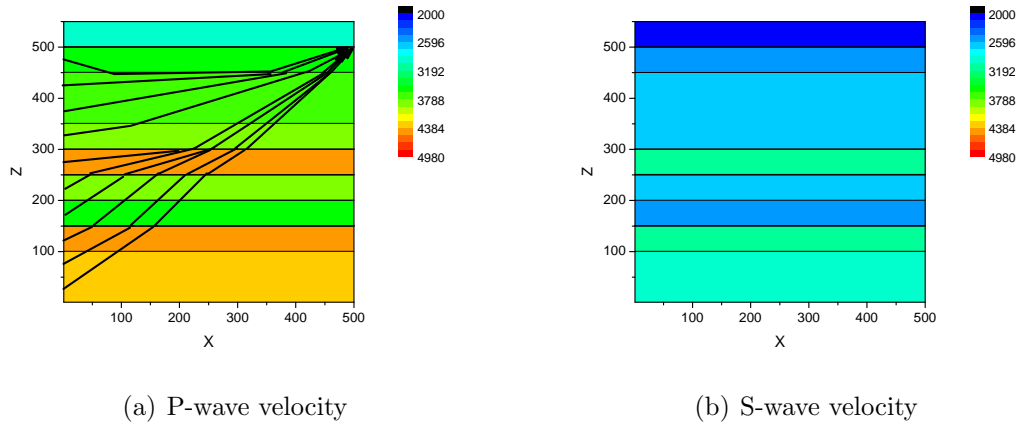


Figure 4.19: Velocity structure

Table 4.9: The true velocity structure

Layer No.	Top depth (ft)	P-wave Velocity(ft/s)	S-wave Velocity(ft/s)
10	7200	11683	8216
9	7300	12391	8660
8	7400	12375	8650
7	7500	12884	8969
6	7600	14814	10186
5	7700	12677	8840
4	7800	11670	8209
3	7900	14793	10173
2	8000	14054	9706
1	8100	14253	9832

Table 4.10: Receiver location in monitor well 1

receiver	x	y	z
1	1000	2000	7100
2	1000	2000	7120
3	1000	2000	7140
4	1000	2000	7160
5	1000	2000	7180
6	1000	2000	7200

Table 4.11: Receiver location in monitor well 2

receiver	x	y	z
1	0	0	7100
2	0	0	7120
3	0	0	7140
4	0	0	7160
5	0	0	7180
6	0	0	7200

Table 4.12: Receiver location in monitor well 3

receiver	x	y	z
1	2000	0	7000
2	2000	0	7020
3	2000	0	7040
4	2000	0	7060
5	2000	0	7080
6	2000	0	7100

In the following sections, we test the impact of uncertainty in velocity structure on the microseismic event location inversion using the EnKF method by considering 4 scenarios:

1. The correct velocity structure is used in inversion.
2. The incorrect velocity structure is used in inversion.
3. An ensemble of velocity structures is used in inversion in order to capture uncertainty in the velocity field.
4. The ensemble of velocity structures that are updated by assimilating the first arrival times from perforation shots is used in inversion.

In all examples, 100 ensemble members are used. The cap rock velocity is known and fixed in all scenarios. The mean absolute error between the true and estimated parameters, i.e., x, y and z coordinates for each event is calculated using,

$$E = \frac{1}{N_{event}} \sum_{i=1}^{N_{event}} |m_{i,est} - m_{i,true}|. \quad (4.14)$$

4.4.2 *Microseismic event location estimated using correct, incorrect and an ensemble of velocity structures*

The initial ensemble of the velocity profile is shown in Fig. 4.21 with each boxchart representing the P-wave velocity of each layer. The black squares are the true velocity profile used to generate the observed first arrival times. The red dots are the layer velocities used in scenario 2 and denoted as “wrong” velocity profile.

The cross-plot of the microseismic event location (x, y, z) and the event occurrence time between the true and the estimated using the true velocity structure, using incorrect velocity structure and using an initial ensemble of velocity structure are shown in Fig. 4.22, Fig. 4.23 and Fig. 4.24, respectively. We obtained good estimates on x-, y-coordinates and occurrence time in these cases. Estimation of the z-coordinate is close to true but there is some noise. Fig. 4.25 compares the z-coordinate estimation in

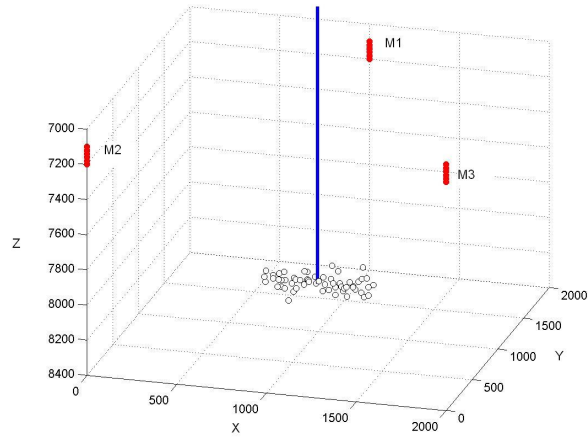
these 3 scenarios by adding a blue line of unit slope for reference. The closer the dots are to the blue line, the more accurate the estimates are. As shown in Fig. 4.25, the estimated z-coordinate is biased from true when using the incorrect velocity structure with a large mean absolute error ($E = 32.3$), and is improved by using an ensemble of velocity structures which considers the uncertainty in velocity. The mean absolute error is reduced to 21.0. Among these three scenarios, estimates obtained using the correct velocity structure is the best of all with the smallest mean absolute error of 15.2.

4.4.3 Microseismic event location estimated using velocity structure updated from assimilating perforation shot microseismic data

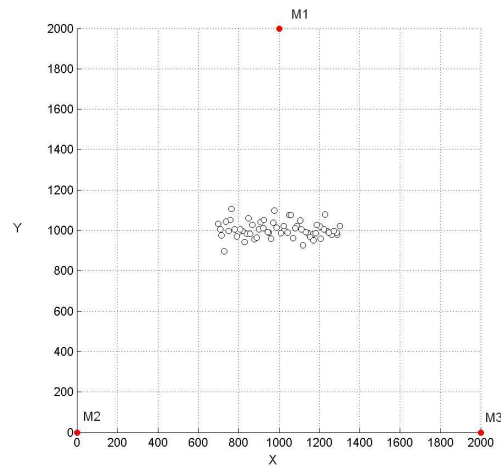
The layer porosities are updated by first assimilating the first arrival times from perforation shots in each layer, and then assimilating pressure transient data. The corresponding velocity structure is then calculated from the updated layer porosity values and shown in Fig. 4.27. As uncertainty of porosity is reduced in most layers (Fig. 4.26), the uncertainty of velocity is significantly reduced correspondingly as shown in Fig. 4.27.

The cross-plot of the microseismic event location (x, y, z) and event occurrence time between the true and the estimated using the updated velocity structure are shown in the various plots of Fig. 4.28. We obtained very close results to those obtained in the previous scenarios. As shown in Fig. 4.29, the z-coordinate estimation using the ensemble of updated velocity updated is very close to the one obtained using the correct velocity.

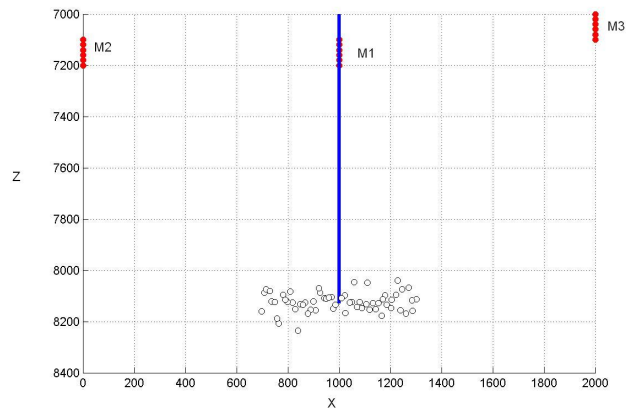
In summary, in event location inversion, using the incorrect velocity may result in biased estimates. Considering the uncertainty in velocity by using an ensemble of velocity structures improves the estimates. Calibrating the velocity by assimilating the first arrival times from perforation shots further improves the estimates. The EnKF method is advantageous for capturing velocity uncertainty in an efficient way.



(a) 3D



(b) X-Y



(c) X-Z

Figure 4.20: True microseismic event location in 3D, X-Y and X-Z plots

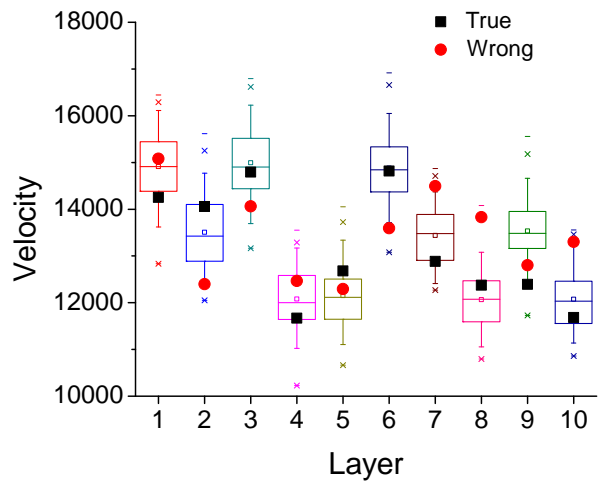
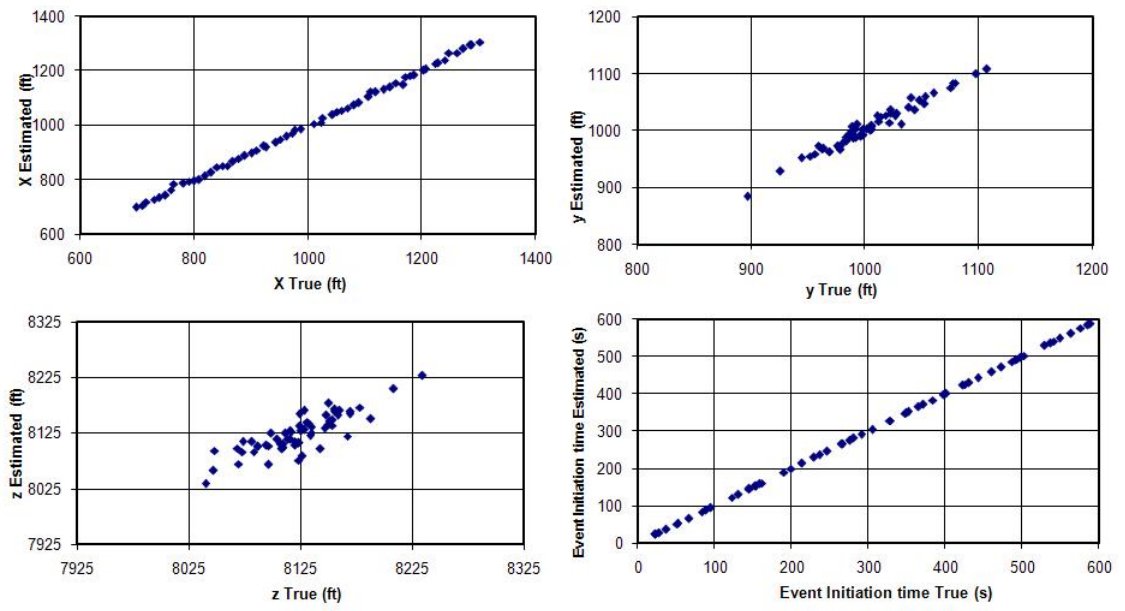
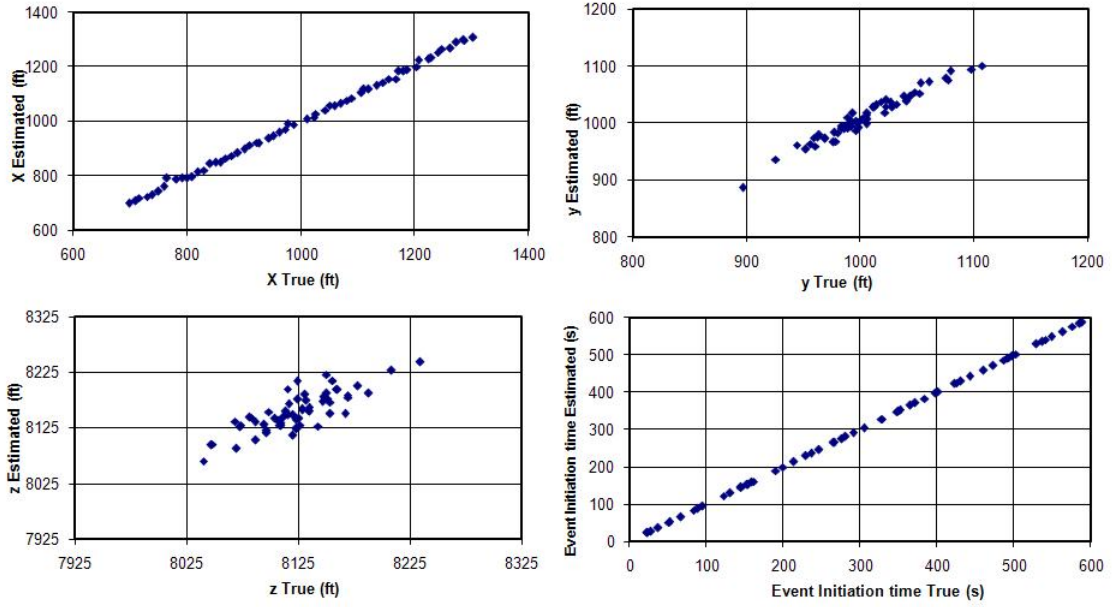


Figure 4.21: Initial ensemble of velocity structure model for scenario 3



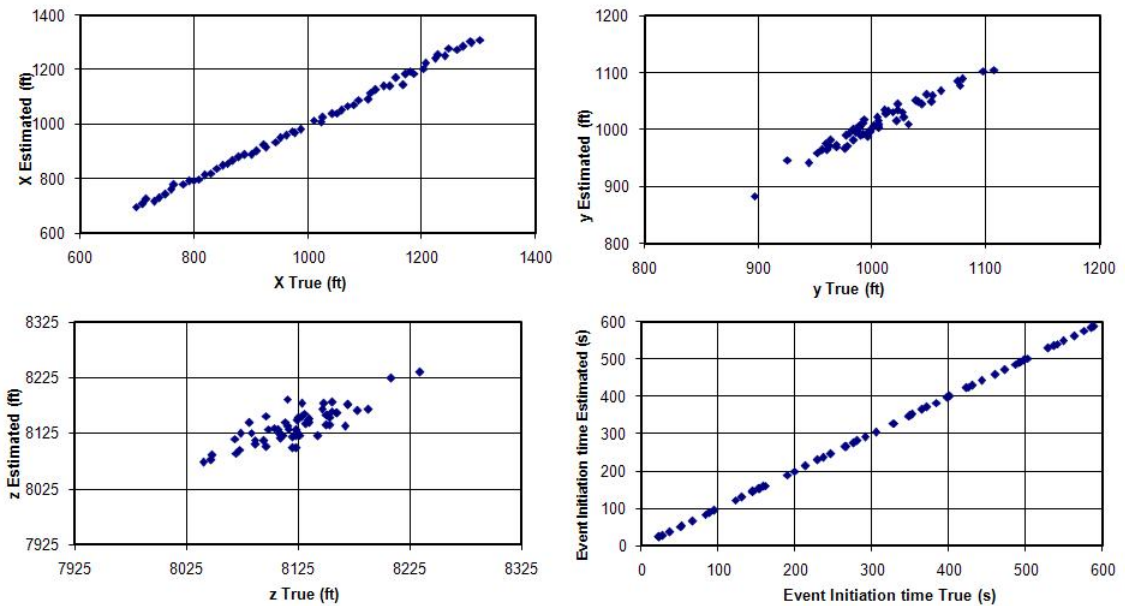
(a)

Figure 4.22: The cross-plot of the microseismic event location (x, y, z) and event occurrence time between the true and the estimated using correct velocity structure



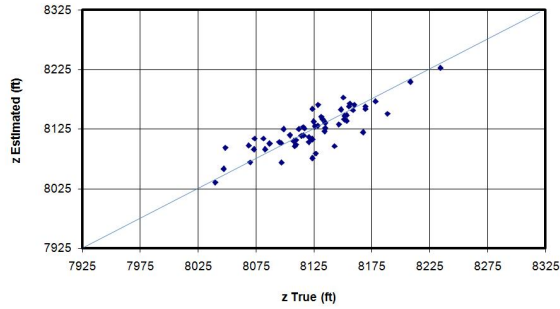
(a)

Figure 4.23: The cross-plot of the microseismic event location (x, y, z) and event occurrence time between the true and the estimated using incorrect velocity structure

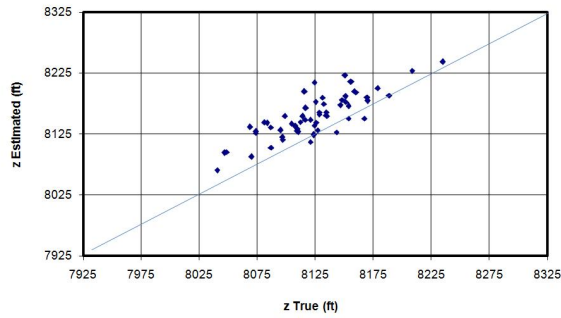


(a)

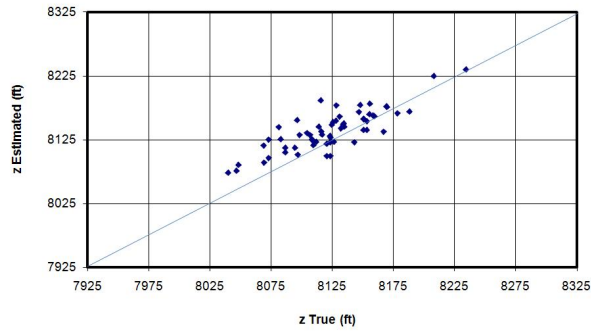
Figure 4.24: The cross-plot of the microseismic event location (x, y, z) and event occurrence time between the true and the estimated using an ensemble of velocity structure



(a) Correct ($E=15.2$)



(b) Incorrect ($E=32.3$)



(c) Ensemble ($E=21.0$)

Figure 4.25: The cross-plot of z -coordinate between the true and the estimated using correct, incorrect and an ensemble of velocity

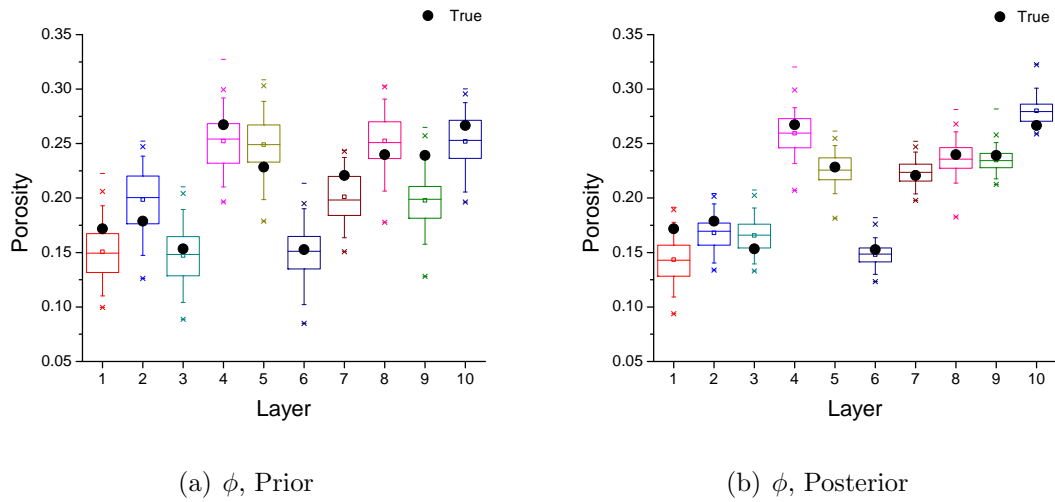


Figure 4.26: Prior and posterior porosity and $\ln k$ assimilating microseismic data

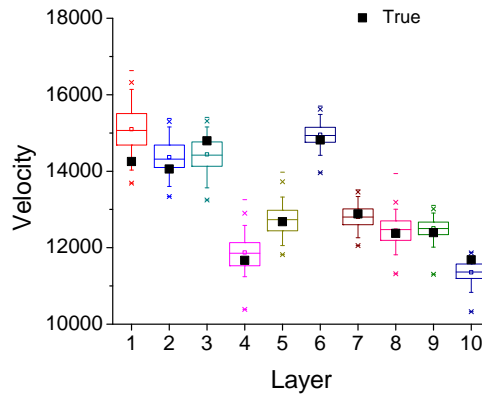
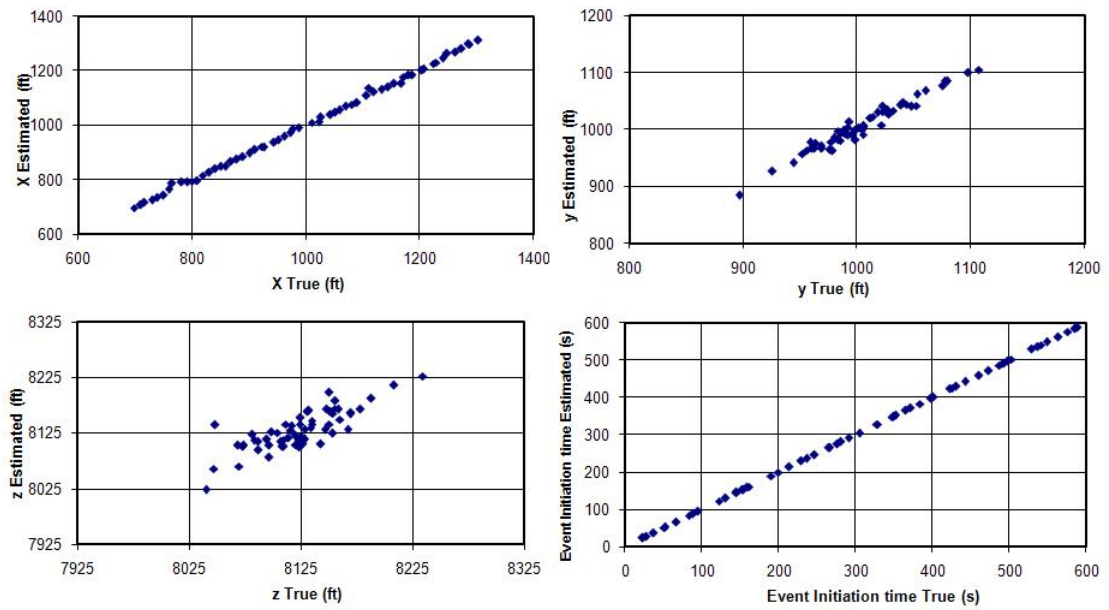
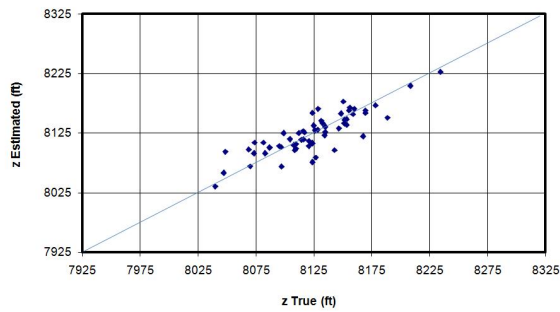


Figure 4.27: Ensemble of velocity structures updated from assimilating first arrival times of the perforation shots

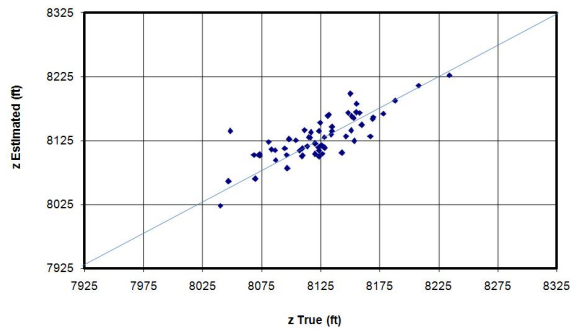


(a)

Figure 4.28: The cross-plot of the microseismic event location (x , y , z) and event occurrence time between the true and the estimated using the updated velocity structure after assimilating first arrival time from perforation shots



(a) correct ($E=15.2$)



(b) updated velocity structure ($E=17.8$)

Figure 4.29: The cross-plot of z -coordinate between the true and the estimated using correct and updated velocity structure

CHAPTER 5

CONCLUSIONS

The following conclusions can be made from this study:

1. EnKF can be applied to assimilate pressure transient data in a heterogeneous reservoir environment. Reasonable data matches are obtained. The estimates of property fields (log-permeability and porosity) obtained after assimilating the pressure transient data (drawdown and buildup) at a fully-penetrating vertical well using EnKF capture the true geological structure and spatial geological features. In the case that the prior means of the rock property fields are erroneous, we can apply a partially doubly stochastic model in the EnKF methodology to obtain significantly better estimates of the rock property fields.
2. For a single layer reservoir, the skin factor can be obtained reasonably well by assimilating the pressure data. However, for a two-layer reservoir, the pressure data alone can not resolve the layer skin factors. Assimilating both layer rates and pressure data gives good estimates of the individual layer skin factors as well as geologically reasonable estimates of the rock property fields.
3. The first arrival times of the P- and S-wave in the microseismic data reflect the average velocity along its raypath. The velocity is related to porosity in a functional form, so the microseismic data (arrival times) can resolve the average porosity in the seismic wave path, but these data are most sensitive to the low porosity (high velocity) layers. The pressure transient data can resolve the thickness-weighted average permeability in a layered reservoir. When log-permeability is used as the model parameters, the pressure is most sensitive to the log-permeability of the high permeability layer when the layer thickness is the same. In case that the

porosity and log-permeability are strongly correlated, the microseismic data and the pressure transient data are complementary in resolving the layer properties of the reservoir. In the two-layer homogeneous example, assimilating microseismic and pressure transient data using EnKF resulted in good data match and large uncertainty reduction in the estimated layer porosities and log-permeabilities. The estimated property values are comparable to those estimated by assimilating the layer rate and pressure data. Assimilating layer rate and pressure data gives accurate estimates of the layer log-permeabilities but less accurate estimates of the layer porosities compared to the case where we assimilate both microseismic and pressure data. In the two-layer heterogeneous example, assimilating microseismic and pressure data yields layer properties that can capture the main geological structure (high permeability channels), while assimilating layer rate and pressure data yields less accurate geological features, as layer rate data reflect rock properties in the region close to the wellbore. On the other hand, microseismic data are sensitive to rock properties in a much larger region between the source in the active well and the receivers in the monitor wells and hence yields more accurate rock property estimates and much smaller mean square error between the true and estimated rock property fields. Assimilating microseismic and pressure data using EnKF with one ensemble may lead to erroneous conclusions, while data assimilation using 10 different initial ensembles yield more accurate characterization of the uncertainty in the rock property fields.

4. Both Gauss-Newton method and EnKF method are applied to microseismic event location inversion. A novel method is devised to calculate the sensitivity of the first arrival times to the event location parameters for the Gauss-Newton method, which uses the reversibility of the wave travel. Accurate estimates can be made to the microseismic event locations using both Gauss-Newton and EnKF methods when the first arrival times are collected from monitor wells of different directions and the velocity structure is known. As the geophones placed in the monitor wells

are usually close the event locations in the z-direction, less accurate estimates of the z-coordinate of the event are obtained, since the gradient of the first arrival times to the event coordinates is proportional to the distance in that direction. Using an incorrect velocity structure yields less accurate event location estimation, while considering the uncertainty using an ensemble of velocity structures can yield more accurate estimated event location parameters. Using an ensemble of velocity structures updated by assimilating the first arrival times from the perforation shots can further improve the accuracy of the estimated event locations and the mean absolute error between the true and estimated event location parameters is similar to that obtained using the true velocity structure.

BIBLIOGRAPHY

- [1] R.G. Agarwal. A new method to account for producing time effects when drawdown type curves are used to analyze pressure buildup and other test data. In *Proceedings of SPE Annual Technical Conference and Exhibition*, Dallas, Texas, 1980.
- [2] K. Aki and P.G. Richards. *Quantitative Seismology theory and methods*. W.H. Freeman and company, San francisco, 2002.
- [3] James N. Albright and Christopher F. Pearson. Acoustic emissions as a tool for hydraulic fracture location: Experience at the fenton hill hot dry rock site. *SPEJ*, 22(4):523–530, 1982.
- [4] A. Bianco, A. Cominelli, L. Dovera, G. Nævdal, and B. Vallès. History matching and production forecast uncertainty by means of the ensemble Kalman filter: A real field application. In *Proceedings of the EAGE/EUROPEC Conference and Exhibition, London, U.K., 11-14 June*, number SPE 107161, 2007.
- [5] L. Block. *Joint hypocenter-velocity inversion of local earthquake arrival time data in two geothermal regions*. PhD thesis, Massachusetts Institute of Technology, 1991.
- [6] L.V. Block, C.H. Cheng, M.C. Fehler, and W.S. Phillips. Seismic imaging using microearthquakes induced by hydraulic fracturing. *Geophysics*, 59:102–112, 1994.
- [7] S. Bowman and T. Urbancic. Determining effective hydraulic fracture volume utilizing pso and seismic deformation. In *Proceedings of CSPG CSEG CWLS CONVENTION*, Calgary, Alberta, Canada, 2009.
- [8] K. P. Bube and J. K. Washborne. Wavetracing: Ray tracing for the propagation of band-limited signals: Part1-theory. *Geophysics*, 73(5):VE377–VE384, 2008.

- [9] P. Bulant. Two-point ray tracing in 3-d. *Pure and Applied Geophysics*, 148(3-4):421–447, 1996.
- [10] V. Cervený, I.A. Molotkov, and I. Psencik. *Ray methods in seismology*. Univ. of Karlova, Press, Prague, 1977.
- [11] J. Chen, J. Teng, and J. Badal. Constraining the anisotropy structure of the crust by joint inversion of seismic reflection travel times and wave polarizations. *Journal of Seismology*, 13(2):219–240, 2009.
- [12] J. Drew, D. Leslie, P. Armstrong, and G. Michaud. Automated microseismic event detection and location by continuous spatial mapping. In *Proceedings of SPE Annual Technical Conference and Exhibition*, number SPE 95513, Dallas, 2005.
- [13] C. A. Ehlig-Economides and J. Joseph. A new test for determination of individual layer properties in a multilayered reservoir. *SPE Formation Evaluation*, 2(3):261–283, 1987.
- [14] L. Eisner, P. M. Duncan, W.M. Heigl, and W.R. Keller. Uncertainties in passive seismic monitoring. *The Leading Edge*, 28(6):648–655, 2009.
- [15] A.A. Emerick. *History Matching and Uncertainty Characterization using ensemble-based methods*. Ph.D. thesis, The University of Tulsa, Tulsa, Oklahoma, 2012.
- [16] S. N. Erickson and R. D. Jarrard. Velocity-porosity relationships for water-saturated siliciclastic sediments. *JOURNAL OF GEOPHYSICAL RESEARCH*, 103(B12):30.385–30.406, 1998.
- [17] Geir Evensen. Sequential data assimilation with a nonlinear quasi-geostrophic model using Monte Carlo methods to forecast error statistics. *Journal of Geophysical Research*, 99(C5):10143–10162, 1994.
- [18] Geir Evensen. The ensemble Kalman filter: Theoretical formulation and practical implementation. *Ocean Dynamics*, 53:343–367, 2003.

- [19] Geir Evensen. The combined parameter and state estimation problem. *Computational Geosciences*, submitted:1–39, 2005.
- [20] Geir Evensen, J. Hove, H. C. Meisingset, E. Reiso, K. S. Seim, and O. Espelid. Using the EnKF for assisted history matching of a North Sea reservoir model. In *Proceedings of the SPE Reservoir Simulation Symposium, Houston, Texas, 26-28 February*, number SPE 106184, 2007.
- [21] E. L. Faria and P. L. Stoffa. Travelttime computation in transversely isotropic media. *Geophysics*, 59(2):272–281, 1994.
- [22] M. Fehler, L. House, and H. Kaieda. Determining planes along which earthquakes occur: Method and application to earthquakes accompanying hydraulic fracturing. *JOURNAL OF GEOPHYSICAL RESEARCH*, 92(B9):9407, 1987.
- [23] J. Jaime Gómez-Hernández and André G. Journel. Joint sequential simulation of multigaussian fields. In A. Soares, editor, *Geostatistic Troia 92*, pages 133–144. 1992.
- [24] V. Haugen, L.-J. Natvik, G. Evensen, A. Berg, K. Flornes, and G. Nævdal. History matching using the ensemble Kalman filter on a North Sea field case. In *Proceedings of the SPE Annual Technical Conference and Exhibition, San Antonio, Texas, 24-27 September*, number SPE 102430, 2006.
- [25] M. F. Jr. Hawkins. A note on the skin effect. *Trans. AIME*, 207:356–357, 1956.
- [26] N. He, A. C. Reynolds, and D. S. Oliver. Three-dimensional reservoir description from multiwell pressure data and prior information. *SPE Journal*, 2(3):312–327, 1997.
- [27] Nanqun He, Dean S. Oliver, and Albert C. Reynolds. Conditioning stochastic reservoir models to well-test data. In *Proceedings of the SPE Annual Technical Conference and Exhibition*, number SPE 38655, 1997.

- [28] Nanqun He, Dean S. Oliver, and Albert C. Reynolds. Conditioning stochastic reservoir models to well-test data. *SPE Reservoir Evaluation & Engineering*, 3(1):74–79, 2000.
- [29] Leigh House. Locating microearthquakes induced by hydraulic fracturing in crystalline rock. *GEOPHYSICAL RESEARCH LETTERS*, 14(9):919–921, 1987.
- [30] I.Lecomte. Finite difference calculation of first traveltimes in anisotropic media. *Geophysical Journal International*, 113(2):318–342, 1993.
- [31] B.R. Julian and D. Gubbins. Three-dimensional seismic ray tracing. *Journal of Geophysics*, 43:95–113, 1977.
- [32] F. J. Kuchuk and T. Habashy. Pressure behavior in horizontal wells in multilayer reservoirs with crossflow. *SPE Formation Evaluation*, 11(1):55–64, 1996.
- [33] F. J. Kuchuk, M. Karakas, and L. Ayestaran. Well testing and analysis techniques fro layered reservoirs. *SPE Formation Evaluation*, 1(4):342–354, 1986.
- [34] D. Kumar, M. Sen, and R.J. Ferguson. Traveltime calculation and prestack depth migration in tilted transversely isotropic media. *Geophysics*, 69(1):37–44, 2004.
- [35] Leif Larsen. Wells producing commingled zones with unequal initial pressures and reservoir properties. In *Proceedings of the SPE Annual Technical Conference and Exhibition*, number SPE 10325, 1981.
- [36] Leif Larsen. Similarities and differences in methods currently used to analyze pressure-transient data from layered reservoirs. In *Proceedings of the SPE Annual Technical Conference and Exhibition*, number SPE 18122, 1988.
- [37] Leif Larsen. Determination of pressure-transient and productivity data for deviated wells in layered reservoirs. *SPE Reservoir Evaluation & Engineering*, 2(1):95–103, 1999.
- [38] T. Lay and T.C. Wallace. *Modern Global Seismology*. Academic Press, 1995.

- [39] H. C. Lefkovits, P. Hazebroek, E. E. Allen, and C. S. Matthews. A study of the behavior of bounded reservoirs composed of stratified layers. *SPE Journal*, pages 43–58, 1961.
- [40] Michael. M. Levitan. Application of water injection/falloff tests for reservoir appraisal: New analytical solution method for two-phase variable rate problems. *SPE Journal*, 8(2):147–159, 2002.
- [41] G. Li, J. Chen, M. Han, A. Gajraj, Y. Xing, F. Wu, H. Liu, and C. Yin. Accurate microseismic event location inversion using a gradient-based method. In *Proceedings of SPE Annual Technical Conference and Exhibition*, number SPE 159187, San Antonio, 2012.
- [42] Gaoming Li, Mei Han, R. Banerjee, and A. C. Reynolds. Integration of well test pressure data into heterogeneous geological reservoir models. *SPE Reservoir Evaluation & Engineering*, 13(3), 2010.
- [43] Gaoming Li and A. C. Reynolds. Iterative ensemble Kalman filters for data assimilation. *SPE Journal*, 14(3):496–505, 2009.
- [44] S. Maxwell. Microseismic location uncertainty. *CSEG Recorder*, 34(4):41–46, 2009.
- [45] F. Miotti, G. Bernasconi, D. Rovetta, P. Dell’Aversana, and P. Milano. Estimation of rock properties from seismic, em and gravity well-log measurements. In *Proceedings of EGM International Workshop*, Capri, Italy, 2010.
- [46] Geir Nævdal, L. M. Johnsen, S. I. Aanonsen, and E. H. Vefring. Reservoir monitoring and continuous model updating using ensemble Kalman filter. *SPE Journal*, 10(1):66–74, 2005.
- [47] I. Nakanishi and K. Yamaguchi. A numerical experiment on nonlinear image reconstruction from first-arrival times for a two-dimensional island arc structure. *Journal of Physics of the Earth*, 34:195–201, 1986.

- [48] Dean S. Oliver. The averaging process in permeability estimation from well-test data. *Transactions of the Society of Petroleum Engineers*, 289:V319–324, 1990.
- [49] Dean S. Oliver, Albert C. Reynolds, and Ning Liu. *Inverse Theory for Petroleum Reservoir Characterization and History Matching*. Cambridge University Press, Cambridge, UK, 2008.
- [50] Donghong Pei, John A. Quirein, Bruce E. Cornish, Erkan Ay, Steve Zannoni, Calvin Kessler, and Will Pettitt. Velocity calibration for microseismic monitoring: Applying smooth layered models with and without perforation timing measurements. In *Proceedings of SPE Annual Technical Conference and Exhibition*, number SPE 115722, Denver, 2008.
- [51] P. Podvin and I.Lecomte. Finite difference computation of traveltimes in very contrasted velocity models: a massively parallel approach and its associated tools. *Geophysical Journal International*, 105(1):271–284, 1991.
- [52] F. Qin, Y. Luo, K.B. Olsen, W. Cai, and G.T. Schuster. Finite-difference solution of the eikonal equation along expanding wavefronts. *Geophysics*, 57(3):478–487, 1992.
- [53] L. L. Raymer, E. R. Hunt, and John S. Gardner. An improved sonic transit time-to-porosity transform. In *Proceedings of SPWLA Annual Logging Symposium*, 1980.
- [54] Albert C. Reynolds, Nanqun He, and Dean S. Oliver. Reducing uncertainty in geostatistical description with well testing pressure data. In Richard A. Schatzinger and John F. Jordan, editors, *Reservoir Characterization—Recent Advances*, pages 149–162. American Association of Petroleum Geologists, 1999.
- [55] E. Rothert and S. A. Shapiro. Microseismic reservoir characterization: Numerical experiments and case studies. In *Proceedings of the SEG Annual Meeting, San Antonio, Texas, 9-14 September*, number 2001-1584, page 4, 2001.

- [56] J.T. Rutledge and W.S. Phillips. Hydraulic stimulation of natural fractures as revealed by induced microearthquakes, carthage cotton valley gas field, east texas. *Geophysics*, 68(2):441–452, 2003.
- [57] W.A. Sambridge, K.A. Ranzinger, A.H. Balch, and C. Kruse. A dynamic programming approach to first arrival travelttime computation in media with arbitrarily distributed velocities. *Geophysics*, 57(1):39–50, 1992.
- [58] S.A. Shapiro, E. Rothert, V.Rath, and J.Rindschwentner. Characterization of fluid transport properties of reservoirs using induced microseismicity. *Geophysics*, 67(1):212–220, 2002.
- [59] S.M. Soukina, D. Gajewski, and B.M. Kashtan. Travelttime computation for 3d anisotropic media by a finite-difference perturbation method. *Geophysical Prospecting*, 51(5):431–441, 2003.
- [60] Kristian Thulin, Gaoming Li, Sigurd Ivar Aanonsen, and Albert C. Reynolds. Estimation of initial fluid contacts by assimilation of production data with EnKF. In *Proceedings of the SPE Annual Technical Conference and Exhibition*, number SPE 109975, 2007.
- [61] C.H. Thurber. Analysis methods for kinematic data from local earthquakes. *REVIEWS OF GEOPHYSICS*, 24(4):793–805, 1986.
- [62] I. Trinks. Travelttime tomography using irregular parameterized grids. *LITHOS Science Report*, pages 53–57, 2001.
- [63] J. Um and C.H. Thurber. A fast algorithm for two-point seismic ray tracing. *Bulletin of the Seismological Society of America*, 77(3):972–986, 1987.
- [64] John Vidale. Finite-difference calculation of travel times. *Bulletin of the Seismological Society of America*, 78(6):2062–2076, 1988.
- [65] John Vidale. Finite-difference calculation of traveltimes in three dimensions. *Geophysics*, 55(5):521–526, 1990.

- [66] N.R. Warpinski, Engler, C.J. Youngl, R. Peterson, P.T. Branagan, J.E. Fix, and E.James. Microseismic mapping of hydraulic fractures using multi-level wireline receivers. In *Proceedings of the SPE Annual Technical Conference and Exhibition, Dallas, Texas, 22-25 October*, number SPE 30507, page 11, 1995.
- [67] N.R. Warpinski, R.B. Sullivan, J.E. Uhl, C.K. Waltman, and S.R. Machovoe. Improved microseismic fracture mapping using perforation timing measurements for velocity calibration. *SPEJ*, 10(1):14–23, 2005.
- [68] J.K. Washbourne, K.P. Bube, P. Carillo, and C. Addington. Wave tracing: Ray tracing for the propagation of band-limited signals: Part 2 applications. *Geophysics*, 73(5):VE385–VE393, 2008.
- [69] C. Xu, P. A. Dowd, K. V. Mardia, and R. J. Fowell. A flexible true plurigaussian code for spatial facies simulations. *Computers and Geosciences*, 32(10):1629–1645, 2006.
- [70] T. Xu, Z. Zhang, E.Gao, G. Xu, and L. Sun. Segmentally iterative ray tracing in complex 2d and 3d heterogeneous block models. *Bulletin of the Seismological Society of America*, 100(2):841–850, 2010.
- [71] R. Xuan and P. Sava. Probabilistic microearthquake location for reservoir monitoring. *Geophysics*, 75(3):MA9–MA26, 2010.
- [72] Mohammad Zafari and Albert C. Reynolds. Assessing the uncertainty in reservoir description and performance predictions with the ensemble Kalman filter. *SPE Journal*, 12(3):382–391, 2007.
- [73] C.A. Zelt. Fast: 3-d first arrival seismic tomography programs. <http://terra.rice.edu/departament/faculty/zelt/fast.html>.
- [74] C.A. Zelt and P.J. Barton. 3d seismic refraction tomography: A comparison of two methods applied to data from the faeroe basin. *Journal of Geophysical Research*, 103:7187–7210, 1998.

- [75] C.A. Zelt and R.B. Smith. Seismic traveltime inversion for 2-d crustal velocity structure. *Geophysical Journal International*, 108(1):16–34, 1992.
- [76] F. Zhang and A. C. Reynolds. Optimization algorithms for automatic history matching of production data. In *Proceedings of 8th European Conference on the Mathematics of Oil Recovery*, 2002.
- [77] L. Zhang, Z. Yao, and J. Chen. Finite difference calculation of seismic first-arrival traveltime. *Progress in Geophysics*, 11(4):47–52, 1996.
- [78] A. Zhao, Z. Zhang, and J. Teng. Minimum travel time tree algorithm for seismic ray tracing: improvement in efficiency. *Journal of Geophysics and Engineering*, 1(4):245–251, 2004.
- [79] P. Zhao. An efficient computer program for wavefront calculation by the finite-difference method. *Computers & Geosciences*, 22(3):239–251, 1996.
- [80] X. Zhu and G. A. McMechan. Numerical simulation of seismic responses of poroelastic reservoirs using biot theory. *Geophysics*, 56(3):328–339, 1991.

APPENDIX A
SENSITIVITY ANALYSIS ON EVENT LOCATION

We assume a microseismic event is occurred at (x, y, z) and its first arrival time is recorded at a receiver (x_r, y_r, z_r) in a 3-D homogenous velocity model with velocity v . The origin time of the microseismic event is t_0 . The first arrival time at the receiver can be calculated as

$$t = t_0 + \frac{\sqrt{(x - x_r)^2 + (y - y_r)^2 + (z - z_r)^2}}{v}. \quad (\text{A.1})$$

The derivatives of first arrival time respect to event location parameters (x, y, z, t_0) are

$$\frac{\partial t}{\partial x} = \frac{x - x_r}{v\sqrt{(x - x_r)^2 + (y - y_r)^2 + (z - z_r)^2}}, \quad (\text{A.2})$$

$$\frac{\partial t}{\partial y} = \frac{y - y_r}{v\sqrt{(x - x_r)^2 + (y - y_r)^2 + (z - z_r)^2}}, \quad (\text{A.3})$$

$$\frac{\partial t}{\partial z} = \frac{z - z_r}{v\sqrt{(x - x_r)^2 + (y - y_r)^2 + (z - z_r)^2}}, \quad (\text{A.4})$$

$$\frac{\partial t}{\partial t_0} = 1. \quad (\text{A.5})$$

As the magnitude of velocity is usually on the order of 10^5 ft/s, the derivatives of the first arrival time respect to location parameters (x, y, z) are usually on the order of 10^{-5} which is much smaller than the derivative of first arrival time with respect to event occurring time which is 1. Thus, the even initiation time is always estimated with good accuracy by assimilating first arrival times. Among the derivatives of first arrival time with respect to the location parameters (x, y, z) , the difference is only in the numerator, which is the distance between event and receiver in its axis. Thus, the accuracy of coordinate estimates depend on the distance in that axis direction.